Multi-Wavelength Extragalactic Surveys: Star Formation of IR-Submm Selected Galaxies

Thesis

The Open University

Multi-wavelength extragalactic surveys: star formation of IR-submm selected galaxies

A thesis submitted for the degree of Doctor of Philosophy

Astronomy Discipline, School of Physical Sciences

Laia Barrufet de Soto

The Open University

May 2018

Abstract

This Thesis aims to identify and analyse galaxy populations over a range of redshifts in order to evaluate the star formation history over cosmic time. Explicitly focusing on the infrared to submillimetre regime, I carried out a comprehensive multiwavelength approach at the North and South Ecliptic Poles (NEP/SEP).

I explore four different methods to select high-z galaxies identifying a new sample of Dusty Star-Forming Galaxies (DSFGs) producing a legacy catalogue for future spectroscopic studies. These sources are modelled using contemporary spectral fitting algorithms. A detailed comparison of these algorithms concludes that the best results are obtained with the CIGALE package, deriving photometric redshifts and other physical properties.

The star formation rate and stellar mass were derived defining their position on the Main Sequence of Galaxies finding a population of DSFGs lying above the MS with high star-formation efficiencies and extreme star-formation possibly due to mergers at early times.

A lower redshift counterpart population at radio wavelengths was studied via radio-optical identification and multiwavelength data, calculating photometric redshifts providing better results than simply cross-matching the catalogue with heterogeneous ancillary redshift data. This sub-milliJansky population is then classified by infrared luminosity finding that the stellar mass and gas mass are one order of magnitude higher in more luminous galaxies than in less luminous galaxies. This population is segregated into AGN and DSFGs using a new infrared colour-colour diagrams concluding that using AKARI bands results in better AGN selection than that from WISE.

Optical data at the SEP is reduced creating a new catalogue filling a vital gap in the multiwavelength data in this field. This new catalogue is combined with Spitzer and Herschel data identifying a population of Dust Obscured Galaxies at $z\sim2$ the peak of the cosmic star-formation history.

Acknowledgements

Firstly thank you to my supervisors Chris Pearson and Stephen Serjeant for taking me on as a PhD student, my former supervisor Glenn White for giving me the opportunity to start a PhD and to Ismael Perez-Fournon for helping me in my first steps.

At RAL Space a special thanks goes to Diego Pardo for his enormous help during this thesis and to Maria del Carmen Campos for making the PhD experience more enjoyable. Thanks to my English teacher Olivera Viljoen-Ciosici for her tuition and support and to Mireya Etxaluze for the tips and supportive chats in the corridor.

At the Open University, thank you to Beatriz Mingo for the help with the radio chapter, and to Helen Davidge and Natalia Pascual. Thank you to Ivano Baronchelli for his help with the optical catalogue and for being my first collaborator.

A thank you to my family, Enric Barrufet, Dolors de Soto, Silvia Barrufet and to Xavier Roldan for believe in me and for never letting me go down before and during this thesis, none of the work of this thesis could have been done without their help.

Finally thanks to Cristina Protasio for being there with supportive chats at any time, Melania Cubas for the never-ending emails and Miren Agote for her support, working until late in her office and for all the coffees! A special thanks to Darren Batey for being my unofficial English teacher and for the hundreds of "keep goings".

Contents

List of Figures

List of Tables

Chapter 1

Introduction

1.1 Overview of Infrared astronomy

1.1.1 Background

The fact that the energy density of the Universe, derived from stars and galaxies, is split almost equally between the optical/ultraviolet regime via stellar emission and the infrared primarily via dust emission of reprocessed starlight has placed great importance on the emerging field of infrared astronomy over the last 35 years. The challenges associated with attempting infrared astronomy from the ground, where water vapour in the Earth's atmosphere absorbs the majority of astrophysical radiation, coupled with the technical advances in detector technology, has led to a rapid advancement in infrared space telescopes.

Infrared observations are necessary to understand the process of star formation in galaxies since young stars are born within dusty clouds with the hot UV/optical emission from young massive stars being absorbed by the dust, reprocessed and remitted at infrared wavelengths. A complete study of how galaxies evolve with cosmic time and what they made of can only be fully achieved with the addition of infrared observations.

The work in this thesis is based on data from surveys in the long wavelength part

of the spectrum, either from the ground (through narrow atmospheric windows) at submillimetre wavelength or from space via infrared space telescopes. In particular, this thesis exploits data taken with the *Herschel* Space Observatory (far infrared and submillimetre wavelengths) and the *AKARI* surveyor mission (near, mid and far infrared wavelengths). This work also exploits and places great emphasis on the advantage of combining these data sets with other multi-wavelength extragalactic surveys provide comprehensive coverage of the spectra of galaxies from radio to X-ray wavelengths.

This first chapter gives a review of the relevant infrared spaces telescopes, the discover of submillimetre galaxies and their contribution to the star formation history of the Universe relating this with the so-called 'main sequence' of galaxies - the extragalactic version of the stellar Hertzsprung-Russell diagram. A brief explanation of radio galaxies and active galactic nuclei (AGN) is provided describing their role in the extragalactic zoo. Finally, the importance of multi-wavelength extragalactic surveys in understanding and interpreting the spectral energy distribution of galaxies and their physical properties is discussed.

1.1.2 A brief history of infrared space missions

IRAS

Launched in 1983, the Infra Red Astronomy Satellite (IRAS; Neugebauer et al. (1984)) was the first IR satellite telescope in space and opened the field of infrared astronomy. IRAS surveyed the entire sky at 4 infrared wavelengths (12, 25, 60 and 100 μm), producing a point source catalogue (PSC) containing more than 250,000 new infrared sources, revolutionising our understanding of star-formation and galaxy evolution.

One of the IRAS mission's main highlights was the discovery of hundreds of extremely bright infrared luminous galaxies - defined by their luminosity and termed luminous infrared galaxies (LIRGs) with $L > 10^{11} L_{\odot}$ and ultra luminous infrared galaxies (ULIRGs) with $L > 10^{12} L_{\odot}$.

The IRAS survey was limited to the local Universe, with a sensitivity of 360 mJy at 60 μm for the IRAS PSC corresponding to a median redshift of median redshift of $z \sim 0.03$ (Saunders et al., 2000). The IRAS Faint Source Catalogue (Moshir, 1991) probed out to fainter fluxes of 360 mJy at 60 μm and detected galaxies out to redshift 2.3 (e.g. the archetypal Hyperluminous galaxy IRAS F10214+4724 (Rowan-Robinson et al., 1991)).

ISO The short lived *IRAS* ($\sim$10 months) gave hints of strong evolution in star-forming galaxies with cosmic time, leading to the launch of ESA's Infrared Space Observatory (ISO; (Kessler et al., 1996)) in 1995. ISO studied star formation in galaxies and its role in galaxy evolution over the wavelength range 2.5 - 240 μm). The largest cosmological survey with ISO covered a mere 12 square degrees (ELAIS, Oliver et al. (2000)) detecting around 1000 galaxies in the most sensitive band at 15μm. ISO pushed studies of galaxy evolution from the local IRAS universe out to redshifts $\sim$1 showing the dusty galaxies evolved strongly, being much brighter at higher redshift. ISO allowed us to distinguish between the star formation in local starburst galaxies and the Active Galactic Nuclei (AGN) contribution, showing that the energy from local ULIRGs is produced by star formation rather than AGN activity and probably related to galaxy mergers (e.g. Rigopoulou et al. (1999)).

However, the data provided by both *IRAS* either *ISO* was still mainly restricted to the nearby and intermediate redshift Universe, with the extreme redshift Universe still only accessible in the rest-frame UV to optical.

Spitzer

The launch of *Spitzer Space Telescope* (Werner et al., 2004a) in 2003 introduced the next generation of infrared extragalactic surveys with sample sizes of a million (i.e. the Spitzer Wide-area Infrared Extragalactic Survey, SWIRE, Lonsdale et al. (2004)). *Spitzer* covered the wavelength range from 3-160μm with 2 survey instruments; the Multi-band Imaging Photometer for *Spitzer* (MIPS; Rieke et al. (2004)) with detector arrays at 24, 70 and 160 μm; and the Infrared Array Camera (IRAC; Fazio et al. (2004)) covering with detector arrays at 3.6, 4.5, 5.8 and 8 μm. Importantly, *Spitzer*

had a long cryogenic lifetime, almost 6 years (3 times more than *ISO* and more than 6 times *IRAS*) and moreover, the IRAC instrument is still operating in the post-cryogen 'warm phase' (with the 2 shortest bands). In fact, *Spitzer* still produces useful data such as the recent observations at the North Ecliptic Pole (NEP) at 3.6, 4.5 μm Nayyeri et al. (2018) that will be used as a future work (see Section 6.2.1).

Spitzer's long lifetime and broad spectral coverage allowed detailed studies of the distant Universe and also complete sampling of the full spectra of galaxies from near- to far-infrared wavelengths allowing a much better understanding of the effect of dust in galaxies. In fact, before *Spitzer* it was necessary to assume a typical shape for the dust attenuation law, e.g. Calzetti et al. (2000). *Spitzer* data has contributed to a better understanding of the properties of dust attenuation and emission.

The exceptional sensitivity of the *Spitzer* 24 μm band allowed the far-infrared cosmic infrared background (CIB), first discovered by the COBE mission (see Figure 1.1), to be resolved into its individual point sources (Dole et al., 2006) . *Spitzer* showed that much of the contribution to the CIB at around 70-160 μm comes from LIRGs at redshift $\sim$1.

New facilities making surveys over an unexplored wavelength range invariably produce new populations of galaxies. *Spitzer* identified a population of Dust Obscured galaxies (DOGs), extremely faint in the optical but bright in the mid-IR due to the absorption of the young starlight by dust (Dey et al., 2008). DOGs represent a family of mid-infrared bright dusty galaxies, ranging from pure starburst, to obscured AGN-dominated sources, to very luminous PAH emitters (Casey, Narayanan & Cooray, 2014). A major part of this thesis deals with different populations and their selection methods and Chapter 5 will specifically analyse a new population of 157 DOGS in the AKARI Deep Field South (ADFS) field based on the 24 μm *Spitzer* catalogue of Clements et al. (2011).

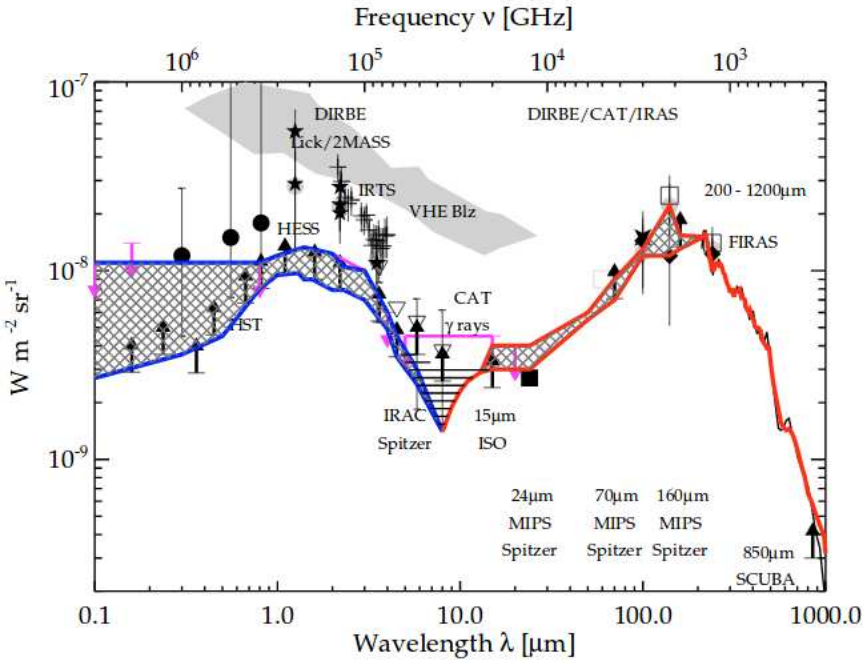

Figure 1.1: Cosmic optical (COB) and infrared background CIB): Image based on (Dole et al., 2006). The CIB measured by COBE-FIRAS and *Spitzer* (in red) contributes nearly equally as the COB (blue). The mid-infrared 24 μm sources contribute more than 70 % of the CIB around the peak between 70 μm and 160 μm.

AKARI

The *AKARI* surveyor telescope, launched in 2006 Murakami et al. (2007), was a small diameter IR telescope ($\sim$ 0.7m) that primarily carried out an All-Sky survey, using the Far Infrared Surveyor instrument (FIS; Kawada et al. (2007)) in four far-infrared bands between 50 and 180 μm, detecting almost 500,000 sources. In addition, *AKARI* carried out deep legacy surveys in the North and South Ecliptic Poles (NEP, SEP respectively). At the SEP, *AKARI* surveyed approximately 12 square degrees with the FIS instrument over the *AKARI* deep field south (ADF-S) legacy field. At the NEP *AKARI* carried out a pair of concentric surveys with its mid-infrared instrument, the InfraRed Camera (IRC; Onaka et al. (2007)) . The IRC incorporated nine bands that provided near continuous coverage from 2-24μm: N2 (2.4 μm), N3 (3.2 (μm), N4 (4.4 μm), S7 (7.3 μm), S9W (9.2μm), S11 (10.9 μm), L15 (16.2 μm), L18 (19.8 μm), L24 (23.3 μm). This continuous coverage allowed a unique view of the near and mid infrared region, allowing us to distinguish between emission from the PAH

features and AGN emission. This property will be used in this Thesis to distinguish AGN in the NEP fields (see Figure 4.5).

The *AKARI* surveys at the NEP form the basis for the multi-wavelength surveys analysed in this thesis (Chapters 2, 3 and 4). The ADF-S provides the multi-wavelength data sets analysed in Chapter 5. These legacy fields are described in detail in Section 1.3.2.

WISE

The Wide-field Infrared Survey Explorer (*WISE*; Wright et al. (2010)) was launched in 2009 and conducted an all-sky survey in the mid-infrared at 3.4 μm (W1), 4.6 μm (W2), 12 μm (W3) and 22 μm (W4). The diameter of the WISE primary mirror was only half the *AKARI* (0.4 m), however WISE contributed to the areas of solar system studies (especially asteroids), stellar and extragalactic astrophysics. Although the WISE 22 μm band was not as sensitive as the *Spitzer* 24 μm band, WISE had the advantage of all sky coverage allowing correlations with other large area surveys such as SDSS. The choice of WISE wavebands were also advantageous in the development of AGN classification by colour-colour diagrams. In Chapter 4, I summarise these colour-colour classifications and extend and improve them with the addition of *AKARI* data.

Herschel

The *Herschel* Space Observatory (HSO; Pilbratt et al. (2010)) was launched in 2009 and observed almost 1/10 of the entire sky over almost four years, detecting more than a million dusty galaxies. *Herschel* was the largest mirror (primary diamter 3.5m) launched into space to date and incorporated three instruments: the Spectral and Photometric Imaging REceiver (SPIRE; Griffin et al. (2010)) covering the submillimetre region between 250 μm, 350 μm and 500 μm, the Photodetector Array Camera and Spectrometer (PACS; Poglitsch et al. (2010)) observing in the far-infrared at 70 μm, 100 μm and 160 μm, and the Heterodyne Instrument for the Far Infrared (HIFI; de Graauw et al. (2010)) providing high resolution spectroscopy in 7 bands from far-infrared to submillimetre wavelengths.

SPIRE, operated in all three of its bands bands simultaneously, and was mainly used for extended surveys of tens - hundreds of squares degrees (Oliver et al., 2012), detecting close to a million galaxies, including observations in both, the North Ecliptic Pole and the South Ecliptic Pole regions. Combining SPIRE data with PACS observations, provides 5 photometric bands (since PACS could only observe in 2 of its 3 bands simultaneously) allowing a detailed characterisation of the far infrared emission peak (rest frame 60-200 μm). In this thesis the data provided by SPIRE (and PACS) has been specifically used to classify and study high-redshift sources (See Chapters 2 and 3.

Herschel marks a revolution in the study of high-z submillimetre galaxies (SMGs), since it was the first time to observe at submillimetre wavelengths at high resolution from space. Previously, almost all observations of SMGs were made from the ground using facilities such as the SCUBA instrument on the JCMT, Hawaii (see Section 1.2.4 for more details on SMGs). *Herschel* has been commonly use to select high-z dusty star forming galaxies (DSFGs) making an unprecedented contribution in the number of these sources at high-z without been limited to cold dust submillimetre sources as is the case with SCUBA-2 (see Casey, Narayanan & Cooray (2014) for review and the Section 1.2.4 in this Introduction).

1.1.3 Wavelength ranges and emission processes in galaxies

Classically the infrared region can be divided into three distinct regions, the near infrared from 0.8-5μm, the mid-infrared region from 2-30μm and the far-infrared from 30-200μm (see Figure 1.2). Additionally, the submillimetre region can be defined as the wavelength range longwards of $\sim$200-1000μm. Infrared continuum emission at mid-far-infrared wavelengths is mainly attributed to a population of carbon/silicon dust grains with a range of sizes from 0.01-1 micrometres (e.g. Draine & Lee (1984), Rowan-Robinson (1992)).

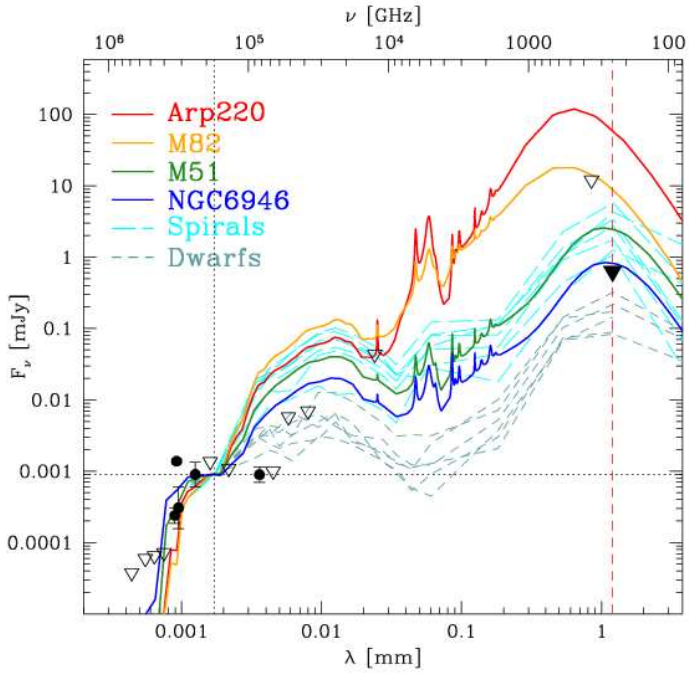

Figure 1.2: Spectral energy distribution (SED) of typical galaxies: the starburst M82 (orange) and Arp220 (red), spirals (blue and green lines) and dwarf galaxies (dashed lines) (Walter et al., 2012). These SEDs are focused at infrared wavelengths, where from 2-5μm shows the near infrared, 5-30μm the mid-infrared region, and 30-200μm the far infrared.

Near Infrared The 0.8-5μm, near-infrared region is typically dominated by the photospheres of red giant and red supergiant stars and therefore representative of the older stellar population. This region includes the 1.6μm feature, due to the strong H^- ion emission in cool stars used as an important redshift indicator in the *Spitzer*-IRAC bands (Sawicki, 2002).

Mid Infrared The 5-30μm, mid-infrared region in star-forming galaxies is dominated by the emission from hot dust (>100K) heated by young massive stars. The mid-infrared spectra of star-forming galaxies is also dominated by a complex set of emission features at 3.3, 6.2, 7.7, 8.6, 11.3 & 12.7μm attributed to Polycyclic Aromatic Hydrocarbon (PAH) molecules, chains of 50-100 carbon atoms (∼5-20 angstroms across) and the silicate absorption feature at 9.7μm (Boulanger et al., 1998),
(Peeters, Spoon & Tielens, 2004) and (Draine & Li, 2007). These PAH features can be as broad as instrumental filter bandwidths and may contribute up to 30% of the in-

frared luminosity of star-forming galaxies and can be used to trace the star-formation rate (e.g. Spoon et al. (2004)). The presence of a central AGN in a dusty galaxy can have a significant effect on the mid-infrared spectrum due to the extreme heating effect of the AGN emission (accretion disk) (see Figure 1.3). The dust torus heated by the central AGN emits strongly over the 5-30μm range with the dust being heated to its sublimation temperature, resulting in the destruction of small grains (including PAHs) and a featureless shallow power law spectrum (e.g. Laurent et al. (2000)). Analysis of these mid-infrared colours can be used to distinguish AGN from star-forming galaxies (e.g. Brand et al. (2006)).

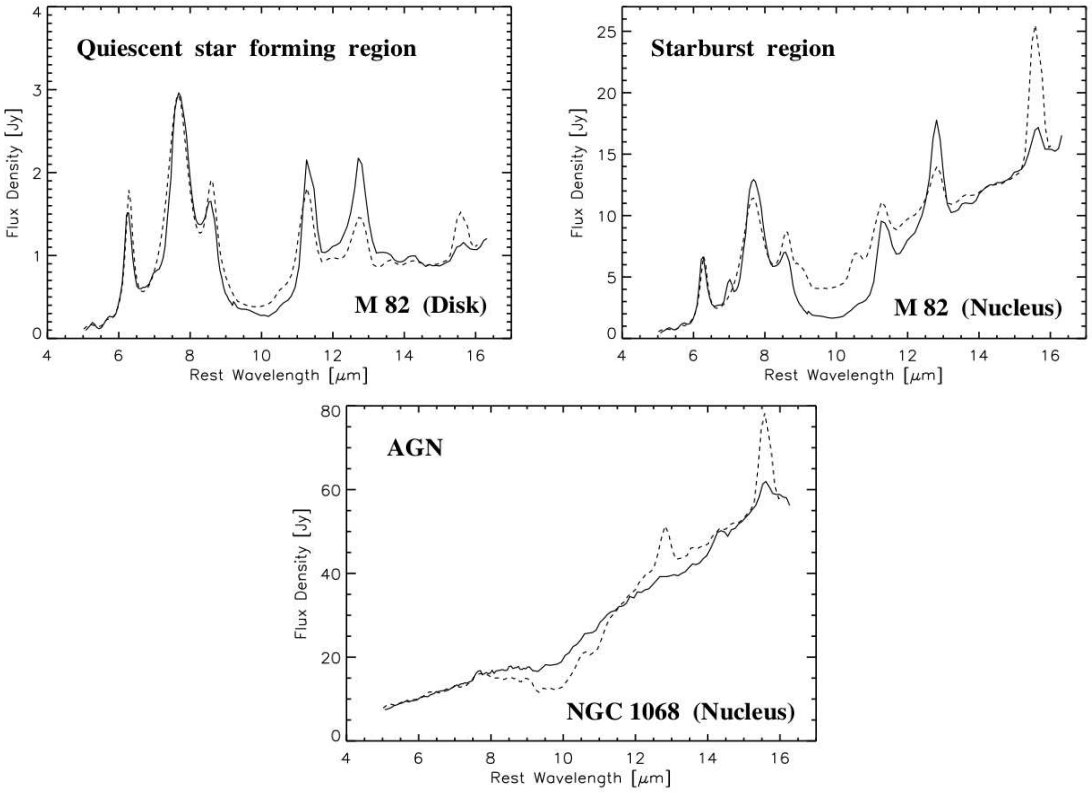

Figure 1.3: Spectral energy distribution (SED) in the mid infrared of the starburst M82 in the disk and in the nucleus (top images) and to a galaxy hosting an AGN (bottom), where the lines are the observation and the dashed lines the models (Laurent et al., 2000). The PAHs features are better defined where there is no an AGN presence since there is no a destruction of the grains due to extreme heating from the AGN.

Far Infrared The 30-200μm, far-infrared region is dominated by the re-radiated of stellar emission by cool dust grains (20-50K). This emission has a characteristic thermal (modified Black Body) shape peaking between 60-200μm, where the observed

flux is defined as f_ν:

$$f_\nu = \frac{M_d}{D^2} \cdot k_{abs} \cdot B_\nu(T_d) \tag{1.1}$$

if assumed all the grains have the same temperature T_d, where M_d is the mass of the dust, D is the distance of the object, k_{abs} is the grain absorption cross section per unit mass and $B_\nu(T_d)$ is the Plank function $B_\nu(T_d) = \frac{2\,h\,\nu^3}{c^2}\left(1/\exp^{\frac{h\,\nu}{k\,T_d}-1}\right)$. Traditionally, the far-infrared galaxy population was divided into populations of cool, relatively quiescent galaxies and warmer star-forming populations depending on their far-infrared (60/100 μm) colours (e.g. Rowan-Robinson & Crawford (1989)). In this scenario the emission from normal galaxies is attributed to the emission from interstellar dust heated by the stellar population. The emission from starburst galaxies is from reprocessed starlight from hot young stars embedded in optically thick dust clouds.

Submillimetre Evidence for the emission from a cold dust component was hinted at by observations at 170μm by *ISO* (Stickel et al., 2000), however, a revolution in the field was made by the SCUBA instrument discovering a population of hitherto unknown submillimetre galaxies (e.g. Smail, Ivison & Blain (1997), Hughes et al. (1998), see Section 1.2.4 for details) containing large amounts of cold (<30K) dust (e.g. Dunne et al. (2000), Mortier et al. (2005)).

1.2 Star formation and AGN feedback

1.2.1 Star-forming galaxies and star formation.

The study of the star formation history allows us to understand how galaxies evolved with cosmic time and built up their stellar masses. The star formation history is captured by the Madau diagram (Madau, Pozzetti & Dickinson, 1998) which plots the star formation rate density over the cosmic time. Initially this study was based on the optical/UV emission from galaxies and suggested that the peak of cosmic star formation occurred at z $\sim$ 1. However, recent studies - which take into account dust obscuration and the reprocessing of starlight at infrared wavelengths as observed by the telescopes introduced in Section 1.1.2 - show that Madau, Pozzetti & Dickinson (1998) underestimated the star formation at early epochs. The star formation rate density increases systematically from early times (z $\approx$ 10, around 500 Myr after the Big Bang) to peak at z $\approx$ 2 (3 Gyrs after the Big Bang), forming most of the stellar mass in the present day Universe between 3 $\gtrsim$ z $\gtrsim$ 1. The star-formation rate then declines rapidly to z = 0. The inclusion of infrared data, in addition to the UV-optical in calculating the star formation rate is essential to accurately define the peak and evolution of star-formation over cosmic time (see Figure 1.4).

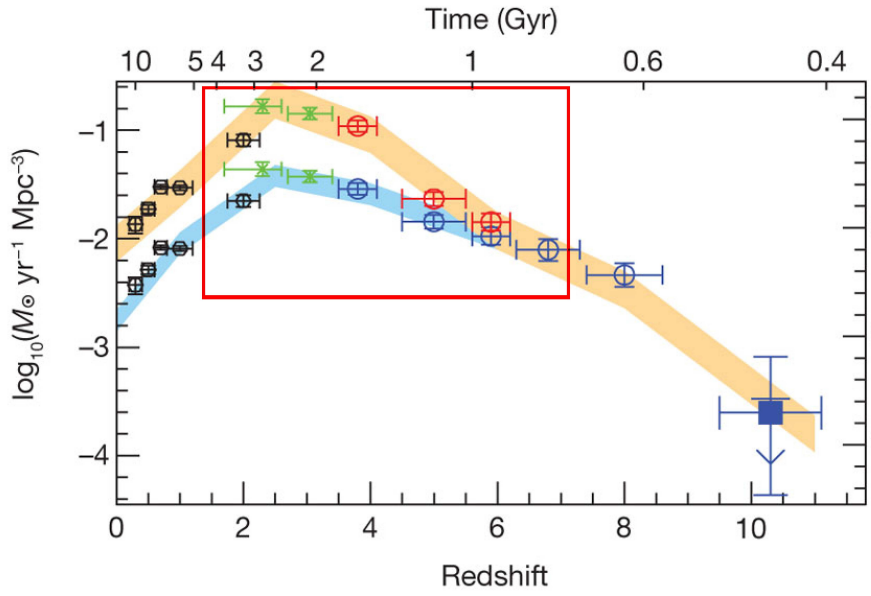

Figure 1.4: The star formation rate density over cosmic time (adapted from Bouwens et al. (2011)). The blue region corresponds the rest-frame continuum UV, whereas the orange region shows the infrared correction. The red square shows where the star formation density grows peaks and decreasing ($6 \gtrsim z \gtrsim 2$) and where Chapters 2 and 3 are focused on studying the star-formation and evolution at infrared and submillimetre wavelengths (figure extracted from the review Casey, Narayanan & Cooray (2014)).

Although the star formation rate density provides a global approach to star formation over cosmic time taking into account the volume, it is common to focus studies on specific sources or populations of sources. In fact, the study of star-forming galaxies (SFG) - extreme galaxies that form stars at the rate of several thousands of solar masses per year - have been the focus of both low and high-z studies. The generic name applied to such galaxies with high star formation rates is starburst, however a more accurate quantitative definition was given by (Elbaz et al., 2011) after Herschel evaluation. In that work, they define a starburst by the excess of specific star formation rate (sSFR) which evolves over the cosmic time: $\mathrm{sSFR_{starburst}[Gyr^{-1}]} > 52 \cdot \mathrm{t_{cosmic}^{-2.2}}$. This definition inevitability relates the star-formation with the stellar mass (sSFR = SFR / $\mathrm{M_{star}}$) of galaxies defining a main sequence of galaxies, defined by $\mathrm{sSFR[Gyr^{-1}]} = 26 \cdot \mathrm{t_{cosmic}^{-2.2}}$ and discussed in detail in Section 1.2.3. Note that this definition takes into account the redshift (directly related to cosmic time) and due to this fact, two sources with the same sSFR can be considered starburst galaxies depending on the redshift (see Figure

1.5).

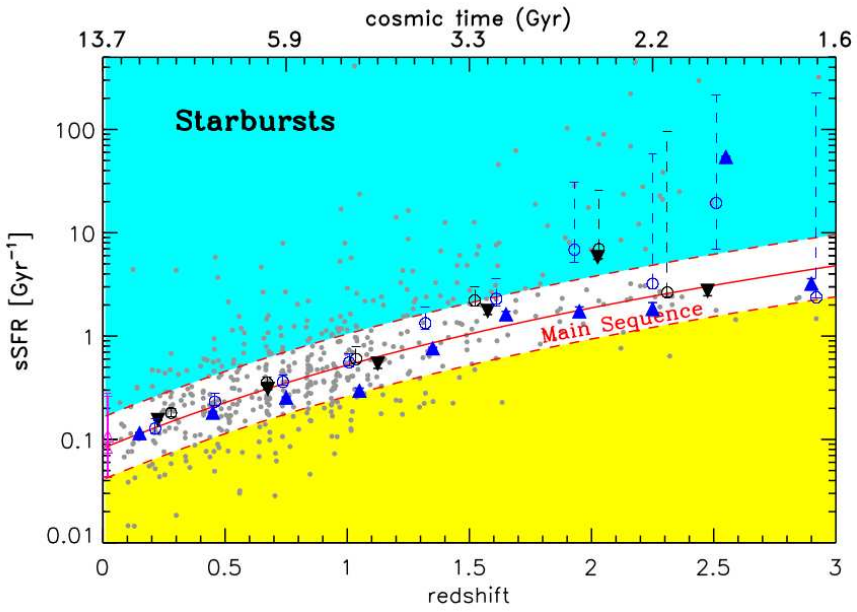

Figure 1.5: Specific star formation rate (sSFR) against redshift (bottom axis) and cosmic time (top axis) for the *Herschel* sample described in Elbaz et al. (2011). The starburst galaxies lie the line defined by $\mathrm{sSFR_{starburst}[Gyr^{-1}]} > 52 \cdot \mathrm{t_{cosmic}^{-2.2}}$, whereas the main sequence of galaxies is defined by the red line as $\mathrm{sSFR[Gyr^{-1}]} = 26 \cdot \mathrm{t_{cosmic}^{-2.2}}$. Therefore, the definition of starburst in this case, are galaxies two times above the main sequence (upper dashed red line).

We have seen in Section 1.1.2 that star-forming galaxies can also be classified by their infrared luminosity, commonly defined as luminous (LIRGs; $\mathrm{L_{IR}} > 10^{11}\mathrm{L_{\odot}}$), ultra-luminous (ULIRGs; $\mathrm{L_{IR}} > 10^{12}\mathrm{L_{\odot}}$) and hyperluminous (HLIRGs; $\mathrm{L_{IR}} > 10^{13}\mathrm{L_{\odot}}$) infrared galaxies. It is now commonly understood that such galaxies evolve strongly with redshift (e.g. Le Floc'h et al. (2005)), and while ULIRGs in particular have an insignificant contribution in the local Universe, their contribution to the star formation history increases with redshift - contributing 10 % at $\mathrm{z} \sim 1$ - peaking at $\mathrm{z} \sim 2$ with a 50 % of contribution in the star formation rate density (see Figure 1.6).

Why does the SFR peak at this specific redshift ($z \sim 2$) and decrease thereafter? Stellar winds that produce a dispersion of the gas may contribute to this decrease, however, other options may be AGN mechanical or radiative feedback or simply the depletion of cold gas available in the galaxy (Bouwens et al., 2011). AGN feedback (Silk & Rees, 1998) produces both a trigger for the first stages of star-formation, then,

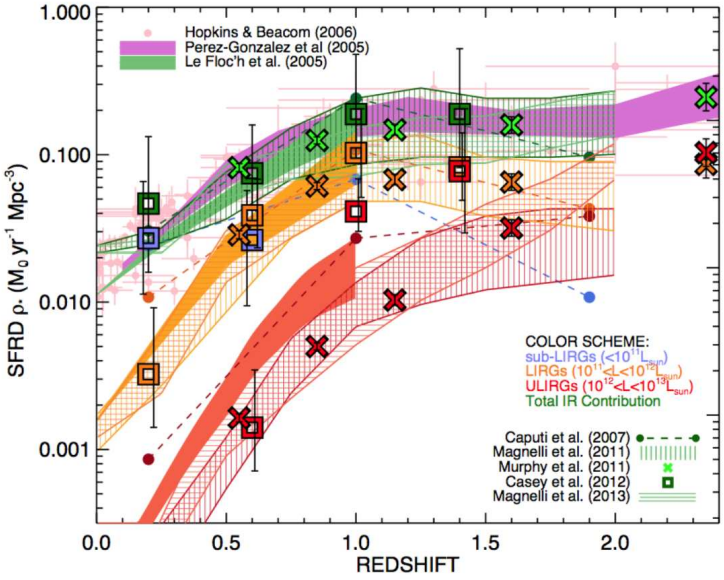

Figure 1.6: Star formation Rate density over cosmic time with the contributions broken down by luminosity class: ULIRGs (in red) are not common in the local Universe, having a small contribution. LIRGs (orange) contribute more to the star formation density due to their larger numbers reaching the peak at z $\sim$ 1 whereas ULIRGs reach the peak of contribution at z $\gtrsim$ 2.

at later stages, a quenching of star formation caused by the gas becoming ionised by the black hole accretion, or blown out completely by radiation pressure, thus preventing the gas from cooling and contracting to form stars. In any case the star-formation and AGN activity in galaxies seems connected as shown in Figure 1.7.

1.2.2 Star formation indicators.

There are different SFR indicators across different wavelengths which enable the study and measurement of various properties related with star formation. Since young massive stars emit a significant fraction in the UV, this wavelength range would appear to be a good tracer for young star formation. However, dust attenuation peaks at UV wavelengths (extinction and reddening effects) and has be corrected in order to retrieve the true star-formation rate. Estimators at optical wavelengths are based on recombinations lines, which measure ionising radiation from young stars, and similarly to the UV should be corrected for dust attenuation More reliable estimations of star-formation, particularly for high redshift sources, must be made at FIR wavelengths.

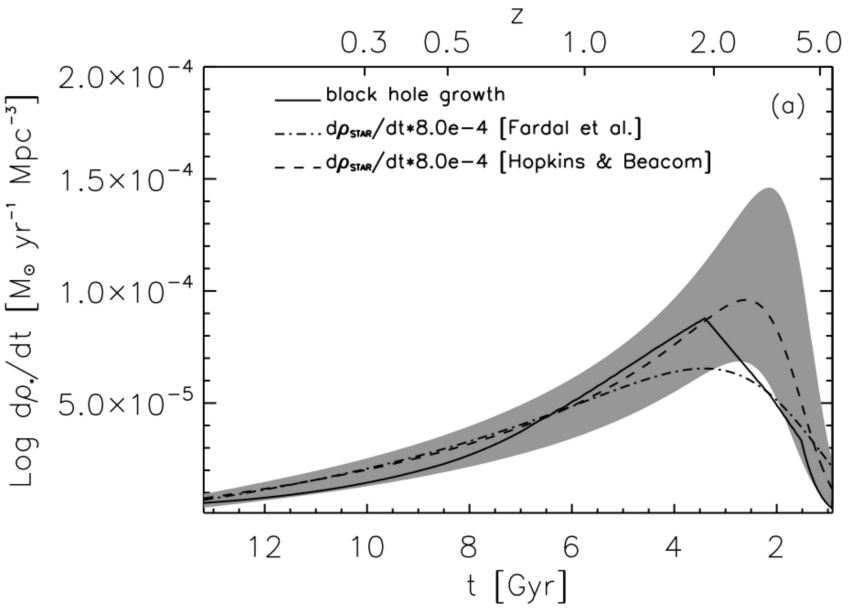

Figure 1.7: Cosmic history of both stellar mass and BH growth (Shankar, Weinberg & Miralda-Escudé, 2009). The figure compares the BH accretion rate to the SFR as a function of redshift, note that both AGN activity and SFR peak at z $\sim$ 2 and then progressively decline.

Star formation at these wavelengths is usually calculated in proportion to the luminosity, the Kennicutt law being the most common method (Kennicutt, 1983). Kennicutt (1998) present an overview of the different SFR equations. The star-formation rate may be calculated using emission lines if possible (like the common H_α), or directly from the luminosity. The use of a monochromatic luminosity is possible, for instance (Elbaz et al., 2011) at 8 μm, however a better measure can be obtained by using a bolometric luminosity defined across a wide wavelength range, e.g. L_{IR} = 8 μm - 1000 μm defined by:

$$\mathrm{SFR} = 1.17\mathrm{x}10^{10}\mathrm{L_{IR}}(\mathrm{L_\odot})\ [\mathrm{M_\odot/yr}] \tag{1.2}$$

which is frequently used in dusty star forming galaxies (see Casey, Narayanan & Cooray (2014) for review) and is adopted as the conversion assumed in Chapter 2 and 5 of this Thesis. However, in Chapters 3 and 4, specific spectral fitting codes have been used to calculate the SFR:

$$\mathrm{SFR} = \mathrm{M_{gal}}/\tau(\mathrm{e}^{\mathrm{t}/\tau} - 1)\ [\mathrm{M_\odot/yr}] \tag{1.3}$$

used by the code Cigale (see Chapter 3 for further information) takes into account the mass of the galaxy and several options for the star formation history in order to calculate the star-formation rate taking into account the entire spectrum and a model for the galaxy, instead of an empirical relationship of the luminosity at different wavelengths - as in the Kennicutt law - which is mainly based on a pre-*Spitzer* (*AKARI*, *WISE*, *Herschel*) perspective of the local Universe.

Furthermore, while Kennicutt laws uses a Salpeter IMF Salpeter (1955) initial function mass (IMF; the mass distribution of a stellar population at the beginning of galaxy formation), equation 1.3 can incorporate several IMFs. The Salpeter IMF was the first definition of an IMF and has been used for its simplicity and historical reasons, however, alternative IMFs have been defined since Salpeter's 1955 work, showing that the IMF of Salpeter (1955) can overestimate low mass stars in the stellar population (see Figure 1.8 for a compilation of IMFs). Furthermore, the more recent Chabrier IMF Chabrier (2003) alters the infrared luminosity to SFR by a factor 1.8 bigger than by using Salpeter IMF (Casey, Narayanan & Cooray, 2014). This Thesis assumes a Chabrier IMF and the equation 1.3 in Chapters 3 and 4.

1.2.3 Main Sequence of galaxies

Star-forming galaxies exhibit a tight correlation between their star-formation rate and their stellar mass ($SFR \propto M_*^{\alpha}$). This has led to the definition of the so-called "Main Sequence of galaxies" (MS, defined by Noeske et al. (2007) for a limited stellar mass ($11 < \log(M/M_{\odot}) < 12$) over a narrow redshift ($0.2 < z < 0.7$) range) in the spirit of the stellar main sequence in the Hertzsprung-Russell diagram.

This relationship between the SFR and the stellar mass was evaluated qualitatively by Daddi et al. (2007), Elbaz et al. (2007)). In this Thesis the more recent definition of the Main sequence of galaxies at different redshift is taken from Speagle et al. (2014) as:

$$\log(SFR) = 0.84 - 0.026t(z)\log(M_* + 0.11t(z) - 6.51) \tag{1.4}$$

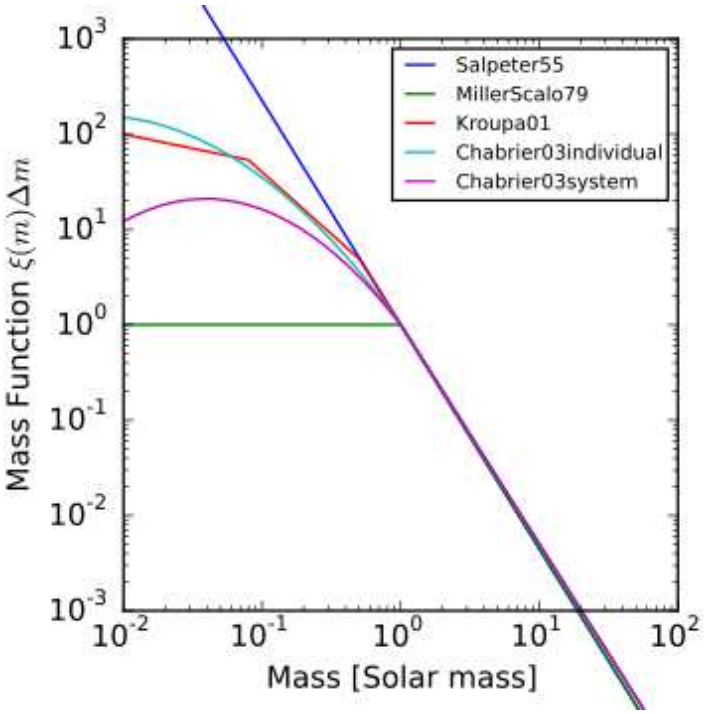

Figure 1.8: Initial mass function from several authors: the blue line shows the first IMF defined by Salpeter (1955) as a power law, whereas alternative IMFs assume some cut-off for for sub-solar masses. The most recent one, and the one used in this Thesis, is the Chabrier (2003) IMF.

where t(z) is the age of the Universe in [Gyr] and M_* is the stellar mass. Speagle et al. (2014) reports a tight relation, with small scatter around the relation. A popular limit for outliers from the MS (above or below) is measured as three times above or below this relation (da Cunha et al., 2015). This approach is slightly different from the starburst galaxy definition used by Elbaz et al. (2007) (see Section 1.2.1) but has it been adopted in this Thesis (Chapter 3) for the validity of the definition at high-z and the consensus in the literature that allows a comparison with previous work such as da Cunha et al. (2015). Furthermore, Speagle et al. (2014) includes 25 studies (including in Elbaz et al. (2007)) that define the MS of galaxies from different approaches (redshifts, IMF, etc) and it is valid up to a z = 6, which make it the more robust definition at the moment.

The common consensus is that the galaxies that lie on the MS form stars over long-time scales ($1-2$ *Gyr*), however, there are galaxies off the MS with much high SFR. These galaxies are often referred to as starburst galaxies and their gas consumption

rate is faster ($0.01 - 0.1\ Gyr$) than those on the MS.

1.2.4 Submillimetre galaxies.

The discovery of a high-z population of bright sources at sub-mm wavelengths (200μm - 1 mm), 20 years ago, the so-called submillimetre galaxies (SMGs) (e.g. Barger et al. (1998) Smail, Ivison & Blain (1997), Hughes et al. (1998)), posed critical questions about the evolution of galaxies in the early Universe. The first discovery of these sources was made with the submillimetre Common-User Bolometer array (SCUBA) camera on the James Clerk Maxwell Telescope (JCMT), Hawaii which detected a new population of bright submillimetre galaxies nearly invisible at ultraviolet and optical wavelengths (see Blain et al. (2002) for review). These observations at submillimetre wavelengths opened the distant dusty Universe as never before, taking advantage of the very negative k-corrections due to the steep nature of the spectrum at submillimetre wavelengths that allows us to see fainter sources with almost a constant brightness from 7 > z > 1 as the steep spectrum balances out the effects due to redshift dimming (see Figure 1.9).

The first SCUBA observations (Hughes et al., 1998) were carried out on a blank-field submillimetre field around the Hubble Deep Field (HDF) due to the depth or ancillary data and historical reasons. Five sources were discovered with $F_{850\mu m} > 2$mJy that corresponded to individual galaxies lying at redshifts $1 < z < 4$. The importance of that discovery was not only the existence of these high-z galaxies themselves but also the star formation rates exhibited of at least five times higher than that inferred from UV observations.

The pioneering development of the SCUBA instrumentation was crucial to obtain these new results and motivated the construction of new cameras (such as SCUBA-2) and new telescopes (such as LMT and ALMA) Recently, the Hubble Ultra-Deep Field was observed by the Atacama Large Millimeter Array (ALMA) in a deep pencil-beam imaging survey, finding 16 sources with secure optical counterparts with mean

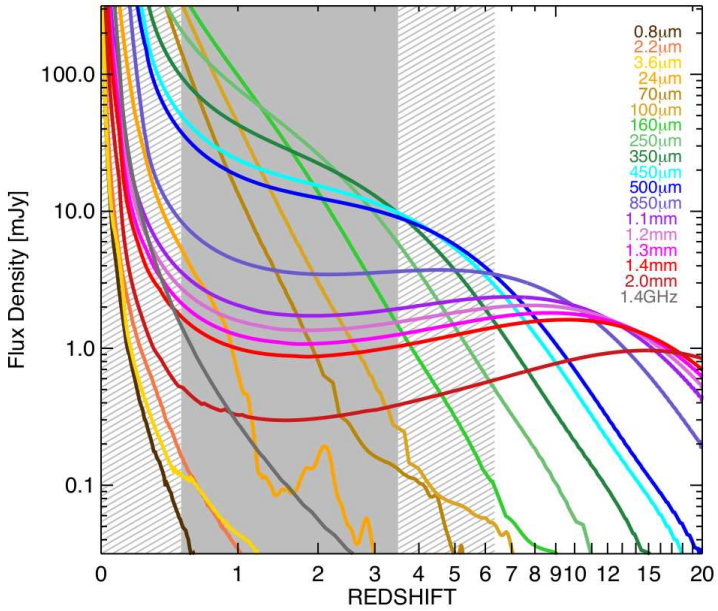

Figure 1.9: Observed flux against the redshift for a specific luminosity ($10^{12.5}L_{\odot}$) at different wavelengths. The flux remains nearly constant for submillimetre - millimetre wavelengths ((500μm - 1.4 mm, as shown in the legend) between $1 < z < 5$ and beyond. The solid grey area shows the peak epoch of dusty star forming galaxies ($0.5 < z < 3.5$), whereas the dashed lines show the areas where the density volume of DSFGs declines (which at the highest redshifts $3.5 < z < 6.4$ could be due to the difficulty of spectroscopic confirmation.

spectroscopic redshift $z = 2.15$ and flux $S_{1.3mm} > 120\mu$Jy (Dunlop et al., 2017). Such counterpart identification was challenging with the original SCUBA image due to resolution constraints (see Figure 1.10 for comparison between the original SCUBA image and a recent ALMA image).

Recent technological improvements have not only allowed an increase the quality of the images, but also an increase in the mapping speed of submillimetre surveys and the corresponding area. In particular the SCUBA-2 instrument on the JCMT (Holland et al., 2006), the replacement for the original SCUBA instrument can achieve mapping speeds 100x faster and has already covered 5 square degrees over 7 fields (see Figure 1.11), which is already 10 times larger than the widest survey carried out with the original SCUBA instrument (Mortier et al., 2005).

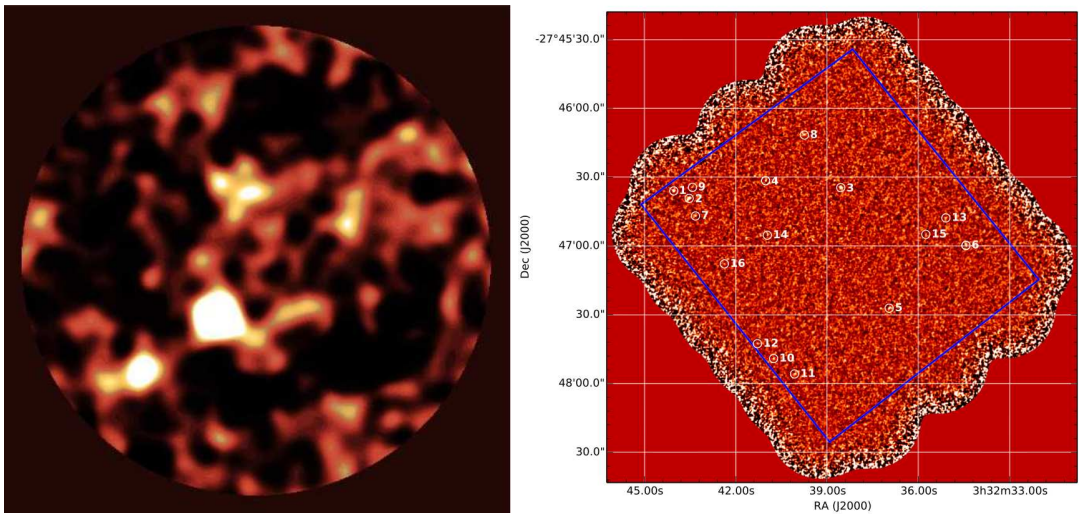

Figure 1.10: Evolution of submillimetre surveys: the Hubble deep Field (HDF), covered by SCUBA at 850μm was one of the first submillimetre surveys (Hughes et al., 1998) (left image) and the Hubble Ultra Deep Field (HUDF) covered recently by ALMA at 1,3 mm (Dunlop et al., 2017) (right image). The image on the right contains 16 sources (encircled by a 3.6 arcseconds diameter circle) with a robust counterpart in a 4.5 arcmin^2 area, whereas on the image on the left contains only 5 sources in a similar area (10.5 arcmin^2). The large beam size (15 arcseconds) of SCUBA made it almost impossible to identify the correct multi-wavelength counterpart in the first studies of SMGs, making ALMA a promising future to studying SMGs.

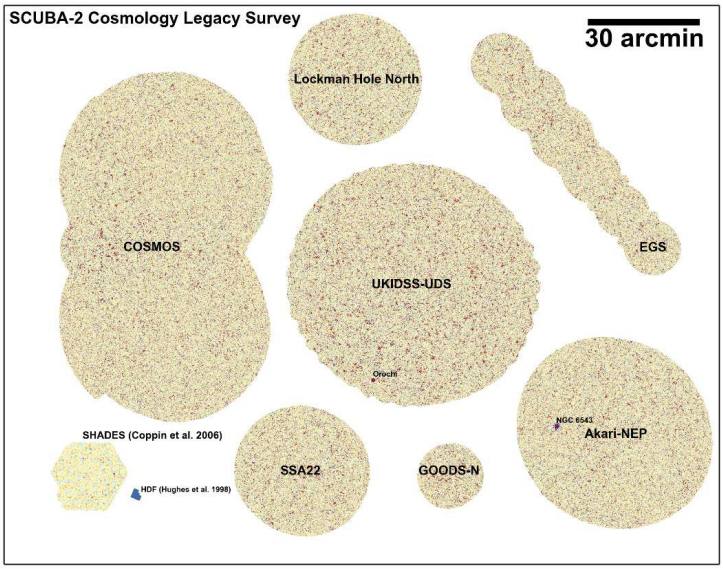

Figure 1.11: Fields observed by the SCUBA-2 instrument from Geach et al. (2016) compared to the original HDF field and SHADES fields (bottom left) observed by the predecessor SCUBA camera. SHADES was the largest survey carried out with SCUBA covering 0.5 square degrees, whereas the total coverage of the new fields with SCUBA-2 to date is already more than 5 square degrees. The data used in this thesis belongs to the AKARI-NEP field (bottom right in the figure).

In addition, the launch of *Herschel* and observations with the SPIRE instrument has enabled surveys over 100's of square degrees allowing searches for rare, exotic objects, including the first SMG at z > 6 with an unexpected level of star formation of thousands of solar masses per year (Riechers et al., 2013). The discovery of such distant dusty star forming galaxies (DSFGs) (see Casey, Narayanan & Cooray (2014) for review) pushes the existence of large amounts of dust in the Universe closer to the epoch of reionization, and sets important constraints on theories of galaxy evolution and the star formation history. However, the number of DSFGs at z > 6 is still remarkably small, concretely, to date, two more sources have been found: z = 6.9 (Strandet et al., 2017) and z = 6.027 (Fudamoto et al., 2017) (Zavala et al., 2018). The efforts to find more of these sources have uncovered many high-z sources (4 < z < 6) showing that the number density of dusty high-z galaxies appears to be at least one order of magnitude higher than predicted by galaxy evolution models (Asboth et al., 2016), (Aravena et al., 2016). This sample of high-z galaxies selected by *Herschel* is more complete that the SCUBA/SCUBA-2 selected sources at 850μm which were biased to cold dust temperatures; the sources that peak at longer wavelengths tend to have lowest temperatures in the 850μm spectral energy distribution (see Figure 1.12 extracted from Casey (2012)). Casey (2012) shows that the criterion $F_{850\mu m} > 5$mJy, commonly used to select SMGs, will exclude around 72 % of SPIRE sources at 1 < z < 2. Furthermore, the redshift distribution of SMGs is different depending on the selection criteria and the wavelength used. Such selection effects limit a broader picture of the properties of SMGs (see Figure 1.13).

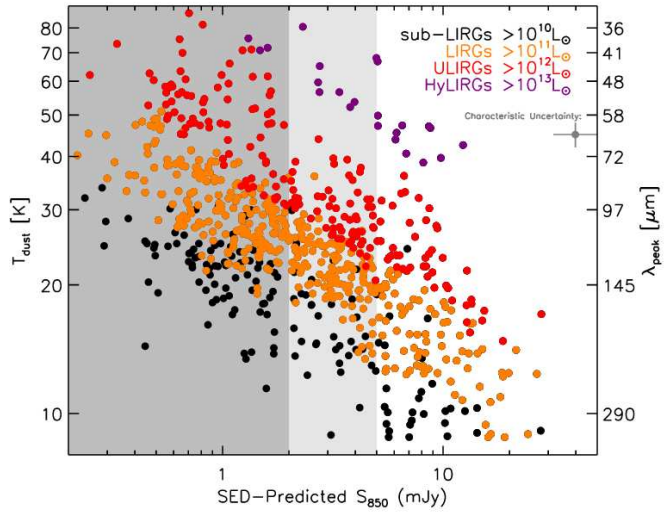

Figure 1.12: Predicted 850μm flux density as a function of the T_{dust} for a sample of starburst galaxies selected with SPIRE data (extracted from (Casey et al., 2012)).

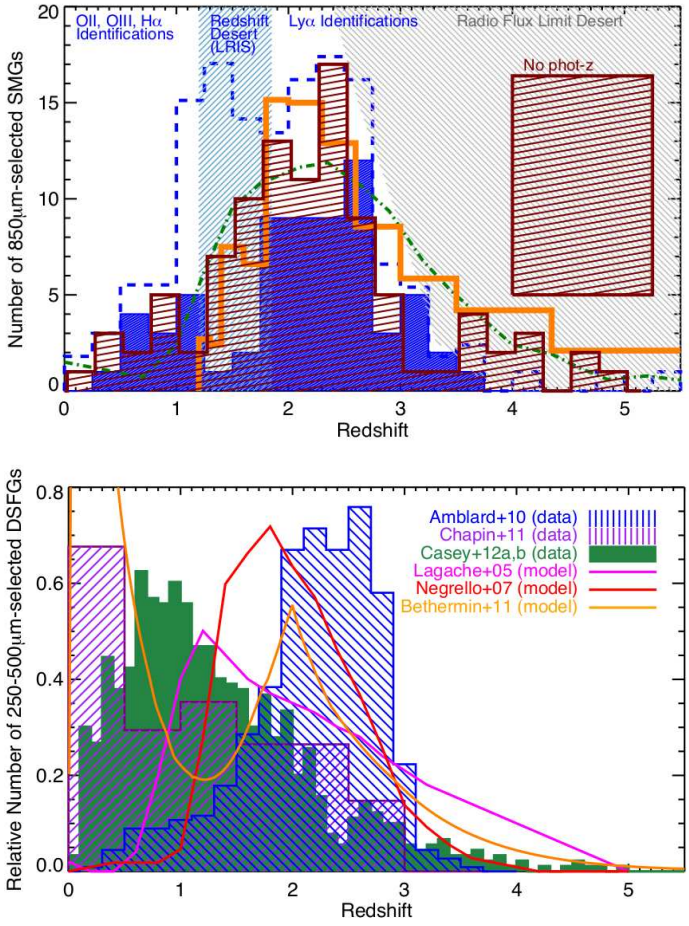

Figure 1.13: The redshift distribution of SMGs from the literature. (Top) Number of sources selected at 850 μm with SCUBA-2 (Bottom) Relative number of sources (due to the large difference in sample sizes) selected in the SPIRE bands (250 μm – 500 μm) highlighting how the selection criteria can affect the redshift distribution, for example, Amblard et al. (2010) finds a higher number of sources at $z \sim 2-3$ compared to other surveys.

There is no doubt that further studies in this area must be done since DSFGs, some of them the brightest systems in the Universe seen only $\sim$800 Myrs after the Big Bang, provide a unique laboratory to study star formation. Science questions remain such as whether they are a scaled up version of local extreme galaxies (such as ULIRGs) or do they have another star forming mechanism? The work in this thesis intends to shed light on this area by increasing the number of the high-z DSFGs and studying their properties in detail via spectral modeling techniques (see Chapters 2 and 3).

1.2.5 AGN classification

Active Galactic Nuclei (AGN) are usually located at the centre of their host galaxies, and appear as compact sources with non-thermal spectra and emission across the spectrum, which exceeds the emission associated with star formation. This additional component is not related with the nuclear fusion from the stars and it is accepted that is connected with the presence of an actively accreting supermassive black hole (SMBH) with $M_{SMBH} > 10^6\ M_\odot$ (see Padovani et al., 2017, for the most recent review).

They can be found in any type of galaxy, from spirals to elliptical, and at any redshift. Most importantly, there exists a relationship between the star formation and the AGN activity (see section 1.2), which can be a consequence of positive or negative feedback, depending on the evolutionary stage (e.g. Page et al. (2012)).

Therefore, understanding how AGNs shape the properties of their host galaxies is essential for understanding galaxy formation and evolution. Moreover, their brightness allows us to study the distant Universe up to look-back times of more than ten billion years. It also enables us to estimate their growth across cosmic time.

As distant AGN emit across a wide range of wavelengths (from radio to γ-rays) large photometric statistical studies offer an interesting approach, obtaining larger data sets than spectroscopic studies. This thesis mainly focuses on photometric surveys in order to identify and segregate AGN from the general galaxy population.

The broadly accepted observational classification of AGN, embraces different objects observed from a variety of perspectives (see Figure 1.14), and unifies them as being part of the same family (e.g. (Netzer, 2015) (Antonucci, 1993). Although all of them share the feature of having a strong non-thermal emission in the core of the host galaxy, they have different properties (mainly observational) between them (e.g (Schneider, 2006) (Baronchelli, 2015)):

- **Quasars** or quasi stellar objects (QSOs) are the most luminous and compact AGN. They incorporate most of the properties of the other types of AGN (Schneider, 2006). Broad emission lines are the main feature in their the UV and optical

spectra. Their continuum spectra are described, over a broad frequency range, by a power law $S_\nu \propto \nu^{-\alpha}$, where α is the spectral index. Another important characteristic is the high redshift nature of the most quasars.

- **Seyfert galaxies** are typically spiral galaxies with a bright core and lower luminosity than quasars. There is an optical sub-classification according to their emission lines: Type-1 (broad and narrow emission lines) and Type-2 (narrow emission lines only)

- **LINERS** (low ionisation nuclear emission-line regions) are another type of AGN, which are similar to Seyferts but with lower ionisation lines.

- **Blazars** have strongly varying emission (some of them on a timescale of $\sim$days) without strong emission or absorption lines, which makes it difficult to determinate their redshift. They are radio sources, and also show energetic and variable γ emission. Their host galaxies are often elliptical.

- **Radio loud galaxies** are typically elliptical galaxies with an active nucleus. Depending on the emission lines, they are classified by their optical spectrum as broad-line radio galaxies (BLRG) or narrow-line radio galaxies (NLRG)

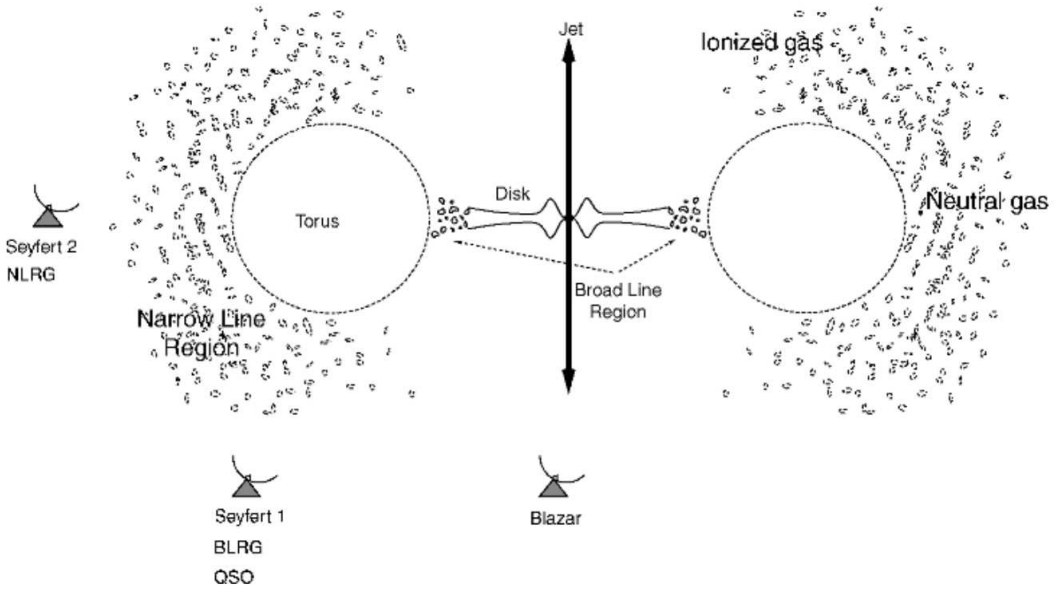

Figure 1.14: Unification AGN types: the type of source at sight may be different depending on the observer (Schneider, 2006)

.

Strong $\gamma - ray$ emission is mainly a characteristic of Blazars and the emission is mainly generated by their jets where the electrons are more energetic than the electrons in the accretion disk.

The X-ray emission corresponds to the black hole accretion process. In the inner region, plasma can scatter photons from the accretion disc through inverse-Compton scattering up to X-ray energies.

The UV-Optical emission presents a peak, the blue bump, related to the accretion disk at the center of the AGN. Their rest frame UV and optical colours are bluer than in non-active galaxies. AGNs have important spectral lines both near the central region (e.g Ly-α, [CIV]) and at larger distances from the nucleus (e.g [OIII]).

The infrared emission is produced by the dusty torus, heated by the accretion disk, and re-emitting at these longer wavelengths. There is peak of emission around $10 - 30$ μm referred to as the infrared bump, which is analogous in shape to the blue bump.

1.2.6 Radio Galaxies and Star Formation

Deep radio observations provide unbiased information on both star forming activity and black hole accretion since the radio emission is not affected by the dust extinction. This is important for the study of AGN and star formation evolution across cosmic time (e.g (Bonzini et al., 2013), (Padovani, 2014), (Bonzini et al., 2015)).

A striking relationship is the degree of correlation between the radio and far-infrared (FIR) emission of star-forming galaxies. It is generally believed that this correlation arises through high-mass stars heating the dust (which then re-emits in the FIR), that also generate supernovae that produce the relativistic electrons responsible for synchrotron radiation at radio wavelengths (e.g. (Condon, 1992), (Kovács et al., 2006). Although the origins of the far-infrared-radio correlation - hereafter FIRC - may not seem particularly surprising, the linearity of the relationship is remarkable because the synchrotron emissivity depends on both the number density of relativistic electrons and the magnetic field strength, which are not necessarily related (e.g. Seymour et al. (2009) , Magnelli et al. (2015), Appleton et al. (2004)). The FIRC is defined with different coefficients depending of the specific wavelength, in Magnelli et al. (2015), where *Herschel* data is used, the FIRC is defined as:

$$q_{IR} = log\left(\frac{L_{IR}\,[W]}{3.75\cdot 10^{12}}\right) - log\left(L_{1.4GHz}\,[WHz^{-1}]\right) \tag{1.5}$$

The FIRC is an important tool in extragalactic astrophysics since in a practical sense it can be used to calibrate the radio luminosity as a star formation indicator, using the $L_{IR} - SFR$ relation, which is specially useful for high redshift galaxies (Magnelli et al., 2015). Furthermore, as well as at high redshift, it has been used to estimate the distance and the dust temperature in starburst galaxies (Carilli & Yun, 1999).

Since the SFR and gas density, which control in part the normalisation of the FIRC, are known to evolve with redshift, a decrease of the value of the FIRC is expected as a consequence. The evolution of FIRC involves the study of galaxy evolution and provide clues as to why high redshift galaxies lie far above the MS galaxies

which are thought to be star-forming with similar FIR properties to the local ULIRGs (Magnelli et al., 2014), however other properties are different such as the size of the star forming regions or the cosmic ray scale heights.

1.3 Overview of Research

1.3.1 Multi-wavelength extragalactic surveys

Over the past few decades, the development of instrumentation and space-borne telescopes has made possible deep, wide-area observations of the Universe across entire electromagnetic spectrum. The approach of using multi-wavelength extragalactic surveys to study the properties of the objects out to high redshift has been central to the progress of our knowledge about their formation and evolution. In particular, it has been essential to understand how the structures in the primitive Universe evolved into the diversity of galaxies that we can see today.

We have seen in Section 1.2.1, the importance of multi-wavelength views of the Universe in order to obtain the full picture of galaxy evolution and star-formation and in Sections 1.2.4, 1.2.5, 1.2.6 how observations at different wavelengths can reveal new galaxy populations.

The aim of this thesis is to study galaxy formation and evolution from a multi-wavelength approach, in particular how do the different members of the extragalactic jigsaw piece together to for a coherent picture of galaxy evolution? How representative is the new high redshift population of sources being discovered and, how AGNs link together with Ultra-luminous Infrared Galaxies (ULIRGs) during their birth and evolution?

These are some of the questions that modern astronomy tries to address and perhaps will be best solved statistically with a large samples of sources based from large surveys using a multi-wavelength approach. In particular, such a multi-wavelength approach allows us to explore in detail the spectral energy distributions (SED) of these

galaxies, obtain photometric redshifts and to investigate the types and ages of the detected galaxies and ultimately constraining their physical properties.

This work will contribute to a better understanding of galaxy evolution and how the galaxy properties evolve through cosmic time, ultimately constraining evolutionary models of galaxy formation/evolution.

This thesis exploits large multi-wavelength data sets at radio wavelengths from the Giant Metrewave Radio Telescope (GMRT) and Westerbork Synthesis Radio Telescope (WSRT), near infrared (NIR) and mid infrared (MIR) data from *AKARI* , far infrared (FIR) data from the *Herschel* space observatory and submillimetre-wavelength data from the ground based James Clerk Maxwell Telescope (JCMT). This data and hence the thesis is located in two key, yet under-exploited extragalactic fields at the ecliptic poles, described in the next section.

1.3.2 The North and South Ecliptic Poles

The North Ecliptic Pole (NEP) and the South Ecliptic Pole (SEP) are natural fields toward which to make deep extragalactic surveys. The ecliptic poles are favoured both by satellites in polar orbits and at the L2 point due to the near continuous viewing zones / high visibilities allowing observations many times a day, see Figure 1.15. Both the NEP and SEP lie off the Galactic plane although the SEP region is relatively close to the LMC.

The region in the vicinity of the NEP was chosen as a calibration/verification field for the *Spitzer*, *AKARI* and *Herschel* missions and has a wealth of ancillary data from X-ray to radio wavelengths including selection as a SCUBA-2 field for the Cosmology Legacy Survey (Geach et al., 2016).

The SEP includes a region of extremely low background contamination from Galactic clouds (cirrus level $I_{100\mu\mathrm{m}}$ <0.5 MJy sr^{-1} (Schlegel, Finkbeiner & Davis, 1998), and correspondingly low hydrogen column density $\sim 5\times10^{19}$ cm^{-2} similar to the better known Lockman Hole. The SEP enjoys multi-wavelength coverage from optical-

submillimetre wavelengths including data from *Spitzer*, *AKARI* and *Herschel*. The data in the SEP is used in Chapter 5 of this Thesis and described in Table 5.1 and Figure 5.1, whereas in Chapter 2 the NEP data is used and described in Table 2.1 and Figure 2.1.

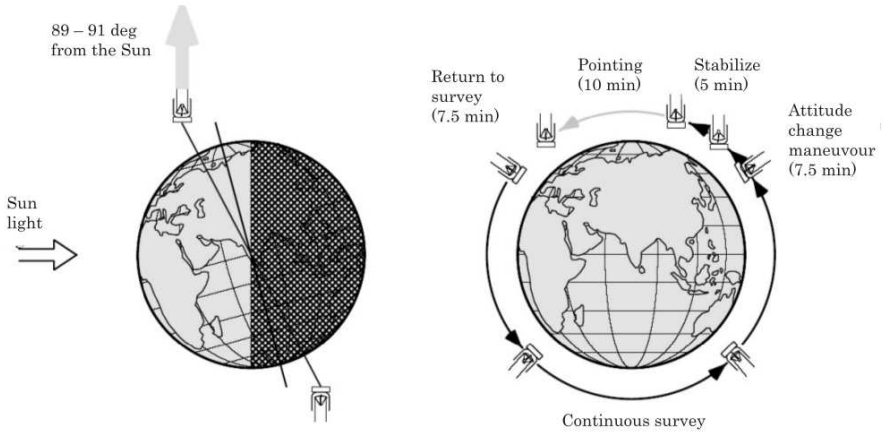

Figure 1.15: Representation of the visibility at the North and South Ecliptic Poles. These fields are prime targets for deep extragalactic surveys as they lie outside the ecliptic plane, and satellites in polar orbits pass over these regularly, allowing long exposures (from Figure 1 Matsuhara et al. (2006)).

Despite their multi-wavelength coverage, both the NEP and SEP region remain relatively unexploited and therefore hold the promise of new discoveries. This thesis will use the multi-wavelength data in these fields in order to study both the local and the high redshift Universe taking advantage especially of the FIR and submillimetre data.

1.3.3 Structure of this Thesis

This thesis attempts to collate the vast amount of photometric data from surveys at the ecliptic poles, concentrating especially but not exclusively on observations at infrared to submillimetre wavelength in order to trace a coherent picture of the effects on galaxy evolution from the local Universe out to the highest redshifts.

The thesis concentrates on the identification and selection of different populations of galaxies over several redshift ranges such as high redshift dusty galaxies, AGN candidates, intermediate redshift galaxies (DOGs) and gravitational lens candidates and the underlying star-formation rate. Different selection criteria are evaluated in their ability to successfully identify the different populations.

For the dusty star forming galaxies, a detailed investigation of their physical characteristics (redshift, stellar mass, star-formation rate and mode) is undertaken using a variety of spectral energy distribution (SED) fitting algorithms. A great deal of attention has been paid into selecting the most appropriate and robust SED fitting techniques for our populations discussing the merits and demerits of each since they form the basis from which the physical conclusions are drawn. These physical characteristics are then used to constrain the position of these galaxies on (or above) the Main Sequence of galaxies.

In Chapter 2 I investigate and evaluate key selection criteria and methods used to identify dusty high redshift galaxies in the NEP. The product of Chapter 2 (a robust catalogue of high-redshift candidate) is then studied in Chapter 3 by applying different SED fitting techniques and modeling the physical properties of the sample. The main physical parameters of the high-z candidates are calculated, such as the photometric redshift, star formation rate, stellar masses, dust temperature, and infrared luminosity, using them to determinate the nature of these galaxies and studying their position on the main sequence of galaxies.

Chapter 4 evaluates the properties of galaxies that emit at radio wavelengths by analysing a small submilliJansky population by SED fitting and evaluating their prop-

erties. The sample is divided by infrared luminosity with the focus on the luminous galaxies, studying their star formation and any AGN presence.

The final science Chapter 5 reports on the data reduction of optical data and the production of an new R-band catalogue at the SEP. This catalogue is then used in conjunction with infrared/submillimetre data in order to select gravitational lens candidates. The catalogue is also used to carry out a pilot study on a population of intermediate redshift dust obscured galaxies (DOGs) and an evaluation of their physical properties.

Finally, Chapter 6 presents the main conclusions of this thesis describes the future work of the four science chapters, each of them divided in a section.

Chapter 2

Selection of high redshift galaxies

This Chapter explores several key methodologies used to select high redshift galaxies (hereafter high-z), focusing on dusty star forming galaxies (DSFGs) selected with submillimetre data. Although submillimetre galaxies were discovered more than 20 years ago, there are still many open questions such as: are the star forming galaxies that have been discovered to date with high gas content representative of the generic high-z population? What is the limit of the redshift for these sources? Here submillimetre selection criteria are proposed in fields with comprehensive multi-wavelength coverage in order to calculate the photometric redshift using all available spectral data to answer these questions. Four different methods to select high-z sources were explored in order to create a new high-z catalogue, increasing the current available sample of DSFGs at high-z. Furthermore, two of these methods, a colour criteria and a drop-out method were compared, and conclude that one of the methods (drop out) finds intrinsically fainter sources than the more commonly used submillimitre colour selection methods. This result shows that the extreme luminous sources found via the most common submillimetre methods may not be representative of the general population of dusty high-z sources, since they are intrinsically faint, with the DSFGS having moderate star formation.

2.1 Introduction

The discovery of a high-z population of bright sources at sub-mm wavelengths (200μm $-$ 1mm), the so-called submillimetre galaxies (SMGs) (Smail, Ivison & Blain, 1997), (Hughes et al., 1998), has posed critical questions about the evolution of galaxies in the early Universe. These submillimetre observations opened the distant Universe as never before, due to the negative k-correction which, because of the steep rising slope in the Rayleigh-Jeans regimes counter acts the dimming of sources with increasing distance allowing brighter sources than at optical wavelengths to be accessible (see Introduction 1.9).

The initial discovery of these sources was made with the SCUBA instrument on the James Clerk Maxwell Telescope in the late nineties. However, further development of the instrumentation was crucial to obtain new results (see Blain et al. (2002) for review). The construction of new instruments - such as SCUBA-2 - and new telescopes - such as the LMT or ALMA - have been fundamental to allow a thorough study of these sources.

The launch of *Herschel* and the SPIRE instrument with detectors at 250μm, 350μm and 500μm - the first space telescope to explore the submillimetre Universe - led to incredible progress in the field. It was not until the full exploitation of the SPIRE data, that the first SMG at z > 6 (approaching the epoch of reionization, key to understand how galaxies formed and evolved) was found, with an unexpected level of star formation of thousands of solar masses per year (Riechers et al., 2013). The discovery of that extreme dusty galaxy, named HFLS3, set a precedent showing the existence of a source with enormous content of gas and star formation, that they were renamed generically as dusty star forming galaxies (DSFGs, see Casey, Narayanan & Cooray (2014) for review).

The existence of DSFGs at z > 6 increased the interest of using submillimetre data for selecting these sources, developing several approaches - most of them using SPIRE data. As a result of the exploitation of the SPIRE data in large fields, several dusty high-

z sources (6 > z > 4) were discovered which has shown that the number density of dusty high-z galaxies appears to be at least one order of magnitude higher than predicted by contemporary galaxy evolution models (Asboth et al., 2016), (Aravena et al., 2016).

However, during the last five years, there have only been further detections of these extreme sources. Concretely, to date, two more sources have been found at z > 6: z = 6.9 (Strandet et al., 2017) and z = 6.027 (Fudamoto et al., 2017) (Zavala et al., 2018). This latest work has set a precedent by showing that the nature of DSFGs is not as extreme as expected, and that they in fact have only a moderate star formation rate of $\sim 380 M_{\odot}/\mathrm{yr}$ and similar gas properties and star formation efficiency as local ULIRGs. This type of source (ULIRGs at z$\sim$ 5-6) could well be the progenitors of quiescent galaxies at z $\sim$ 2-3, solving the problem posed by the discovery of extreme starbursts HFLS3. However, these questions cannot be answered by analysis of a single source representing this population, since such sources may well be as rare as the extreme starbursts.

Therefore a larger sample of dusty star forming galaxies is urgently needed, along with a framework with which to characterise their properties. Current published papers have two different approaches:

1. select a large number of high-z candidates in fields with poor multi-wavelength data (sacrificing detail for numbers)

2. spectroscopic studies of single sources in order to define their physical properties (sacrificing numbers for detail).

Both approaches are insufficient to fully examine the nature of DSFGs. The first approach allows the detection of high-z candidates with only a few photometric detections - between three and five - estimating the (photometric) redshift by fitting with SED templates taking into account solely the FIR peak (Duivenvoorden et al., 2018). Unfortunately, this makes an accurate calculation of the redshift near impossible due to the dust temperature degeneracy; redshifting a fixed template affects the observed colors in the same way as changing the dust temperature. Furthermore, other properties -

such as stellar mass, mass of the gas - can not be evaluated using only submillimetre data and there is need for ancillary UV, optical and IR data. The second approach, although more accurate is yet insufficient for a general understanding of DSFGs, since the small - usually exotic - sample is not large enough to determine if these sources are representative of the population or only of extreme cases.

Since the beginning of the study of SMGs, astronomers have sought to combine observations at other wavelengths to characterise submillimetre galaxies, although this has proved challenging due to the faintness of these objects at other wavelengths (Blain et al., 2002). The solution proposed in this Chapter is to select these high-z SMGs in fields having good deep multi-wavelength coverage in order to produce an analysis of the average statistical properties of the source population (see Chapter 3).

This Chapter presents the results of a search for high redshift galaxies in the North Ecliptic Pole (NEP) field using a multi-wavelength data set comprising optical, infrared and submillimetre data. In Section 2.2 the available data in the field is presented, and cross-matched catalogue of SMGs is produced for the study. Section 2.3 introduces the four methods for searching high redshift candidates by using the submilimitre data. In Section 2.4 a summary is given together with the high-z catalogue as the main result and a comparison of the effectiveness of the different selection methods.

2.2 Observations.

The North Ecliptic Pole (NEP), due to its high visibility, is a natural location for an extragalactic deep field and has been observed by several space telescopes (see Introduction 1.3.2 for details). This Legacy field is comprised of 2 distinct areas: The NEP-Deep field, centered at $RA = 17h\ 55m\ 24s$ $Dec = 66^\circ\ 37'\ 32''$ (0.54 deg^2 circular shape) and NEP-Wide field, centered at $RA = 18h\ 00m\ 00s$ $Dec = 66^\circ\ 36'\ 00''$ (6.2 deg^2 circular shape) (Matsuhara et al., 2006).

There is a large, growing resource of archival and ancillary data for this field, with observations extending across the spectrum from radio to X-ray wavelengths (see Table

2.1).

In this Section, ancillary wavelength data from the UV to radio wavelengths have been used (see Figure 2.1) to create a multi-wavelength catalogue based on the sub-millimetre selection of high-z candidates. The data used is described in the following subsections:

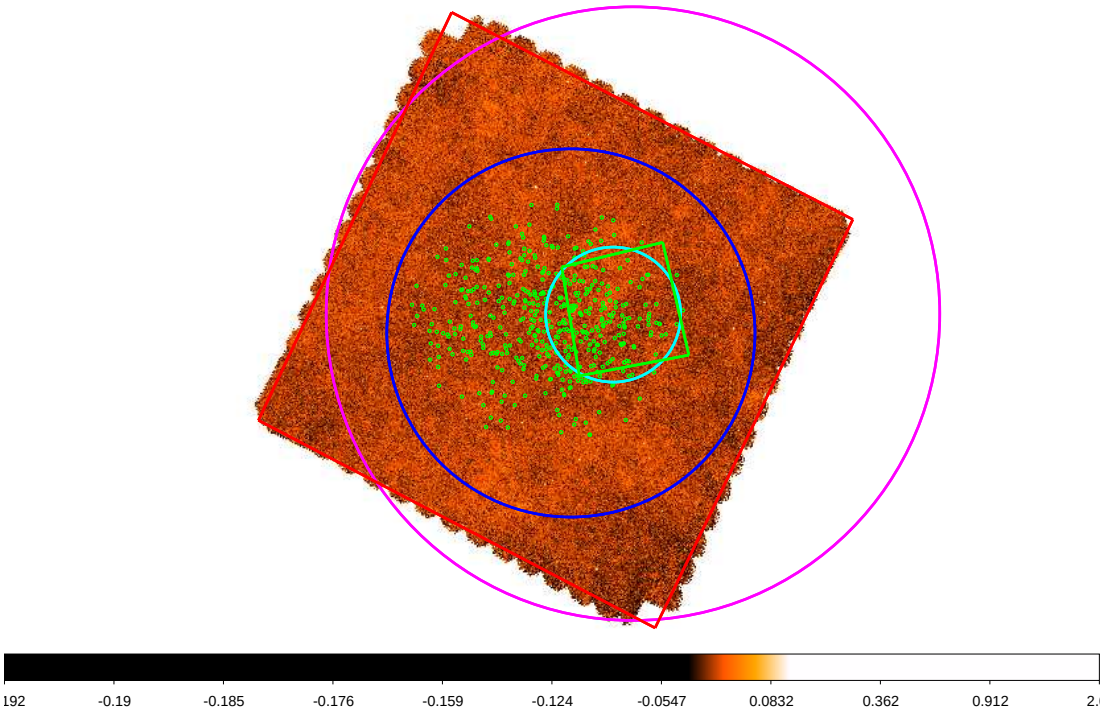

Figure 2.1: Main surveys in the NEP field. The cyan circle is the AKARI Deep field (0.5 deg^2) which is covered by AKARI, CFHT and SUBARU ((Murata et al., 2013)). The external blue circle is the AKARI Wide field 6 deg^2 covered by shallower AKARI data, CFHT (Kim et al., 2012) and SUBARU (Oi et al. in prep.) The violet circle shows the GALEX survey, whereas the Herschel data covers the big red rectangle area (SPIRE) and the small green rectangle (PACS) (Pearson, 2018). Finally, the green dots show WSRT radio sources (White et al., 2010).

2.2.1 Far infrared and submillimetre data

IR and submillimetre surveys are essential to allow us to select and study the obscured component of the star formation in galaxies. Furthermore, there are a plethora of methods available for selecting high-z sources using submillimetre data (e.g. Amblard et al., 2010). For that reason the high-z catalogue focuses on submillimetre observations. The entire NEP region has been observed by the Herschel Space Observatory (HSO)

(Pilbratt et al., 2010) with a total area of $\sim 9\text{deg}^2$ is covered by the Spectral and Photometric Imaging Receiver (SPIRE) (Griffin et al., 2010) at 250 μm, 350 μm and 500 μm. In addition, a smaller inner area of $\sim 0.69\text{deg}^2$, covering the NEP-Deep region, was observed by Herschel at shorter wavelengths of 100 μm and 160 μm with the Photodetector Array Camera and Spectrometer (PACS) instrument (Poglitsch et al., 2010). This same area was also covered by the James Clerk Maxwell Telescope (JCMT) with the Submillimetre Common-User Bolometer Array 2 (SCUBA-2) at 850 μm.

The core of the submillimetre catalogue is the SPIRE data (Pearson, 2018) and the 850 μm data from the SCUBA-2 cosmology legacy surveys (Geach et al., 2016), and their submillimetre fluxes as the basis for the selection of high-z sources.

The published SCUBA-2 catalogue at the NEP contains 330 sources whereas the SPIRE catalogue contains 4820. These catalogues were cross-correlated using a search radius of 9 arcseconds - half of the SPIRE beam FWHM at 250 μm - producing a base catalogue that contains 5054 sources which includes the sources with detections in both catalogues as well as the no cross-matches. Therefore there are 96 ($\sim 30\%$) of the SCUBA-2 sources that have no detection in the SPIRE catalogue. The next steps are to cross-match these sources with the rest of the data available in the field.

The PACS data in the green band, 100 μm, and red band, 160 μm, were analysed to produce a final catalogue of 409 sources and 142 sources respectively (Pearson, 2018). The PACS catalogue was joined to the baseline submillimetre data by cross-matching the more reliable green band position to the SPIRE 250 μm position using a search radius smaller than 9 arcseconds choosing the closest counterpart. The result of this band-merging is a FIR-submillimetre catalogue with six photometric detections allowing us a good sampling that constrains of the FIR dust emission peak.

2.2.2 Optical and IR data

The IR observations are important to give us information about the dust properties, emission features (e.g. PAH) and AGN dust torus characteristics, whereas optical ob-

servations can provide the information necessary to estimate the stellar mass of the galaxies. In addition, the near-mid-IR spectral region is key to finding the correct optical counterpart of the submillimetre sources, bridging the wavelength gap from the longer wavelength observations.

The AKARI mission (Murakami et al., 2007) gave us a unique vision of the NEP since, due to its high visibility it was observed several times per day, producing a deep near-mid-infrared image of this region. Furthermore, the NEP has been observed by the SUBARU and CFHT optical telescopes on Mauna Kea, Hawaii.

There are publicly available band-merged catalogues of optical and IR data in the NEP-Deep and NEP-Wide areas respectively. In the NEP deep, the final band-merged catalogue contains a total of 27,770 sources with good coverage from optical to mid-IR wavelengths (Murata et al., 2013). The NEP-Wide field has been covered by shallower near-mid-IR and optical data (coverage of $\sim 2\text{deg}^2$ by CFHT), the catalogue contains 114,974 sources (Kim et al., 2012) with positions derived from near-IR data.

To date there is an obvious lack of optical coverage, particularly in the NEP-Wide area, since only the sources covered by the CFHT have optical detections. For this reason, I used a new catalogue in preparation (Oi et el. in preparation) that covers both the NEP-Wide and deep field with the Hyper Suprime camera (HSC) on the SUBARU telescope. Using this catalogue we cross-matched with the catalogues of Murata et al. (2013) and Kim et al. (2012) in the deep and wide fields respectively using a searching radius < 1 arcsecond and selecting the closest counterpart.

2.2.3 Ultraviolet data

The addition of UV data is important to constrain the star formation of galaxies as it traces the emission from hot OB stars, and can therefore be used in order to improve the SED fitting. The publicly available UV catalogue in the NEP region comes from the Galaxy Evolution Explorer (GALEX) space telescope (Martin et al., 2005) and contains 36,263 sources over the entire NEP (Bianchi, 2014). Since GALEX is

essentially an all sky survey, the data is relatively shallow with sensitivity of 23 mag, therefore a relatively low number of matches, since most of our sources will too faint to be detected by GALEX. In fact, only 13 sources of the final sample have a UV counterpart.

Telescope [Catalogue]	Wavelength	Area	Angular resolution
GMRT (White, in prep.)	610 MHz	~ 5 deg^2	5"
WSRT (White et al., 2010)	1.4 GHz	1.7 deg^2	10"
Herschel-SPIRE (Pearson, 2018)	250 - 350 - 500 [μm]	9 deg^2	18" - 25" - 36"
Herschel-PACS (Pearson, 2018)	100 - 160 [μm]	0.69 deg^2	8" - 13"
JCMT-SCUBA-2 (Geach et al., 2016)	850 [μm]	0.69 deg^2	4.5"
AKARI (Murata et al., 2013)	2.4 - 3.2 - 4.4 - 7.3 - 9.2 - 10.9 - 16.2 - 19.8 - 23.3 [μm]	0.69 deg^2	$\sim$ 2" - 24"
AKARI (Kim et al., 2012)	2.4 - 3.2 - 4.4 - 7.3 - 9.2 - 10.9 - 16.2 - 19.8 - 23.3 [μm]	5.4 deg^2	2" - 24"
SUBARU (Murata et al., 2013)	3591 - 4410 - 5489 - 6577 - 8071 [Å]	0.25 deg^2	0.2"
SUBARU/HSC (Oi-Matsuhara in prep)	4777 - 6288 - 7683 - 9105 - 9791 [Å]	5.4 deg^2	0.2"
CHFT (Murata et al., 2013)	3811 - 4862 - 6258 - 7552 - 8871 [Å]	0.69 deg^2	0.3"
CHFT (Kim et al., 2012)	3811 - 4862 - 6258 - 7552 - 8871 [Å]	~ 2 deg^2	0.3"
GALEX (Bianchi, 2014)	1538 - 2315 [Å]	All sky	6"
CHANDRA (Krumpe et al., 2015)	$0.5-7$keV (total band)	~ 1 deg^2	<1"

Table 2.1: Overview of observational data at the NEP from radio to the X-rays in both the deep and the wide field. The fist column indicates the telescope and the reference from where the catalogue was taken, the second column indicates the observation bands of each telescope, the third column the area in square degrees and the last column indicates the angular resolution. In general, catalogues covering 0.69 deg^2 of area correspond to the NEP-Deep field are deeper than the equivalent catalogues that cover wider areas. For this study, only the Herschel, AKARI, SUBARU, CFHT and GALEX catalogues have been used. All these catalogues have a astrometry error below than 2".

2.3 Sample selection of high-z candidates

Although the search for dusty high-z galaxies has progressed over the last few years there are still only three spectroscopically confirmed examples of these sources at z $>$ 6 (Riechers et al. (2013), Fudamoto et al. (2017) and Strandet et al. (2017)). A larger, statistically significant sample of these extreme sources - and in general dusty high-z galaxies - is urgently needed, together with robust methods to select them.

The properties of the SED around the FIR dust emission peak allow the use of shifting of submillimetre fluxes across the peak as a redshift indicator, since the dust temperatures of distant Dust Star Forming Galaxies (DSFGs) are in the range of 20-80K (Casey, Narayanan & Cooray, 2014). The observed Herschel colours are therefore useful to select potential high-z sources (see Figure 2.2) as they sample the peak well at different redshifts.

2.3.1 High-z selection through submillimetre colours

Submillimetre-far-infrared colour-colour diagrams are commonly used to find high redshift candidates (e.g. Amblard et al. (2010), Ivison (2012)) for example with the 500 μm riser method: sources with SPIRE flux densities increasing from 250 μm to 350 μm and then onwards to 500 μm (e.g. Asboth et al. (2016) Ivison (2012)). The use of the colours to select high-z candidates relies on the redshifting of the SED through the observation bands, defining the colour-colour space where high-z sources will lie. To illustrate this, a SPIRE colour-colour (c-c) diagram was produced to evaluate and indicate the colour space for submillimetre fluxes. The SEDs of two well-known galaxies, the archetypal ULIRG (Arp220) and starburst (M82) are also plotted showing the evolution colour tracks for increasing redshift. From the Figure the area of the colour space populated by high-z objects lies in the upper right part of the diagram for both archetypal SEDs (see Figure 2.3).

These selection criteria were applied to our NEP SPIRE catalogue (Pearson, 2018) to select potential high-z candidates. In total, 268 high-z candidates were selected

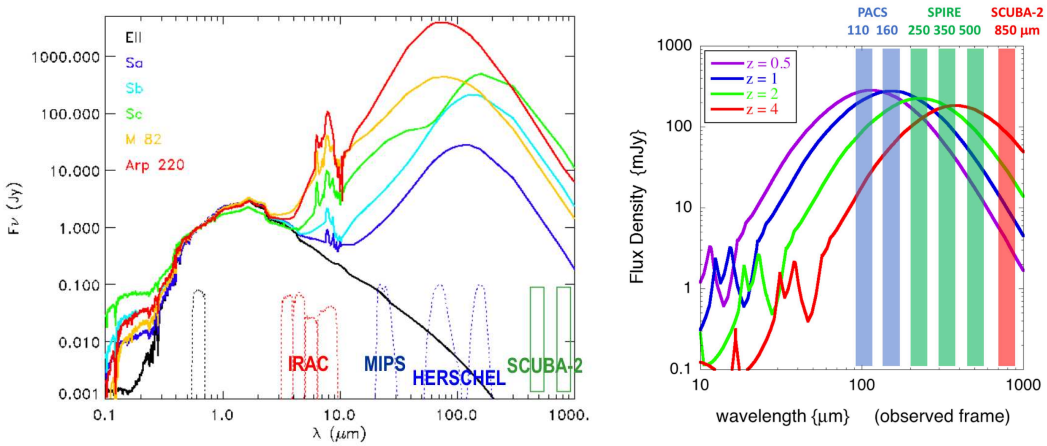

Figure 2.2: The importance of observations at submillimetre wavelengths for the selection of high-z galaxies: (Left) Galaxy SED templates (Berta et al. (2013) and Polletta et al. (2007)) and the bands for IR-submm telescopes. Luminous dusty galaxies emit much of their light in the IR to submm regime, which are convenient to study high-z sources since the peak usually lies around 100μm in the emitted frame. (Right) Model SED shifted through redshift such that the FIR peak moves through the three SPIRE bands (shown as the green bands, with PACS shown for reference as blue bands). The SED is shown in purple for z = 0.5 where the FIR emission peaks at 1000μm, whereas at z = 1 (blue) and z = 2 (green) the spectrum peaks are longer wavelengths, due to the negative cosmological K-correction, where the peak is shifted to 350μm, and 500μm bands in the observed frame respectively. The longer wavelength the observational band where the peak is located, the higher is the redshift. By using this same concept, SCUBA-2 data can be introduced at the longer wavelength of 850μm (the red band) to select galaxies out to redshift 4 and above (SED shown in red). (Figure modified from Pearson presentation).

following the criterion $F_{350\mu m} > 35$mJy and $F_{500\mu m}/F_{250\mu m} > 0.75$ that selects sources potentially at z $>$ 2 (Amblard et al., 2010). The 268 high-z candidates are represented in the colour-colour diagram shown in Figure 3.2, where they lie as expected in the upper part of the diagram.

Following this, the 500μm riser ($F_{500\mu m} > F_{350\mu m} > F_{250\mu m}$) criterion was applied selecting 41 high-z candidates, with only 23 of them being included in the previous criterion. These 18 new detections were incorporated into the candidate list. Note that the 500 μm flux cut assumed by (Asboth et al., 2016) was not applied because this allows us to have a bigger sample which has been cross-matched with other catalogues and studied with SED fitting codes (see Chapter 3). This more flexible assumption will allow a larger sample - with the caveat being that some will inevitably be sources at

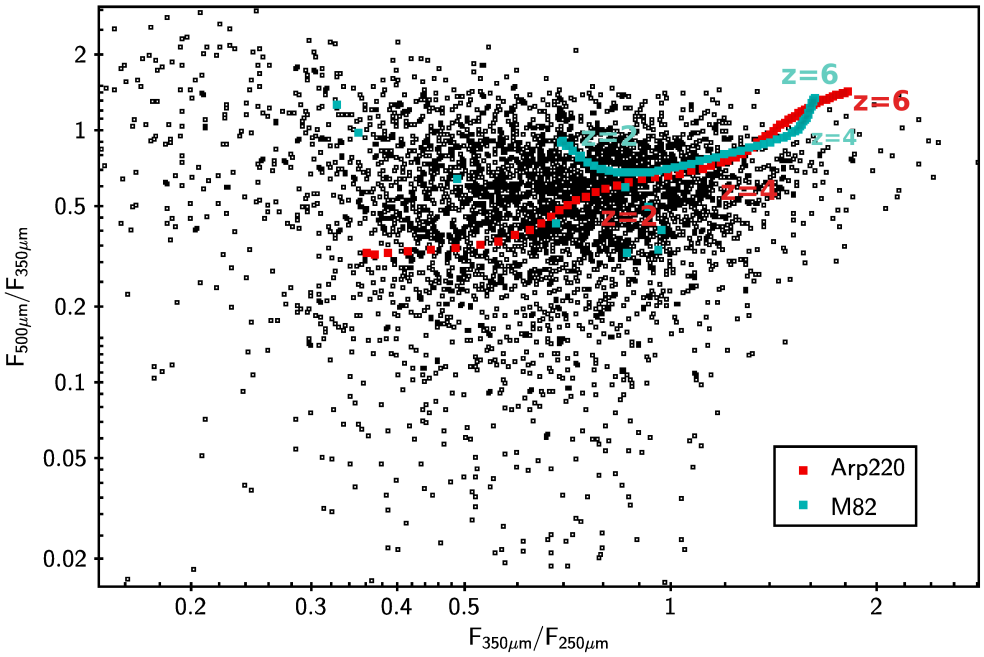

Figure 2.3: Colour-colour diagram for sources with 3 SPIRE fluxes in the NEP. Overplotted are the evolutionary tracks for Arp220 (red track) and M82 (blue track). The tracks evolve from redshift $0 < z < 6$ with redshift steps of $\delta z = 0.1$ from left to right (see Section 3.2.2 for a detailed explication of the tracks determination by using LePHARE). This highlights that the region in the diagram where the high-z population may be selected lies in the upper right of the diagram for both tracks. The tracks have similar evolution since both are local dusty star forming galaxies.

lower redshift - to study the properties of the high-z population over the entire spectrum and not only limiting the study to really extreme high-z DSFGs.

2.3.2 High-z selection through submillimetre source position

In addition, two further, new methods were used to search for the high-z population based on the extraction of the sources by using the maps instead of the catalogue. The use of standard catalogues is a more conservative way to select sources since the catalogues already have a degree of robustness built into their production (multiple detections in many bands or some bright flux cut). However, in order to find the faintest, rarest sources, the use of the maps directly is crucial (see e.g. Dowell et al. (2014) for a similar method). Since the SPIRE catalogue was produced assuring a detection in

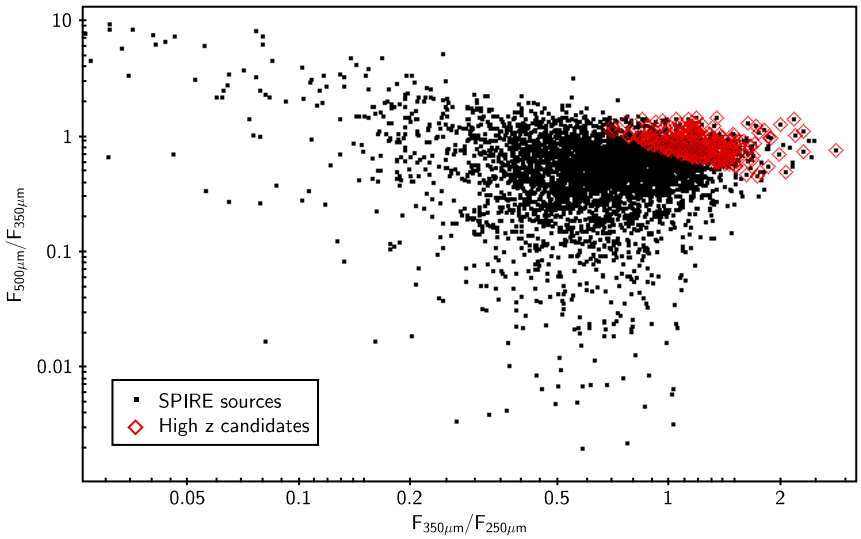

Figure 2.4: The $F_{500\mu m}/F_{350\mu m}$ against $F_{350\mu m}/F_{250\mu m}$ c-c diagram shows that the potential high-z candidates (in red) lie in a specific part of the diagram (upper right) selected by the colour criteria discussed in the text. Although there are many different SPIRE c-c diagrams in the literature with slightly different colour criteria, the general underlying concept is that the high-z sources lie in an specific part on the diagram due to the way the SED is sampled with redshift.

the 250 μm band, red 500 μm sources can be missed by using only the catalogues.

The first additional method consists of producing the photometry of the SPIRE maps at the SCUBA-2 source positions for any sources that are not listed in the SPIRE catalogue. In fact, only $\sim$ 30% of sources - in the best case scenario with a search radius of 9 arcseconds - of SCUBA-2 sources have an entry in the SPIRE catalogue. In order to ensure a reliable detection, sources that are at least 3 times above the confusion limit (Nguyen et al., 2010) in the 250μm band have been selected which together with the SCUBA-2 detection, guarantees a real source. After this, the 500μm risers criteria was applied, finding 36 candidates which were then analysed by SED fitting. Both the SPIRE and SCUBA-2 photometry are in agreement for 36 of these candidates, moreover, all sources were double checked by eye and postage stamps produced in order to confirm the detection in the image (see Figure 2.5).

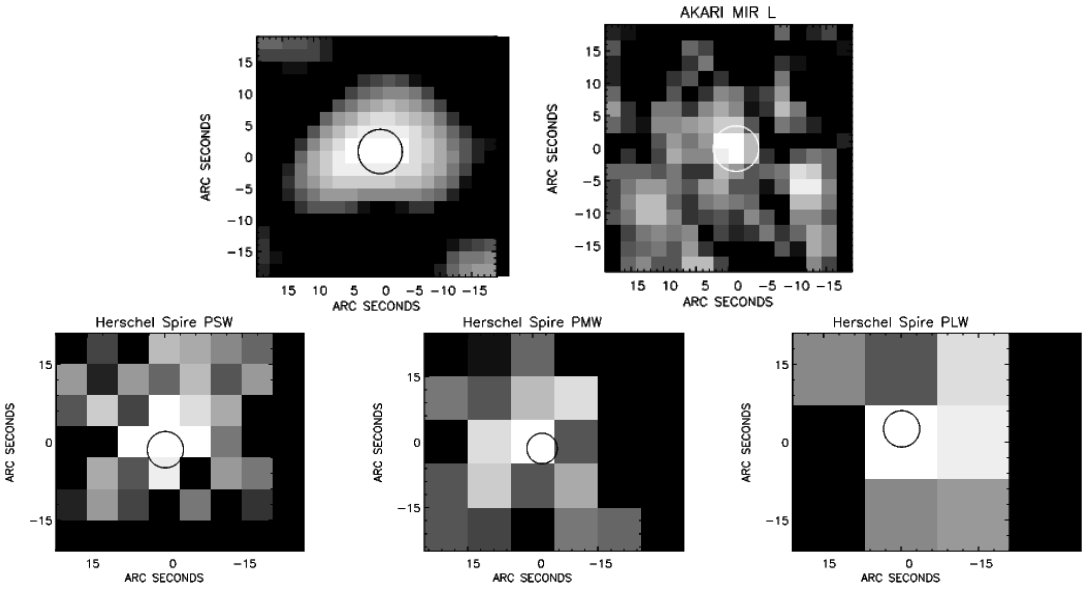

Figure 2.5: Postage stamps of one of the 36 sources selected by the SCUBA2-SPIRE method described in the text: SPIRE 500 μm risers selected using the SCUBA-2 position to carry out photometry in the three SPIRE maps. The first row shows a clear detection the SCUBA-2 image (left) and the AKARI band at 24 μm (right). The second row shows the 3 SPIRE bands at 250 μm, 350 μm and 500 μm respectively, showing a faint detection although this source was missed in the SPIRE catalogue.

2.3.3 High-z selection through single band detection

The second additional method introduced for high-z selection is based on the search for faint sources in the 3 SPIRE maps. As described above, the standard SPIRE catalogue at the NEP was produced by detecting and extracting a source using the 250 μm map and then using the 250 μm position to carry out photometry in all 3 SPIRE maps the photometry in that position for the three SPIRE images (250 μm, 350 μm and 500 μm Pearson (2018)). This is a reasonable and robust procedure to reliably find high-z sources from the SPIRE data, however, since our interest is to find extreme sources, the reddest 500 μm sources may yet be missed. Therefore, the source extraction and photometry was produced in the three SPIRE maps individually. After producing an individual catalogue for each SPIRE map, the catalogues were cross-correlated with a search radius smaller than 18 arcseconds (half of the SPIRE beam at 500 μm). We selected sources with all 3-bands above the SPIRE confusion limit that were 500 μm risers with $F_{500\mu m} > 30$mJy and colour $F_{500\mu m}/F350\mu m > 1.3$ (Riechers et al., 2013),

finding 14 sources likely at $4 < z < 6$.

All in all, 336 (268 using c-c diagrams + 18 500μm risers + 36 SCUBA-2 selected + 14 extracted directly from the single band SPIRE catalogues) high-z candidates, potentially at $z > 2$ were selected. The definitive list of sources is given in the Appendix A.

The efficacy and reliability of the two new methods investigated in this Chapter are compared using estimations of photometric redshift, calculated using simple SED template fitting (see Section 3.2.1 in Chapter 3). The first method, (photometry of the SPIRE maps in the SCUBA-2 positions), was found to identify moderate high redshift candidates ($z \sim 2$), whereas the second method, (single band catalogues derived from SPIRE maps independently), finds higher redshift candidates (see Figure 2.6). Thus the SPIRE maps method with the the 500 μm riser criteria, is clearly more efficient for the detection of sources at $z > 4$. The issue with the first method, is likely due to the fact that at the SCUBA-2 positions, if there is a SPIRE detection 3x above the confusion limit, there is not an extreme high-z source (since one may expect that for a true high redshift SCUBA-2 source the SPIRE detection would be extremely faint). Therefore, I propose to study true SPIRE dropouts at the SCUBA-2 source positions, i.e. sources with SCUBA-2 detection and no, or extremely faint SPIRE detection, even after combining the three SPIRE maps (see Section 2.3.4).

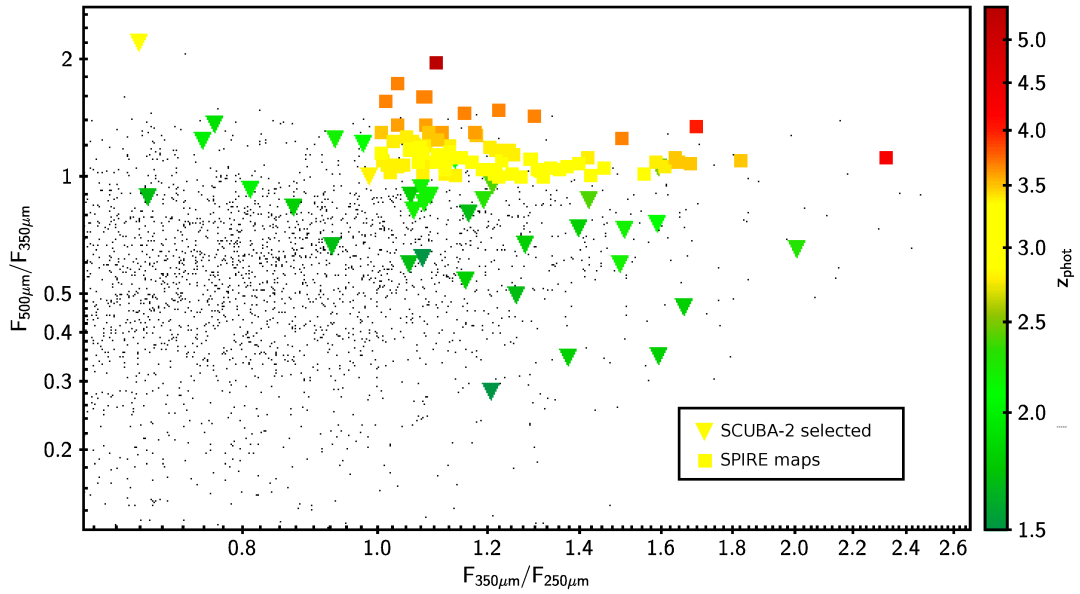

Figure 2.6: Colour-colour diagram amplifying the high redshift area of the parameter space where the high-z population is expected to lie. The first method - based on the SPIRE photometry at the SCUBA-2 position tends to find moderate high-z sources $z \sim 2$ (triangles). However, the second method - based on the detection in individual SPIRE maps - selects higher redshift sources on average.

The new high-z catalogue was then cross-correlated with the rest of the photometric data in the NEP field (see Section 2.2) in order to study the physical properties of the sample. Although the number of sources is reduced due to the lack of other multi-wavelength data, this approach makes possible a thorough study of the sample as presented in the next Chapter. Optical and infrared data from Murata et al. (2013) and Kim et al. (2012) (see Section 2.2.2) from the NEP-Deep and Wide fields respectively were used to cross match with the high-z catalogue. In both cases, a search radius of 9 arcseconds was used - half of the SPIRE 250μm beam - considering the possible matches inside this search radius. There were optical matches for 296 sources with 74 of them having a multiple detection. Note that a significant difference between the 2 optical catalogues was found regarding the multiplicity of sources. Using the wide field catalogue approximately 25 % of matches had multiple sources whereas in the deep field 73 % of the sources have multiple counterparts. This is simply due to the deeper field catalogue containing a higher density of sources than the wide field catalogue, especially for the faint optical sources that are the typical counterpart of DSFGs.

For both catalogues, in order to select the correct optical counterpart, the 15μm and 18μm bands were used effectively as an "IR-bridge": choosing the optical detection associated with the brighter IR detection. Furthermore I examined by eye to ensure that for each source, the selected counterpart corresponded to the correct source in the optical R-band image by using SUBARU and CFHT data in the Deep and Wide fields respectively (see Figure 2.7).

This final high-z multi-wavelength catalogue was studied by different SED fitting codes and is presented in next Chapter 3.

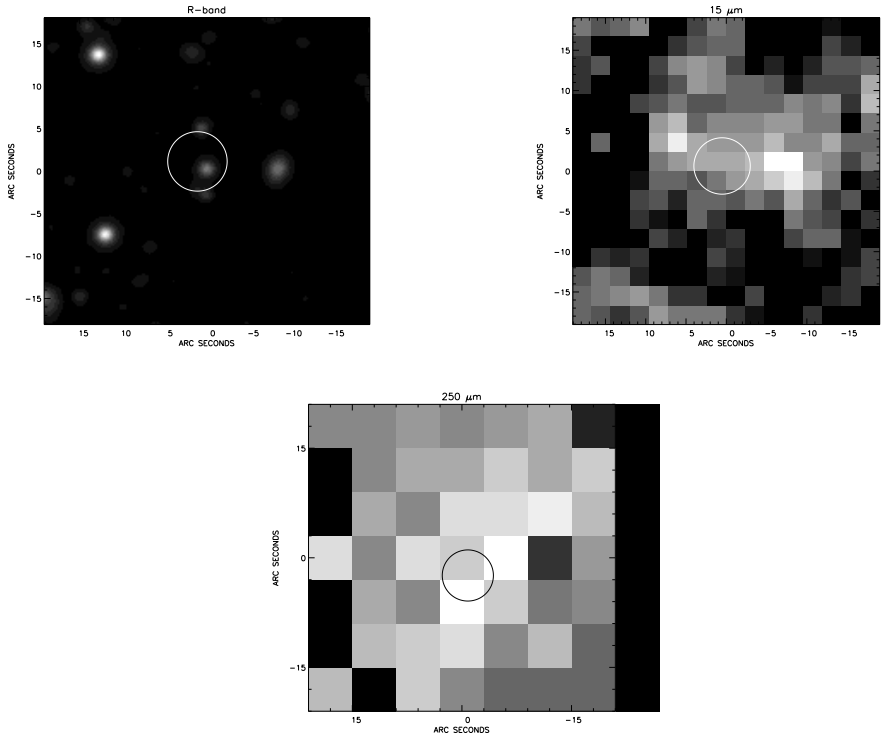

Figure 2.7: Postage stamps of the same high-z candidate with SUBARU R-band (left), AKARI 18μm band (middle) and SPIRE band at 250μm (left) within a 5 arcsecond diameter circle. An 'IR bridge' criteria is used in order to search for the most likely counterpart between the submillimetre data to the optical.

2.3.4 High-z selection through SPIRE dropout method

The use of the dropouts at submillimetre wavelengths to find high-z sources is based on the concept of the redshifting of the FIR dust emission peak of a galaxy SED through longer wavelength observation bands which sample the peak to higher redshift. At z > 6 it is not possible to observe SPIRE sources since the dust mission peak has been redshifted out of the longest wavelength 500 μm band however, it is possible to observe this emission in the SCUBA-2 870 μm band(see Figure 2.8). This lack of emission/detection in the three SPIRE bands and a detection at longer wavelength is referred to as the so-called 'SPIRE-dropout' phenomenon. This method has previously been successfully applied in SPIRE fields e.g. Clements (2017). Here I adapt this method for the SPIRE NEP field with our SCUBA-2 data at 850 μm.

An important caveat that must be considered in this section is that this work in this Section 2.3.4 is drawn from an earlier study which used a preliminary SCUBA-2 catalogue that contained only 136 sources instead of the final 330 sources (Geach et al., 2016). Although some of these preliminary sources are a subset of the final catalogue, this study will be repeated with the published version of the catalogue (see Future work 6.2.1).

In order to apply the SPIRE dropout method for the detection of high-z candidates in the NEP, using our SPIRE and SCUBA-2 data the following procedure was applied (summarised in Figure 2.9):

- Cross-match the SPIRE catalogue (Pearson, 2018) with SCUBA-2 catalogue (Geach et al., 2016) with a search radius of 9 arcseconds.
- Filter to retain sources with only a SCUBA-2 detection (i.e. a SPIRE Dropout)
- An RGB (red-green-blue) image is created with the 3 SPIRE maps at 250 μm, 350 μm and 500 μm respectively.
- Flux contour plots from the SCUBA-2 maps are over-plotted on the SPIRE RGB image at the SPIRE Dropout positions.

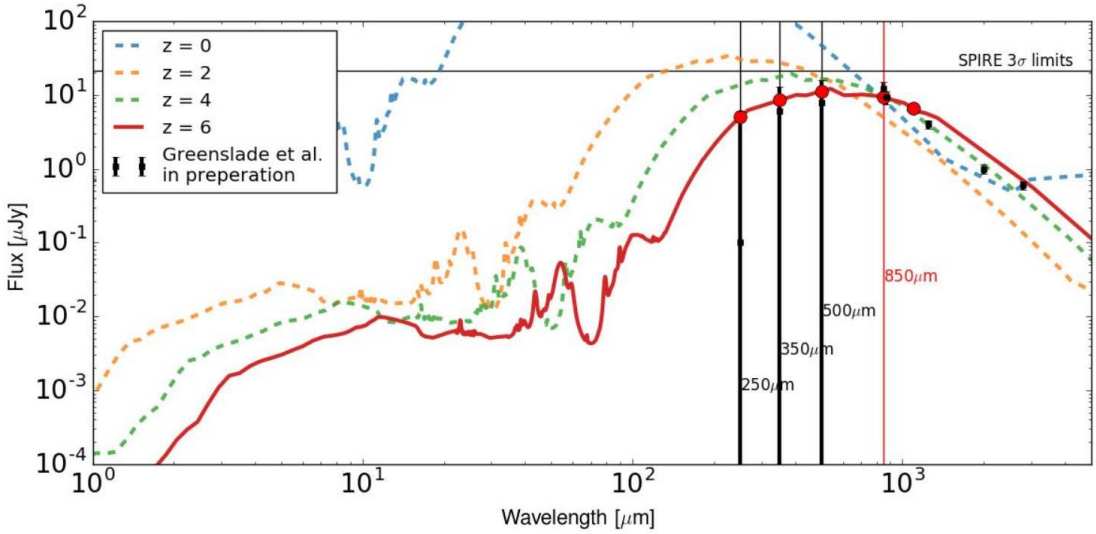

Figure 2.8: An artificial SED shifted with redshift: z = 0 (blue line), z = 2 (yellow line), z = 4 (green line) and z = 6 (red line). The red line is an example of a SED of a so-called 'SPIRE dropout': sources that do not have emission in the SPIRE bands, however they do have detectable emission at longer wavelengths, which indicates that the SED is highly red-shifted (Greenslade 2018 personal communication).

For these sources, there are no detections in any of the 3 SPIRE bands, but the contour plot from SCUBA-2 shows a source. The peak of the dust emission spectrum has been shifted into the SCUBA-2 band. However, the SPIRE bands can no longer detect the galaxy (see Figure 2.9). The SPIRE dropout method finds 46 sources with $F_{850\mu m} > 6.1$mJy nearly double the flux provided by the catalogue Geach et al. (2016) which has a 3σ detection.

The sample of 46 SPIRE dropouts was cross-matched with the rest of the data available in the field in order to calculate the photometric redshift and extract the physical properties of the sources, such as infrared luminosity and star formation rate. The SCUBA-2 data was cross-matched with optical-NIR data (Murata et al., 2013) using a search radius of $5''$, since both cover the NEP Deep field.

The SED fitting was made by using the LePHARE package (Arnouts & Ilbert, 2011) which compares the observational detections with well-defined SED templates (see next Chapter 3.2.2). Only sources with at least 5 photometric points were considered (e.g. Rowan-Robinson et al. (2016)) and the SED templates used were taken from the Berta et al. (2013) and Polletta et al. (2007) libraries. By definition, the SPIRE

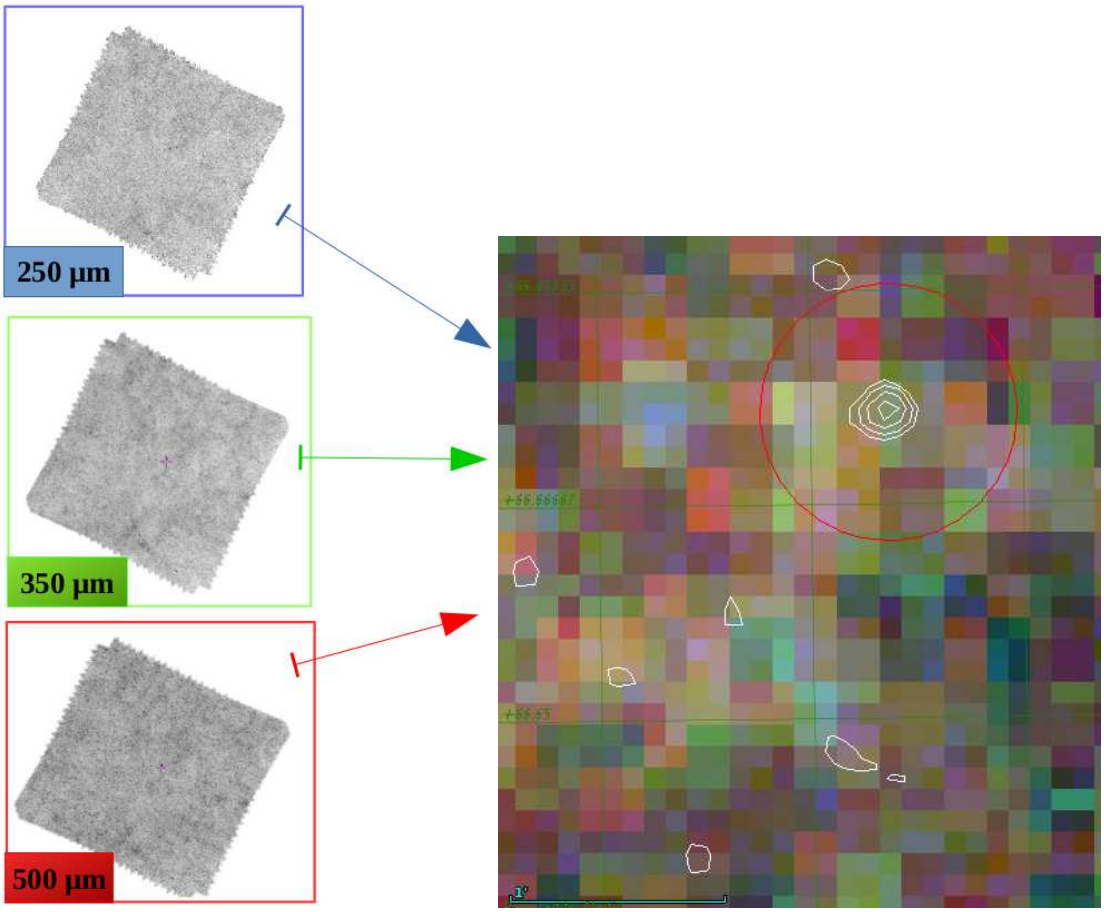

Figure 2.9: Summary of the SPIRE dropout method using both SPIRE and SCUBA-2 maps. The three SPIRE maps (left) are combined to create a RGB image on which the contour plots of the SCUBA-2 source detections are over-plotted (in this case at RA = 269.109 and Dec = 66.673 degrees with a flux of $F_{850\mu m} = 6.5mJy$
).

dropouts have only a single detection across the FIR peak, which severely limits the redshift estimation and therefore the accuracy of the rest of the physical parameters. Since LePHARE only uses the optical bands to calculate the photometric redshift, the lack of data in the FIR peak is less important compared to other fitting codes such as MAGPHYS or CIGALE (see Section 3.2). Galaxies are classified by the best fit UV-optical templates as follows:

72% of the sources as SFGs (dust attenuated optical selection), out of which 33% have an Active Galactic Nuclei (AGN) presence.

20% of the sources fit with Spiral galaxies templates, related with low star formation

8% are Irregular galaxies.

For comparison the 268 high-z candidates selected with c-c diagram criteria in Section 2.3.1 - the most common method - were studied with LePHARE in order to contrast both methods. The SED fitting classifies a larger number of the sources as star forming galaxies with more significant presence of an AGN: 81% of the population are SFGs (42% have an AGN presence), 17% Spirals and 2% Irregular (see Figure 2.10 which shows the SEDs of the sources selected with both methods).

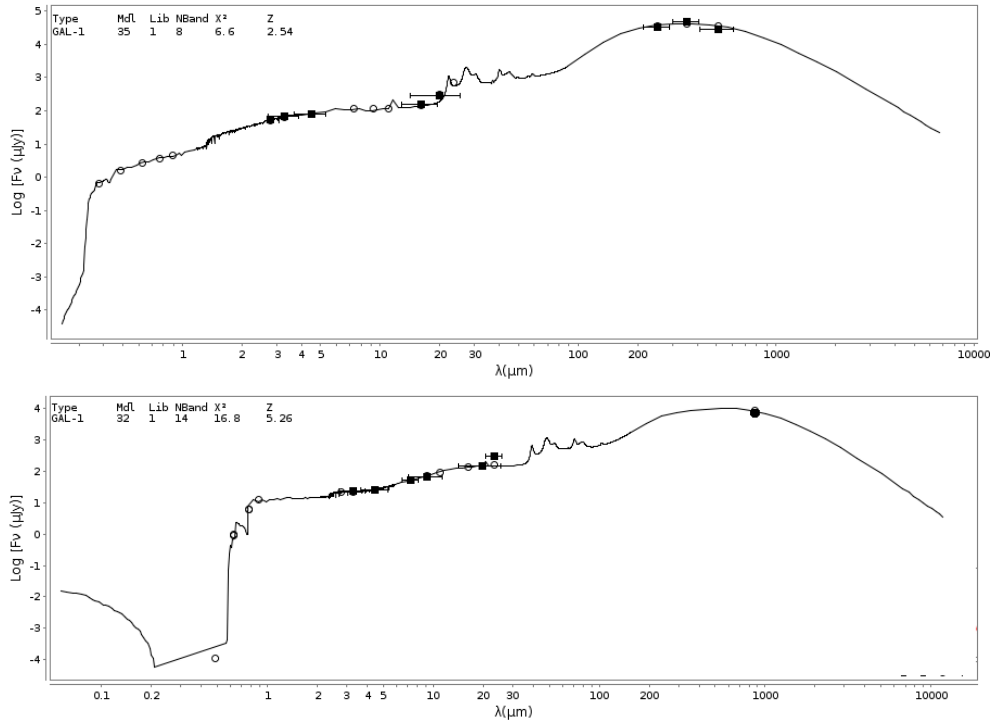

Figure 2.10: SED example of two high-z candidates fitted with the LePHARE package. The black line is the fitted SED using the libraries Berta et al. (2013) and Polletta et al. (2007) that best fits the observations (black squares). The upper left part of both images shows the following parameters: "Type" which can be GAL if the template is a galaxy or QSO if the template is a quasar, "Mdl" indicates the template selected in the library "Lib", the "Nband" parameter stands for the number of detections used in each fit with the goodness of the fit χ^2 and finally z is the output of LePHARE's photometric redshift. (Top) SED fitting of one of the 268 candidates ($z_{phot} = 2.54$ and $\chi^2 = 6.6$) selected with the SPIRE colour criteria in Section 2.3.1. (Bottom) SED fitting of a candidate ($z_{phot} = 5.26$ and $\chi^2 = 16.8$) selected by the SPIRE dropout method which enable us to find higher redshift sources than the FIR colour diagram method.

The reliability for the two methods in terms of photometric redshift is the same, since LePHARE only uses the optical bands to calculate the redshift, therefore the dif-

ference of the detections across the FIR peak is irrelevant. However, this is a limitation in the reliability of the photometric redshift, since it is calculated with a few bands and using a template approach without taking into account the redshift-temperature degeneracy (see Chapter 3 for further detail in the different SED fitting approaches and codes).

The c-c diagram method finds candidates at lower photometric redshift, on average $\bar{z}_{phot} = 2.25$, whereas the SPIRE-dropouts method finds higher redshift candidates with $1.70 < z_{phot} < 5.71$ (see Figure 2.11 that compares the redshift distribution between the two methods).

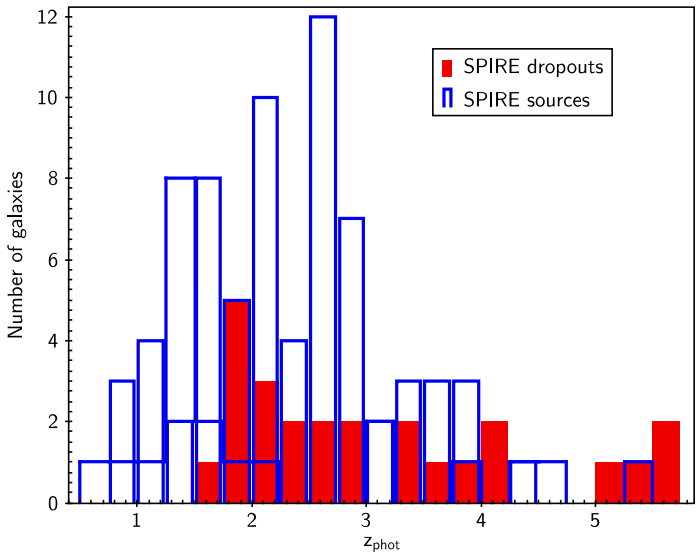

Figure 2.11: Number of sources against redshift for the two different selection methods. The SPIRE dropouts method (in red) appears to select sources at higher redshift than the SPIRE colour-colour method (in blue).

However, the sources selected using the SPIRE dropout method appear to be intrinsically fainter sources with infrared luminosities $10^{11.64}L_{\odot} < L_{IR} < 10^{13.13}L_{\odot}$ in the case of the SPIRE dropouts and $10^{11.80}L_{\odot} < L_{IR} < 10^{13.96}L_{\odot}$ for the c-c method. The star formation rate (SFR) was calculated by the Kennicutt law (Kennicutt, 1998) that assumes the SFR is proportional to the luminosity (see Introduction 1.2.2). Since the dropouts have lower luminosity than the sources selected with the c-c diagrams, the SPIRE dropouts have lower SFR ($7M_{\odot}/yr < SFR < 236M_{\odot}/yr$), whereas the c-

c selected sample high-z candidates on average have $11M_{\odot}/yr < SFR < 1590M_{\odot}/yr$ which are values more expected for these types of galaxies (Rowan-Robinson et al., 2016).

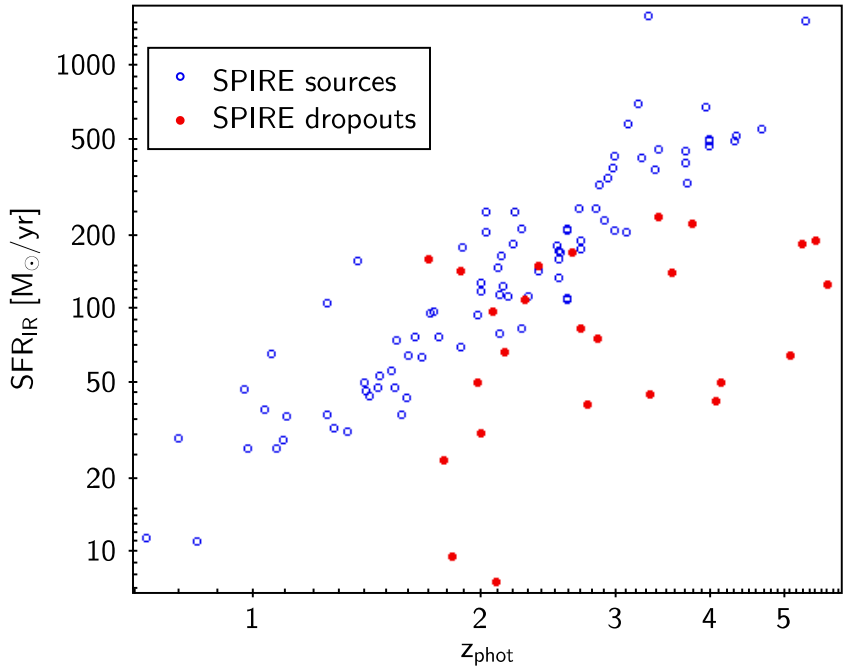

Figure 2.12: The SFR_{IR} against the photometric redshift calculated with LePHARE. The SPIRE dropout galaxies (in red) have lower star formation rates than the SPIRE c-c selected sources (in blue), however the former are at higher redshift.

These results indicate that the SPIRE dropouts are the fainter sources that SPIRE was not able to observe, however, they have a similar nature to the SPIRE sources and they are not extreme starburst like the source studied in Riechers et al. (2013). This result shows the existence of dusty high-z sources that are intrinsically faint, revealing that the nature of DSFGS has moderate star formation as Zavala et al. (2018) indicates and not extreme starbust as in Riechers et al. (2013). However, this analysis must be repeated with the published catalogue and the photometric redshift should be corroborated with spectroscopic observations.

2.4 Summary

The aim of this Chapter was to study the various methods that can be potentially used to select dusty high-z sources leading to the production of a high-z catalogue. The methods are summarised as follows:

- The common c-c diagrams which find 286 sources potentially at z > 2
- High-z selection through submillimetre source position, producing the photometry of the SPIRE sources at the SCUBA-2 positions. This method selects 36 potential sources with photometric redshift at z > 2.
- High-z selection through single band detection, source detection and photometry from each individual SPIRE band map separately, then cross-matching resulting catalogues and applying the 500 μm risers criterion, with a flux cut $F_{500\mu m} > 30$ mJy and colour cut $F_{500\mu m}/F_{500\mu m} > 1.3$ (Riechers et al., 2013). This method finds 14 sources at potential redshift 4 < z < 6.
- SPIRE dropouts: sources with a clear SCUBA-2 detection and a lack of SPIRE detection in the three bands. The method selects 46 sources with $1.70 < z_{phot} < 5.71$

The most successful method, the SPIRE dropouts method, was compared with the most standard method, the c-c diagrams, concluding that the SPIRE dropouts are intrinsically faint sources that SPIRE does not have the sensitivity to detect. The c-c selected SPIRE sources are found to have higher star formation rates than the SPIRE dropouts, which shows the existence of dusty high-z sources that are intrinsically faint, revealing that the nature of DSFGS have moderate star formation as Zavala et al. (2018) indicates and not extreme starbust as Riechers et al. (2013), who used a similar colour method to select their extreme high-z source. Furthermore, the SPIRE sources that are classified by SED fitting as being starbursts are 10 % higher than the SPIRE dropouts, the same percentage difference with an AGN presence is found in the SED fitting. However,

this result must be repeated with the published catalogue and the photometric redshift confirmed by spectroscopic observations.

All in all (taking into account the repeated sources and without including the SPIRE dropouts), a catalogue containing 336 high-z sources at $z > 2$ (see Appendix for the complete list) was created. This catalogue will be analysed in the next Chapter 3.

Chapter 3

Physical properties of the high-redshift population of galaxies

The physical properties of high-z dusty star forming galaxies (DSFGs) are not fully understood and even simple questions such as the mechanisms and nature of their star formation is still being debated. Has star formation in DSFGs been driven by similar physical processes during the last 12.8 Gyrs ($0 < z < 6$); or have the mechanisms to form stars changed or evolved over this time? Some suggest that the star formation rates during this time may not have changed significantly and that they have always had moderate star formation (Zavala et al., 2018). However there is clear spectroscopic evidence of extreme star formation, of a few thousand of solar masses per year, in these sources, (Riechers et al., 2013). Are these then exceptionally luminous galaxies, more common in the high-z Universe than in the local Universe, and if so, does it imply that major mergers dominated at early times? This work aims to tackle these questions by studying a sample of high redshift DSFGs in fields with good multi-wavelength coverage, in particular, at the North Ecliptic Pole (NEP), the continuous viewing zone for many space telescopes. The selection of the dusty high-z was carried out by a submillimetre selection with the aim to study their physical properties and their location in and association to the main sequence of galaxies. The high-z sample (on average $\mathrm{z} = 2.59 \pm 0.13$*; 15 of them with* $4 < \mathrm{z_{phot}} < 6.2$*) are found to lie either*

on the Main Sequence of galaxies (MS), whilst 30% lie clearly above the MS, having higher star formation efficiencies (SFE) which is related to the age of the burst in the galaxy: the earlier the starburst in the galaxy the more efficient the star formation.

3.1 Introduction

Submillimeter galaxies (SMG) are the among the most luminous dusty galaxies in the Universe (Wilkinson et al., 2017), however it is technically difficult to observe them at really high-z and to date, only three examples of them have been found above z = 6.

Larger samples of dusty high-z galaxies are urgently needed, along with a framework in which to characterise their properties. The aim of this Chapter is to study the sample selected in Chapter 2, which contains a broad distribution of redshift $6 > z > 2$ in order to model their physical properties, focusing on their star formation. The nature of these galaxies is approached using their position in the Main Sequence of Galaxies (MS): the relation between the star formation rate and the stellar mass, where most galaxies lie due to the correlation between these two parameters (Sargent et al., 2014).

There is a clear disagreement in the literature regarding the location of SMGs on the MS: while some studies strongly suggest that they have high SFR, lying off the MS of galaxies (Miettinen et al., 2017) (da Cunha et al., 2015), other studies have found a more moderate SFR following a normal mode of star formation (e.g. Koprowski et al. (2016), Dunlop et al. (2017)). The latter study was a deep pencil-beam ALMA survey in the Hubble Deep Field (HDF), and hence was sensitive to lower SFRs, over comparable stellar masses, whereas the sources from the other studies mentioned above have often been part of some selected sample. Therefore, the different results could be due to some selection effect. These two scenarios can also co-exist if there is a genuine bimodality of star formation in SMGs (Elbaz et al., 2017), but the reasons for the different star formation modes needs to be explained within the general sphere of galaxy evolution.

A plausible explanation could be that the morphology of the galaxies can be related

to the mergers which influence the SFR (Elbaz et al., 2017), specifically that mergers enhance the star formation in these early stages (Riechers et al., 2017). If so, are the nature of starforming galaxies such as HFLS3 ($z = 6.3$ with SFR $\sim 2900 M_{\odot} yr^{-1}$) (Riechers et al., 2013) representative of SMGs? Recent studies indicate that DSFGs at $z > 6$ can also have moderate star formation, with similar gas and dust properties to local ULIRGs, which suggests- albeit only with a sample of a single source - a universal star-formation efficiency during the last 12.8 Gyr for dusty star-forming galaxies (Zavala et al., 2018). Summarizing, the mode of star formation - and in general, the nature - of SMGs is still unclear; determining their position on (or off) the MS and the reasons of their mode(s) of star-formation is key to a better understanding of their nature.

The star formation efficiency relates the star formation with the gas of the galaxy. Therefore, finding some parameter that correlates with the SFE can also relate to the triggering, or quenching of star formation. This Chapter presents the results of the estimation of the physical properties - calculated by spectral energy distribution (SED) fitting - of submillimetre high redshift selected galaxies in the North Ecliptic Pole field (NEP) using a multi-wavelength data set comprising of optical, mid-infrared through to submillimetre data. In Section 3.2 several SED fitting codes are discussed, presenting the analysis with the two more successful codes in Section 3.3 and 3.4 respectively and comparing them in Section 3.5. In Section 3.6 the photometric redshift, together with other physical parameters - such as stellar masses or SFR - are calculated, describing the position of the sample on the MS of galaxies In Section 3.7 the results are discussed.

3.2 Spectral fitting techniques and codes

During the last two decades the advances in both ground, and especially space, telescopes have seen an increase in the data available in both survey area and wavelength coverage (see Introduction, Section 1.3.1 for a review). The multitude of photometric observations has made spectral energy distribution (SED) analysis a key tool to gather

information from multiple wavelengths in order to extract the physical properties of galaxies. Galaxies emit radiation across the electromagnetic spectrum, from UV to submillimetre. This emission arises from stars, either directly (UV to optical) or via reprocessing by the gas and dust of the surrounding interstellar medium (ISM). SED fitting techniques has proven a useful technique to effectively derive star formation rates, photometric redshifts, and dust and stellar masses, although there are still challenges to overcome and there is not yet a unique SED fitting code or approach (see Walcher et al. (2011) for a general SED fitting technique review).

There are broadly two type of SED fitting codes:

1. Fitting based on existing spectral template libraries to fit the observations.

2. Fitting based on producing SEDs through assumed physical properties / initial parameters that are fit to the observations.

The template based methods have the advantage of being simple and quick to compare large samples with libraries based on well studied SEDs of other galaxies. If a spectroscopic redshift is given, they can give good results in terms of physical parameters such as SFR and luminosity. However, the number of libraries is always limited and the sample must have similar characteristics to at least a subset of the templates available in the libraries.

Fitting methods often use Bayesian inference of the physical properties assuming Gaussian uncertainties given a probabilistic distribution function (PDF) for each parameter evaluated, where the probability of the data D, given the model M, is P(D|M) $\propto e^{-\chi^2/2}$. These codes have the advantage that all the measurements contribute to the fit result and they do not depend on any set template, since they are based on models. The probabilistic analysis allows for the production of likelihood distribution functions that show if the parameters are well constrained. The disadvantages are the computing time, the complexity of the use of the code and, for some of the codes, the variety of inputs that the user has to introduce, such as the selection of the models or the grids of values for the physical parameters.

The most important parameter by far for producing accurate SED fitting is the redshift, and whether the redshift is photometric (calculated with photometric detections in different wavelength bands) or spectroscopic (measured using emission lines, ideally several). The redshift gives an important input to the properties of the galaxy, fixing the SED to a specific emitted wavelength and cosmic time and giving direct information about the intrinsic parameters, such as the luminosity. Furthermore, having this input avoids the possibility of having degeneracies, such as the redshift dust temperature which has an important relevance in galaxies selected via submillimetre colours. In the following sections I will be building on this concept and the importance of the redshift, and explaining the differences between standard publicly available methods and codes.

There are multiple SED fitting codes that are focused on different uses and approaches. The most recent and those most used in the literature are summarised in Table 3.1.

Code	Based on	Redshift range	Main characteristics
LePHARE (Arnouts & Ilbert, 2011)	Templates	Any	Designed for UV-optical analysis (limitations at longer wavelengths) Plenty of libraries
MAGPHYS (da Cunha et al., 2015) (da Cunha, Charlot & Elbaz, 2008)	Physical properties	$z > 1$	Focused on the study of high-z DSFGs Needs as input a spectroscopic redshift Simplistic approach to the dust emission
CIGALE (Noll et al., 2009)	Physical properties	Any	Calculates the photometric redshift Versatility of contributing emission models in each part of the spectra
EAZY (Brammer, van Dokkum & Coppi, 2008)	Templates	$z < 4$	Limitations at FIR wavelengths Limited to use at lower redshifts

Table 3.1: Table of the most popular spectral fitting codes commonly used for DSFGs (see www.sedfitting.org for a comprehensive general list). The first column shows the SED codes with their references. The second column shows whether they are template based or based on physical properties derived fro models. The third column shows the usable redshift range. The fourth column refers to the main characteristics focusing on advantages and disadvantages.

3.2.1 Single templates

Before discussing the available SED fitting codes, it should be noted that fitting using a single selected SED template is still widely used in the literature (e.g. adopting M82 as an archetypal starburst or Arp220 for ULIRGs). This method is based on fitting the photometric detections with well-known templates that are expected to be similar to the sample. This has the merit of being a very quick way to calculate the redshift, following a similar but much simpler approach to SED fitting codes based on template libraries, taking into account the shift of the SED due to the redshift in order to get an idea if the source is a high-z candidate. Although this method is used in the literature (e.g. Michałowski, Hjorth & Watson (2010), Rowan-Robinson et al. (2016)), it is limited by the templates that define the physical properties of the sample. However, the use of such simple templates is still useful for studying high-z submillimetre selected galaxies (see Chapter 2), comparing with SMG templates at $z > 4$ if the obvious limitations are taken into account.

Using this method, the photometric redshift can be estimated using the submillimetre bands in order to give only an indication of the expected redshift (see Figure 3.1 as an example). In this example, the redshift can be estimated by fitting the SPIRE and SCUBA-2 photometry, sampling the dust emission hump, to a SMGs template from Michałowski, Hjorth & Watson (2010). It shows the success of the colour criteria in selecting high-z candidates,as shown in Figure 3.2. However, a more reliable photometric redshift, which takes into account physical properties of the whole spectrum, was calculated with CIGALE (see Section 3.4), showing significant differences between the photometric redshifts estimated by the two methods.

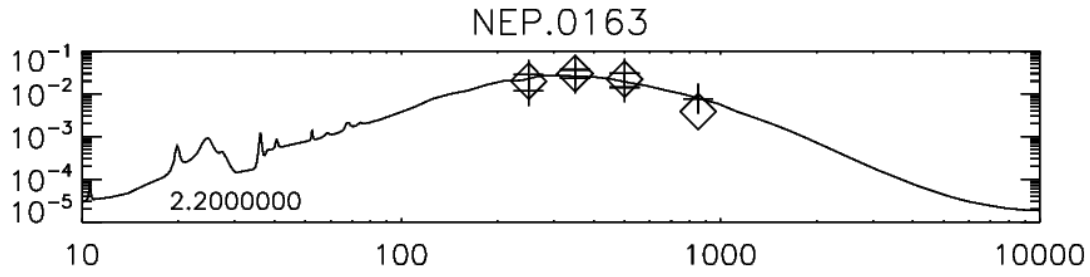

Figure 3.1: SED fitting for one of the high-z sources ($z_{phot} = 2.2$) using SPIRE and SCUBA-2 data sampling the dust emission hump. This photometric redshift is only an indication and robust photometric redshifts must be calculated by taking into account observations across the entire spectrum.

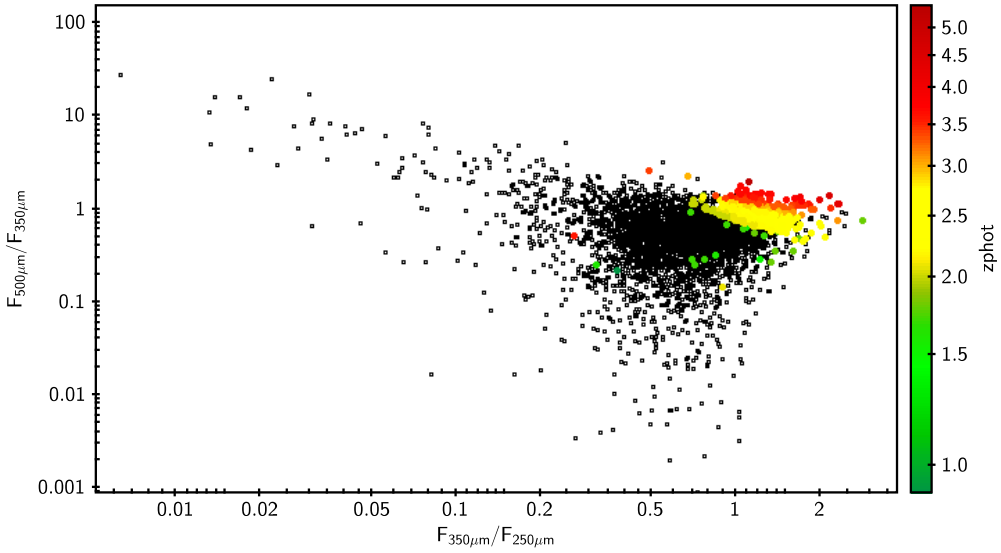

Figure 3.2: Colour-colour diagram of the SPIRE sources (black) with the photometric redshift - calculated as is shown in Figure 3.1 - in the colour bar, showing that the high-z population lies in the right upper part of the c-c diagram.

3.2.2 LePHARE

The Photometric Analysis for Redshift Estimations (LePHARE) code (Arnouts & Ilbert, 2011) is a (Fortran based) SED fitting code that fits observations with SED templates of other well-know sources (stars, galaxies and quasars). LePHARE is clearly a better choice than using a single template since the code introduces physical parameters (such as the transmission of the filters, the reddening, emission lines, etc.) which are not taken into account when comparing with individual templates. The main disadvan-

tages of LePHARE - as with any other code based on templates - is the limitation in templates, however, amongst the publicly available codes, some authors state that LePHARE is "the most accurate redshift from template approach" (Walcher et al., 2011) and also allows the set of templates to be updated by the user (and does not have limitations in redshift as Easy and Accurate Zphot from Yale (EAZY) code). However, LePHARE was initially created only for use at UV-optical wavelengths and treatment of the FIR was included a posteriori, in fact LePHARE only uses the UV-optical for calculating the photometric redshift and does not take into account the IR for calculating most of the physical parameters. Furthermore, most of the libraries provide templates at only short wavelengths (see Figure 3.3) and even the updated version of the code that includes FIR libraries requires a previous fitting with UV-optical templates, only using the FIR as a second step to improve the fitting.

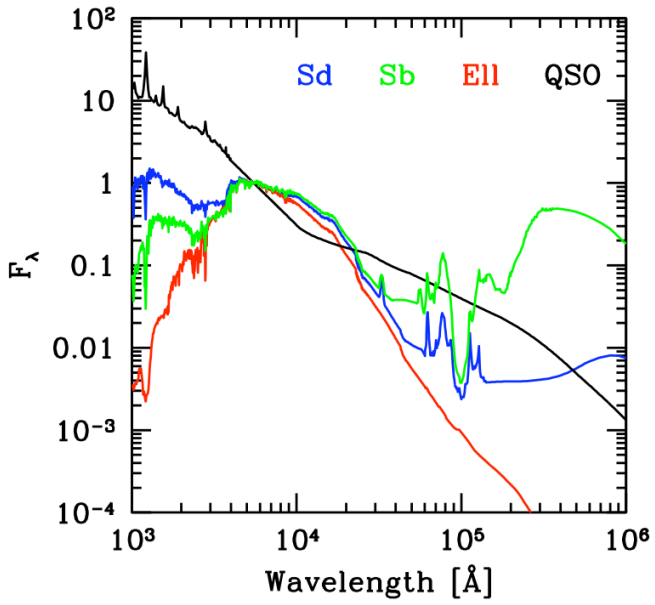

Figure 3.3: The Figure shows 4 of the 20 Polletta et al. (2007) templates that are part of the extended version of LePHARE FIR libraries. All the templates cover UV to FIR wavelengths; the blue and green SEDs are Spiral galaxy templates, whereas the red line represents an elliptical galaxy and the black line is a quasar template. (Figure extracted from Walcher et al. (2011))

In this thesis LePHARE was used for two purposes for our sources in the NEP region: firstly, to estimate the photometric redshift and secondly to produce simulated redshift tracks of galaxies to compare colour-colour distributions, etc. For the first

Parameters	Description
Inputs:	
STAR LIB	Stellar library (list file)
QSO LIB	Quasar library (list file)
GAL LIB	Galaxy library (list file)
MAGTYPE	Magnitude type (AB or VEGA)
Z STEP	Define the maximun and minimum
CONTEXT	Number that define the filters used in each source
Outputs:	
ZBEST	Photometric redshift for the best fitting
CHIBEST	lowest χ^2
MODBEST	Library and template for the best fitting
SFR	Star formatin rate for the best fitting
LDUST	Dust luminosity [$L_\odot$]
LUM NUV	UV luminosity [$L_\odot$]
LUM R	Optical luminosity [$L_\odot$]

Table 3.2: Example of the main input parameters (defined by and contained in the .para file) and outputs (produced by the code as an ASCII file) for a LePHARE configuration. The inputs mainly consist of information such as libraries, the units or the steps in redshift. The outputs are the main physical parameters, such a redshift, SFR or luminosity.

purpose, the current use of LePHARE was verified with previous photometric redshift data in the field from Oi (2014) which also utilises LePHARE. This reproduction of results was only done for pedagogical purposes in order to verify that the code was used correctly by comparing both results. After reproducing successfully the results in the literature (see Figure 3.4), LePHARE was used in order to compare two samples selected by different selection criterion to avoid bias due to the different FIR-submillimetre data information. Furthermore, the method to calculate the photometric redshift was improved with respect the Oi (2014) catalogue, since only by using optical data and templates for calculating the redshift is indeed less reliable than by using a more comprehensive wavelength range and more physical models (see Section 2.3.4 Chapter 2).

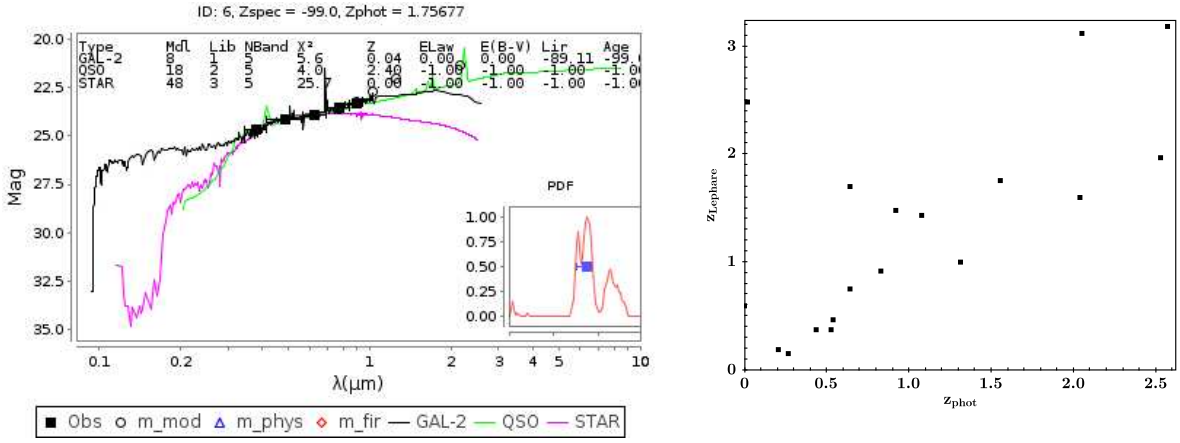

Figure 3.4: (Left) The figure shows a LePHARE SED output - without any cleaning parameters - for one of the sources from the catalogue of Oi (2014). The black squares are the observations (in magnitudes), whereas the lines correspond to an assumed galaxy template (black), a quasar template (green) and finally a stellar template (purple). The resultant photometric redshift calculated with LePHARE is $z_{phot} = 1.75$ (see title bar of the plot) whereas the value reported by Oi (2014) is $z_{phot} = 1.6$. (Right) The Figure compares the photometric redshifts from the original photometric catalogue against the new redshift obtained with LePHARE, which are in reasonable agreement. where the errors in the photometric redshift are lower than ± 0.11 for $z_{phot} < 1$ and ± 0.15 for $1 < z_{phot} < 2.5$ on average, but the errors are not given in the catalogue (Oi, 2014), whereas the errors in this sample given by LEPHARE are ± 0.2.

LePHARE was also used to produce redshift evolutionary tracks for evaluating the high-z colour space in the SPIRE colour-colour diagrams produced in the previous Chapter 2. The SEDs of two well-known star forming galaxies (Arp220 and M82)

were evolved with LePHARE introducing redshift steps of $\delta z = 0.1$ and extracting the output (using the LePHARE application mag-lib) of the fluxes of these SEDs in the SPIRE bands at 250 μm, 350 μm and 500 μm (see Figure 2.3). LePHARE uses this same resource for producing the SED fitting itself, providing the values of the SED fluxes as an output.

3.2.3 MAGPHYS

Multi-wavelength Analysis of Galaxy Physical Properties (MAGPHYS) is a SED fitting code based on the physical properties of galaxies (da Cunha, Charlot & Elbaz, 2008). This work uses an updated version of MAGPHYS (da Cunha et al., 2015) which is focused on the study of high-z (z > 1) DSFGs.

MAGPHYS estimates the properties of the sources in 2 steps but requires the redshift of the source a priori. Firstly, it generates 2 libraries (one for the optical emission and another for the IR emission) of SED models using the redshift of the source as the only input. Following this, MAGPHYS compares the observations with the models, deriving the likelihood distribution of each physical parameter i (e.g. SFR, M_*, M_{dust}, etc). MAGPHYS is written in Fortran language, but there is a small piece of IDL code to produce quick plots of the SED and the reliability of some physical parameters through the likelihood distribution (see Figure 3.5).

Significantly, the only information that the user can introduce are the details of the observations (and the redshift) as the filters and observations files (see Table 3.3 for the main inputs and outputs in the code). The rest of the possible parameters are a black-box that the user cannot control and all the modeling is produced with the libraries: $starformhist - cb07 - z.lbr$ and $infrared - dce08 - z.lbr$ that correspond to the optical and infrared emission respectively. These two libraries simply require the redshift as input (contained in the observation file), therefore, the code does not take in consideration any specific a priori physical parameters of the galaxy. Moreover, the simplistic approach of the models in the infrared emission can make some of the out-

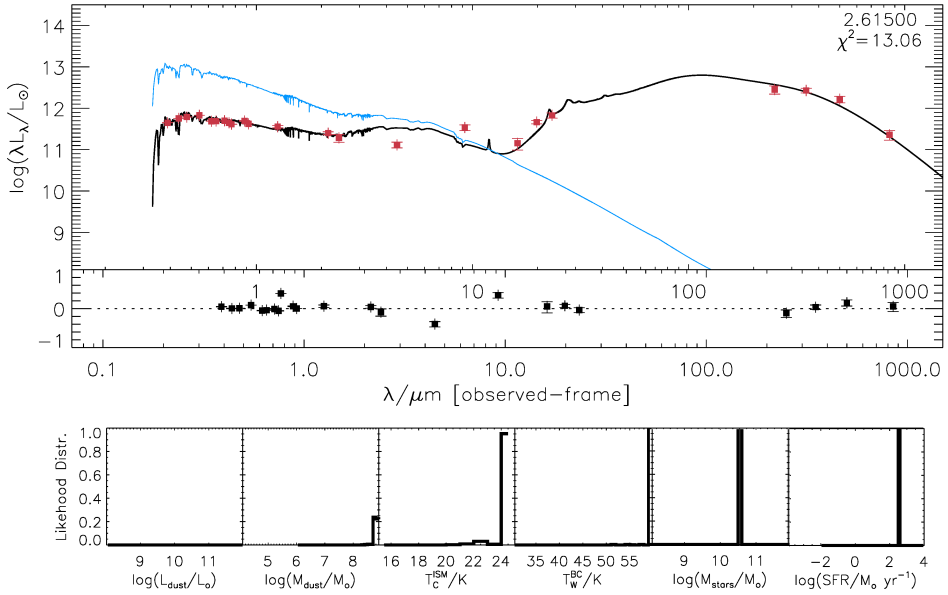

Figure 3.5: The figure shows the SED fitting extracted with MAGPHYS of one of the NEP sources with a spectroscopic redshift. The final SED is composed of both optical and infrared models (black line), whereas the stellar emission (blue line) is extracted from the optical library. The red squares show the observations in 22 photometric bands. This is the best fitting model ($\chi^2 = 13.06$ with 24 photometric detections) obtained with MAGPHYS for this high-z source ($z_{spec} = 2.615$). The plots below show the likelihood distribution for the parameters: dust luminosity, mass dust, temperature of the ISM, temperature of the birth clouds, stellar mass and SFR respectively. This likelihood distribution shows that the parameters are well constrained and therefore reliable.

puts unreliable (as described in Section 3.5). Due to these limitations it is mandatory to know in advance, the redshift in order to produce the model SEDs to compare with the observations. Unfortunately, this defeats the object in the sense that once the spectroscopic redshift is known, much simpler codes based on templates can make similar work. For the case of our sample, the lack of spectroscopic data meant that the use of the MAGPHYS code was not continued in this work (in addition with some evidence that the code tends to overestimate the stellar masses which is a key parameter in the study of the galaxy MS in this Chapter). However, some of the results produced during this investigation are presented in Section 3.3.

Parameters	Description
Inputs:	
filters.dat	Filters file
observations.dat	Observations file
Outputs:	
sfr	SFR [$M_\odot$/yr]
M_*	Stellar mass [$M_\odot$]
M_g	Gas mass [$M_\odot$]
T_W^{BC} and T_C^{ISM}	Temperature of the birth clouds and the interstellar medium [K]
L_d^{tot}	Total dust luminosity [$L_\odot$]

Table 3.3: Example of the main inputs with MAGPHYS: a filters file describing the photometric bands and an observations file containing the photometric points and the redshift. The main outputs (produced by the code as an ASCII file) are the physical parameters, SFR, stellar and gas mass, dust/gas temperatures and the dust luminosity.

3.2.4 CIGALE

CIGALE (Code Investigating GALaxy Emission) is a SED fitting code based on the physical properties of galaxies (Noll et al., 2009) that covers SEDs from UV to radio wavelengths taking into account the balance between the energy emitted in the UV-optical, absorbed by dust and remitted in the IR. CIGALE builds stellar population models first before considering the dust emission by reddening the stellar SEDs and re-emitting the absorbed energy at longer wavelengths.

The main advantage of CIGALE compared to the other SED fitting codes considered in this work, is its versatility, since the user can choose several models for each part of the spectra with plenty of parameters to select. Moreover, this flexibility allows new modules to be written by the user calling them from the main program. These new modules can be tailor made to the needs of each user making this functionality an extremely powerful tool.

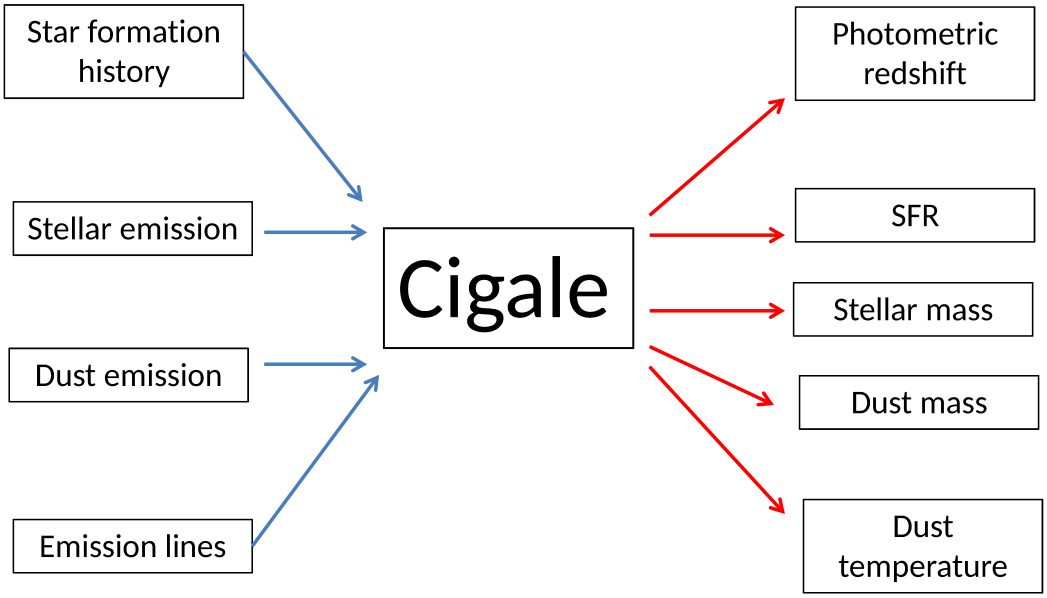

Figure 3.6: CIGALE in a nutshell: on the left side of the image are the main physical considerations defined by several models that must be chosen - or coded - by the user and on the right side, the main physical parameters that CIGALE gives as an output producing a Bayesian analysis of the outputs the user requests.

Depending on the models introduced, CIGALE can be used to fit a very wide rango of samples. The main modules, based on different models, with their main parameters are summarized in Table 3.5 and the modules are described below:

Stellar component

The first step of CIGALE is to build the stellar population and define the energy that is emitted by stars. There are several modules that can be used for this purpose. The widely used Bruzual & Charlot (2003) models assume a single stellar population by isochrone synthesis, which takes the stars at the same age and then integrates the spectra of all stars to compute the total flux. The disadvantage is that the isochrones are calculated in discrete steps in time and therefore any stellar evolution more rapid than these time steps is not well represented.

CIGALE was originally created for use with the Maraston (2005) models, which also assumes a single stellar population, but the main difference with Bruzual & Charlot (2003) is the assumption for approaching single stellar populations. Instead of isochrones,

Maraston (2005) uses the fuel assumption approach, which uses the turn-off of the stellar main sequence in the Hertzsprung-Russell diagram - integrated along the evolutionary track - and takes into account the luminosity of the post-main sequence stars which are the most luminous. This reduces the impact of shortly lived stars - such as thermally pulsing asymptotic giant stars (TP-AGB) - that due to their high luminosities can alter the M_*/L ratio of intermediate age populations.

Star formation history

The stellar component takes into account the Star formation History (SFH), although it is defined in an independent module in CIGALE. This is the key parameter to calculate the SFR.

There are several SFHs that describe the star formation of galaxies across the cosmic time and that give totally different SFRs considering physical processes depending on the nature of the galaxy (see Figure 3.7 for the most common examples).

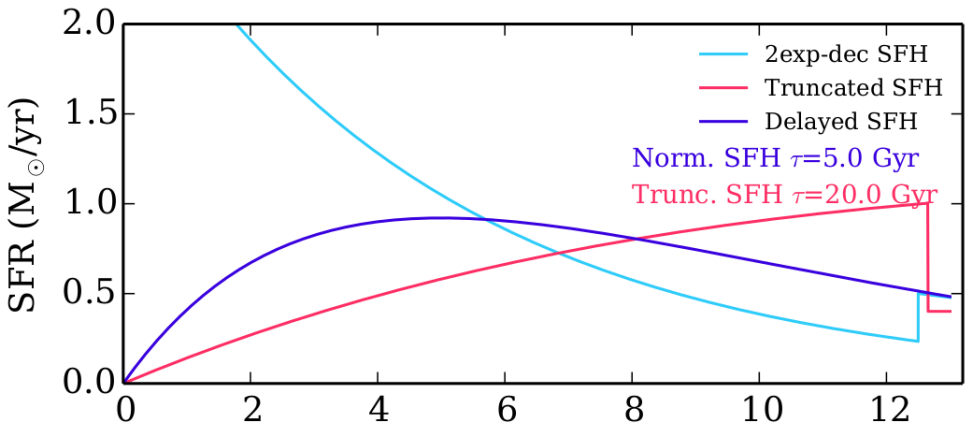

Figure 3.7: The figure shows several possible star formation history (SFH) scenarios, the evolution of star formation with cosmic time, assuming a delayed SFH (blue), a two-exponential decreasing SFH (cyan) and a truncated SFH (magenta). (Figure extracted from Ciesla et al. (2016)).

The delayed star formation, represented by a decreasing exponential function ($SFR(t) \propto t \cdot \exp(-t/\tau_{main})$ where t is the age of the galaxy and τ_{main} is the age of the main stellar population) is the most common star formation (Ciesla et al., 2016). CIGALE calculates the SFR using the mass of the galaxy (both stellar and gas mass).

Specifically, the delayed SFH scenario uses $\mathrm{SFR} = \mathrm{M_{gal}}/\tau(\mathrm{e}^{\mathrm{t}/\tau} - 1)$ instead of the usual Kennicutt law (see Chapter 1 for details).

Ideally, a more specific SFH should be introduced depending on the nature of the sample. For instance, for secular processes in the galaxy, a SFH with a quenching of star formation in the later stages of the galaxy's evolution (referred to as truncated SFH) is commonly used, whereas for galaxy mergers it is more common to use a burst of star formation (see Figure 3.8). The sample of dusty high-z galaxies studied in this chapter needs a more specific SFH which is able to reproduce a burst of star formation at different intensities and ages. Several SFHs were tested during this work, taking into account the common delayed SFH and introducing a starburst that can be produced at any cosmic time (see Figure 3.8). This SFH is tailor made for galaxies with a big burst of star formation as indicated by samples of dusty high-z galaxies. However, the resulting output SFR can be extremely high ($\mathrm{SFR} > 60{,}000\,\mathrm{M_\odot/yr}$), therefore ultimately, the double decreasing SFH was selected as the best representation of the high-z sample (see Section 3.4). After several tests, the SFH that is able to reproduce a SED that fits the observations is a double exponential, which assumes a double delayed star formation with a presence of a starbust (see Section 3.6).

Dust attenuation

The dust attenuation describes the effects of dust on the UV-optical emission and is often described by two main parameters: the reddening and the total obscuration. Shorter wavelength photons are more ready scattered and absorbed by the dust, causing a redding effect that is parametrized by the color excess E (B - V), the difference between a source's observed and real colour index. The obscuration is parametrized by the extinction (A_λ), a factor of the absorbed or scattered out of the line of sight. The decrease of intensity is measured by the attenuation law as $\mathrm{I}(\lambda) = \mathrm{I_{star}}\mathrm{e}^{-\tau(\lambda)}$ where $\tau(\lambda)$ is the optical depth of the dust screen (Calzetti, 2001).

The most common attenuation law is Calzetti et al. (2000), an empirical law for star-forming galaxies, described by a single attenuation curve which proves insufficient to describe SFGs particularly at high-z (Noll et al., 2009). On the other hand,

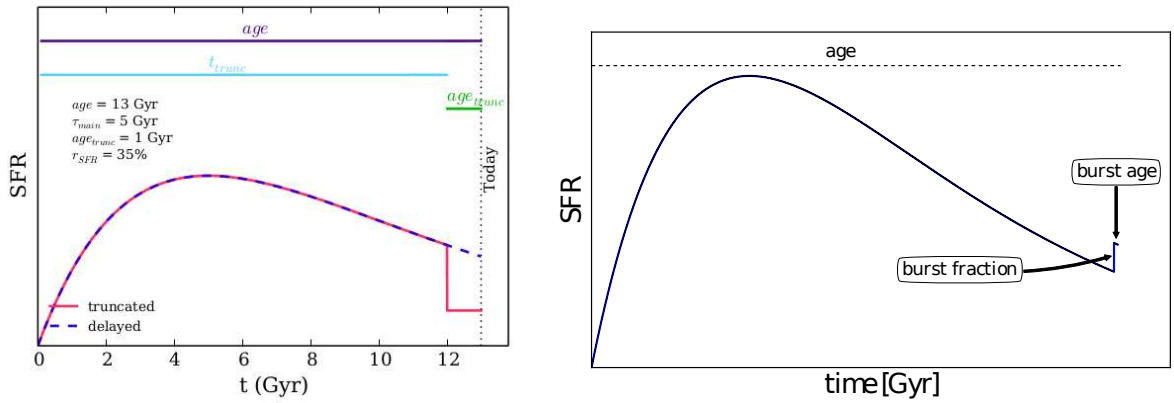

Figure 3.8: Examples of Star formation histories (SFH). (Left) From Ciesla et al. (2016) shows the SFR extracted by CIGALE comparing the delayed SFH (dashed line) with the truncated SFH (continuous pink line). The delayed SFH is the most common to apply in SED fitting, however, for specific cases, it is more convenient to apply an alternative SFH, such as the truncated SFH for local galaxies with a rapid decrease in the star formation at some moment in the galaxy. (Right) SFH tested during this work, a delayed star formation with a starbusrt that can be introduced at any age of the galaxy (age_{burst}), with different intensities described by a fraction of the total SHR ($frac_{burst}$) [Courtesy K. Malek].

Charlot & Fall (2000) proposes a simpler attenuation law which reproduces the power law, assuming that all the stars are attenuated by diffuse dust in the same manner. It is able to reproduce effectively the attenuation although it does not take into account the geometry. However, this is a sufficient approximation for point source galaxies and is therefore used in this Chapter (see 3.4).

Dust emission

The dust emission in an important module in CIGALE, specially for dusty sources, and is connected with the dust absorption models. The models focus on both mid-infrared and submillimetre wavelengths. The FIR-submillimetre contiuum radiation originates from dust grains in thermal equilibrium and can be represented by either a single black body spectrum (BB), where $F_{FIR} \propto B_\lambda(T_{dust})$ or a modified black body (MBB) where $F_{FIR} \propto B_\lambda\ (T_{dust})\lambda^{-\beta}$ (see Introduction 1.1.3). This latter is broadly accepted for fitting the FIR-submillimetre, since it follows the idea of the warm and cold components of the interstellar medium and is used the represent the two main

dust emission models used in this Chapter, Draine & Li (2007) and Schreiber et al. (2016). Models for the emission at mid-infrared (MIR) wavelengths are more complex since they require the addition of PAHs emission, dust features which are extremely size grain dependent. The sample of dusty high-z galaxies were carefully tested with both the Draine & Li (2007) and Schreiber et al. (2016) models. Draine & Li (2007) takes into account the emission from small dust grains and the characteristics of intense MIR emission (extreme heating environments tend to stop the process of the dust formation) which can applied to atypical star forming galaxies. On the other hand, the Schreiber et al. (2016) model is a more simple model with regards to the PAH emission and instead is more focused on the FIR-submillimetre peak, allowing higher dust temperatures. This may be a contributing reason for this model providing a better fit to the extreme high-z sources of the sample.

Nebular emission

The *nebular.py* module in CIGALE describes the spectral (line) emission, which can increase the average of fluxes by up to 10% in the case of the strongest spectral lines (Noll et al., 2009). This module produces a spectral line correction using empirical templates, that in practice corresponds to an increase of the flux of the total SED in the output of the SED fitting. The approach is simplistic, but it improves the SED fit by increasing the general flux of the SED, which is enough for this study given that we are interested only in the photometric data (see Section 3.4).

AGN component

The AGN emission can break the balance between the absorption and dust emission due to their characteristic non-thermal emission. Fritz, Franceschini & Hatziminaoglou (2006) provides the main model in CIGALE that represents the AGN contribution which, in terms of the SED fitting, is mainly an additional mid-infrared dust emission component. Although Fritz, Franceschini & Hatziminaoglou (2006) takes into account accurately the AGN contribution, described by several parameters (such as the radii

and opening angle of the dust torus, angle between AGN axis and line of sight and the percentage of the AGN contribution in the galaxy), CIGALE adopts a relatively simple approach by defining a broad grid to represent the AGN contribution (see Section 3.4). This allows a broad classification of AGN presence, or non-presence, in the galaxy which is sufficient for this study.

CIGALE takes into account the different parts of the spectra explained above and produce SED fittings, showing the best probabilistic result as in Figure 3.9.

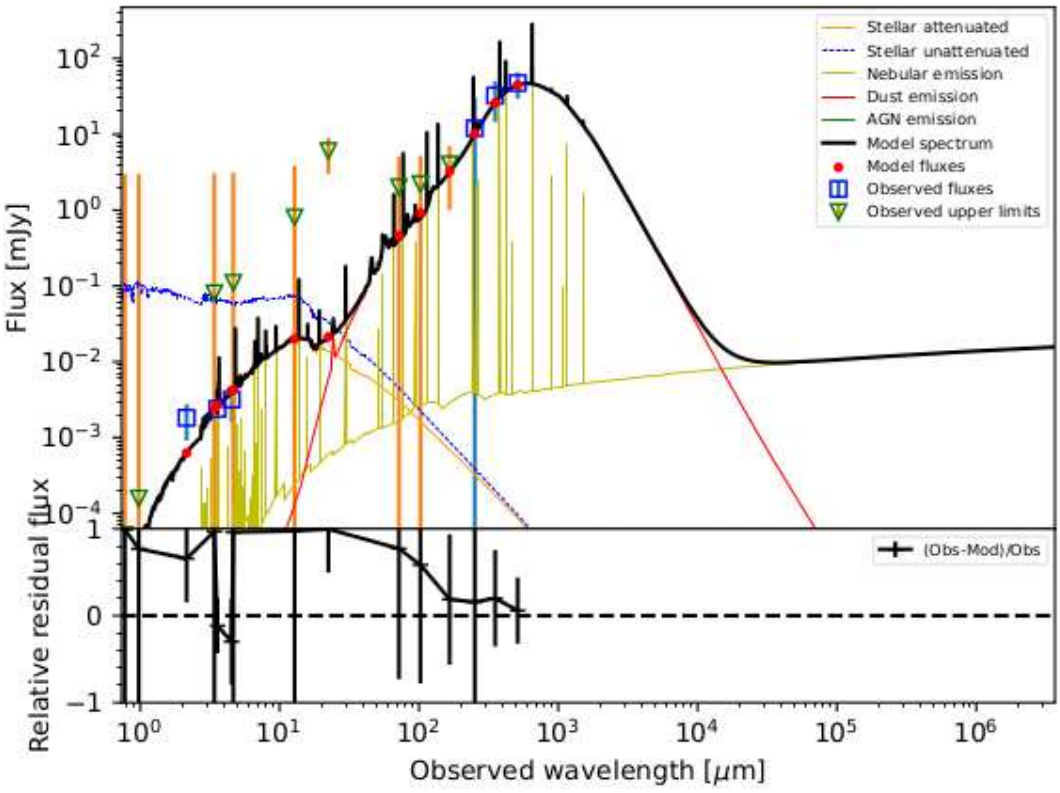

Figure 3.9: This Figure shows an example of SED that CIGALE gives as an output. The blue squares are the observed fluxes in mJy whereas the red dots represent the corresponding predicted fluxes by CIGALE that lie on the black line model fit. The green triangles (with the yellow line) show the upper limits (which the user gives if there in no detection in one of the bands). The different modules are shown in the legend. The stellar component is represented by the orange line which is the stellar attenuation and the blue line shows the unattenuated stellar emission. The green line is the AGN component (if there is no green line, like in this case, then the AGN presence is null). The dust component is represented by the red line whereas the the emission lines are represented in pale yellow.

Parameters	Description
Inputs:	
redshift	Grid of redshift defined in "redshifting" module
fracAGN	AGN fraction (Fritz, Franceschini & Hatziminaoglou, 2006)
imf	Initial function mass (imf=0: Salpeter, imf=1: Chabrier) (Bruzual & Charlot, 2003)
Z	metallity (Bruzual & Charlot, 2003)
qpah	Mass fraction of PAH (Draine & Li, 2007)
Tdust	Dust temperature only from Schreiber et al. (2016) models
fburst	Fraction of the starburst [%]
age	Age of the main stellar population in the galaxy [Myr]
burst age	Age of the late burst [Myr]
Outputs:	
bayes.universe.redshift	Photometric redshift
bayes.sfh.sfr	SFR [$M_{\odot}/yr$] for the SFH given
bayes.stellar.mstar	Stellar mass of the galaxy [$M_{\odot}$]
bayes.stellar.mgas	Gas mass of the galaxy
bayes.dust.luminosity	Dust Luminosity
bayes.agn.fracAGN	AGN contribution needs for the fitting [%]
bayes.dust.luminosity	Estimated dust luminosity using an energy balance [W]

Table 3.4: Example of CIGALE main inputs (defined in the 'pcigale.ini' file) which may be different depending on the model used and the outputs for the the best fit found ('results.fits' file). CIGALE also provides the facility of plotting the SED fits, producing mock catalogs and a probabilistic distribution function for each physical parameter derived. If a Bayesian analysis is required for the user, the value will have an output "bayes.", otherwise, the value will be "best." referring of one of the discrete values introduced in the fit.

3.3 Analysis with MAGPHYS

The updated version of the original MAGPHYS (da Cunha, Charlot & Elbaz, 2008), adapted for high-z DSFGs galaxies (da Cunha et al., 2015) makes the code promising for studying our high-z selected population, that provides a robust sample to study the star formation and dust properties at an early epoch. The results would be directly comparable to previous results from other samples of galaxies using the same framework (e.g. Miettinen et al. (2017)). However, the need of the redshift as an input is a clear limitation for the MAGPHYS code. Therefore, the idea of calculating the photometric redshift via a template fitting code (such as LePHARE or EAZY) and then incorporating this photometric redshift as an input to MAGPHYS was evaluated in order to study the high-z sample defined in the previous chapter.

In order to verify the reliability of MAGPHYS, the code was tested with a spectroscopic sub-sample which contains several kind of sources (Takagi et al. in prep). This spectroscopic catalogue was cross-correlated with the SPIRE catalogue (Pearson, 2018), SCUBA-2 catalogue (Geach et al., 2016), and the NEP optical and infrared catalogue of Murata et al. (2013). This multi-wavelength approach allows SED fitting using more than 15 photometric bands of a submillimetre selected sample (i.e. all sources are also SMGs).

In general, the MAGPHYS code fits better the lower redshift sources and has problems in reproducing the SED of the highest z sources. A possible reason for this is that MAGPHYS fits the galaxies at high and low redshifts with the same kind of model templates and it is incapable of producing a template with more dust emission around the FIR peak or more defined features in the PAHs (see Figure 3.10). This could be due to the fact that the modeling of the MIR emission and the FIR peak is too simplistic to reproduce the more extreme properties of dusty galaxies at high-z and a more complex dust emission model should be introduced (see Section 3.5).

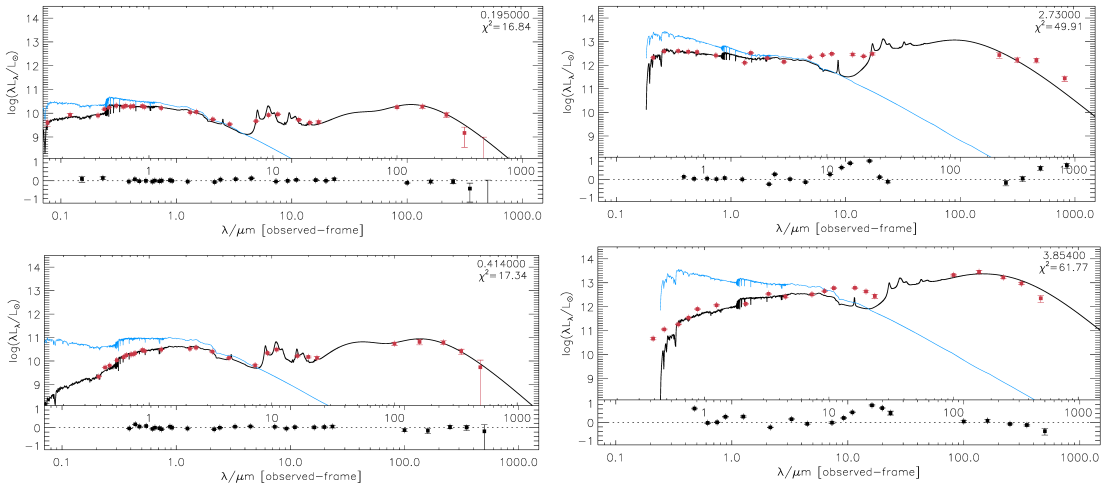

Figure 3.10: SED fitting with MAGPHYS of two low redshift sources (column on the left) and two of the the highest redshift sources of the sample (column on the right). The final SED is composed from both the optical and infrared libraries (black line), whereas the stellar emission (blue line) is extracted with the optical library. The observations - with the errors - are plotted in red. The two SEDs on the left correspond to galaxies at z = 0.19 ($\chi^2 \sim 17$ and 26 photometric detections) and z = 0.41 ($\chi^2 \sim 17$ and 24 photometric detections) respectively and show a better fit than the two galaxies on the right at z = 2.7 ($\chi^2 \sim 50$ and 20 photometric detections) and z = 3.8 ($\chi^2 \sim 62$ and 19 photometric detections).

This analysis with MAGPHYS was compared with the results of da Cunha et al. (2015): another sample of SMGs at different redshifts. The SFR obtained for our high-z sources are higher than expected with some of the sources at a few thousands of solar masses per year (see Figure 3.11). However, there are similar results in da Cunha et al. (2015), with examples of moderate median of star formation but some extreme SMGs exhibiting very high SFR of $\sim 4000 M_{\odot}/\mathrm{yr}$.

The position of the sources on the MS diagram of galaxies was evaluated, dividing the sample into four redshift bins (z = 0.25, 1, 2 and 3.5) to disentangle the evolution of the MS with redshift, using Speagle et al. (2014), and the same definition used in da Cunha et al. (2015). The lower redshift bins (z = 0.25 and z = 1) contain enough sources to give statistically significant results, however, the highest redshift bins only contain a few sources.

Although the results are not completely consistent with da Cunha et al. (2015), the high-z sample is too small to lead to any conclusion (see Figure 3.12). The lower red-

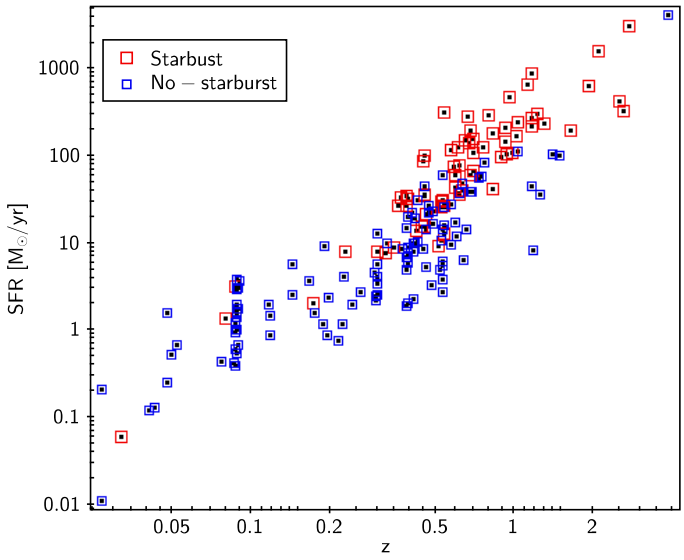

Figure 3.11: The SFR against redshift for the sample studied with MAGPHYS. There is a clear correlation between redshift and SFR - as expected - for both starburst (red squares) and non-starbusrt (blue squares) by using the starburst definition from Elbaz et al. (2011). The starburst are predominant at higher redshifts, whereas at z < 0.5 most of the sources are non-starburst.

shift bin of galaxies has only the highest redshift sources within the bin lying above the MS (possible evolution), whereas nearly all the sources in the bin z = 2 are above the main sequence (5 out of 6, which again could be due to selection effects). The z = 1 bin contains a large fraction of the sources above the MS. Elbaz et al. (2011) reported a lower number of sources (selected in the *Herschel* bands) lying above the main sequence at these lower redshifts. All these results could be explained if there has been an overestimation of the SFR and taking into account that MAGPHYS often overestimates both stellar and gas mass this could be possible. Another possible explication could be that the spectroscopic subset is not representative, and this the major inconvenience in using MAGPHYS - the enormous dependence on an accurate spectroscopic redshift.

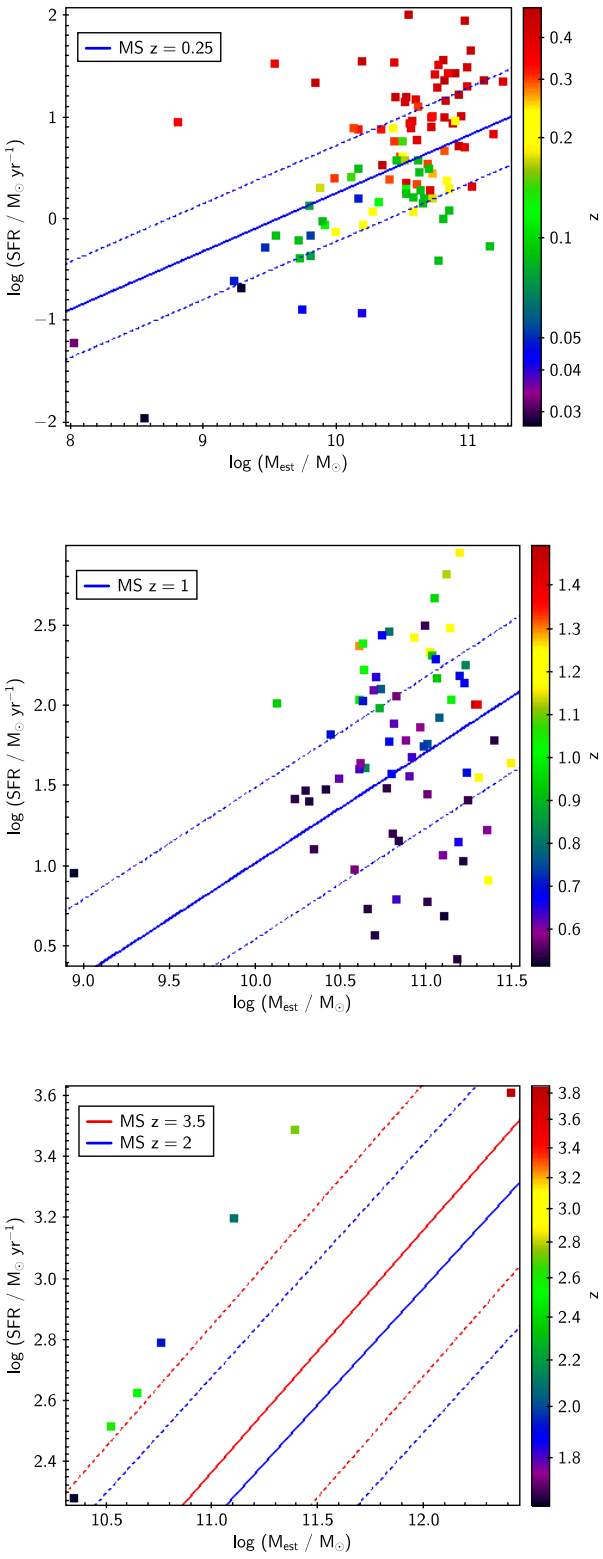

Figure 3.12: Main sequence of galaxies (Speagle et al., 2014) with the spectroscopic redshift represented in the colour-bar for the three subsets of the sample at redshifts between $> 0.1 < z < 0.5$ (MS at z = 0.25), $0.5 < z < 1.5$ (MS at z = 1) and $1.5 < z < 4$ (MS at z = 2; blue line and MS at z = 3.5 red line) respectively (the dashed lines represented three times above and below the MS). Taking into account the three bins, most of the galaxies lie on the MS (59%), whereas 31% lie on the MS and the remaining 10% lie below the MS.

The definition of starburst galaxies, which is intrinsically related to the MS (see Introduction 1.2.3), was applied to the entire sample (see Figure 3.13). The evolution of the MS with redshift is taken into account in this definition through the relationship between specific SFR and cosmic time ($sSFR_{SB}[Gyr^{-1}] > 52 \cdot t_{cosmic}^{-2.2}$, Elbaz et al. (2011)), avoiding the need to divide the sample by redshift bins and evaluating the sample as a whole. However, the starburst galaxies are only two times above the definitions of MS ($sSFR[Gyr^{-1}] = 26 \cdot t_{cosmic}^{-2.2}$), instead of the three times above defined in da Cunha et al. (2015) which uses Speagle et al. (2014) definition. Possible due to this fact, the results of galaxies that lie on the MS is completely different: while Speagle et al. (2014) definition (which has a broader correlation) classifies most of them, 59%, by using Elbaz et al. (2011) definition only classifies 19%. However, the sources classified as starburst do not differ heavily, being the 31% of the sources by using Speagle et al. (2014), whereas is the 39% using Elbaz et al. (2011) instead.

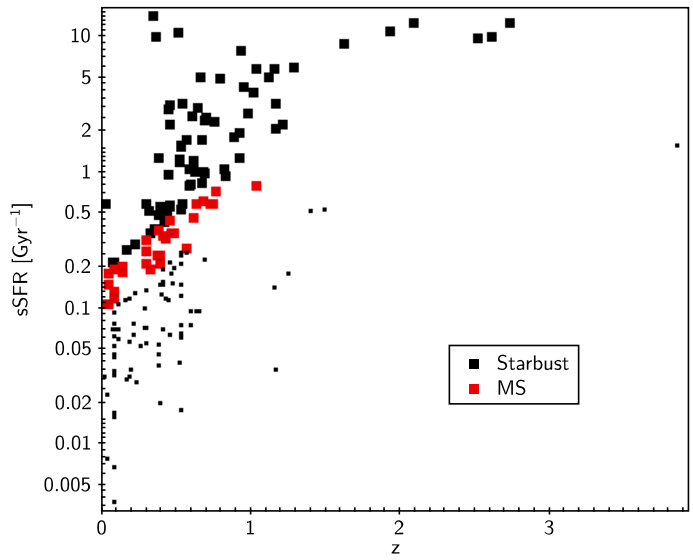

Figure 3.13: The specific star formation rate ($sSFR = SFR/M_{\odot}$) against redshift for the entire sample, divided by starbursts (black squares), MS (red squares) and the rest of the sample (black dots) by using Elbaz et al. (2011) MS definition. The classification differs from Speagle et al. (2014), classifying similar number of sources above and below the MS (39% and 42% respectively) and only the remaining 19% of the sources lie on the MS. However, starburst galaxies dominate at higher redshifts.

Due to the difference in the results by applying different definitions of MS, a de-

cision had to be made to standardise the definition for the purposes of this thesis. Speagle et al. (2014) includes 25 studies that define the MS of galaxies from different approaches (redshifts, IMF, etc) and produce a re definition valid up to a z=6 taking into account the 25 studies (see Introduction 1.2.3). However, Elbaz et al. (2011) - which is included in Speagle et al. (2014) - is based on the information of *Herschel* sources and takes into account SEDs of starburst at $0 < z < 2$. Therefore, due to the high-z nature of the sample ($2 < z < 6$), I decided to use Speagle et al. (2014) and the use da Cunha et al. (2015) for the consideration of above and below the MS in order to compare the results of this Thesis.

The results from this study, from a SED fitting point of view, were not convincing and together with a better understanding of the code, a better alternative was found in CIGALE (see 3.5). Therefore, the idea of calculating the photometric redshift with another code in order to provide it as an input to MAGPHYS was dismissed and the effort was concentrated on CIGALE (see Section 3.4).

3.4 Methodology: Analysis with CIGALE

Our high-z sample was evaluated with CIGALE since the versatility of the code and the possibility to calculate the photometric redshift make it a good 'candidate code' to study such sources. The most difficult part of any SED fitting code is the estimation of the redshift. Once the redshift is well constrained, it gives key information for deriving the rest of the physical parameters. For that reason the reliability of CIGALE in calculating the photometric redshift was checked with a small subset of spectroscopic data, introducing a few parameters into the models with the aim of obtaining a quick photometric redshift. The spectroscopic reference catalogue (Takagi et al. in prep) contains a few sources which in turn are contained in the general *AKARI* catalogue in the NEP field (Murata et al., 2013) avoiding mis-matching problems when the photometric detections were introduced in CIGALE. The sample is not biased to any particular type of source (as in Shim et al. (2013)) and describes the quality of redshift by the quality and quantity of lines detected, which make them a good sample with which to exercise CIGALE. A comparison of the derived photometric redshift with the true spectroscopic redshift proves that CIGALE is able to calculate the photometric redshift with accuracy (see Figure 3.14).

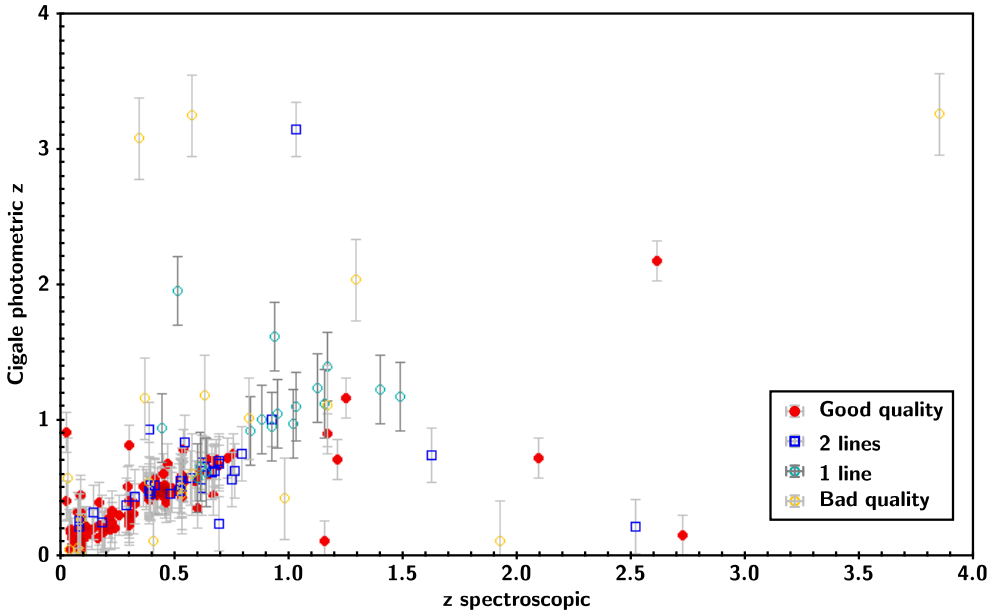

Figure 3.14: Comparison of the spectroscopic redshift (Takagi in prep.) with the photometric redshift derived by CIGALE for the same sources. The red circles shows good quality spectroscopic redshifts (more than two reliable emission lines) and these sources correlate better with CIGALE, whereas the rest of the sources (two emission line -blue squares-, one emission line - cyan circles - and no lines - yellow circles) show weaker correlation.

The general characteristics of CIGALE (described in 3.2.4) give an idea of the models to use and the nature of the sample suggests the use of a limited number of parameters. However, the combination of modules and parameters still produces millions of models that require hours of computational time. Therefore, some optimisation in the use of CIGALE is important, whilst maintaining the reliability of the SED fitting. To this effect, different tests were carried out by comparing the outputs for the same sources in the main modules used in CIGALE. In this Chapter (see Section 3.6), the properties of DSFGs were characterised by calculating first the photometric redshift in Section 3.6.1 by checking their reliability by the goodness of the fit and the probability density function (PDF) (see Figure 3.15) and then the rest of physical parameters.

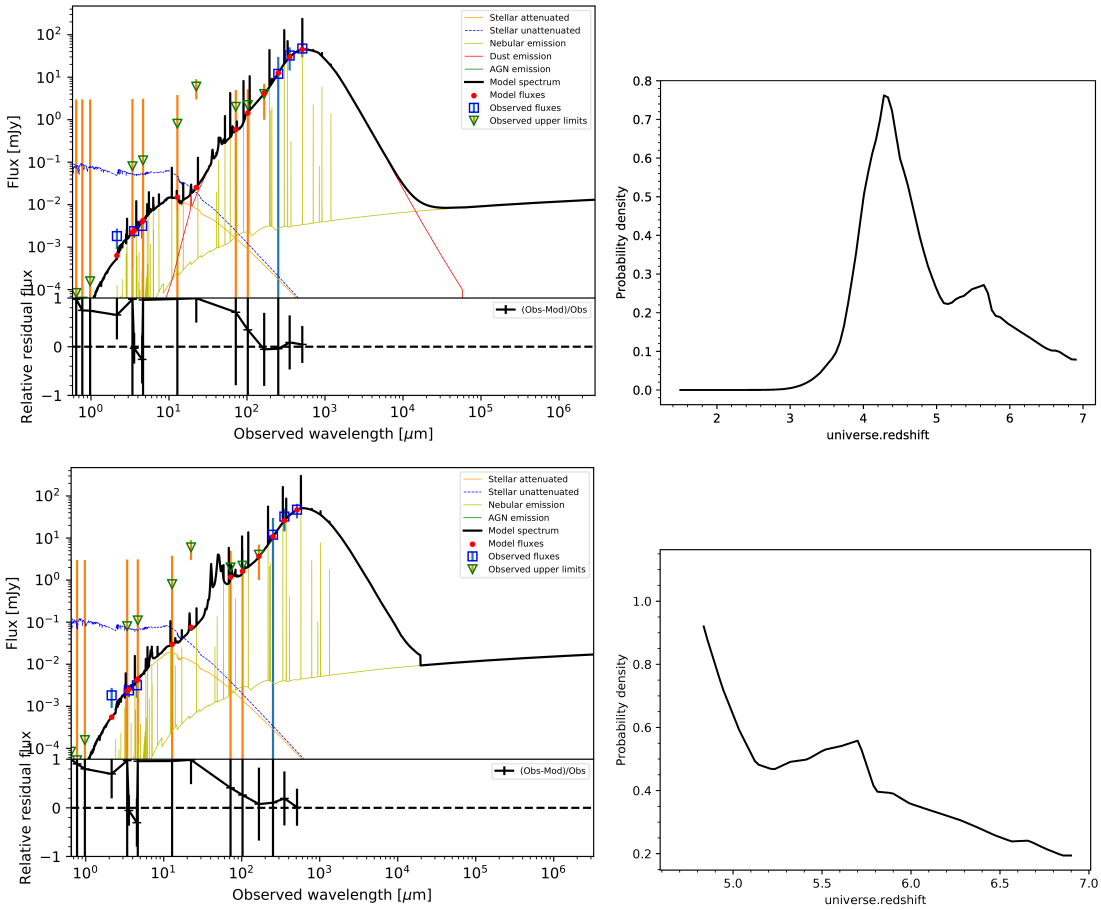

Figure 3.15: (Top) SED fitting of the best model of a high-z DFSG using the Draine & Li (2007) dust emission model. CIGALE gives the PDF (on the right) which peaks at redshift z = 4.8. (Bottom) SED fitting for the same source using Schreiber et al. (2016) dust emission model instead the PDF (on the right) shows the best model at z = 5.7, however, it is less constraint than the Figure on top although the fit is good as well. In this chapter the PDFs have been taken into account to measure the quality of the fit, together with the χ^2 and the quality of the fitting in the FIR peak.

The coverage of the photometric data, especially around the FIR spectral peak is also very important, since this can lead to completely different values of photometric redshift (see Figure 3.16). The maximum data possible in this wavelength range was carefully cross-matched and it is an ongoing work to incorporate more data (see 6.2.1 for details).

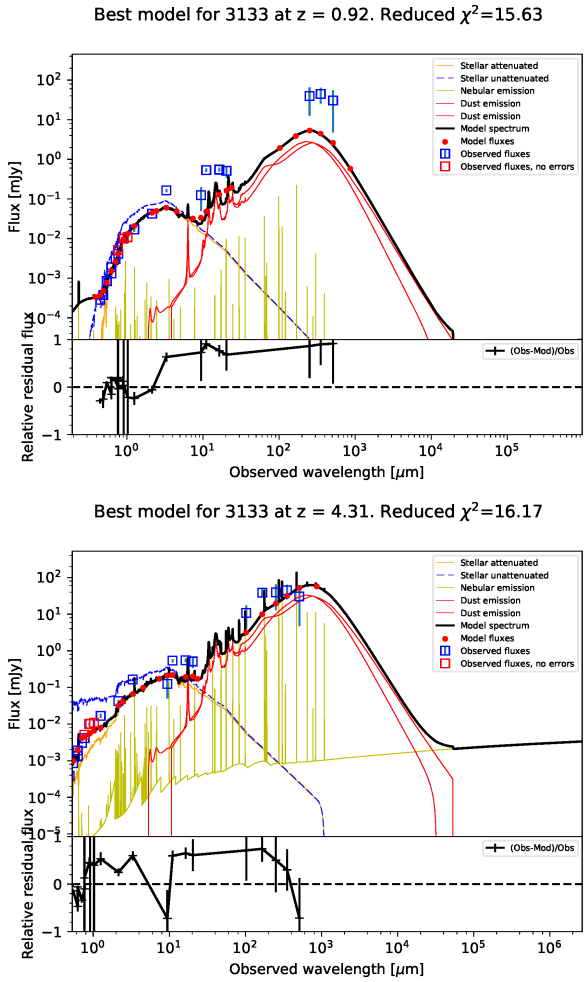

Figure 3.16: SED fitting of the same source (ID 3133) using different photometric data, but exactly the same models and parameters. (Top) The SED fitting was produced without using 100-160μm PACS data ($z_{phot} = 0.92$), whereas (Bottom) SED fitting with PACS data gives a completely different photometric redshift ($z_{phot} = 4.31$). The SED fitting produced in this chapter has been carried out by carefully analysing the CIGALE modules and parameters, however this plot clearly shows the importance of comprehensive photometric coverage around the FIR peak.

In addition to the observational data, good selection of the models that best characterise the sample and the selection of the appropriate grid of physical parameters for each model are important for obtaining reliable SED fits. The goodness of the fitting cannot solely rely on the best fit (lowest χ^2) and it is also important to verify by eye that the entire spectrum is well fitted, without miss-associations between optical-FIR data. For that reason, when there is a possible miss-match in the fits to the observational data, several changes in the models were made in order to verify if the nature

of the poor fitting is a misuse of the code or a real limitation in the data. Moreover, selecting the correct parameters of a model to characterise the source is key to finding robust outputs since even a relatively good fit can in principal lead to a completely different redshift and therefore a totally different set of derived physical properties for the source. Indeed, the SED of cold sources at low redshift can be confused with the SED of warm sources at high-z because of the dependence of these two parameters (see Figure 3.17).

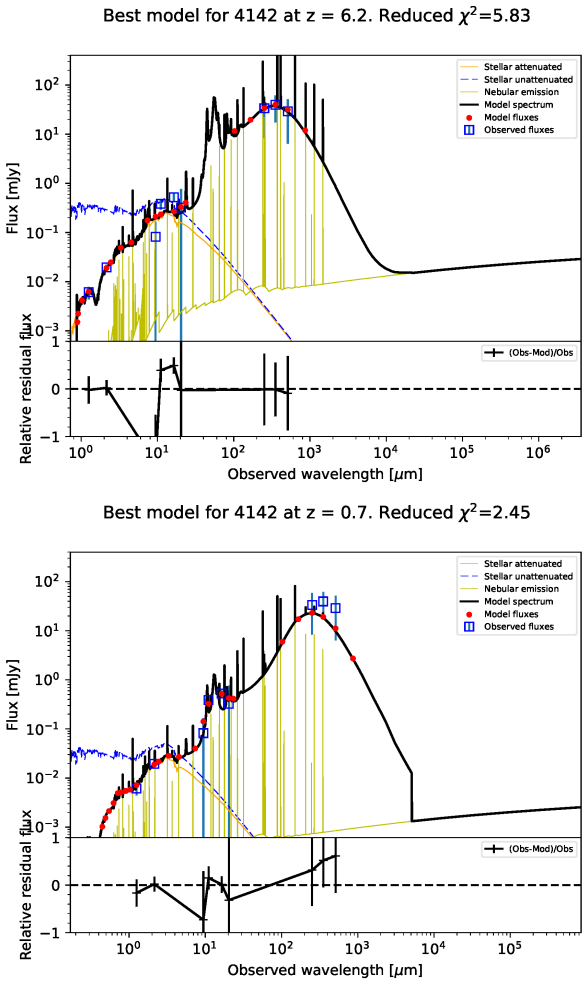

Figure 3.17: The SED of the same source (ID = 4142) fitted with the same models, but changing the dust temperature. The upper plot indicates a warm ($T_{dust} = 60K$) high-z source ($z_{phot} = 6.2$) with a reasonable fit. The plot on the bottom shows a much colder $T_{dust} = 20K$) low redshift source ($z_{phot} = 0.7$). After further analysis, a better fit was found and the redshift of this source indicated in the Appendix is $z_{phot} = 3.1 \pm 0.2$ which shows the importance of obtaining a good fitting over the entire SED, especially around the FIR peak.

The most challenging part of the SED fitting was to produce models that characterise correctly the FIR peak. The dust temperature is a key factor, because of the degeneracy with redshift, therefore, several dust emission models were checked (see Section 3.2.4 for the description of the different dust emission models).

Casey (2012) dust emission models were tested since they are produced specifically for DSFGs (see Casey, Narayanan & Cooray (2014) for a review). However, they are limited to temperatures higher than $T_{dust} = 35K$. The conflict of the dust temperature redshift degeneracy was resolved by introducing a broad grid of temperatures and freedom to the parameters that influence the dust emission.

The Draine & Li (2007) model has also been proven to give good results and is a well tested model used in several papers that use the CIGALE code (Ciesla et al., 2016). On the other hand, the models of Schreiber et al. (2016) can define both the dust temperature and the PAH fraction and they are focused in dusty high-z galaxies, but they appear to give resulting values of extremely high SFRs (over several thousands of solar masses per year). Furthermore, depending on the temperature, the photometric redshift can be very different, however this was alleviated with this model by defining a grid of redshift broad enough (see Figure 3.18).

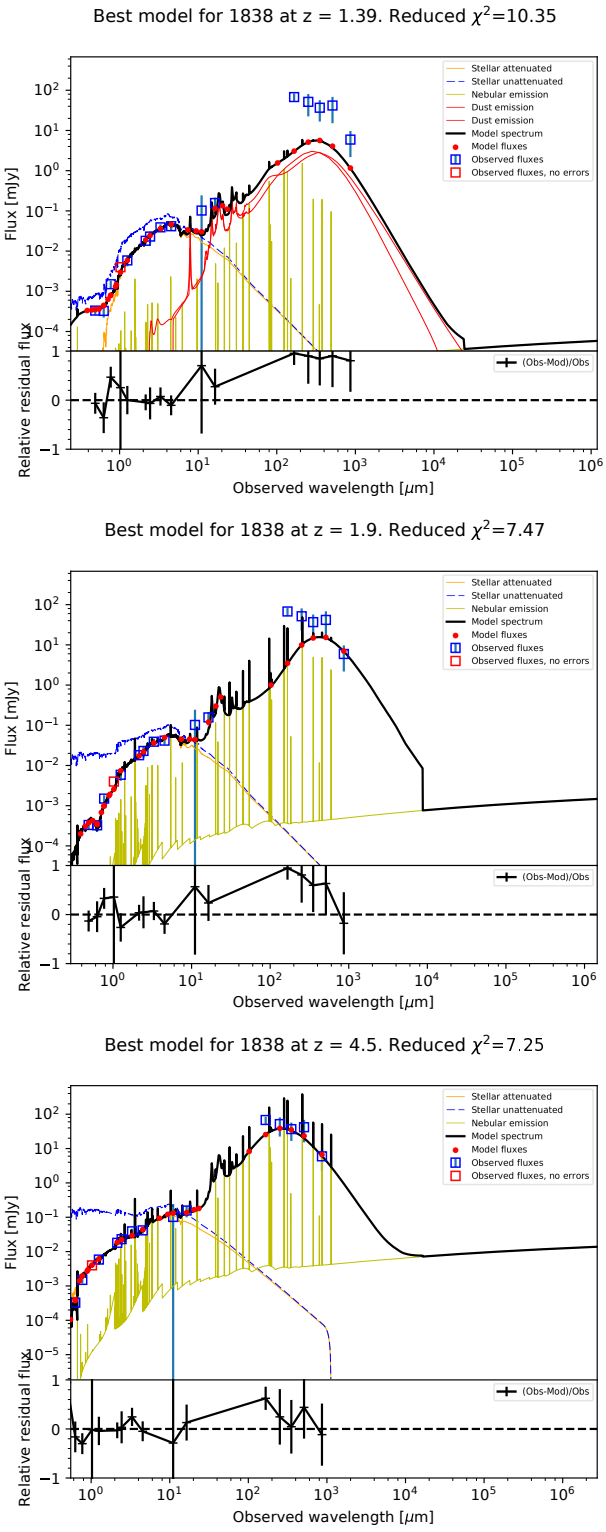

Figure 3.18: This Figure shows the same high-z candidate (ID 1838) for different dust emission models with different dust temperatures. The top plot shows a SED fit produced with the Draine & Li (2007) dust model (red line) which clearly is not able to reproduce the dust temperature for the observations (blue squares). However, this is not due to a miss-match of the optical-FIR data, and by choosing a correct dust emission model for this source (Schreiber et al., 2016) it is possible to fit the observations (middle plot). Furthermore, giving a wider range of temperatures ($T_{dust} = 20 - 60$K with δT= 5K) of dust emission it is possible to find a model that fits better (bottom plot). Note as well the difference of photometric redshift: z = 1.39, 1.9 and 4.5 respectively.

In summary, the conclusion was to use both the Draine & Li (2007) and Schreiber et al. (2016) dust emission models with a broad grid to define the dust temperature and compare the outputs of both models, choosing the best fit in each case.

If the FIR peak is properly sampled the problem of constraining the redshift can be overcome, as is the case with the so-called 500 μm risers, In this case, even changing dust emission models or the parameters in the model, the photometric redshift is similar (see Figure 3.19). The advantage that 500 μm risers offer have been exploited in the literature and it is the most common method to select high-z sources with submillimetre data (see e.g. Riechers et al. (2013), Dowell et al. (2014) or Asboth et al. (2016)). However, most of the sources selected with this method are extreme sources and cannot be representative of the general dusty high-z population. In order to find a general representative sample of dusty high-z sources, a robust method to produce reliable SED fitting is needed.

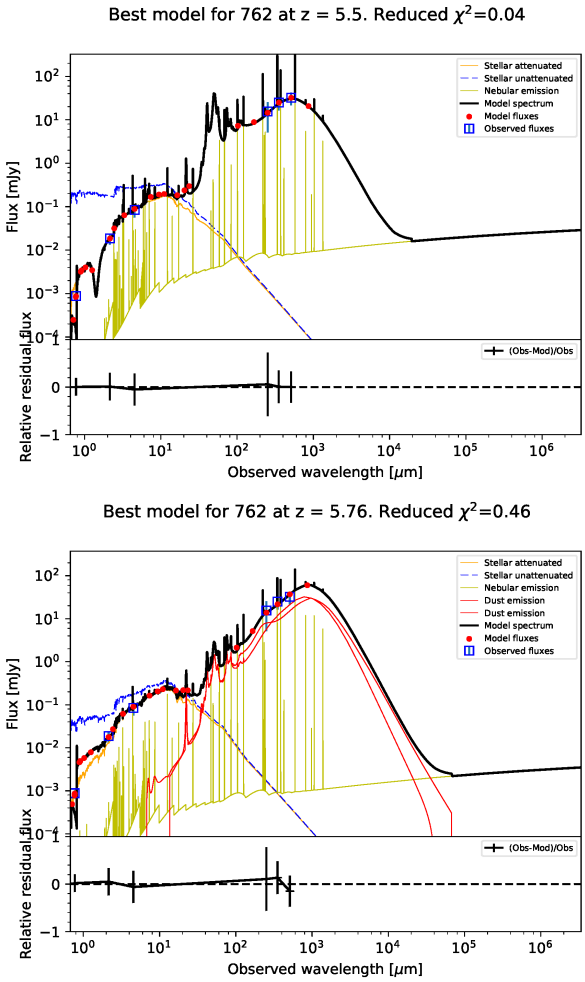

Figure 3.19: Example of a 500 μm riser source (ID = 762) fitted with 2 different dust emission models: Schreiber et al. (2016) (top) and Draine & Li (2007) (bottom). Both show similar redshift and similar goodness of fit. This source at $z_{phot} \sim 5.7$ was submitted for a spectroscopic proposal in the SMA (see Future work 6.2.2).

The assumed star formation history (SFH) determines the SFR output from the SED fitting. Since one of the aims of this Chapter is to evaluate the position of dusty high-z sources on the main sequence of galaxies, an investigation of the SFH was also carried out. In conclusion it was decided that a double decreasing exponential SFH should be assumed because, in general, it gives the best results in the SED fitting (see figure 3.20), possibly due to the fact that it stimulates higher star formation rates in the IR which means more luminosity in the FIR peak (see Section 3.2.4).

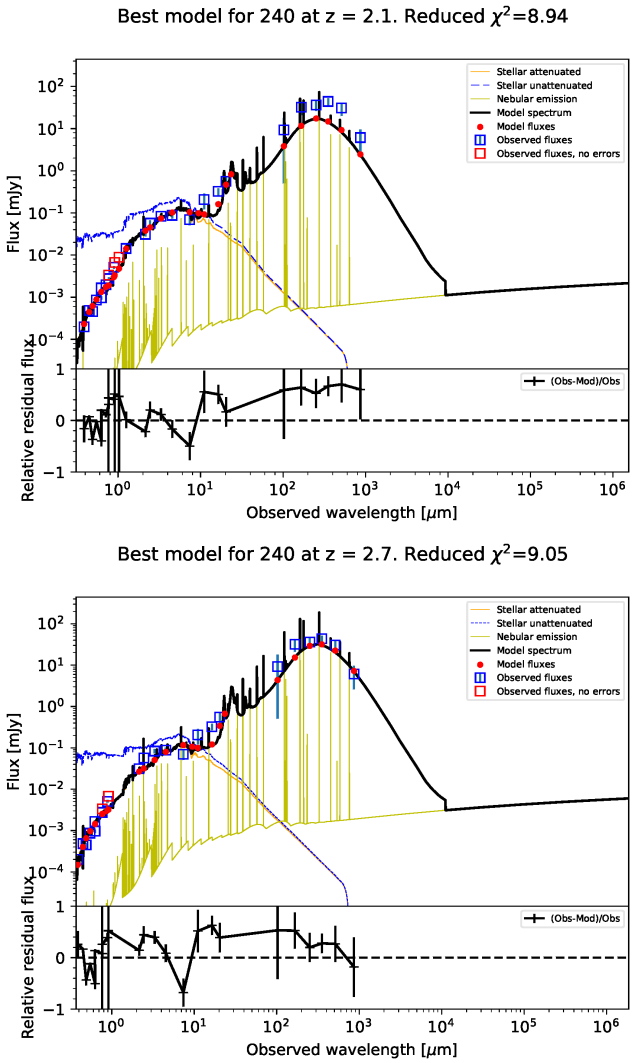

Figure 3.20: Comparison of the same source (ID 240) using different SFHs. (Left) the SED by using a delayed SFH. (Right) decreasing exponential SFH which provides a better fit around the FIR peak. Specifically for this source, it proved difficult to find a model that fit the FIR peak irrespective of the dust emission model, which were unsuccessful, the solution was found by changing the SFH.

In conclusion, differences between models can give extremely varied results with relative good fits, even in cases with plenty of photometric points. Therefore, an accurate understanding of the models applied and the sample to characterise is necessary. All the knowledge gained in the production of these tests was applied in the results section using CIGALE 3.6.

3.5 Comparison CIGALE vs MAGPHYS

The two main codes used in this Chapter were evaluated in order to decide which one was the more appropriate to use for our sample.

The possibility to calculate the photometric redshift with another code - CIGALE or a template based code - to introduce it to MAGPHYS was evaluated since the most recent version of MAGPHYS is focused on DSFGs at high-z, which is tailor made for our sample. MAGPHYS describes the energetic balance between the energy emitted by the UV-optical light and redistributed in the IR-submillimetre assuming simple emission properties for the dust, such a modified black-body. MAGPHYS makes the assumption that birth clouds dominate the emission in shorter wavelengths and the ISM at longer wavelengths in order to produce templates with the fewer parameters as possible (see Figure 3.21).

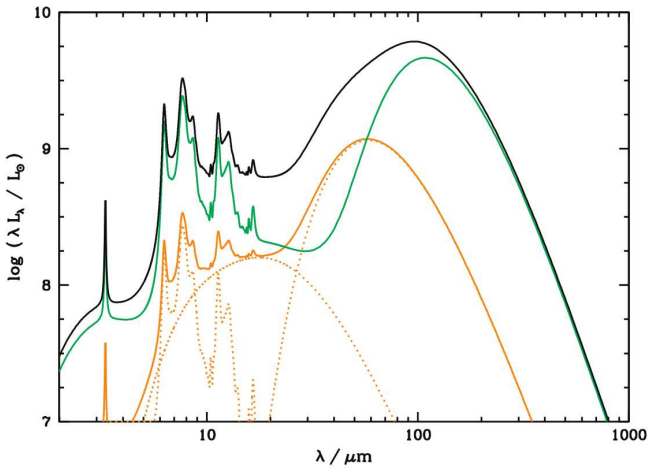

Figure 3.21: This Figure, extracted from da Cunha, Charlot & Elbaz (2008) shows the infrared emission of a simulated galaxy, where the dust from the birth cloud (orange line) represents a lower contribution and at shorter wavelengths than the diffuse ISM (green line). The total emission is the addition of the two contributions (black line).

Indeed, the dust temperature and the shape of the dust emission are based on assumptions and not constrained directly by the UV-optical absorption. Therefore, it is not surprising that the code needs the input of a redshift in order to give a realistic value for the derived parameters such as infrared SFR or infrared luminosity (Walcher et al., 2011). Therefore, the approach of using photometric redshifts are not accurate enough,

and reliable spectroscopic redshifts are needed for the analysis.

Moreover, there is evidence in the literature that MAGPHYS overestimates the stellar masses due to insufficient consideration of the AGB stars which highly contribute from red optical to NIR. A validation study where Bruzual & Charlot (2003) stellar model was compared with other models such as Maraston (2005) for intermediate sSFR (-12 < log(sSFR) < -9) concludes that the stellar masses are overestimated by 50% with respect to other models (Walcher et al., 2008). However, the Bruzual & Charlot (2003) models are widely used and the consideration of a 0.2 dex for SFGs with an important population of intermediate-age stars is included in CIGALE (Noll et al., 2009). Since once of the objectives of this study is to locate DSFGs on the MS of galaxies, the use of MAGPHYS for this approach is not valid. The updated version of MAGPHYS (da Cunha et al., 2015) tried to solve the problem, which takes into consideration the FIR to calculate the star formation, since UV-optical fluxes alone are unreliable of the SFR in DSFGs (see Figure 3.22). However, the detailed explanations of the implementation of the code are not fully explained in the literature and after producing this work, could be that the considerations of MAGPHYS for DSFGs are not enough for obtaining good results.

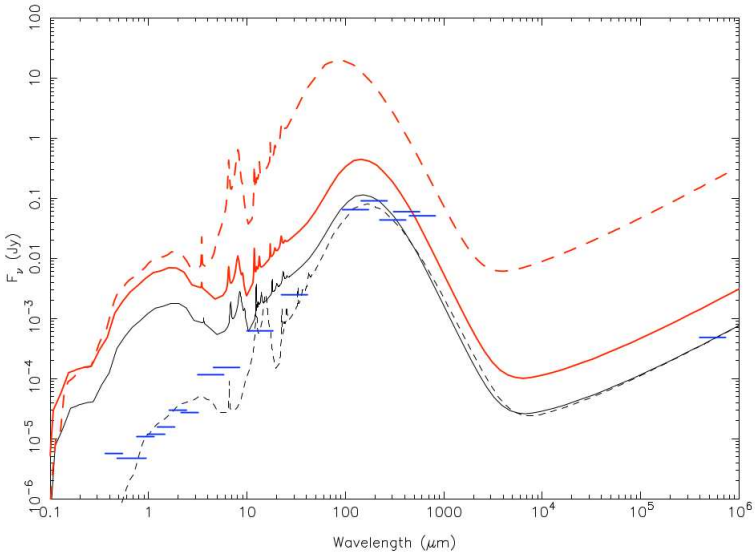

Figure 3.22: Dust in galaxies: the lower three SEDs in the plot show galaxies with small amounts of dust / IR star formation, whereas the top SED - dashed red line - shows a dusty star forming galaxy. Due to the large amount of dust and gas, coming presumably from giant molecular clouds, the contribution in optical is low, whereas it contributes a lot in infrared emission. Therefore using only the UV-optical to calculate the star formation of such dusty galaxies is clearly not reliable (figure extracted from Walcher et al. (2011)).

CIGALE provides a much better modeling of the energy balance considering the full UV-IR SED treating the absorption and emission simultaneously and taking into account more factors such as the different ages that are included in the star formation history models. Furthermore, CIGALE can also take other models for the IR attenuation and the IR emission albeit at the price of a slower computational speed, producing millions of models, the results are significantly better, allowing the calculation of accurate photometric redshifts.

In order to fully compare the merits of both codes, a sample of DSFGs with spectroscopic redshift is needed. However, for *this* study the conclusion is that CIGALE estimates the properties of high-z DSFGs better than MAGPHYS in the absence of any spectroscopic redshift. Furthermore, CIGALE works with different modules for each part of the spectrum that can be modified by the user or even introduced from scratch. This versatility makes it very useful for any possible future work, hence it is CIGALE that is adopted moving forward in this Chapter and in Future work (see Section 6.2.2).

3.6 Results with CIGALE

After the analysis and evaluation produced in the previous sections, I concluded that the best code to characterise the high-z sample is CIGALE. The versatility of CIGALE allows me to model parts of the spectra separately choosing the more appropriate model to the dusty high-z sample. Furthermore it takes into account all the bands for calculating the photometric redshift which is key since the selection of high-z candidates was produced by using infrared colours (see previous Chapter 2). Another important factor is the possibility of mismatches and by producing the SED fitting as a whole it allows me to discard mismatches between catalogues as shown later in this Chapter.

Although comprehensive photometric coverage is important, it should be noted that since the SPIRE observations at the NEP cover a wider area than the *AKARI* Wide field itself (see Figure 2.1), some of the high-z candidates will only have SPIRE data. Therefore, the following analysis is carried out for the 186 sources which have at least four photometric detections from two or more telescopes. The final list of 341 high-z candidates is presented in the appendix A.1;

In order to study the physical properties of the high-z sample (see Section 2.3), SED fitting with CIGALE was produced using the physical parameters of each module as shown in Table 3.5.

For the stellar emission I assume the Bruzual & Charlot (2003) setting with the Chabrier initial function mass and metallicity similar to $Z_{\odot}$.

Since the accuracy of the SFR is crucial for this study, I tried different Star Formation Histories (SFH). As discussed in the previous sections, the delayed star formation module, which assumes a declining star formation with ($SFR \propto \exp(-t/\tau)$), is the most common module, but it does not fit well the sample. Therefore, the double decreasing exponential SFH is used in preference assuming different ages of the main stellar population in the galaxy (1 Gyr < age < 10Gyrs), the age of the galaxy when the starburst happened ($50\text{Myr} < \text{age}_{\text{burst}} < 200\text{Myr}$). Furthermore it takes into account how big the starburst was, considering the percentage of the mass fraction of the burst,

including the possibility of a null burst ($f_{burst} \sim 0$) until a big burst of star formation ($f_{burst} \sim 0.5$, which it would correspond to 50% of the mass of the galaxy).

For the dust attenuation, three different possibilities were investigated: Calzetti et al. (2000) dust attenuation law, Charlot & Fall (2000) which follows as well a power law attenuation and finally another module that implements 2 power dust attenuation laws. This last one combines the birth cloud attenuation and the interstellar medium attenuation both by a power law. In this way, it makes a distinction between young and old stellar emission; the younger stellar emission is attenuated by the birth cloud whereas the old population emission is only affected by the interstellar medium. Due to this distinction in the stellar emission and the flexibility of the module I finally used this module, although there were not dramatic differences in the sample among the three models.

The dust emission was the most challenging part to model in the sample since it is a high-z DSFG selection and affects the estimation of the photometric redshift, since it is related with the dust temperature (see Figure 3.23). As discussed in the previous sections, out of the 3 models available: Casey (2012), Draine & Li (2007) and (Schreiber et al., 2016), the results are presented by using both the (Draine & Li, 2007) and (Schreiber et al., 2016) models and choosing the best fit for each case.

The AGN emission was included by using Fritz, Franceschini & Hatziminaoglou (2006) models but without specifying any of the torus properties or other parameters in the model in order to only consider an AGN presence.

Finally, nebular emission was assumed in the total spectrum, making possible the simulation of the emission lines which has improved the quality of the fits, although it does not contribute to the calculation of the redshift.

All the combinations of these modules with the grid of parameters selected as shown in Table 3.5 produce between $\sim$35 to $\sim$100 million models from which CIGALE selects one as the best fit for each source (see Figure 3.26).

CIGALE module	Main parameters	Description
SFH (2 decreasing exponentials)	$f_{burst} = 0.05 - 0.5$ age $= 250 - 8000$ [Myr] $age_{burst} = 50 - 200$ [Myr]	Mass fraction of the late burst Age of the main stellar population in the galaxy Age of the late burst
Dust attenuation (Charlot & Fall, 2000)	Av $= 0.3 - 3.8$ $slope_{BC} = -0.7$	V-band attenuation in the birth clouds Power law slope of the attenuation in the birth clouds
Dust emission models (Draine & Li, 2007)	$q_{pah} = 0.47 - 3.9$ $u_{min} = 5 - 25$	Mass fraction of PAHs Minimum radiation field
Dust emission models (Schreiber et al., 2016)	T= 20 - 60 [K] $f_{pah} = 0.05 - 0.5$ [%]	Dust temperature Mass fraction of PAHs
AGN component (Fritz et al. 2006)	fracAGN = 0.05 - 0.25 [%] $r_{ratio} = 60$ psy = 0.001	AGN fraction Opening angle of the dust torus Angle between AGN axis and line of sight

Table 3.5: Main modules and input parameters used in CIGALE for the analysis of the high-z sample. The first column lists the CIGALE model and the part of the spectrum on which is focused, the second column shows the main parameters and the range of values selected. The third column provides a brief description of each parameter. Notice that the two dust emission models, Draine & Li (2007) and Schreiber et al. (2016) were not used at the same time. Therefore, for both set of models have 10 degrees of freedom (DOF).

3.6.1 Photometric redshift

The photometric redshift - and therefore the rest of the physical parameters - clearly depend on the models assumed in CIGALE. In particular, the SFR is highly dependent on the SFH assumed. As noted in Section 3.4) the inclusion of a episodic starburst in the SFH model improves the fit especially around the FIR peak, important for the calculation of the redshift. The photometric redshifts were computed using up to a maximum of 29 photometric bands in the NEP deep field and 23 in the NEP Wide field, following the methodology described in Section 3.4. The average redshift for the sources with more than 4 photometric detections (186 sources) is as follows:

- SCUBA-2 maps method selected sample (36 candidates): $z = 2.8$ ($0.8 < z < 4.9$)
- SPIRE colours method selected sample: $z = 3.4$ ($1.2 < z < 6.2$)

Therefore, with the SCUBA-2 maps I find on average slightly lower redshift sources than with the SPIRE colours method and these with consequently lower star formation (see Figure 3.27).

Since CIGALE takes into account all the model continuum spectra to calculate the photometric redshift, the selection of the dust emission model can result in different photometric redshift results. Although for $T_{dust} < 45$K both models are in agreement, they differ for warmer galaxies (see Figure 3.23). I found that for warmer galaxies Schreiber et al. (2016) gives a photometric redshift and fits the SEDs better for 18% of the sample, therefore I choose this model for this part of the sample. The remaining 82% are better fit using the Draine & Li (2007) model.

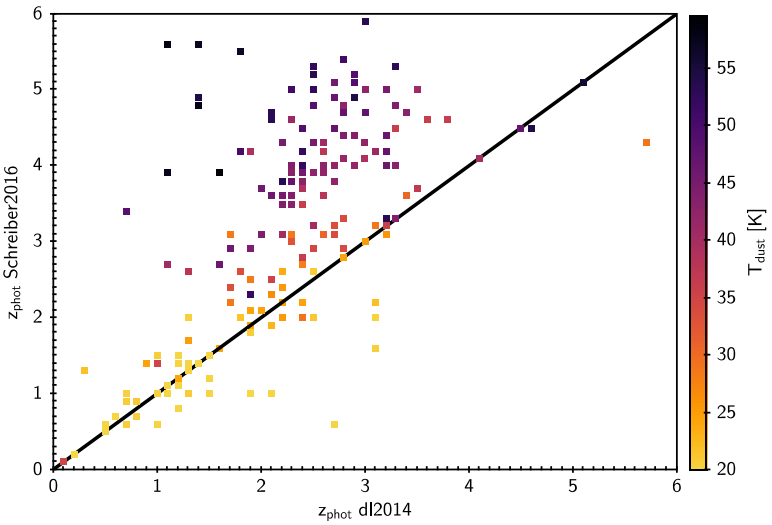

Figure 3.23: Comparison of the photometric redshift obtained by the two dust emission models (Schreiber et al. (2016) against Draine & Li (2007)) with the temperature represented in the colour bar. The photometric redshift errors are 0.1 < error z_{phot} < 0.3 in both models. The two models are in agreement for lower dust temperatures and redshifts, however the Schreiber et al. (2016) model predicts higher redshifts associated with galaxies with extreme SFR. The Draine & Li (2007) model provides the best fit for most of the sources, however for the very high-z galaxies (18%), the Schreiber et al. (2016) model works better. The percentage of the sources successfully fitted by using the Draine & Li (2007) dust model is 82%. Note that although the Casey (2012) dust model was also investigated, it did not provide good fits so this model was not taken into account in this study.

Overall, the average redshift for the entire sample is $z_{phot} = 2.59 \pm 0.13$ ($0.7 < z_{phot} < 6.2$) with 15 sources at $z_{phot} > 4$, which together with galaxies clearly above the MS, will be the object of a future spectroscopic follow-up study using ground based facilities (see Section 6.2.2). The number of sources detected at z > 4 via the various selection methods (a total of 15 sources) are compared with the contemporary galaxy evolution models of Pearson (2018). Over a similar area these models predict around 20 sources above the SPIRE confusion limit at redshift bigger than four, broadly consistent with the numbers presented here. The differences can be due to selection effects and also field to field variation. The redshift distribution peaks around redshift $z \sim 2.5$ with most of the sources around this redshift and only a few sources at very high redshift (see Figure 3.24). This shows that the selection criteria and the photometric redshift are consistent with previous work that have used SPIRE colours

(e.g. Amblard et al. (2010)) and the lower redshift distribution obtained in some other studies (Casey, Narayanan & Cooray, 2014) could be due to the bias in optical spectroscopic redshift samples used to select the samples, excluding higher redshift galaxies (see Figure 1.13 in the Introduction).

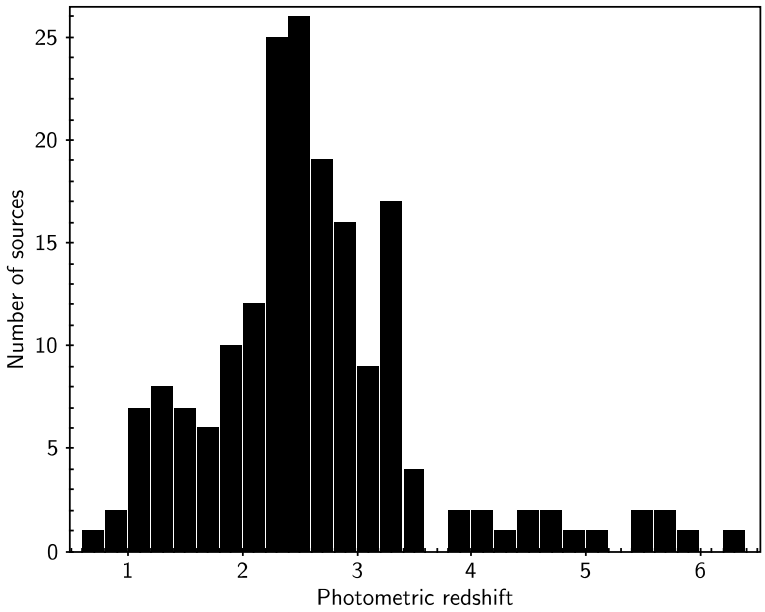

Figure 3.24: The redshift distribution for the dusty high-z sample, where most of the sources lie at $z \sim 2-3$, probably due to our selection criteria using the $250\mu m - 500\mu m$ SPIRE bands. There are 15 sources at $z > 4$ that will be subject of a future spectroscopic proposal.

3.6.2 Star formation Rate and stellar masses

The SFR and the stellar mass were computed using CIGALE with the aim to elucidate their position on the Main Sequence of galaxies: answering the question of whether submillimetre galaxies lie on the MS or are they starbursts off the MS? Furthermore, the mass of the gas in the galaxy was calculated in order to find out if the efficiency is enhanced for some physical parameter or whether it is simply related to the abundance of the gas.

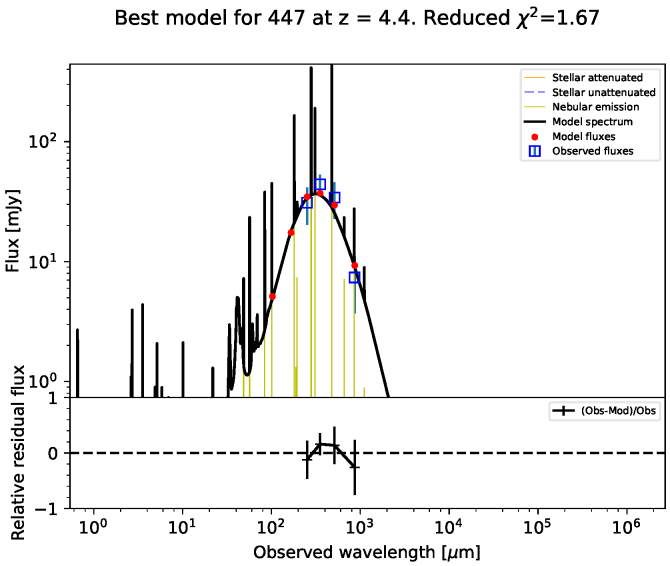

Figure 3.25: Example high-z candidate (zphot = 4.4) with SPIRE and SCUBA-2 detections. The sources with four photometric detections were included if the source was detection by two different telescopes. In such cases the lack of detection at any other (shorter) wavelengths means that such sources may lie at extremely high redshift.

3.6.3 Main sequence of galaxies

The main modules that influence the SFR are the star formation history and the dust emission (see Section 3.4). For the dust emission, both Schreiber et al. (2016) and Draine & Li (2007) models were used, giving higher values of SFR with the former than with the latter. On average, the star formation is high SFR $= 2367 \pm 310 M_{\odot} yr^{-1}$ in the total sample, since I specifically select a submillimetre sample to contain dusty high-z galaxies.

The two selection criteria (SCUBA, SPIRE colours) were compared in order to see if they select different type of sources. Both methods find sources at similar redshift and with similar SFR (see Figure 3.27) which shows that the SCUBA-2 maps method can be used to find high-z sources and it will potentially find sources with similar physical properties to other submillimetre galaxies.

The main sequence of galaxies evolves with redshift (see Introduction 1 for details) and for this work, the definition from Speagle et al. (2014) was applied:
$\log(\mathrm{SFR}) = 0.84\ -0.026\mathrm{t(z)}\log(\mathrm{M}_* + 0.11\mathrm{t(z)} - 6.51)$ where t(z) is the age of the Universe in [Gyr]. This definition is similar to other definitions in the literature and

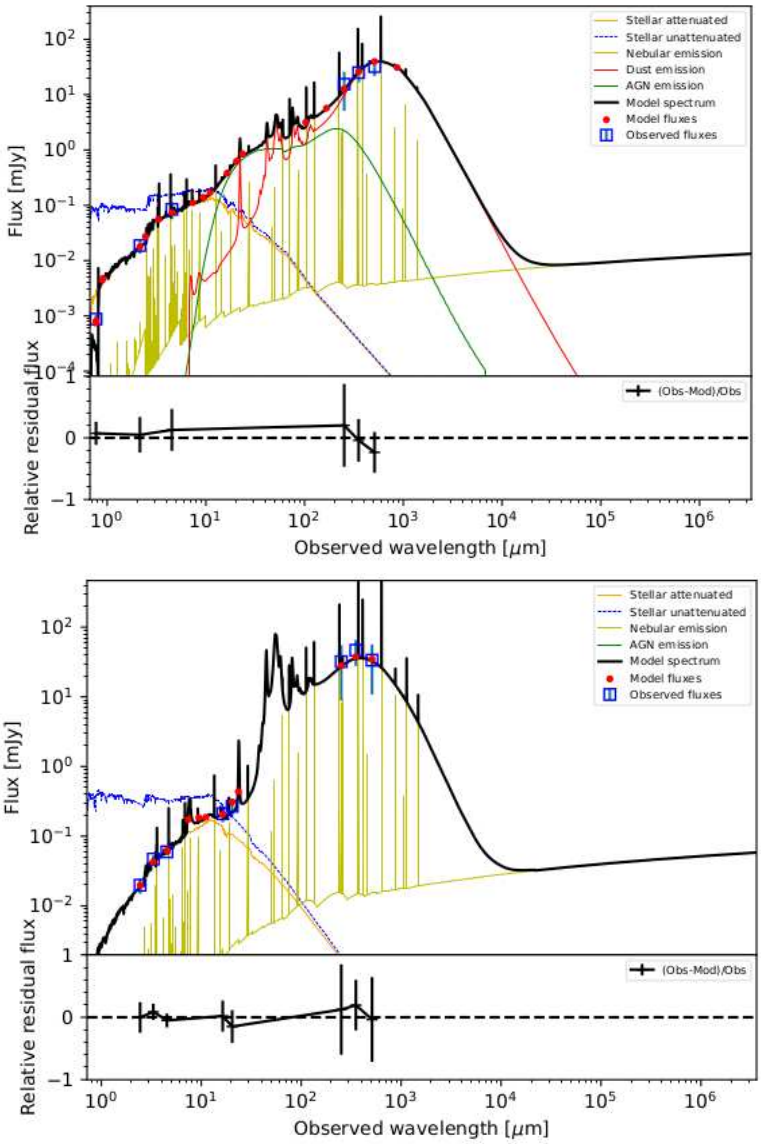

Figure 3.26: Example of two SEDs produced with CIGALE which show the different modules taken into account. The blue squares are the observed fluxes in mJy whereas the red dots represent the corresponding predicted fluxes by CIGALE that lie on the black line model fit. The different modules are shown in the legend. The stellar component is represented by the Bruzual & Charlot (2003) model; the orange line represents the stellar attenuation and the blue line shows the unattenuated stellar emission. The green line is the AGN component, represented by the Fritz, Franceschini & Hatziminaoglou (2006) model. If there is no green line then the AGN presence is null. The dust component is represented by the red line (Draine & Li, 2007) and without any line if the Schreiber et al. (2016) model was used instead. The emission lines are represented in pale green. Top: The SED of a $z_{phot} = 5.7 \pm 0.3$ source which is clearly a 500μm riser. Bottom: Highest redshift candidate in the sample at $z_{phot} = 6.2 \pm 0.3$.

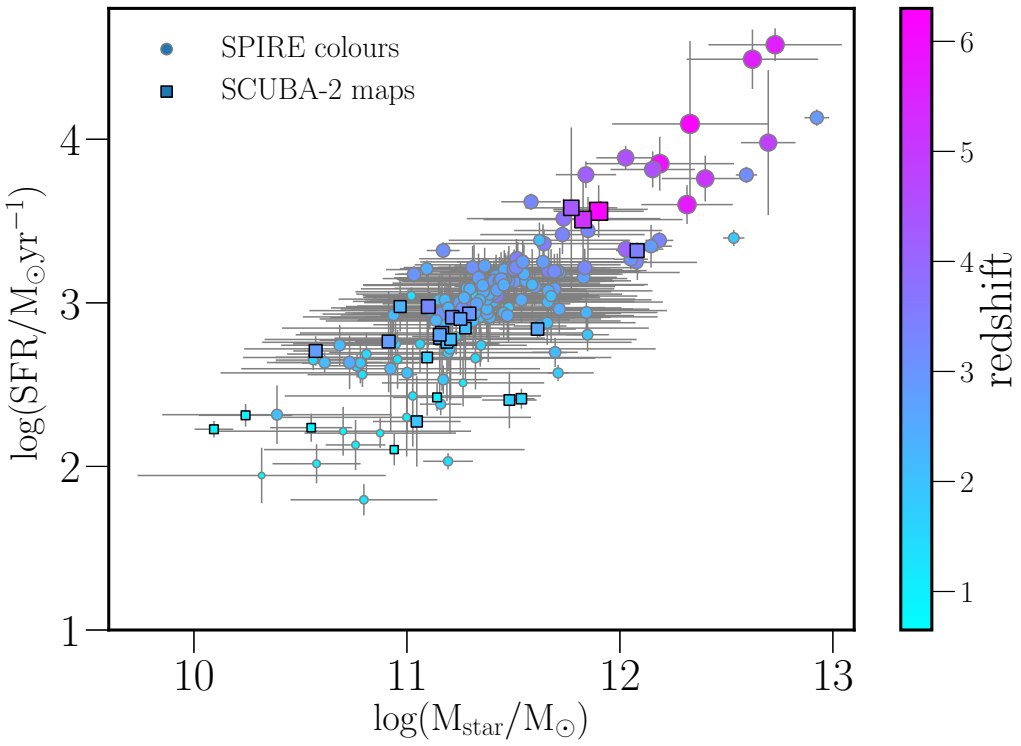

Figure 3.27: Star formation rate against stellar mass M_* with the redshift represented in the colour bar. The SCUBA-2 maps method finds similar redshift and SFR to the SPIRE colour method, although this latter method finds more extreme sources with higher SFR. Both selection criteria find similar redshift sources on average.

is often used in most of the work I compared the sample with (e.g. da Cunha et al. (2015), Dunlop et al. (2017)). Since the definition of the main sequence is a linear correlation, usually the definition of 'above the MS' is a numer of times the MS line. da Cunha et al. (2015) uses three times above the MS definition taked from Speagle et al. (2014), although others assume only two times above, such as Elbaz et al. (2011), which defines the MS as a function of cosmic time (see Section 1) and considers the sources above two times the main sequence starburst galaxies. Here, sources three times above the line of the main sequence are considered above the main sequence and starbust galaxies, in order to compare with da Cunha et al. (2015) and (Dunlop et al., 2017) since this works assumes the same definition of MS from Speagle et al. (2014).

The number of galaxies that lie above the MS in our submillimetre sample is 30% on average across the 5 bins. However, this percentage depends on the redshift bin:

the number of galaxies that lie above the main sequence is 51% at z = 2, whereas the proportion of starburst decreases with increasing redshift bin (see Figure 3.28). This corroborates previous studies, although at lower percentage than other studies such as Ikarashi et al. (2017) where 72% of their submillimetre sample selection lies above the MS with $1.4 \leq z < 2.5$ or Miettinen et al. (2017) measuring 63%. However, other submillimetre samples such as Dunlop et al. (2017) obtain a very different result that all their sources lie on the main sequence. The first obvious reason for this differences is that Dunlop et al. (2017) is a deep pencil-beam survey, and is therefore sensitive to lower SFRs but comparable stellar masses, whereas Miettinen et al. (2017) is a 1.1 mm selected survey with previous spectroscopic redshift and may select a different population. If both approaches, on and off the MS, are correct, it will imply a bimodality in the star formation in SMGs, with both an extreme star-formation mode and a moderate mode of star formation existing as in Zavala et al. (2018). This bimodality was evaluated recently by Elbaz et al. (2017) who finds a population of SMGs clearly above the MS with enhanced gas fractions and another more compact group of sources that lie on the MS. The different factors that could be related to the star formation will be evaluated in this Chapter.

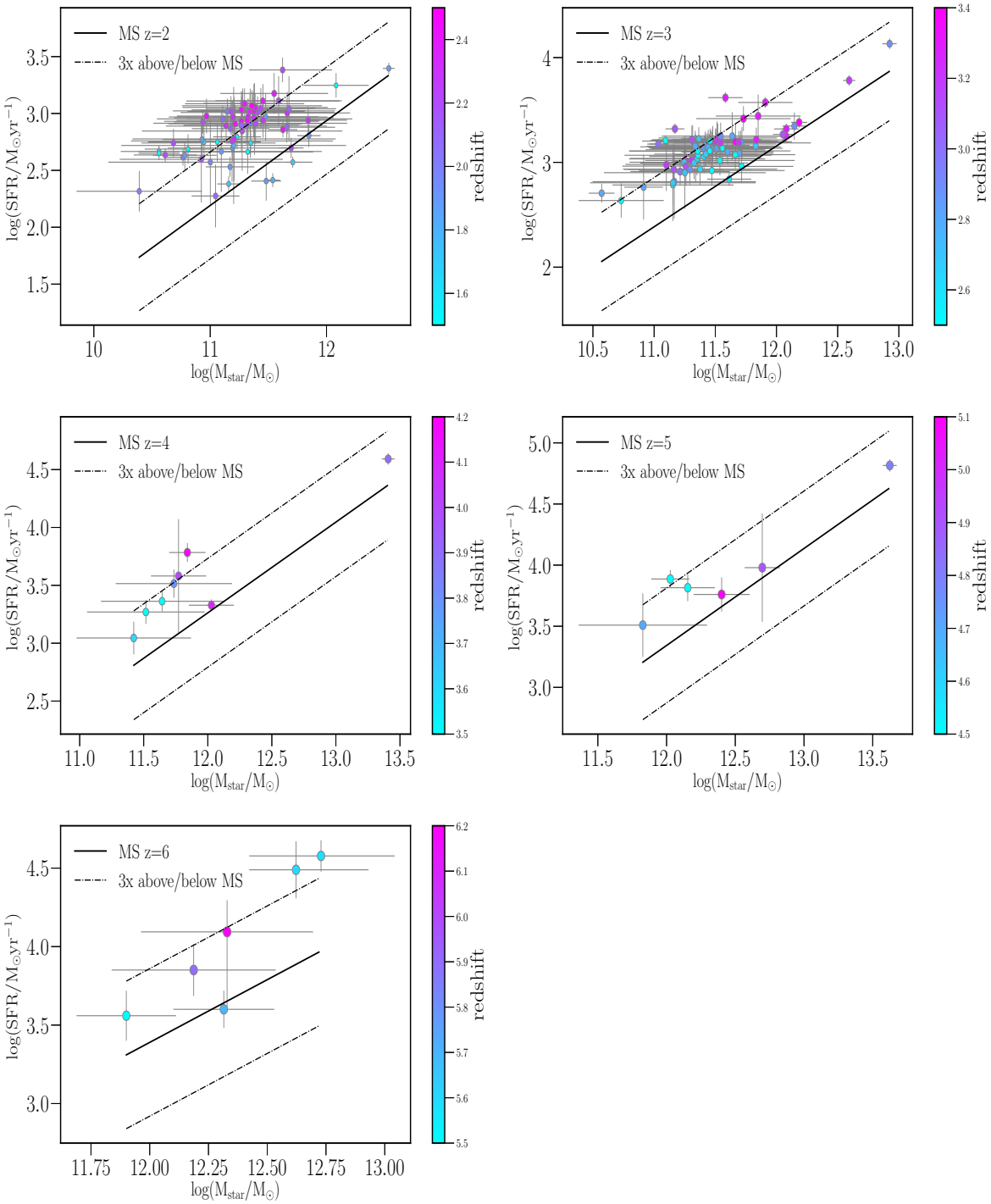

Figure 3.28: The Figure shows the main sequence of galaxies for 5 redshift bins ($1.5 \leq z < 2.5$, $2.5 \leq z < 3.5$, $3.5 \leq z < 4.5$, $4.5 \leq z < 5.5$, $5.5 \leq z < 7$. The black line show the MS for redshift $z = 2, 3, 4, 5, 6$ respectively in each plot following the definition from Speagle et al. (2014), whereas the dashed lines show three times above and below the line of the MS definition for each redshift bin. It is commonly considered "above the MS" if the source is 3 times above the definition of the MS line, since the correlation is not strictly a line and it has some scatter (da Cunha et al., 2015). The percentage of sources above the MS is bigger in z = 2 bin (51%), whereas in the rest of the bins it is smaller, although the higher redshift bins contain less sources and the percentage can be affected by small number statistics and selection effects.

Other parameters that can affect the star formation, such as the AGN presence or the PAH concentration (Elbaz et al., 2011), were evaluated. From the CIGALE results, the percentage of high-z candidates that have some AGN presence is around the 50%, similar to the sources classified as starburst, however, there is no correlation between the presence of the AGN with the SFR (see Figure 3.29). There is no connection between the galaxies that lie above the MS and any AGN presence, however, in order to make some discussion about this connection a deeper study in this topic should be done. I do not find any PAH deficit in the starburst galaxies and the fraction of PAHs is similar in both samples above or on the MS (see Figure 3.29). The PAH deficit is commonly accepted in luminous galaxies and it was expected to find a difference in the fraction of PAHs between galaxies above and on the MS. The possible physical explanation could be a higher presence of an AGN that does not allow the formation of PAHs, however, with the results available is difficult to confirm this and it is left as a future work when spectroscopic observations are finally obtained.

The Star Formation Efficiency (SFE) relates the star formation with the gas mass ($SFE = SFR/M_{gas}$) and allows us to analyse the factors that trigger the star formation. The SFE is studied in both galaxies above and on the MS in order to see if there is a factor that can trigger the star formation or if it is only the fact that they simply contain more gas. There is no evidence of a relation between the AGN fraction or the PAHs with the SFE which was expected from the previous lack of correlation between these parameters with the star formation. However, I find a clear trend between the age of the starburst (in the age of the galaxy) with the efficiency of the star formation: the earlier the starburst the more efficient the star formation (see Figure 3.30). The fraction of the starburst has some relevance, the more massive the starburst the bigger the triggering of star formation. However, there is no relation with the age of the main stellar population in the galaxy only with the time than the starburst is produced in the galaxy. The presence of a starburst could be due to a merger, but in order to confirm this, the morphology of the source would be required, since perturbed galaxies are expected in the case of major mergers (Elbaz et al., 2017). Elbaz et al. (2017) presents

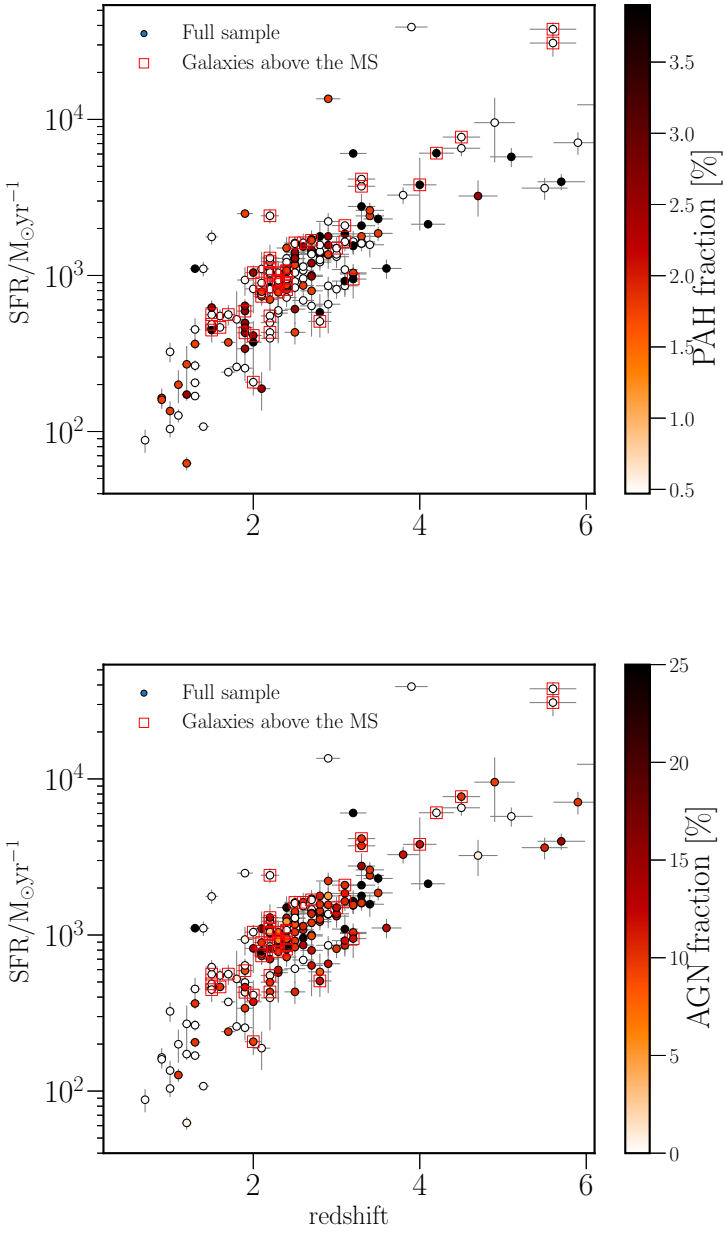

Figure 3.29: The SFR against redshift with the PAH fraction (top) and the AGN fraction (bottom) in the colour bar. The galaxies that lie above the MS are highlighted with red squares. There is not a higher presence of PAHs on average in the starburst galaxies nor of any dependence on AGN presence.

the state of the merger influences in the SFR, hence the time that the merger occurs in the live of the galaxy could influence in the SFE. The compactness could be another factor related to and effecting the star formation (Elbaz et al., 2007), however, due to the lack of spectroscopic data this has to be left as future work.

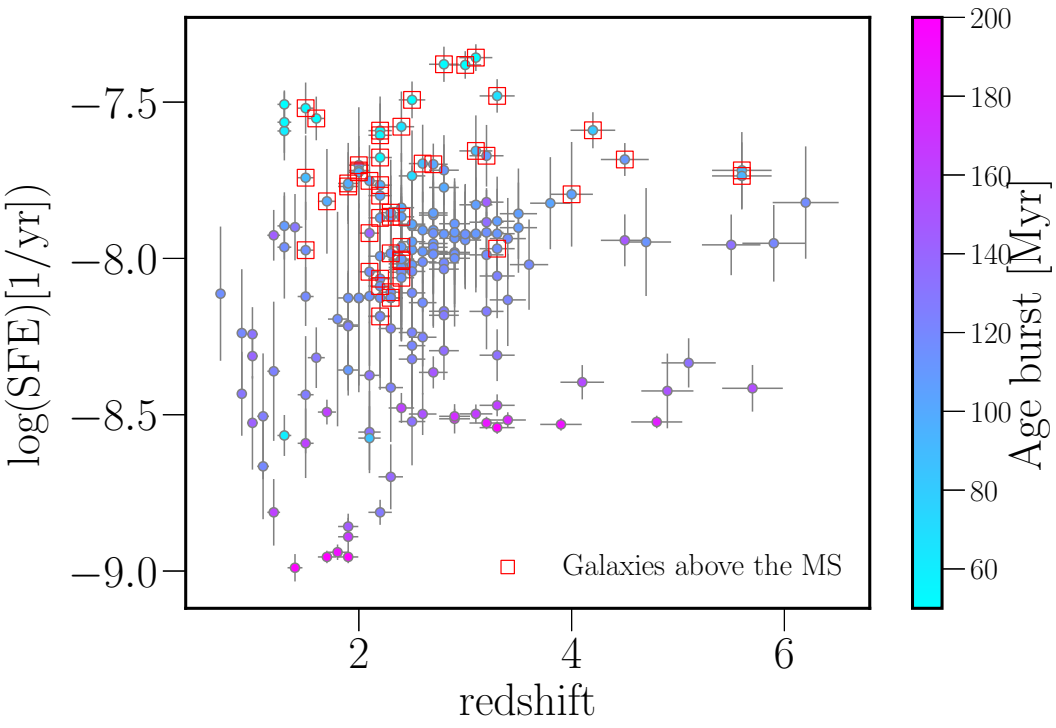

Figure 3.30: The plot shows the SFE against redshift with the age of the burst in the galaxy in the colour bar. The red squares show the galaxies that lie on the MS, which lie in the upper part of the diagram for different redshifts. There is a clear dependence between the efficiency of star formation with the age of the starburst: the sooner the starburst the more efficient the star formation.

There is no evolution with redshift: the lack of faint luminous galaxies at $z < 2$ is a selection effect produced by the selection of luminous galaxies and at $z > 2$ the relation between SFE with the redshift remains steady.

The star formation rate is calculated with the galaxy mass (see Chapter 1) and it clearly depends on the SFH model, more specifically on the age of the main population (Ciesla, Elbaz & Fensch, 2017). There is a general agreement on the difficulty of recovering the age of the galaxy from SED fitting (Buat et al., 2014), who concludes that the best fits are obtained with two population models. Although the SFH modifies the SFR-M_* relation, when two stellar populations are introduced the SFH has a modest impact (Buat et al., 2014). This corroborates the conclusion of using a double decreasing exponential as a SFH model with two stellar populations: a main population defined by the age of the main stellar population (age) and the age of a possible burst of

star formation in the galaxy (age_{burst}). I do not find a strong correlation between the age of the main population and the SFR, probably due to the consideration in this chapter of introducing a two populations whereas in (Ciesla, Elbaz & Fensch, 2017) are only considered single populations focused on the MS of galaxies. (Ciesla, Elbaz & Fensch, 2017) gives hints in the use of more than one stellar population by allowing a flexibility in the recent SFH, which provides very good estimates of the SFR in the MS, therefore, for galaxies above the MS I conclude that the use of two stellar populations is adequate for the sample and minimizes the problem with the SFR-age degeneracy.

3.7 Summary and conclusions

The high-z population at the NEP was studied using several SED fitting codes, concluding that the most successful for studying dusty high-z galaxies is CIGALE, which is able to estimate photometric redshifts successfully. The next best alternative, MAGPHYS needs reliable spectroscopic redshifts in order to produce a successful SED fit and it is not able to reproduce the properties of high-z dusty galaxies. The high-z sample is on average $z = 2.59 \pm 0.13$ and 15 of the source are at $4 < z_{phot} < 6.2$, this results are broadly consistent with with the contemporary galaxy evolution models of Pearson (2018).

The physical properties of these sources - such as SFR and stellar masses - were calculated using CIGALE and their positions on the MS of galaxies was evaluated. I find clearly that the high-z population have high SFRs, meaning that in total 30% of them lie above the MS. For the specific redshift bin of $z \sim 2$ the percentage of galaxies above the MS is high at 51%. This value is compared with other studies of SMGs at $z \sim 2$ (Ikarashi et al., 2017) (Miettinen et al., 2017), finding around 10% less of sources above the MS, whereas the percentage agrees with (da Cunha et al., 2015). However, other studies find no galaxies above the MS for the same redshift bin (Dunlop et al., 2017), where the selection of the sources in a small area (~ 4.5 deg^2) is produced by a deep pencil-beam. Hence, the study is sensitive to find lower SFRs at similar stellar masses and not rare exotic sources, only finding 16 sources. The big discrepancies in the results between these studies seems to indicate a bias effect since Ikarashi et al. (2017) and Miettinen et al. (2017) are longer wavelength submillimetre selected samples.

Elbaz et al. (2011) discuss the lower presence of PAHs in the galaxies that lie above the MS with the mid-IR deficit. However, I do not find such a difference in the PAH fraction between the starburst galaxies and galaxies that lie on the main sequence, implying that there is no evidence for evolution in the solid-state phases of the interstellar medium for ultraluminous galaxies at redshifts $0 < z < 1$. Since PAHs are produced in

the outer regions of giant molecular clouds, this may indicate an unevolving geometry or filling factor of the star formation regions in ultraluminous galaxies, at variance with the results of Elbaz et al. (2011). This difference in results can be due to the dust models used that are possibly not sensitive enough to detect this lack of IR emission and mid-IR spectroscopy would be necessary to confirm this result. The presence of any AGN is similar in starburst as in normal MS galaxies and there is no correlation between the star formation with the AGN presence. I do not find evidence that an AGN can cause produce a higher star formation efficiency.

The star formation efficiency relates the star formation with the gas within the galaxy. Therefore, finding some parameter that correlates with the SFE can also provide a link to the triggering, or quenching, of star formation.

I find a relation between the age of the starburst in the galaxy and the SFE, the earlier the starburst the more efficient the star formation. The morphology of the galaxies can be related to mergers, which influences the SFR (Elbaz et al., 2017). The presence of the starburst could be caused by a merger and the age of this starburst could in turn be related to the state of the merger. This could be the reason behind the bimodality of star formation in SMGs and it could be the reason - or one of the reasons - why high-z ULIRGs are more common than local ULIRGs. There is spectroscopic evidence that mergers enhance the star formation in its early stages (Riechers et al., 2017), however, spectroscopic observations of the sample are required in order to pursue and confirm this.

I conclude that the SFE depends on the age of the burst in the galaxy, but not on the presence of AGN or the age of the main population in the galaxy, which could indicate that secular processes are less important - specific in the high-z DSFGs - than external processes such as mergers.

Galaxies such as HFLS3 probably are not representative of the SMGs population, however, more galaxies like HFLS3 could be found by the proposed selection methods. Finally, I conclude that a multi-wavelength approach in deep fields, with good coverage of photometric data such as at the NEP, is necessary for a better understanding of this

population. This will however require spectroscopic observations, that will be the subject of future work.

Chapter 4

Radio properties of galaxies

This chapter explores several samples of galaxies that emits in radio, trying to answer questions such as what is the role of Active Galactic Nuclei (AGN) in the star formation history of the galaxy? A method to calculate photometric redshifts by using a multi-wavelength approach for a submilliJansky population was developed. The sample was classified by infrared luminosity finding that the AGN contribution of luminous infrared galaxies evolves with redshift. Infrared colour-colour diagrams were produced to classify AGNs, proposing a new colour criteria that use AKARI data. Furthermore, there is shown evidence that AKARI bands can be used for classifying AGNs more effectively than WISE data. The radio population was studied from the far-infrared radio point of view. A correlation was found between the GMRT data at 610 MHz and the Herschel data at 250μm *which was used to define a spectral index which shows no evolution against redshift. Radio colour-infrared diagrams can be used as a redshift indicator. These results are published in Barrufet et al. (2017).*

4.1 Introduction

The radio emission of galaxies can be caused by a combination of (nuclear) starbursts and Active Galactic Nuclei (AGN) activity, but also can be caused purely by AGN activity. Excluding the luminous Faranoff-Riley class 2 AGN, the first case corresponds

mostly to galaxies with faint radio emission, the called submJy population which is a mix of starburst, post-starburst and elliptical galaxies (e.g. Padovani (2009), Windhorst (2003) for review), whereas the second case the emission came from the AGN that is hosted by the galaxy.

In this chapter is presented a study of the radio population at the North Ecliptic Pole (NEP) in which a submilliJansky population was studied, a radio-optical selection of the sources was carried out, as well as study of the radio-FIR correlation. The AKARI NEP is a natural location to accomplish deep extragalactic surveys as it is supported by comprehensive ancillary data extending from radio to X-ray wavelengths (see Section 1.3.2).

A striking relationship in far-IR astronomy is the degree of correlation between the radio and far-infrared (FIR) fluxes of star-forming galaxies. This is generally believed to be a consequence of high-mass stars heating the dust (which then re-emits in the FIR), while supernovae in turn produce the relativistic electrons responsible for synchrotron radiation (e.g. Condon, 1992; Kovács et al., 2006). Although the origins of the far-infrared-radio correlation - hereafter FIRC - seem to be understood (Magnelli et al., 2015) the linearity of the relationship is not so obvious, since the synchrotron emissivity depends on both the number density of relativistic electrons and the magnetic field strength, which are not necessarily related. Furthermore, the question about whether the slopes of the FIRC evolve with redshift is still open: some studies have suggested that they do (e.g. Seymour et al., 2009; Magnelli et al., 2015) but some others cast serious doubts (e.g. Appleton et al., 2004). Since the star formation rate (SFR) and the gas density, which in part control normalization of the FIRC, are both known to evolve with redshift and a decrease of the slope of the FIRC is expected as a consequence. Understanding the evolution of the FIRC involves the study of galaxy evolution, and can allow us to understand why some high redshift galaxies lie far above the main sequence trend, in a starburst mode with similar FIR properties to the local ULIRG population (Magnelli et al., 2014). However, other properties differ such as the size of the star forming regions or the scale heights.

In addition, the FIRC is an important tool which is frequently used in extragalactic astrophysics. Firstly, it can, in a practical sense, be used as a part of the calibration of radio luminosity as a star formation indicator by using the infrared luminosity-SFR relation, which is especially useful for high redshift galaxies (Magnelli et al., 2015). Furthermore, as well as at high redshifts, the FIRC relationship has been used to estimate the distance and the dust temperature in starburst galaxies (Carilli & Yun, 1999).

In this Chapter, a radio-optical identification and the radio properties of the sample at the NEP are presented in 4.2. The results of the first part was published in (White et al., 2017), whereas the radio samples used in Sections 4.3 4.4 will be part of the paper in preparation White (in prep.). Section 4.5 describes the AGN population classification in the NEP proposing a new effective method to classifying AGN by using AKARI data. The Radio-FIR correlation in the NEP is presented in Section 4.6 (results published in Barrufet et al. (2017)). Finally, Section 4.9 summarizes the results.

4.2 Optical identification of radio sources in the NEP

Radio sources are often extended and pinpointing the true host is challenging, which makes the identification of the correct optical counterpart in radio surveys important. The radio source appear can appear to be associated with multiple optical sources, particularly in deep optical surveys. This section shows the results of the multi-wavelength analysis of the radio sources from the updated version of the Giant Meterwave Radio Telescope (GMRT) 610 MHz catalogue. It covers $\sim 2\text{deg}^2$ located at the AKARI North Ecliptic Pole Field (ADF-N) and contains 1318 radio components in the 5σ source catalogue (White, in prep.). This final version was corrected for astrometric and systematic uncertainties and around 100 new sources were added, with respect to White et al. (2017).

Several methods to calculate the photometric redshift from a multi-wavelength approach have been described and considered during this Thesis (see Chapter 3) and I concluded that there is a need to use a more robust method to calculate the photometric redshift and other physical parameters, which more fully take into consideration the whole spectrum. SED fitting techniques allow us to achieve these goals, and to explore this further, several different SED fitting codes were tested against each other and against a sample of sources which also had spectroscopic redshifts (see Section 3.2 in Chapter 3 for details). The code selected for this purpose was CIGALE (Noll et al., 2009), since the objective was to calculate physical parameters of the radio-source host galaxies such as AGN fraction (see Section 3.2.4).

The photometric redshift catalogue available in the field (Oi, 2014) ensures a good estimator for two cases:

- $z < 1$ if the magnitude in the z CFHT band is zmag < 24
- $z < 2.2$ if the magnitude zmag < 22

which is indeed a limitation since there are plenty of faint radio-source hosts and some high-z sources in the sample. Therefore, this catalogue does not guarantee a reliable

redshift in the radio sample, moreover, the photometric redshift catalogue was produced with the code LePhare which only uses optical available on the field. In addition, LePhare uses templates of nearby galaxies and although it is useful in some cases, I believe it is not the best code to extract the photometric redshift because it is based on templates where the redshift is a key input parameter. However, LePhare can be useful for calculating physical properties once the spectroscopic redshift is known or assumed (see Section 3.2.2 in Chapter 3 for details).

White (in prep.) presents the total catalogue cross-matched with Murata et al. (2013) using a five arcseconds search radius which determines $\sim$90% probability to find reliable cross-matches (White, in prep.). As a pilot study, the multi-wavelength catalogue of the 169 radio-sources with available redshifts was used to test and train the algorithm. This sample is a subset of the GMRT catalogue which includes optical-NIR data from CFHT, IR data from AKARI and submillimetre data from SPIRE. Most of the sources (90%) have at least 10 photometric detections. This analysis will be extended to the total sample from White (in prep.).

4.3 Analysis of the radio sources by SED fitting

The photometric redshift was calculated with CIGALE and compared with the other redshift data sets in order to check their reliability. The redshift was calculated by producing a grid from $5 > z > 0.1$ with steps δz=0.1 and it produces a Bayesian analysis (see CIGALE code in Section 3.2.4 for details) with a probability density function (PDF) of the redshift, as shown in Figure 4.1. This Figure suggests the use of smaller redshift steps that will be produced as a future work with a smaller grid and a broader step.

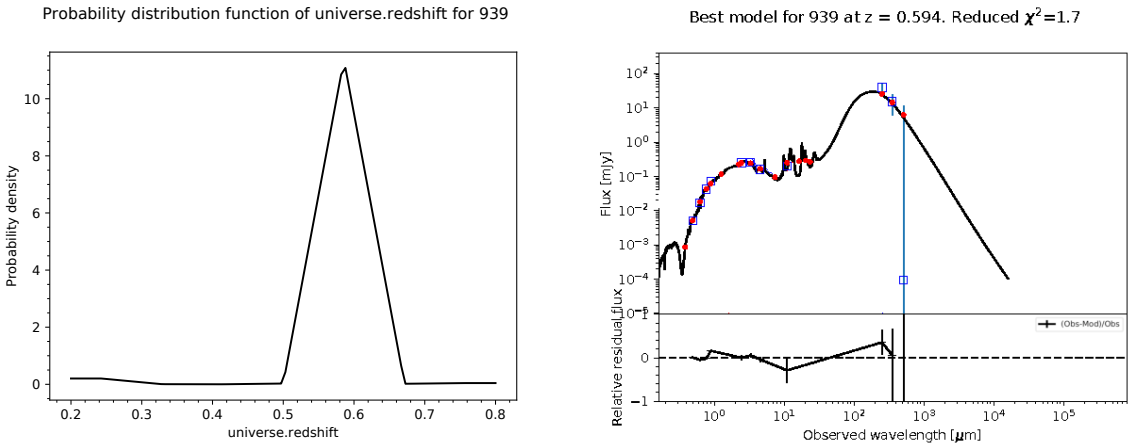

Figure 4.1: Example of one of the plots extracted with CIGALE code for one source (ID=939): (Left) Probability density function (PDF) of the redshift (universe.redshift) for one of the sources extracted with CIGALE module *redshifting* which takes the most likely value the peak at z=0.594. (Right) Best SED fit of the same source where the photometric redshift extracted in the previous step was an input. The blue squares are the observed fluxes [mJy] whereas the red dots show the predicted fluxes by the best model that fits the observations (black line).

The spectroscopic redshift has to be reliable, with at least two emission lines, otherwise there may be systematic errors in in the rest of the parameters. The photometric redshift calculated by using optical data alone with Lephare was found to be not sufficiently robust, and in both cases it is better to leave the redshift as a free parameter.

The photometric redshift estimates were then compared with the direct photometric redshifts of Oi (2014) - calculated with LePhare and limited for faint and high-z sources- and the preliminary spectroscopic redshift catalogue in the NEP (Takagi in prep.) to test the efficacy of the redshift provided by CIGALE. I find that the photometric redshifts are in reasonable agreement up to $z_{phot} \sim 0.7$ in the case of Oi (2014) and for the good quality spectroscopic redshift measurement (see Figure 4.2).

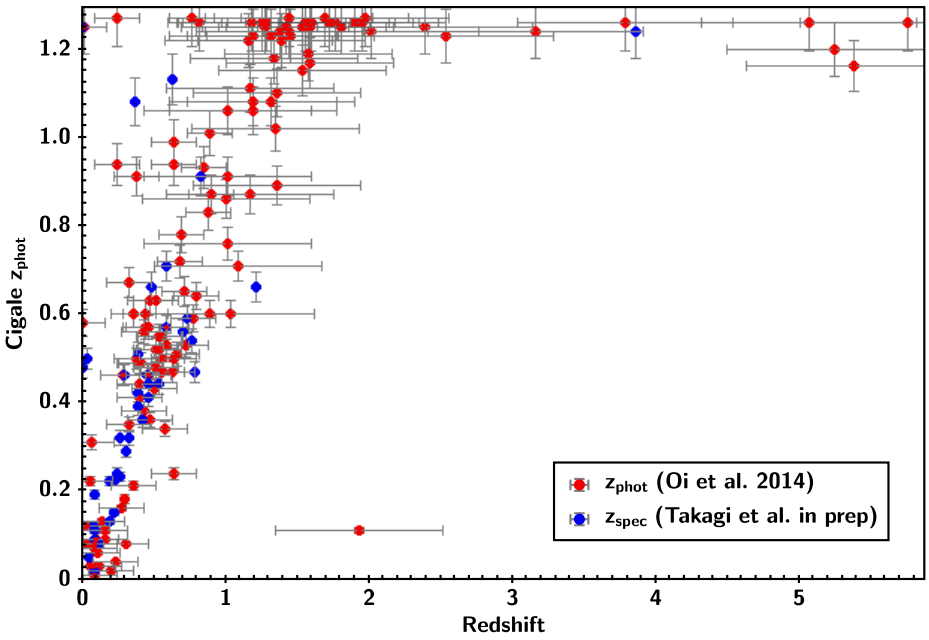

Figure 4.2: The plot compares photometric redshift estimated from CIGALE versus the direct spectroscopic redshift in blue squares (Takagi et al. in prep.) and photometric redshift in red circles (Oi, 2014). There is certain agreement until z $\sim$ 0.7, where the comparative photometric redshift is reliable. Furthermore, the spectroscopic redshift that have good quality spectral lines are in agreement with CIGALE's photometric redshift.

Furthermore, the SEDs were calculated by giving the redshift from Oi (2014) and (Takagi et al. in prep) as an input. The code is only able to find a model that fits the observations for 77% of the sources, however, when the redshift is a free parameter, it finds models for all the sources of the sample with better SED fitting. I produced the SED fitting for both catalogues and the photometric redshift estimated from CIGALE, and comparing the fitting by eye in the 169 cases. For all the sources a better (or equal) quality of fitting is produced with CIGALE photo-z input (see Figure 4.3).

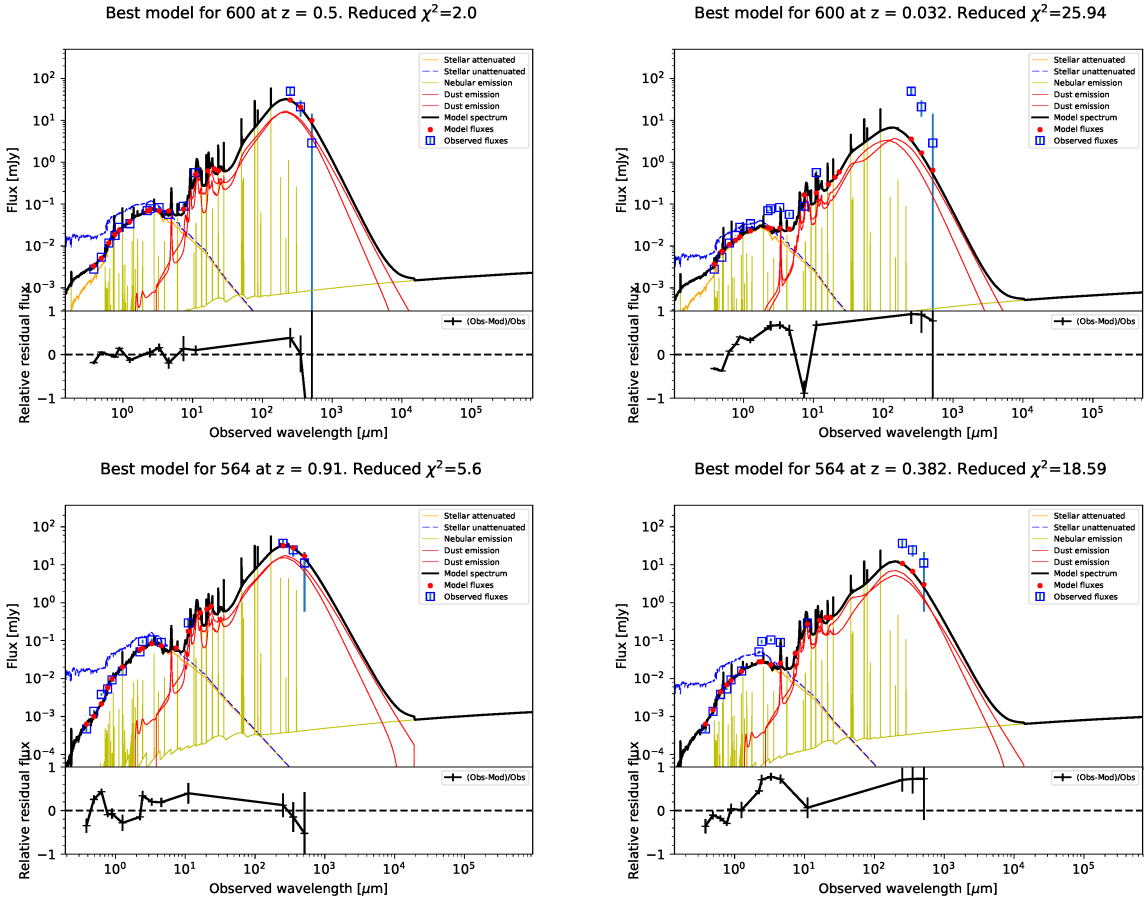

Figure 4.3: The figure shows the SED for two different radio-sources in each row (ID=600,564 respectively); the first column shows the SED estimated using the photometric redshift calculated with CIGALE, whereas in the second column the SEDs calculated with the redshift data available in the field are shown. The first row shows the SED fitted with the photometric redshift ($z_{phot} = 0.5$) obtained with CIGALE (on the left) and the Same source -same fluxes- fitted with the spectroscopic redshift (z=0.032) (Takagi et al. in prep) as an input which has a redshift flag: D = probable redshift but unreliable. Clearly the results are better if the redshift is calculated with CIGALE that with a uncertain (flag D) spectroscopic redshift: the FIR observations are clearly in better agreement in the top SED and the $\chi^2 = 2.0$ vs. $\chi^2 = 25.94$ show better fit (both have the same photometric detections, 15 in total) The second row shows a comparison of the photometric redshift calculated with CIGALE as a free parameter ($z_{phot} = 0.91$) with the SED with the photometric redshift catalogue from Oi (2014) ($z_{phot} = 0.382$), where the χ^2 is three times higher and the model does not fit either the FIR peak nor the optical (both with 13 photometric detections).

CIGALE allows us to estimate the SED from UV to radio taking the balance between the energy absorbed by dust and remitted in the IR into account. A more detailed explanation of the code and module selection is described in Chapter 3. The code assumes a combination of modules that model different physical aspects of the spectra,

where it is necessary to adopt the physical parameters of each module (see Table 3.5). The star formation history (SFH) was modeled as a declining exponential star formation SFR $\propto t \cdot \exp(-t/\tau)$. This assumption differs to the SFH in Chapter 3 due to the population to model is not expected to have high star formation and it is not necessary to introduce the present of a starburst to fit the SED. The stellar emission contribution was chosen following Bruzual & Charlot (2003), and setting the Chabrier initial mass function and metallicity similar to $Z_{\odot}$. The dust attenuation assumes a power law (Charlot & Fall, 2000). The Draine & Li (2007) models were adopted to define the dust emission, introducing the presence of PAHs and the radiation field. Since one of the aims was to study the AGN contribution in radio galaxies, the AGN emission was specifically defined with broad grids in several parameters and varying small steps in the values (see Table 4.1). The nebular emission - which simulates the emission lines - was considered in the first test where the photometric redshift was tested (see Figure 4.3) and I concluded that it does not contribute significantly to the main parameter estimates. For this reason it was removed from the rest of the analysis since it was computationally expensive, increasing the models produced by a few million. In total, this combination of physical parameters (see Table 4.1) resulted in 33592320 models, and it chooses the best fit for each source.

As future work, the photometric redshift and the physical properties of the 1318 radio sources will be calculated White (in prep.) and denser redshift grids will be defined by using radio-flux colour diagrams (see Future work 6.2.3).

CIGALE module	Main parameters	Description
SFH $SFR \propto t \cdot \exp(t/\tau)$	$\tau_{main} = 250 - 8000$	Main stellar population [Myr]
Stellar emission (Bruzual & Charlot, 2003)	IMF=1 Z=0.02	Chabrier IFM Metallicity
Dust attenuation (Charlot & Fall, 2000)	$Av_{young} = 0 - 4$ $powerlaw_{slope} = -0.7$ $Av_{old} = 0.1 - 1$ $UV_{bump\lambda} = 217.5$	Attenuation V band Slope delta of the power law Reduction factor compared to Av_{young} Central λ [nm] of the UV bump
Dust emision models (Draine & Li, 2007)	$q_{pah} = 0.47 - 5.26$ $u_{min} = 1.05.0$	Mass fraction of PAHs Minimum radiation field
AGN component (Fritz, 2006)	fracAGN = 0 - 0.5 $r_{ratio} = 60 - 140$ $psy = 0^\circ - 90^\circ$	AGN fraction [%] Opening angle of the dust torus Angle between AGN axis and line of sight

Table 4.1: Main modules and input parameters used in CIGALE for the analysis of the 169 radio-source sample. The Star formation history (SFH) assumed is a decreasing expontential. The stellar emission model is as commonly used (Bruzual & Charlot, 2003) and defined by the Chabrier initial function mass, and with a metallicity similar to the solar ($Z_\odot$). The dust attenuation is defined by a power law (Charlot & Fall, 2000) that allows for a wide range of PAH values. The AGN component assumes a broad range of parameters such as the AGN fraction and physical parameters of the torus (Fritz, Franceschini & Hatziminaoglou, 2006). The model - which is used in all the fits for this chapter- have 10 degrees of freedom.

4.4 Physical radio properties of galaxies

The faint radio sources - below 1 mJy - are most commonly associated with star formation, since the radio emission has its origin from supernovae events, however there is a mix of galaxy populations around these fluxes and is not well determined the dependence of star forming galaxies and AGN on epoch is not well determined (Padovani, 2009). Remark that the sample was chosen for the availability of redshift (either photometric or spectroscopic), which implies the presence of optical host, which bias the sample compared to the general submJy population.

The Bayesian analysis in CIGALE gives the most probable values for all the relevant parameters described in the models. To study the sample of galaxies with faint radio emission the following parameters were selected for the probabilistic analysis: star formation rate (SFR), stellar mass, gas mass, AGN fraction, PAH concentration and luminosity of the dust as being the most important. This study is focused on obtaining the physical properties of galaxies with faint radio emission, especially the AGN contribution in these sources together with the star formation.

Furthermore, the SEDs were checked by eye to ensure good agreement across the whole spectrum. Although models were found for all of the sources, three of them were excluded since the estimated SED did not fit the whole spectrum, provided an uncertain mismatch between the optical and the FIR data (see Figure 4.5). For the rest of the sources the good association between the FIR data and the optical data is guaranteed. As future work, the radio detection will be included in the SED fitting analysis in order to check the radio-optical association, although currently there are no SED fitting codes that include the relevant radio wavelength modules to allow incorporating low frequency data such as the GMRT (610MHz) radio observations. Checking the fit by eye can be another confirmation of the efficacy of the fit, as it was in Chapter 5 for a small sample.

Most of the fits (90%) have data from more than 10 photometric bands, which assures us of a reliable SED fitting. Moreover, all of the fits have $\chi^2 < 13.2$ and on

average $\chi^2 = 3.06$ with $10 <$ photometric detections < 18. All the 169 fits are included in the Appendix (see Figure A.1).

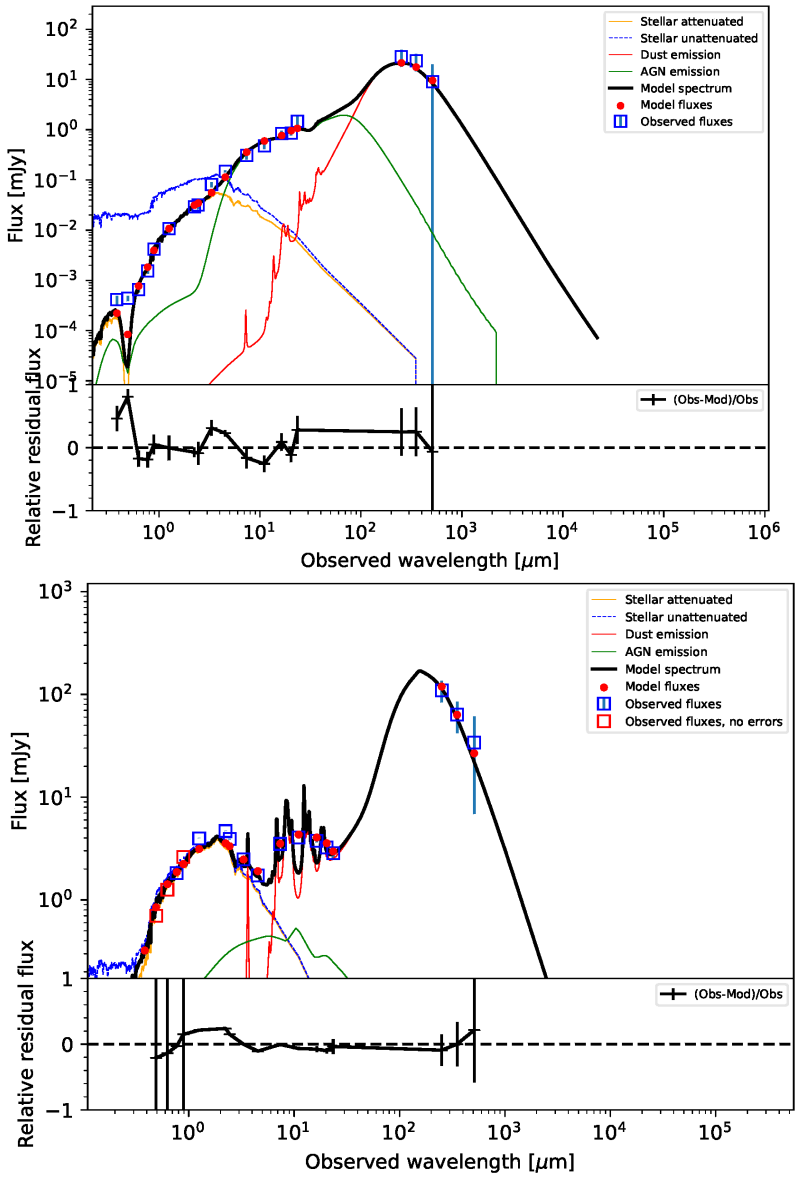

Figure 4.4: Examples of SED fittings extracted with CIGALE where the blue squares are the observed fluxes [mJy] whereas the red dots the predicted fluxes by the best model that fits the observations (black line). CIGALE modules are represented in the legend: the blue line is the stellar emission (Bruzual & Charlot, 2003), the yellow line defines the dust attenuation whereas (Charlot & Fall, 2000) the dust emission is defined by the red line (Draine & Li, 2007) and the green line defines the AGN emission (Fritz, Franceschini & Hatziminaoglou, 2006). (Top) The Figure shows the highest redshift source found $z_{phot} = 1.19$ (ID=454). It clearly has a power law spectrum which - together with the AGN fraction (50%) - indicates that the galaxy host an AGN. The fit is robust, $\chi^2 = 6.47$ for the 18 photometric detections and there is an agreement between the optical/near-IR with the FIR peak, which indicates that the cross-match is consistent. (Bottom) Example of a representative source of the sample (ID=101) at low redshift ($z_{phot} = 0.1$), high presence of PAHs and lower contribution of AGN (green line). Robust fitting with $\chi^2 = 1.3$ for the 17 photometric detections, three of them without error in the photometric detection (red squares) which the code takes into account as a less reliable detection.

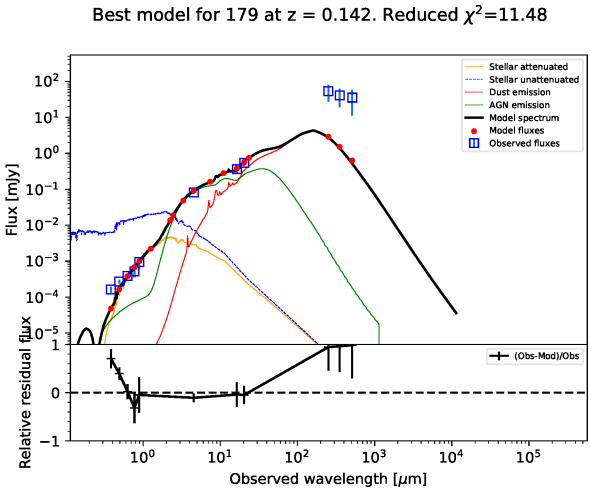

Figure 4.5: This plot shows one of the sources excluded from the analysis (IDs=179,752,770 see appendix). The fit is good in the optical and near-IR, however, the fit in the FIR peak was not reliable, although it is possible to find a template to fit the FIR peak independently to the rest of the data. The impossibility to find a template that fits both optical and IR is suspicious to be in consequence of either a double source or a mismatch in the multi-wavelength catalogue. Another interpretation is that the double source is a strong gravitational lens, in which a foreground infrared-luminous galaxy is magnifying the source of the far-infrared flux (Rowan-Robinson, 2014). The rest of the sources indicate reliable associations between the catalogues.

The photometric redshift distribution of the radio sources indicates moderate redshift with $0.1 < z_{phot} < 1.2$ with mean $z_{phot} = 0.55 \pm 0.03$ and the highest number of sources at $z_{phot} = 0.1$. The distribution of redshift shows no sources at high redshift (see Figure 4.6 Top). This can be due to the subsample of sources being biased, since the 169 sources were selected for having either spectroscopic redshift or photometric redshift and that sample is not representative of the radio population since had other science proposes (Oi, 2014). The consequences of this low redshift biases implies a flux-limited sample and the distribution of redshifts is compatible with the submillijansky population (see Figure 4.6 Bottom). It is expected that higher redshift sources will be found in the total radio sample and a more heterogeneous distribution.

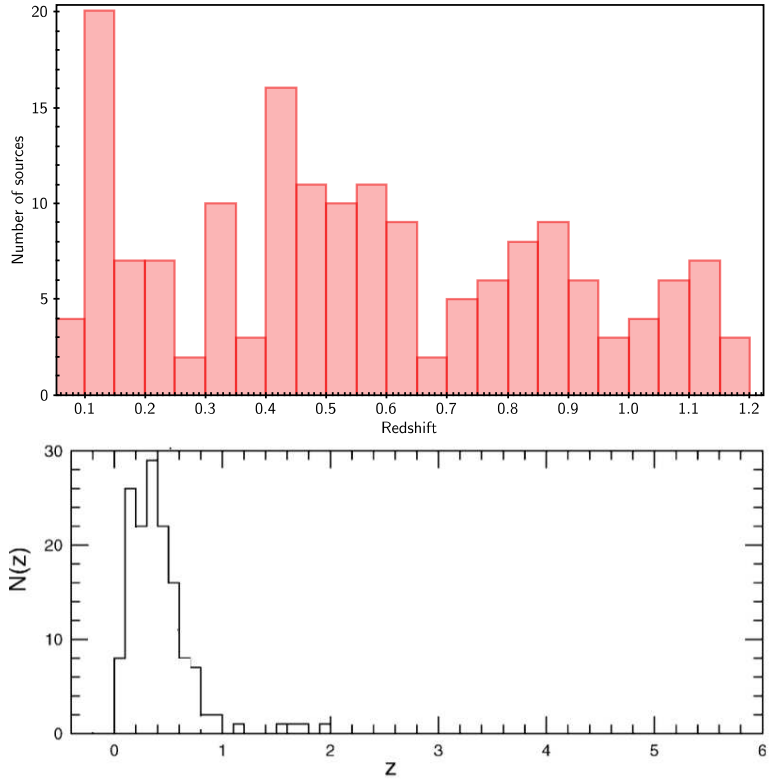

Figure 4.6: (Top) Distribution of photometric redshifts for the 169 radio sources in the NEP deep field. These tend to have moderate photometric redshifts, probably because it is a sample of the sources that have both photometric and spectroscopic redshift in the area. The same procedure should be applied in the whole sample ($\sim$ 1300 sources) in order to confirm these results. (Bottom) Number of sources representative of a submilliJansky population extracted from the review Windhorst (2003), middle Figure 5 corresponding to the submilliJansky population.

The radio flux of the 169 available sources shows that the sample is composed of low radio fluxes with 92% of sources with $F_{610\ \mathrm{MHz}} < 1$mJy. Therefore, the sample is representative of the submilliJansky population which is star forming dominated instead of be AGN-driven (Padovani, 2009). In the complete catalogue from White (in prep.) 24% of the sources have radio flux bigger than 1 mJy, which clearly shows that the sample of 169 galaxies is biased to low radio fluxes compared to the total catalogue. In the literature (see Windhorst (2003) for review) the microJansky population is a mix of galaxy types: starburst, post-starburst and elliptical galaxies. The radio emission at these fluxes is caused by a combination of (nuclear) starbursts and weak AGN activity. Possibly due to this fact, the distribution of the radio sources is independent of the AGN fraction since it was expected to find higher AGN fraction for brighter

radio sources (see Figure 4.7), which shows the sources with higher AGN contribution (AGN fraction > 20%) and the correlation is non-existent, however, there is only one source with F > 1 mJy and this can explain the lack of correlation.

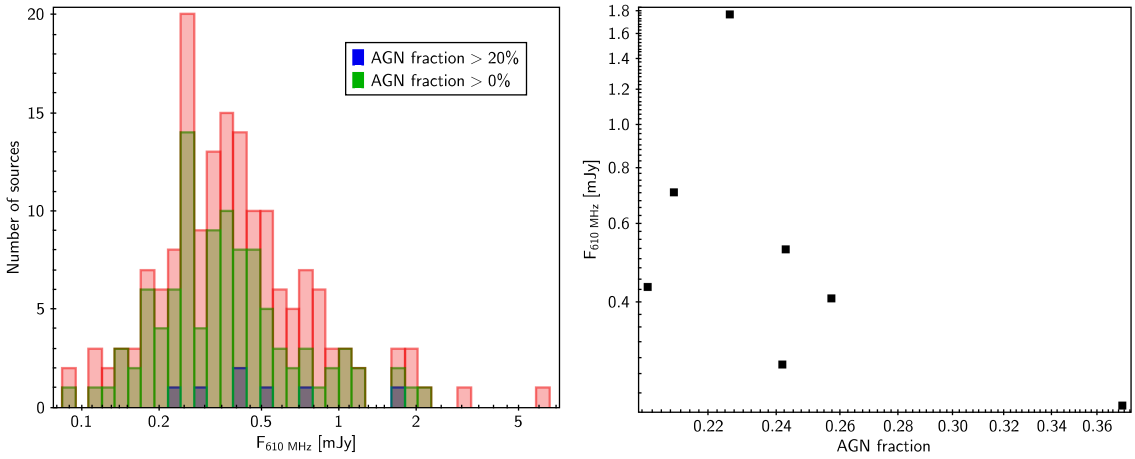

Figure 4.7: (Left) The radio flux histogram shows a distribution of faint radio sources, 92% of them with $F_{610\ MHz} < 1$mJy, due to a biased selection. The total number of radio sources are plotted in red, whereas the sources with AGN contribution are overplotted in green (AGN fraction > 0%) and in blue (AGN fraction > 20%). (Right) Radio flux F_{610MHz} against the AGN fraction extracted with CIGALE. The correlation between the two parameters is inexistent due to the lack of bright radio sources in the sample that expect to be AGN dominant. The uncertainties are 0.05 mJy < eFlux < 0.2 mJy in flux and in the AGN fraction 0.02 < error AGN fraction < 0.08

The far-IR luminosity is proportional to the amount of star formation. The different ranges of these IR luminosities are a classified as follows: luminous IR galaxies (LIRGs) with $10^{12} \cdot L > L_{\odot} > L_{IR} > 10^{11} \cdot L_{\odot}$), ultra-luminous IR galaxies (ULIRGs) ($10^{12} \cdot L_{\odot} > L_{IR} > 10^{11} \cdot L_{\odot}$) and hyper-luminous IR galaxies (HLIRGs) ($L_{IR} > 10^{13} \cdot L_{\odot}$) (see Lonsdale, Farrah & Smith (2006) for review). The radio sample was classified by infrared luminosity in order to study the characteristics of these populations (see Figure 4.8). The luminosity presented in this Section was corrected for AGN contamination: the contribution from the AGN luminosity was extracted from the total IR luminosity of the galaxy. CIGALE gives the most probable value for both luminosities by calculating their probability density function (PDF) (see Figure 4.9).

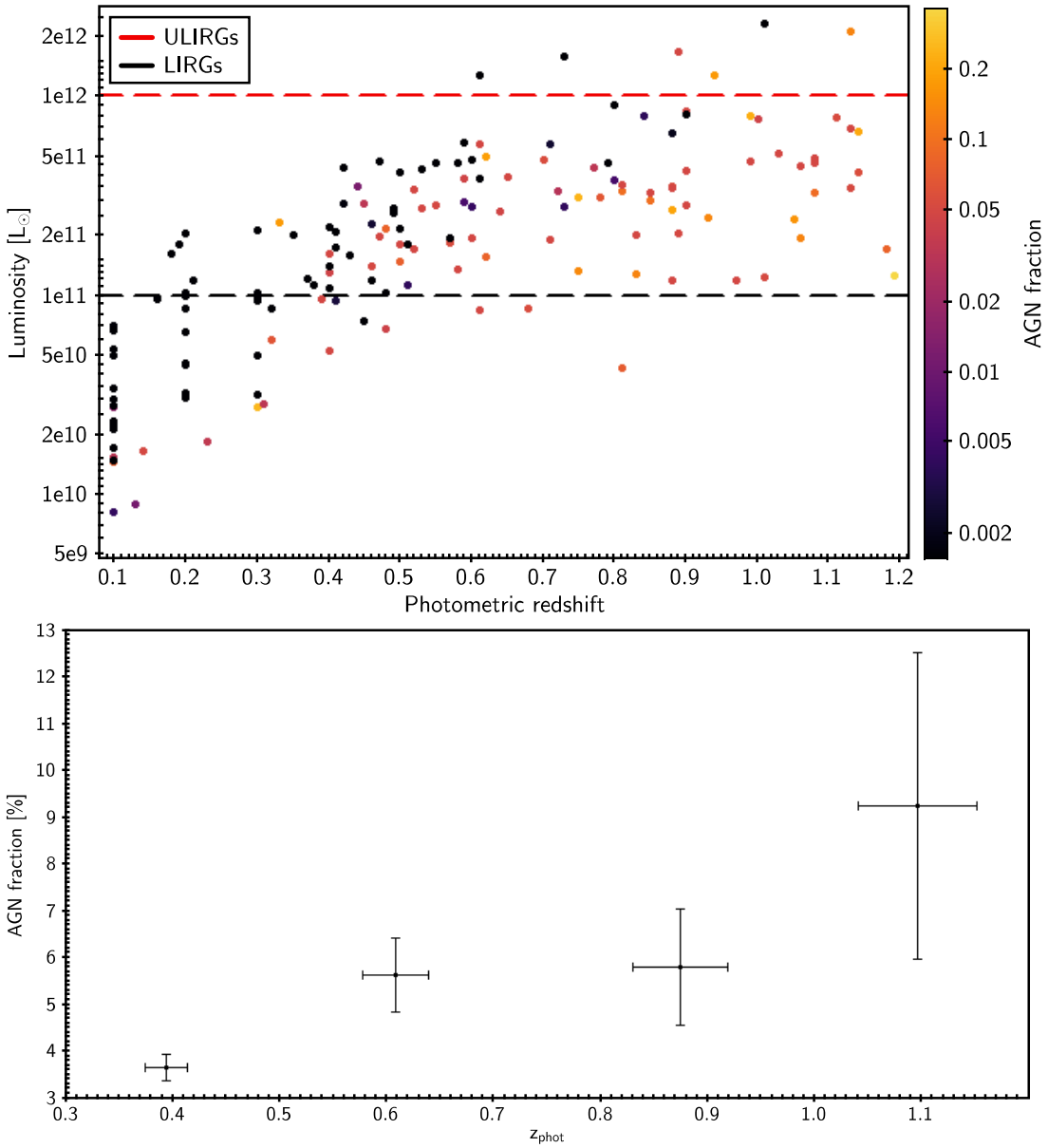

Figure 4.8: (Top) Infrared luminosity - corrected for AGN contribution - against the photometric redshift presents a correlation that stabilizes after $z \sim 0.5$. The sample is divided by luminosity in the plot, where the black dashed line shows the limit for LIRGs and the red line shows the limit for ULIRGs ($L_{IR} > 10^{12} \cdot L_{\odot}$) . The AGN fraction is given in the third axis; it has a trend with either luminosity and redshift: at higher AGN fraction in this sample, higher is the redshift and the luminosity. The photometric errors are between $0.005 < ez_{phot} < 0.06$, whereas the uncertainty in the IR luminosity correspond to the 11 % of the value on average. (Bottom) AGN fraction against redshift (with four redshift bins) for the LIRGs subsample.

The classification of the 169 radio sources is non-HLIRGs, 4% of ULIRGs, 66% of LIRGs and 24% of lower luminosity. It relates to the redshift nature of the sample: ULIRGs are rare sources but with higher presence in the high-z Universe. Since the

radio sample is restricted in redshift, it is expected that there are larger numbers of luminous galaxies in the entire sample of ∼1300 sources. This is corroborated with average redshift; for the higher luminosity sources are on average at higher redshift: $z_{ULIRGs} = 0.88$, $z_{LIRGs} = 0.66$, whereas for the lower luminosity sample is $z = 0.26$.

The radio-SFR conversion allows to convert the IR luminosity in radio luminosity (Condon, 1992) due to the FIR-radio correlation showed in Figure 4.22, where the radio-infrared correlation span a reasonable range of SFRs for star forming galaxies. Following the same procedure that was followed for the FIR-radio correlation, a source with $F_{1.4GHz} = 1$mJy at z=0.3 would have a radio luminosity of $2.6 \cdot 10^{23}$W/Hz. According to the conversion used in (Serjeant, Gruppioni & Oliver, 2002, equation 2), this luminosity would correspond to a SFR $\sim 300 M_{\odot}/yr$ which is well within the range for starburst galaxies.

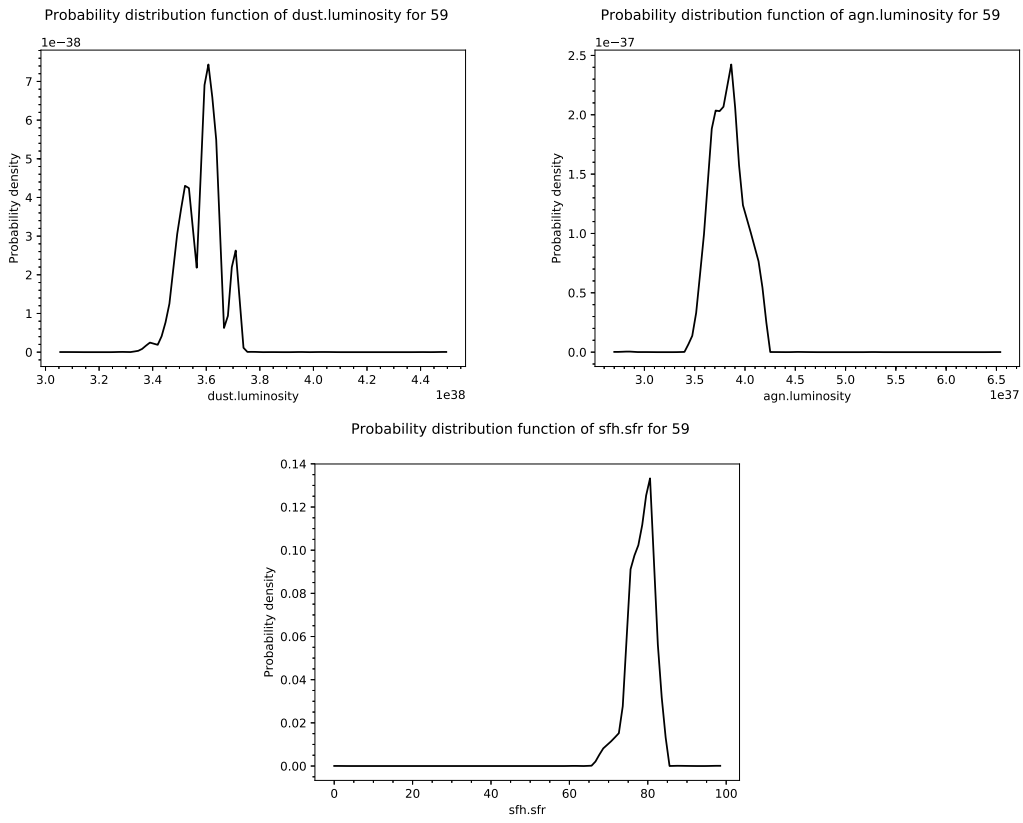

Figure 4.9: (Top) PDFs of the dust luminosity corresponding to the infrared $(8-1000\mu m)$ and of the AGN luminosity that corresponds to the estimation of the AGN contribution. (Bottom) PDF of the SFR for the same source (ID=59). In this example the Bayesian values are: $L = 3.58 \pm 0.18 \cdot 10^{18}$ W, $L_{AGN} = 0.38 \pm 0.02 \cdot 10^{18}$ W $M = 78 \pm 4$ $M_{\odot}/yr$ respectively

There is evidence that shows the presence of an AGN can regulate the properties of the galaxy, and it is key to study galaxy properties (Bower et al., 2006). This radio sample contains some evidence of AGN activity in 56% of the sources in order to fit with CIGALE, but in only 4% are the AGN dominant, contributing to the galaxy between 20% and 38%. The average AGN fraction for the total sample is 7% and the explanation of this unexpected low AGN contribution is the low radio flux. Generally in the sample the AGN fraction shows a trend with either luminosity and redshift: at higher AGN fraction in this sample, higher is the redshift and the luminosity. In order to evaluate this possible correlation, the LIRGs sample was selected (in order to avoid Malmquist bias) and 4 redshift bins were produced, showing that there is a correlation between the AGN fraction and the redshift. (see Figure 4.8). However, the AGN fraction is not dominant in the total sample and the percentages are lower than 10%. It is necessary to evaluate the sample by luminosity: both ULIRGs and sources with $L_{IR} < 10^{11} L_{\odot}$ show 50% of AGN presence, whereas LIRGs have the highest AGN presence of the sample (59%) and galaxies at lower luminosities contain the lower AGN presence (42%). Regarding the AGN contribution in each subsample, it is six, five and two percent for ULIRGs, LIRGS, and lower luminosity sources respectively. Therefore in this sample the AGN presence is not related to the luminosity, however, at higher luminosity, the sources that host an AGN the contribution of the AGN is two to three times stronger than the less luminous galaxies.

There is currently no agreement on whether AGN trigger or quench star formation, while studies as Barger et al. (2015) suggests that the star formation can be suppressed by the AGN, other authors infer the opposite (e.g. Juneau et al., 2013)). However, it is accepted that both phenomena should be related (e.g. $\sigma - M_{SMBH}$, the empirical correlation between the stellar velocity dispersion of a galaxy bulge and the mass of the super massive black hole) and there is a similarity between the growth of the AGN and the star formation history (see Figure 1.7 in Introduction). The star formation history (SFH) chosen is the delayed module in CIGALE which assumes a star formation rate that decreases exponentially over cosmic time. The SFR resulting from CIGALE

	ULIRGs	**LIRGs**	$L < 10^{11} L_{\odot}$
Percentage of sources	4%	66%	30%
AGN presence	50%	59%	42%
Average of AGN fraction	6%	5%	2%
SFR [$M_{\odot}$/yr]	143	26	3.8
M_* [$M_{\odot}$]	$4.8 \cdot 10^{11}$	$1.43 \cdot 10^{11}$	$5.19 \cdot 10^{10}$
M_{gas} [$M_{\odot}$]	$3.5 \cdot 10^{11}$	$1.1 \cdot 10^{11}$	$4.14 \cdot 10^{10}$
Photometric redshift	0.88	0.66	0.26

Table 4.2: The Table shows the main parameters analysed by the IR luminosity classification: ULIRGs, LIRGs and lower infrared luminosity galaxies, showing that the dominant population is a high infrared luminosity (LIRGS). More than half of the sources need some AGN contribution for the fit, however they present low AGN fractions, which means they are not AGN dominated. The SFR which is significantly higher in higher luminosity sources as it was expected. The stellar mass and gas mass is one order of magnitude higher in high infrared luminous galaxies, which can indicate that the higher luminosity and SFR can be due to the high stellar emission.

clearly depends on the models introduced on the star formation history (SFH), therefore I chose a common SFH that is representative of moderate redshift galaxies with no starburst population. The SEDs and the PDFs are robust (see Figure 4.9), which shows that the SFH chosen is self-consistent and the population does not have extreme star formation (Ciesla et al., 2016). The star formation rate of the radio sources is low, $SFR = 24 \pm 4 [M_{\odot}/yr]$ on average, probably due to the lower redshift sample. SFR is proportional to the far-IR luminosity, therefore ULIRGs have the highest value of the sample with $SFR_{ULIRGs} = 143 \pm 4 [M_{\odot}/yr]$, more than 5 times than the LIRGs and 37 times more than the rest of sources. Another parameter to measure the star formation activity of the galaxy is the star formation efficiency (SFE), which relates the SFR with the amount of gas in the galaxy: $SFE = SFR/M_{gas}$. Since the ratio of these two parameters is scale-independent, it was expected to find a proportional plot, however, while the mass of the gas correlates with the luminosity for all the redshifts, the SFE do not correlate in the same way (see Figure 4.10). This could shows that there is another parameter that triggers star formation. In fact, ULIRGs are nearly three times more effective at forming galaxies than sources with low infrared luminosity.

I evaluated the role of the PAHs in star formation through the comparison be-

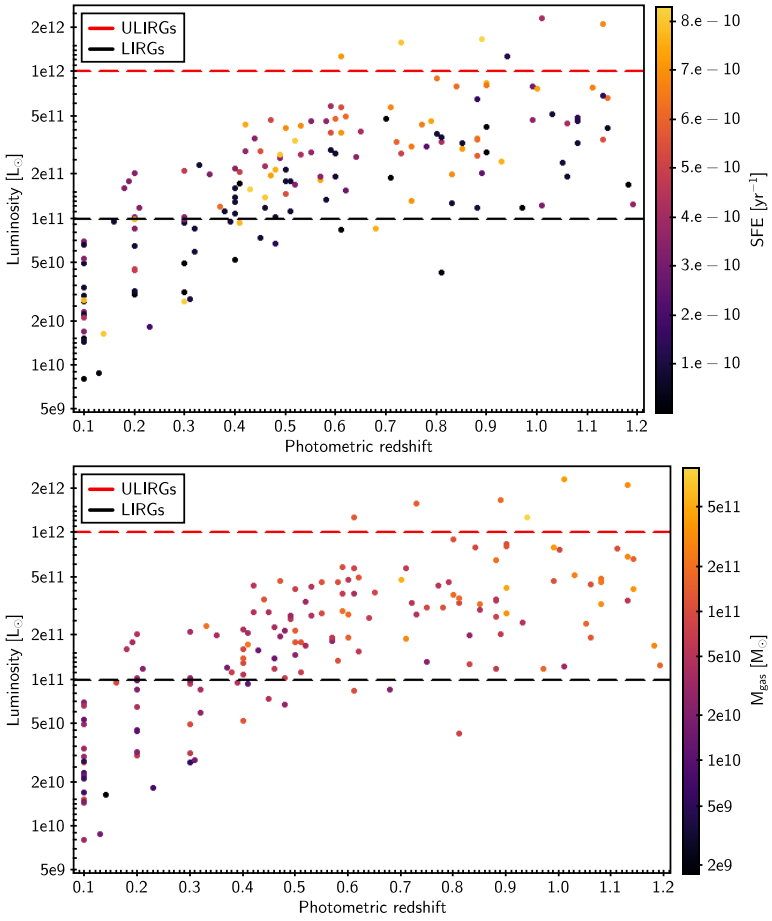

Figure 4.10: Comparison between the mass of the gas (left) with the star formation efficiency (right) by plotting the infrared luminosity [$L_\odot$] against redshift. The SFE is defined as the SFR/Mgas therefore it is expected to find a proportional plot. However, while the mass of the gas is proportional to the luminosity of the galaxy, the star formation efficiency does not follow the same proportion. It can indicates that the star formation is related with another mechanism and not only with the gas of the galaxy. The photometric errors are between $0.005 < ez_{phot} < 0.06$, whereas the uncertainty in the IR luminosity correspond to the 11 % of the value on average.

tween luminosity and PAH fraction (see Figure 4.11). There is no clear correlation between the luminosity of the galaxy and the presence of PAHs. However, on average ULIRGs appear to have only about half of the PAHs than galaxies with luminosity below $10^{11} \cdot L_\odot$ which together with the higher redshift of this subsample (see Table 4.2), indicates that part of the high luminosity could came from AGN activity instead of star formation.

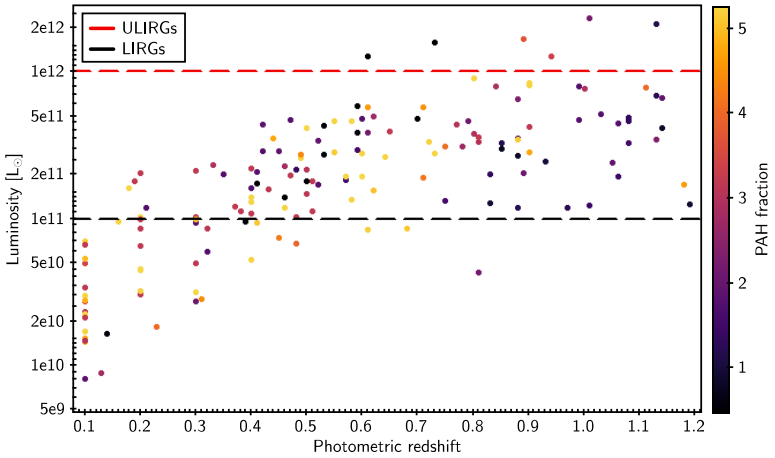

Figure 4.11: The plot shows the infrared luminosity against photometric redshift with the PAHs fraction in the third axis. There is no clear correlation between PAHs and infrared luminosity neither with redshift. However, on average the ULIRGs - sources above the dashed red line - appear to have only about half of the PAHs that galaxies with $L_{IR} < 10 \cdot 10^{11} L_{\odot}$ (sources below the dashed black line) The photometric errors are between $0.005 < ez_{phot} < 0.06$, whereas the uncertainty in the IR luminosity correspond to the 11 % of the value on average.

4.5 Infrared colour-colour diagrams to classify AGN.

The aim of this section is to find an effective c-c diagram with AKARI colours to classify AGN in the NEP.

The mid-infrared (MIR) bands are commonly used for this purpose due to the fact that they are sensitive to the physical processes that occur when a galaxy hosts an AGN. The radiation emitted by the accretion disk is absorbed by the surrounding dust and thermally re-emitted at longer mid-IR wavelengths which the peak of emission around $20-30\ \mu$m. This clearly peaks at shorter wavelengths compared to the emission from the heated dust from stars. Furthermore, due to the intense radiation, the AGN spectrum has an approximately power-law behavior in the MIR, without PAHs features due to the impossibility to form them (and the destruction) in the presence of hard radiation fields. Furthermore, the MID intensity dominates the SED of most galaxies in these wavelength range, which make these range of the spectrum unique to distinguish between AGN and galaxies (see Figure 4.12).

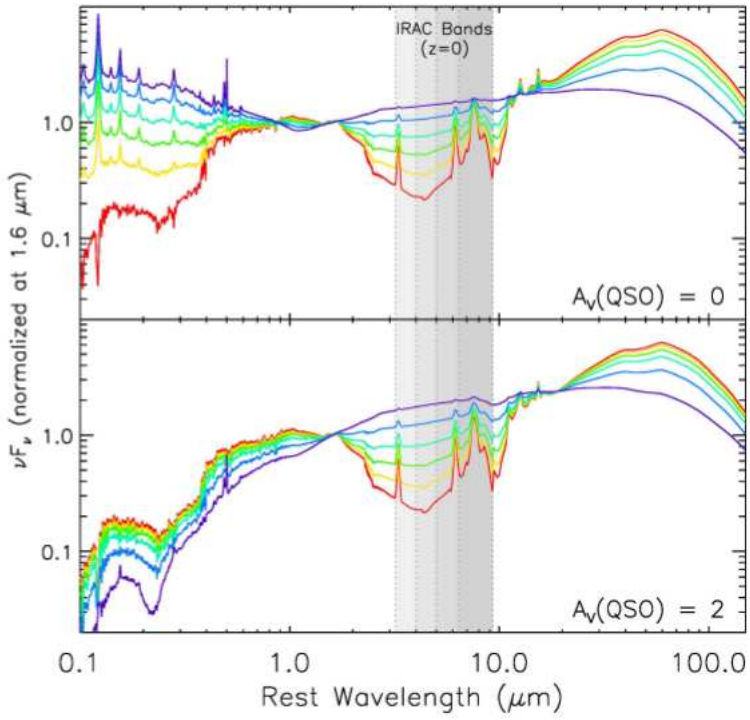

Figure 4.12: The plot shows several SEDs highlighting the IRAC bands in gray (3.6, 4.5, 5.8 and 8.0 μm) which lie in the part of the spectrum where the PAHs are located (extracted from Donley (2012)). The red line shows no AGN presence - with the characteristic PAHs features- whereas the purple SED is highly AGN dominated with the characteristic power-law thermal continuum across the four IRAC bands. This part of the spectrum - between 2 and 10 μm in the rest-frame wavelength - is the most distinctive between this population and makes it easy to use the colour to classify AGN candidates.

Colour-colour diagrams have been shown to be effective at segregating population with IRAC/Spitzer data (Donley, 2012) as well as WISE data (e.g. Lake et al., 2012; Mingo et al., 2016)). There are several examples in the literature following the same principle of combining IR colours with the best data available in each field (see Table 4.3 for compilation). However, the only data available in the NEP to perform an infrared AGN classification are from WISE and AKARI (IRAC/Spitzer data in the NEP have been incorporated recently, see Future work 6.2.3).

The AKARI data are particularly comprehensive in the NEP (see Introduction 1.3.2). Although the AKARI data have not been regularly used in the selection of AGN candidates, there are numerous studies where WISE data have been used, since WISE covers the whole sky and the bands are broad. There are differences between the

AKARI and WISE bands, especially the broad-band WISE3 filter, however, approximate equivalences of the AKARI and WISE bands can be found (see Figure 4.13).

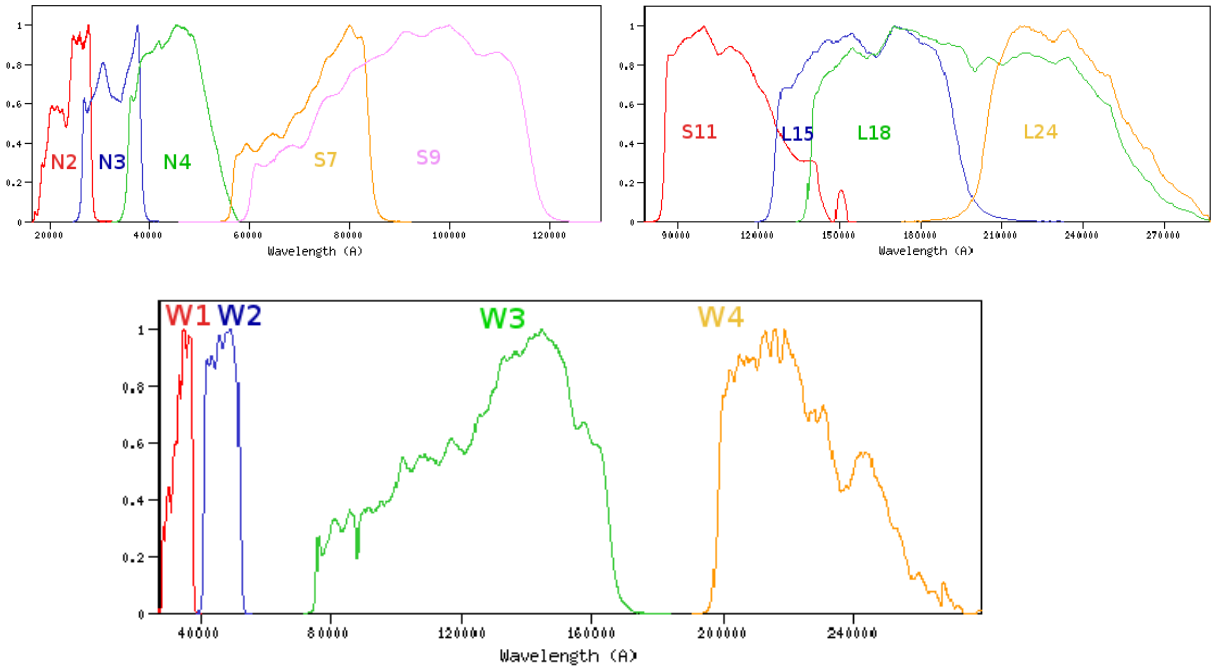

Figure 4.13: The two plots on top show the transmission curves of the nine AKARI filters (left) N2, N3, N4, S7, S9W (at 2.2, 3.2, 4.4, 7.3, 9.2 μm) and (right) S11, L15, L18W, L24 (at 10.9, 16.1, 19.8, 23.3 μm) whereas the plot on bottom shows the four WISE filters: W1, W2, W3, W4 (at 3.4, 4.6, 11.6 and 22 μm) WISE filters are commonly used in colour-colour diagrams to classify AGN and the equivalent - or similar - AKARI bands can be used instead of WISE: W1 for the N2 or N3, W2 for N4, W3 for S11 or S15 and W4 for L18 or L24.

Reference	Data	Diagram (criteria)
(Lacy, 2004) (Lacy, 2007)	IRAC/Spitzer	I4/I2 vs I3/I1
(Stern et al., 2005) (Stern, 2012)	IRAC/Spitzer IRAC/Spitzer & WISE	I1 – I2 vs I3 – I4 W1 – W2 vs I3 – I4 (W1 - W2 > 0.8)
(Donley, 2012)	IRAC/Spitzer	Combine (Lacy, 2004) & (Stern et al., 2005)
(Mingo et al., 2016) (based on Lake et al. (2012))	WISE	W1-W2 vs W2-W3 (W1 – W2 $\gtrsim$ 0.5 & W2-W3 < 4.4)
(Baronchelli, 2015)	Spitzer/MIPS24 AKARI (N4, N3, S7, L15)	(MIPS24 + L15)/S7 (N4/N3 > 0.2)
(Assef et al., 2010)	WISE	W3 - W4 > 2.1 W1 - W2 > 0.85
This work	AKARI	N4 N2 S7 S11 N2 - N4 > 0.1 and 1.5 > S7 - S11 > 0

Table 4.3: Compilation of the main colour-colour diagrams used for AGN selection which to date have mainly used Spitzer and WISE data (the divisions indicates the use of fluxes and the subtraction the use of AB magnitudes). The use of Spitzer/IRAC and WISE is well-established for classifying AGN, however AKARI data are not commonly used in the literature and that is one of the results presented in this thesis. The first 3 bands of WISE are used: W1 (3.4μm), W2 (4.6μm), W3 (11.6μm) and the 4 Spitzer IRAC bands are used: I1 (3.6μm), I2 (4.5μm), I3 (5.8μm), I4(8μm and Spitzer/MIPS (24μm). The AKARI bands used are: N3 3.3μm, N4 4.4μm, S7 7.3μm and L15 16.5μm).

I studied the possible AGN classifications in the NEP using both WISE and AKARI data and comparing with the spectroscopic classification available in the field in order to check their effectiveness.

WISE is an all sky survey (Wright et al., 2010), specifically, in the NEP it contains 119,040 sources whereas the equivalent area of the AKARI wide field catalogue contains 114,794 (Kim et al., 2012). The NEP-Wide AKARI catalogue reaches the 5 σ detection limit of $\sim$21 magnitudes (Kim et al., 2012), whereas the WISE catalogue in this area reaches $\sim$19 magnitudes for similar bands (Wright et al., 2010). Furthermore, AKARI has 5 filters more than WISE in the same wavelength coverage, which make it unique for the AGN selection (see Introduction 1.1.2 for details).

Since the aim is to compare the efficacy of the WISE and AKARI data in select AGN, it was used two catalogues that cover the same area. The deeper AKARI catalogue was not used because it only covers the deep field and the sample for the comparison will be smaller. However, as future work, the results can be extend to this deeper catalogue. Furthermore, spectroscopic data were used - both spectroscopic redshift and optical lines - that cover the NEP-Wide field, this comprises a total of 1796 sources (Shim et al., 2013), where the sources as classified as follows:

- 13% AGN
- 64% galaxies
- 5% stars
- 19% unknown lie throught out the survey field. The spectra did not have enough reliable lines to make a classification.

In order to compare with the spectroscopic data, both catalogues - AKARI and WISE - were cross-matched with a 1 arcsecond searching radius with the spectroscopic catalogue, finding 1379 and 1271 identifications respectively. In both cases the number of AGN sources (using the label of the spectroscopic catalogue) are similar, with 12%

and 13% of the AKARI and WISE sample respectively, which is similar to the original spectroscopic catalogue.

Firstly, the WISE catalogue with spectroscopic data was selected in order to ensure that the sources follow the same classification as in Lake et al. (2012), discarding mismatched associations between WISE and the spectroscopic catalogue. Figure 4.14 shows that WISE data follow the expected trend and it will assure a reliable comparison between AKARI and WISE data effectiveness to classify AGN. The galaxies are extended in the lower part of the colour-colour plot whereas the AGN are located in the upper part. The 19% classified as unknown for the lack of a clear spectroscopic line, lie randomly over the diagram and therefore, they were not represented in the diagram to avoid confusion. The colour-colour classification has limitations and sources can be misclassified, but they follow a general trend that is useful for big sample classification.

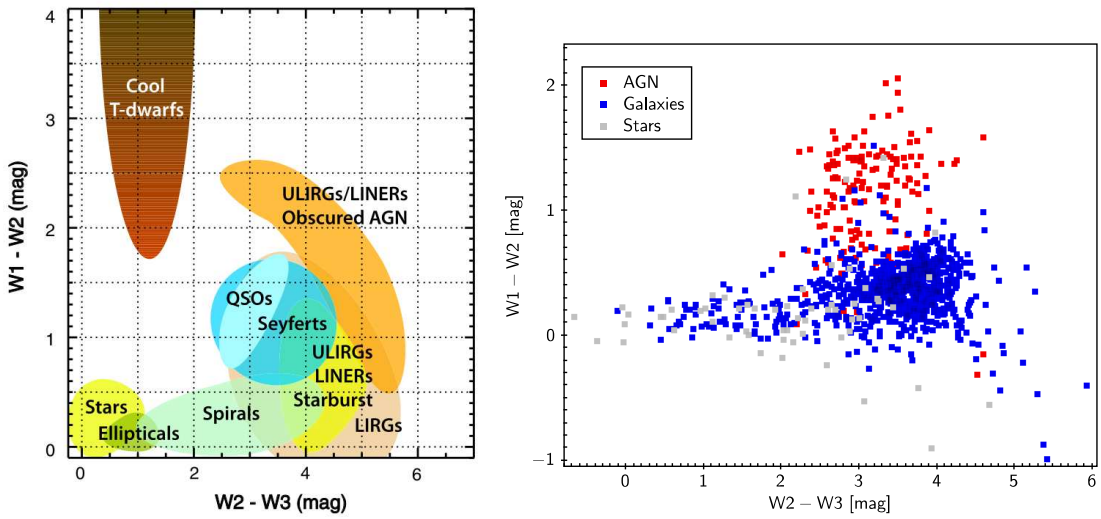

Figure 4.14: (Left) WISE colour-colour diagram that uses W1, W2, W3 to classify sources, finding that the AGN lie in the upper left part of the digram (Lake et al., 2012) also used for Mingo et al. (2016). (Right) The same colour-colour diagram with spectroscopic classification by Shim et al. (2013): galaxies are plotted in blue, AGN in red and stars in grey. The diagrams are in agreement, confirming both the reliability of the classification with WISE data and the spectroscopic classification of the sources.

The colour-colour diagram (W1 - W2) vs. (W2 - W3) was plotted with the complete NEP WISE catalogue following the selection criteria from Mingo et al. (2016) that were applied to both the total sample and the subsample with spectroscopic data

(see Figure 4.15). In the total WISE sample, there are 20250 AGN candidates (17% of the NEP WISE sample) that follow the criteria $(W1-W2) \gtrsim 0.5$ and $(W2-W3) < 4.4$, whereas in the WISE subset that has been cross-matched with the Shim et al. (2013) catalogue, the AGN fraction is 33% (415 of the total 1271). This difference in percentage could be due to the fact that part of the focus in Shim et al. (2013) is the study of AGN. After comparing with the spectroscopic data, these 415 sources classified as AGN by the WISE colour-colour criterion, are classified spectroscopically as follows:

- 33% AGN
- 46% either stars or galaxies
- 17% unknown

Therefore, the criteria applied in the NEP could be only ever be valid up to the 64% of the sample, since the classification fails for 46% of the sources. This could be due to the colour-colour cuts proposed in Mingo et al. (2016) only being indicative and the clear overlaps of between different populations. This could be due to the AGN cut selecting only very bright AGN, while faint AGN in hosts with star formation will not pass the colour-colour cut and they will occupy the same parameter space as the spiral galaxies.

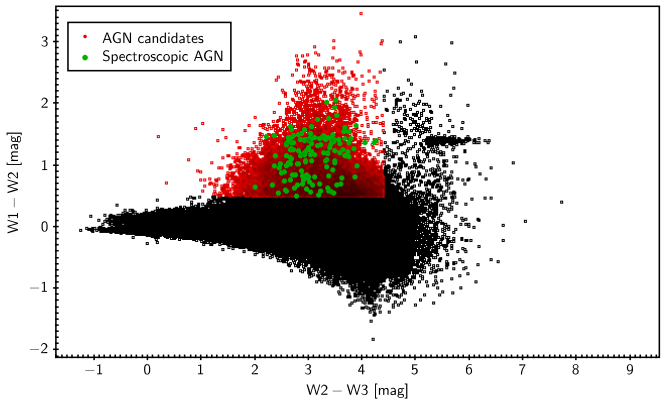

Figure 4.15: Colour-colour diagram with WISE data in the NEP: (W1 - W2) vs. (W2 - W3) like in Mingo et al. (2016) resulting 20250 AGN candidates - in red - by following the criteria $(W1-W2) \gtrsim 0.5$ and $(W2-W3) < 4.4$. Applying these criteria to the WISE sample cross-matched with Shim et al. (2013), 35% of the sources are classified spectroscopically as AGN selected (in green) and 17% unknown, therefore the classification fails for 46% either stars or galaxies).

The equivalent to the WISE diagram with the AKARI data (see Figure 4.13 for the transmission curves of the filters) was applied in order to produce an AKARI selection. The W1 (3.4μm) band was replaced with N2 (2.2μm) which, although it is centered at a shorter wavelength, is still sensitive to the possible power law spectrum (see Figure 4.13). The second band of WISE (4.5μm) has been replaced with N4 (4.4μm) because of the proximity of the wavelength and because it is broader than N3. Finally, the W3 11.6μm band, which is key in the AGN selection because of its breadth, could have been replaced with either S11 (10.9μm) or S15 (16.1μm) due to the breadth of this later filter. Therefore, I checked in both of them the position of the AGN classified with the spectroscopic data to decide which filter to use, concluding that the most similar result to WISE is the colour the S11 band (see Figure 4.16). This could be due to the fact that the closer the bands are, the more prominent power law spectra are that come from the AGN emission. However, the key part of the classification is the y-axis, where the colour $(\mathrm{N2}-\mathrm{N4}) > 0.1$ picks most of the AGN. These criteria used for the AKARI data result in the following classifications:

- 53% AGN classified sources with spectroscopic confirmation.
- 21% stars or galaxies.
- 26% as unknown because of the lack of reliable spectroscopic data.

Therefore, this criterion only fails in the 21% of the sources and it could have a reliability near to $\sim$80%.

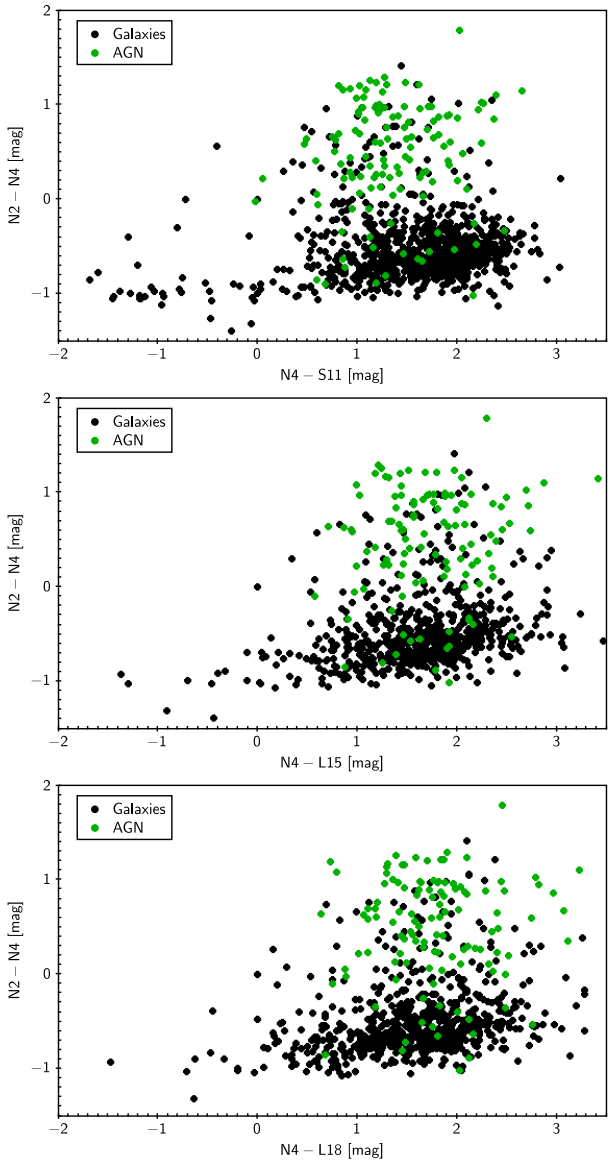

Figure 4.16: Comparison of colour-colour diagrams with the spectroscopic data: the y-axis is the equivalent to the WISE colour with AKARI data (N4 - N2) and the x-axis is the AKARI version of the W3 filter for S11, L15 and L18 respectively. The sources represented as AGN are plotted in green, whereas the galaxies of the sources are plotted in black. The key colour for the classification is the y-axis colour N2-N4. The difference between the three diagrams represented are not big, but the colour N4-S11 was better at located AGN, whereas the other two colours (N4-L15 and N4-L18) appeared more dispersed. For all of three effectiveness in selecting AGN is similar since the x-axis does not introduce a significant change in the selection.

The advantage of AKARI data is that is equipped with multiple filters, so I was able to look for another colour that can add another condition to the (N2 - N4) > 0.1 and improve the previous result of nearly 80% of effectiveness classifying AGN. The colour S7-S11 was used in previous sections of this Chapter following Shim et al. (2013) spectroscopic work and showing good results. Therefore, different colours were checked in the x-axis of the colour-colour diagram finding that shorter wavelengths better concentrate the AGN in a part of the diagram (see Figure 4.16). This condition set the power law condition at longer wavelengths, furthermore, it confines the spectroscopic AGN in the same region (see Figure 4.17). The optimum condition is - in addition to apply the previous condition $(\mathrm{N2}-\mathrm{N4})>0.1$ - the restriction $1.5>\mathrm{S7}-\mathrm{S11}>0$, where 69% of the sources are spectroscopically classified as AGN, decreasing the failure to 10% and therefore raising an effectiveness to 90%. The use of two different colours with close wavelengths (4.4 μm - 2.4 μm and 10.9 μm - 7.3 μm) allow me to identify two different parts of the mid-IR spaectra. This is a clear advantage respect to WISE, since with only four bands is not possible to select two colors with such as closer bands. The two colours allow to detect the prominent drop in galaxy emission and the power law spectrum in two different parts of the mid-IR (see Figure 4.12). This allow me to locate the AGNs in a narrow region in the colour-colour space (see Figure 4.17), which makes the selection more effective.

These results allow me to conclude that the most effective colour-colour selection is produced by these specific AKARI colours instead of the equivalent WISE bands. Furthermore, AKARI shows more higher completeness in classifying AGN than WISE due to the multiple band coverage in the near and mid infrared.

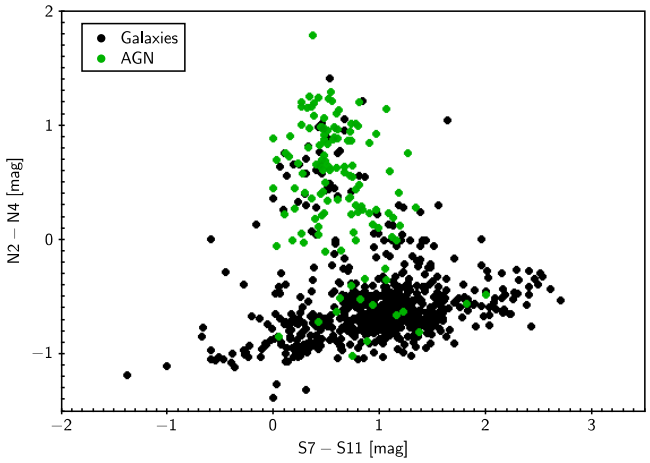

Figure 4.17: This Figure shows the most effective AKARI colour-colour diagram: N2-N4 colour against S7-S11, which confines the AGN with spectroscopic confirmation (in green) splitting them from the galaxies (black). Following the conditions N4-N2 > 0.1 and 1.5 > S7-S11 > 0 could classify correctly the 90% of the sources as AGN (69% are spectroscopic confirmed, 11% are classified as unknown and only fails in the 10% of the cases where the sources are spectroscopically classify as either stars or galaxies).

The most effective criteria found with AKARI bands (N2 - N4 > 0.1 and 1.5 > S7 - S11 > 0) was applied to the total AKARI sample (Kim et al., 2012) (see Figure 4.18) finding 704 AGN candidates in which only there are a 10% of contamination. So far, the previous results demonstrate that AKARI bands are able to classify AGN, possibly better than WISE data. This sample, together with other possible candidates using the deeper catalogue in the central area of the NEP (Murata et al., 2013) and the new Spitzer/IRAC data, will be object of further study (see Future work 6.2.3).

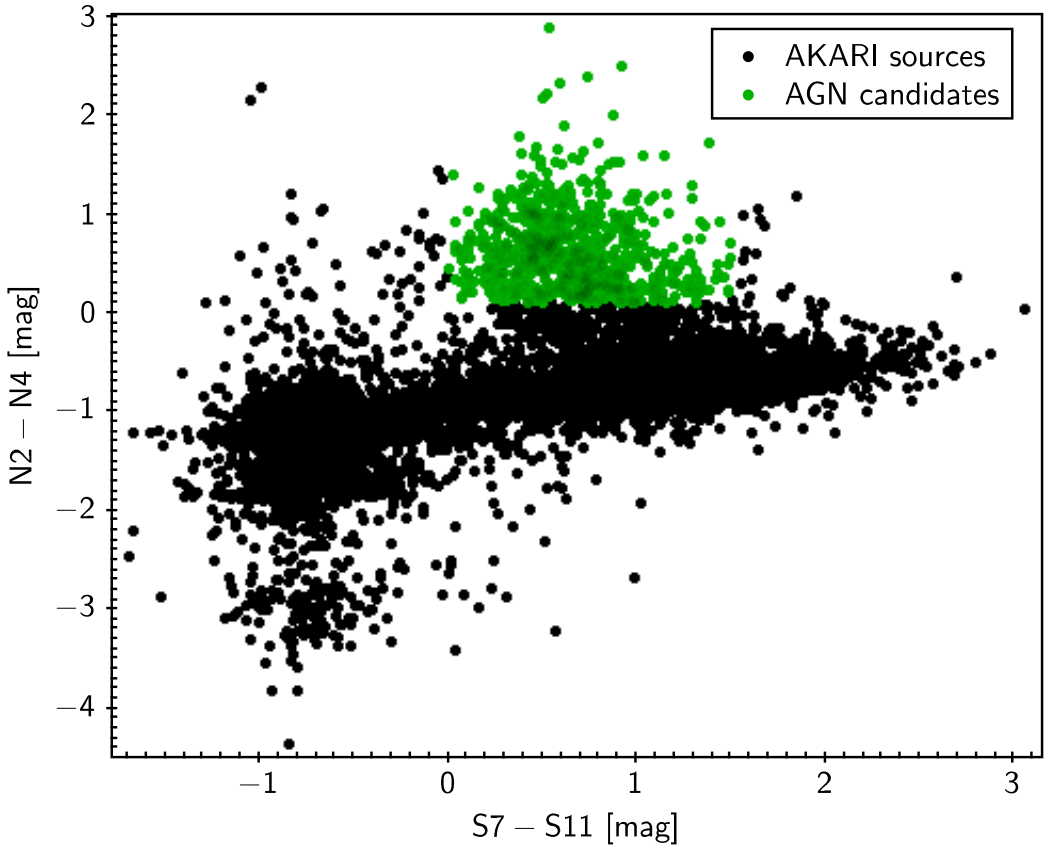

Figure 4.18: This Figure shows the most effective AKARI colour-colour diagram: N2-N4 colour against S7-S11 for the total number of sources in the AKARI catalogue (Kim et al., 2012) represented in black, with 704 AGN candidates represented in green.

Another selection criteria was examined, such as in the Baronchelli (2015), which follows N4/N3 > 0.2 and which only classify 11% of the sources as AGN and fails in 71% of the sources. However, before producing the study of AGN in the NEP, this selection criteria were used in a spectroscopic proposal for the SALT telescope where the OU was awarded with three hours of observation time. Unfortunately the observations could not be scheduled due to the weather. Since the objective was to obtain the largest number of AGN candidates, several mid-IR colour-colour criteria were applied, including the criteria of Baronchelli (2015), Lacy (2004), Stern (2012) and Donley (2012). There are plotted in the colour-colour diagram in Figure 4.19). This different results could be due to the fact than the Baronchelli (2015) sample spans different redshift and luminosity ranges and it is possible that different selections work better for different samples. The recent published Baronchelli et al. (2018) shows new

colour criteria that have been evaluated resulting in a more effective selection than Baronchelli (2015) and this will be evaluated as a future work.

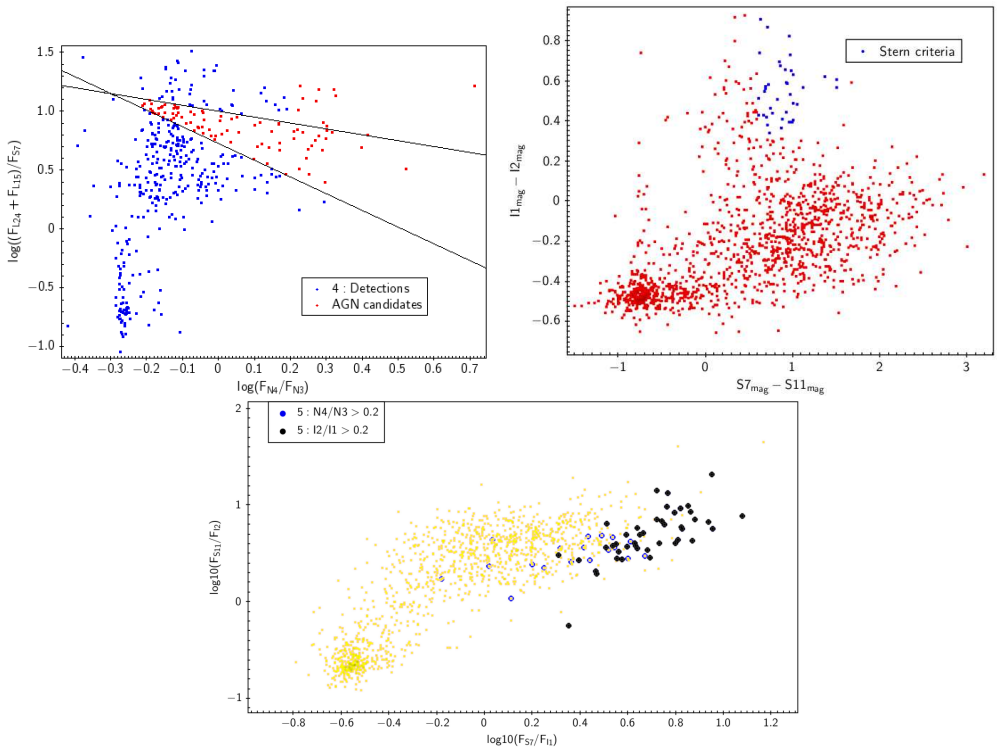

Figure 4.19: Draft plots used in the spectroscopic proposal submitted to the SALT telescope in 2015 illustrating the different IR colour-colour criteria used for candidate selection. The first plot uses five different mid-infrared bands and reproduce the criteria from Baronchelli (2015) . The second colour-colour diagram shows four different bands and the criteria for the selection are that the bands around $F_{\sim 4\mu m}/F_{\sim 3\mu m} > 0.2$ (Donley, 2012). The last diagram shows a diagram which uses four different bands following the Stern criteria (Donley, 2012).

4.5.1 Radio colour-colour diagram

The sample of 169 sources is representative of the microJansky population which makes that the AGN contribution is not dominant in the galaxy, although exists some presence. Therefore, I checked the association between the infrared selected AGNs and the AGN fraction value estimated from the radio sources by using the colour-colour diagram refereed to in Section 4.5. The Figure 4.20 shows that the N2/N4 colour is dependent of the AGN fraction extracted from the CIGALE analysis, however, the limit N2/N4 > 0.2 is conservative and it could be improved by taking into account radio data.

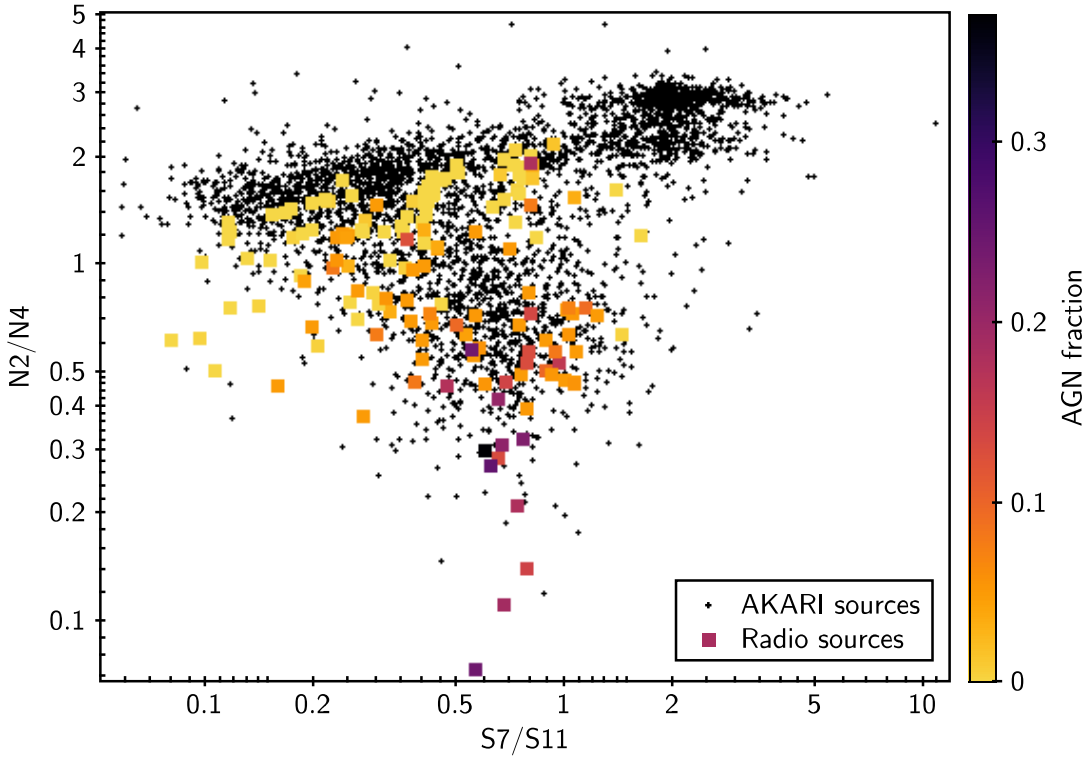

Figure 4.20: The figure shows a colour-colour diagram (N2/N4 vs S7/S11) with AKARI data (black diamonds) with the AGN fraction for the radio-sources (coloured rectangles). There is a trend of increasing AGN fraction for bigger N2/N4 colours, where lie the sources classified as AGN.

4.6 Radio-FIR correlation

This study is based on the catalogue obtained by cross-matching the AKARI data (Murata et al., 2013) with FIR data from Herschel (Pearson, 2018) and radio data at 610 MHz from an unupdated version of the GMRT catalogue (the new version will be public in White (in prep.)), in the NEP Deep field. These catalogues were cross-correlated by positional matches using an optical catalogue as a reference and half of the synthesized beam size as a search radius. I also adopted a nine arcseconds search radius for the SPIRE catalogue using the 250μm position and four arcseconds for the radio position. Furthermore, a photometric redshift catalogue (Oi, 2014) was included, aiming to both study the radio sources and calculate the luminosity.

There is evidence for the FIR-radio correlation in other data sets (Ivison et al., 2010). This correlation was checked for all the AKARI and Herschel bands. Although there is not a clear correlation for most of the bands, a clear correlation between the radio flux and the $F_{250\mu m}$ is found (see Figure 4.21), which is why the study was focused on those bands. The plot shows that the radio fluxes are one order of magnitude fainter than the FIR fluxes, however, there are a few sources in the upper left part of the diagram with high radio flux - a radio excess - that are presumably radio-loud AGN and will be the subject of further work.

The FIR and radio luminosities were calculated by using the photometric redshift from Oi (2014) and it shows a strong correlation similar than the flux correlation (see Figure 4.22).

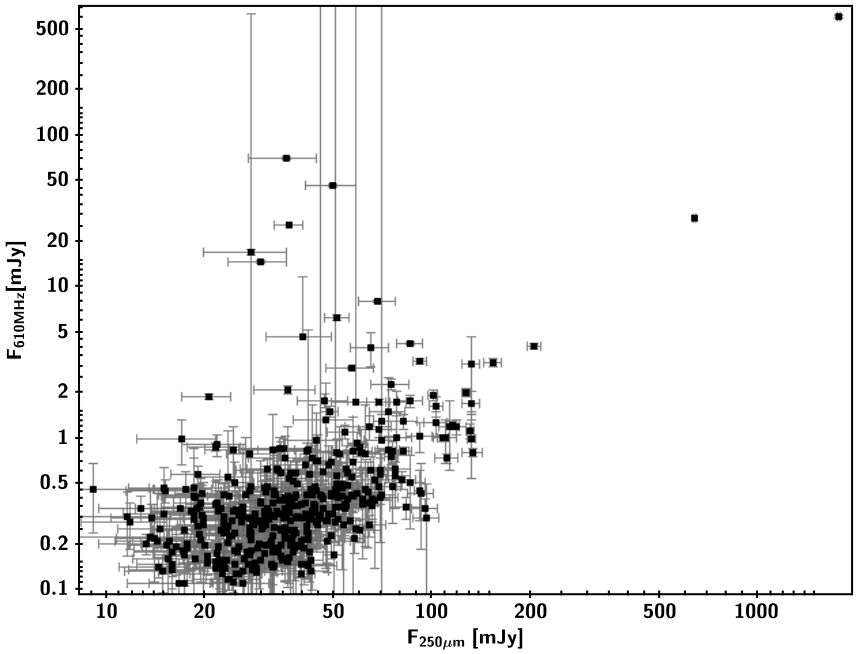

Figure 4.21: The Figure shows the Herschel 250μm flux against the radio flux at 610 MHz, which is the best correlation of the radio data with the other IR and submillimetre wavelengths. The radio flux is one order of magnitude smaller than the FIR flux, however, there are some sources with radio excess in the upper left part of the diagram.

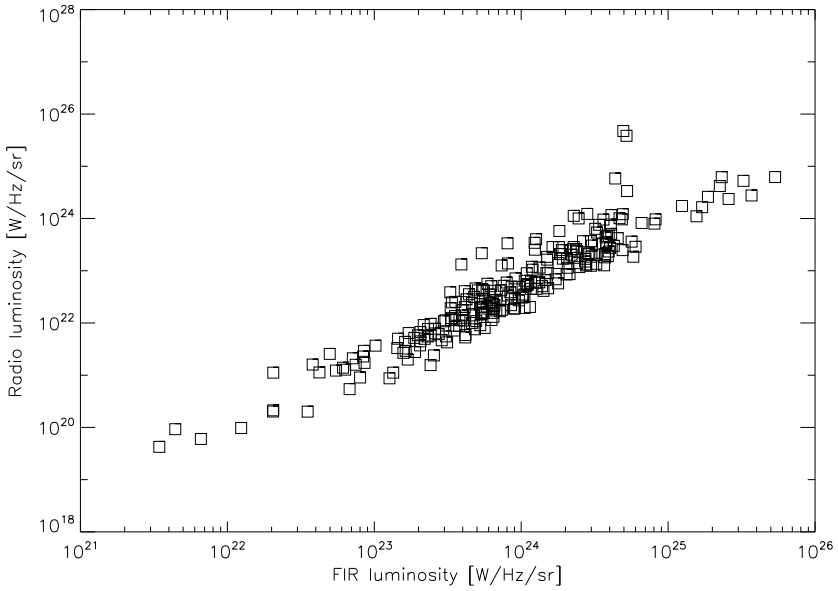

Figure 4.22: The Figure shows the FIR luminosity against the radio luminosity which shows a correlation.

4.7 Spectral index

To further examine the FIRC, the FIR-radio spectral index $\alpha_{250\mu\mathrm{m}}$ was introduced by using an adaptation from Vlahakis, Eales & Dunne (2007): $\alpha_{\mathrm{FIR}} \propto \log\left(\frac{\text{Flux (250 }\mu\text{m)}}{\text{Flux (1.4 GHz)}}\right)$ The first step was to remove the Active Galactic Nuclei (AGN) contamination using an approach based on IR colour-colour diagrams. This method has been demonstrated to be effective at other wavelengths than the IR AKARI bands (Donley, 2012). I applied different IR colour-colour diagrams as used in the literature (Lacy, 2004; Stern, 2012) using the AKARI data (Murata et al., 2013) instead of WISE data. The optical positions were cross-matched with the 610 MHz GMRT detections based on the five arcseconds search radius, which has allowed me to identify a sample of 45 radio AGN candidates. These were then removed from the total sample of radio sources in order to study the FIRC.

The spectral index was plotted against photometric redshift and there is no apparent evolution with redshift (see Figure 4.23). Vlahakis, Eales & Dunne (2007) finds the opposite result at longer submillimetre wavelengths (850μm), showing that the relation between submillimetre and radio can change due to the higher presence of cold dust. However, at 250μm the correlation between the FIR-submm and radio is the same at any redshift, probably due to the the K-corrections at 250μm and radio are not sufficiently different for any evolution in α_{FIR}.

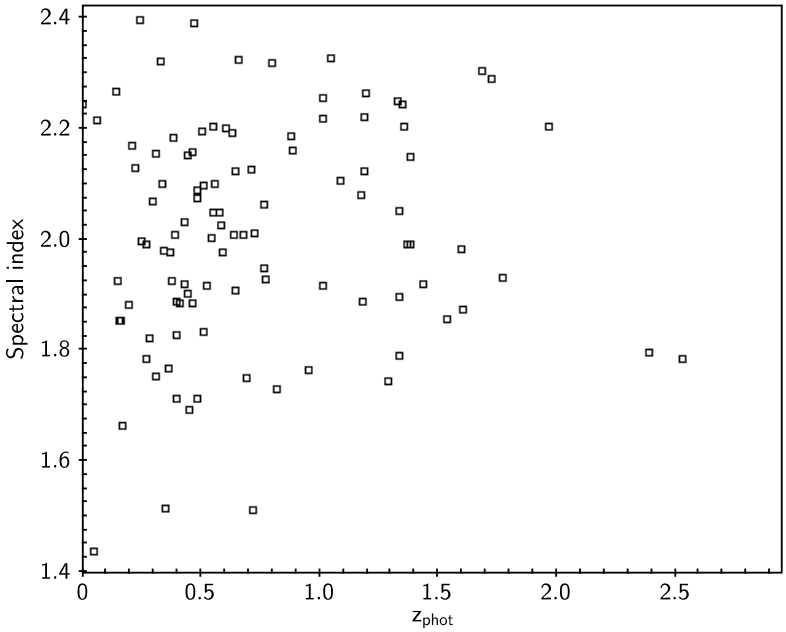

Figure 4.23: This Figure shows the radio-FIR spectral index against redshift; there is not an obvious evolution of the FIRC with redshift, where the errors in the photometric redshift are lower than ± 0.11 for $z_{phot} < 1$ and ± 0.15 for $1 < z_{phot} < 2.5$ on average, but the errors are not given in the catalogue (Oi, 2014) and the uncertainty spectral index is on average 20 %.

4.8 Radio flux - colour diagrams

The aim of this Section is to find a colour redshift indicator for the radio sources in our sample. There is evidence that the combination of data sets at different wavelengths may be a useful method for finding redshift indicators (Magnelli et al., 2015).

I combined the optical-IR colours and radio luminosity fluxes and tried different colours taking into account a SED evolution with redshift. The colour that splits the redshift most effectively, is the difference between the R-band and the N2 AKARI band (2.4μm), which shows higher redshifts when the difference of colour is bigger than 1 (see Figure 4.24), which can have been applied in other sample, since this property is independent of the radio flux. However, it shows once more the effectiveness of using multi-wavelength data for extracting different information of the spectra.

The IR-optical colour can be used as a redshift indicator by plotting the radio flux

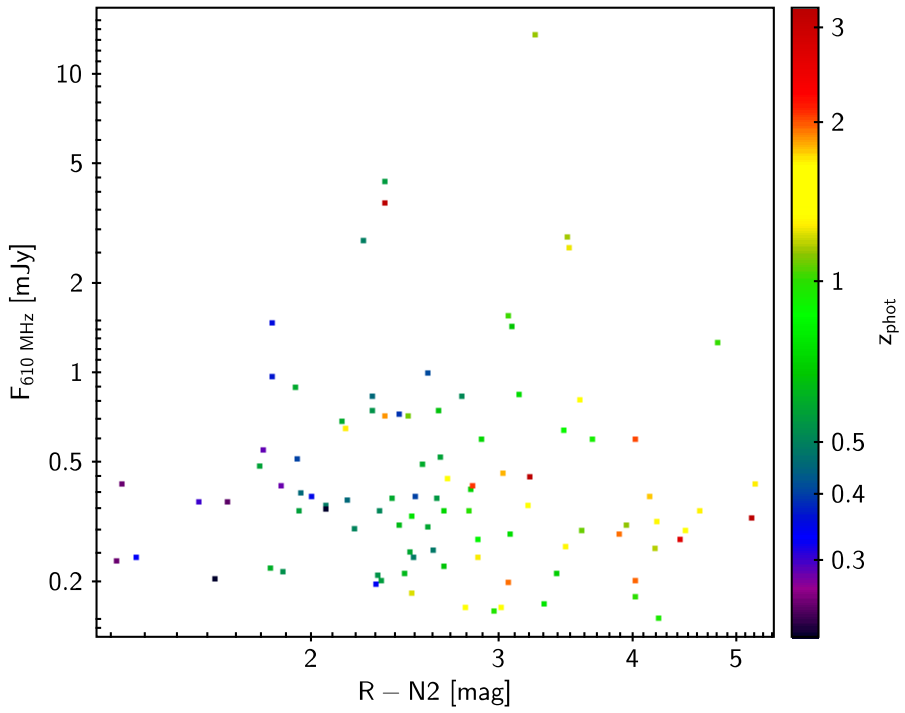

Figure 4.24: Flux colour diagram: radio flux against the colour R-N2 bands and redshift shown in the colour bar. The colour, can be used in this sample (and in other samples without radio emission) to split the radio-sources by redshift: larger colour differences indicate higher redshifts.

against the colour, where the higher redshift sources lie in the left hand part of the diagram (see Figure 4.24). This was a preliminary result and better methods were found to calculate photometric redshift as in Section 4.2. However, the grid of redshift in that section was defined from $5 > z > 0$ with a step δz=0.1 without any restriction. Finally, the distribution of redshifts in the sample is $1.2 > z > 0$, therefore, there was computing time wasted that can be optimized by using the R-N2 colour as redshift indicator - as a preliminary result - narrowing the redshift down.

4.9 Summary and conclusions

I developed a method to calculate photometric redshifts in radio samples by using a multi-wavelength approach which obtains better results than cross-matching the catalogue with ancillary redshift data.

This subsample is represented by the microJansky population and contains a moderate redshift distribution, however, there are some radio sources at $z_{phot} > 1$ and that it is expected to find higher redshift sources in the total sample. The radio sample is made up of sources with low radio fluxes and redshifts which clearly influences the AGN domination fraction.

The classification of the radio sample by infrared luminosity gives a high number of luminous sources: LIRGs represent 66% of the sample, whereas the ULIRGs are only 4% and sources with $L_{IR} < 10^{11} \cdot L_{\odot}$ are the remaining 30%.

The radio sample contains 56% of sources that require some AGN presence at some level for the SED fitting but only 7 sources are AGN dominated (AGN fraction > 20%). In most cases, the contribution of these AGNs is low, 4% on average and only a small part of the sample has AGN contribution bigger than 20%. Evaluating this property by L_{IR} shows that ULIRGs require three times more AGN contribution to produce the SED fitting than lower luminosity galaxies. The AGN presence was evaluated in the LIRGs population, showing an increasing trend of the AGN fraction with redshift that if continuous it would peak at $z \sim 2$, which is the peak of star formation and super massive black hole growth. The PAH concentration is not significant, however, on average ULIRGs appear to have only about half of the PAH strength than galaxies with lower IR luminosities, finding an expected PAH deficit in the most luminous sources which tend to be at higher redshift in the sample (Elbaz et al., 2011). This disagrees with the results in Chapter 4, probably due to the nature of the sample: in this Chapter the work was produced in a sample with radio emission, with a presence of AGN, whereas in Chapter 4 is a submillimetre selected sample. Therefore, it is something expected since the AGN emission destroys and make difficult the creation of the PAHs.

However, a bigger sample of ULIRGs with radio emission is needed to confirm this result.

As expected for the high luminosity, sources have clearly higher star formation than lower luminosity galaxies, concretely, ULIRGs, in this sample, have 37 times higher SFR than galaxies at $L_{IR} < 10^{11} \cdot L_{\odot}$ and they are three times more efficient at forming stars.

The gas mass (and the stellar mass) are one order of magnitude in higher luminosity galaxies (both LIRGs and ULIRGs) than in lower luminous galaxies. These higher masses indicate higher star formation rates, showing that the high luminosities could proceed from the star formation instead of an AGN presence. However, this idea is not straightforward and the mass of the gas does not have the same trend as the star formation efficiency which means that there is another - or more than one - factor that influences in the star formation. For the LIRGs there is an evolution of the AGN fraction with redshift indicating that at high IR luminosities (therefore at high SFR) the AGN presence is higher at higher redshifts. These results, together which the PAH deficit and the AGN fraction, indicate that part of the luminosity could be contributed from AGN activity instead of star formation. Therefore, I conclude that the main source of the high luminosity is the star formation, although it can be enhanced for AGN presence and the evolution of AGN fraction in LIRGs may be related in the coupling between AGN activity and stellar mass assembly.

Although the radio source populations are not distinguishable in the far-IR (*Herschel*) colour-colour space, the additional constraints provided by these longer wavelength colours can be used as an indicator of high redshift sources, classifying 268 high redshift candidates.

The mid-IR data is key to classify AGNs via colour-colour diagrams. I found that the AKARI data can be used for classifying AGN in a more reliable way than by using WISE data since they have 5 more bands in a similar wavelength coverage. I found efficient colour-colour criteria to classify AGN with AKARI data that could achieve a completeness of 90%. The criteria consist of using four different bands to create

two colours that identify the power-law characteristic of AGN: N4-N2 > 0.1 and 1.5 > S7-S11 > 0. The use of two different colours with close wavelengths (4.4 μm - 2.4 μm and 10.9 μm - 7.3 μm) detect the prominent drop in galaxy emission and the power law spectrum in two different parts of the mid-IR. This allow me to locate the AGNs in a narrow region in the colour-colour space.

A clear correlation is seen between the radio and the IR fluxes in the NEP Deep Field, for both low and high redshift objects. We have used this property to study the FIRC against redshift by estimating the spectral index. However, there is no compelling evidence for evolution of the spectral index with redshift. I do however find that a radio flux colour diagram that can be used as a redshift indicator.

Chapter 5

Optical catalogue of IR sources at the South Ecliptic Pole

Dust Obscured Galaxies (DOGs) are vital to the understanding of cosmological evolution of AGN and starburst phases. How many dust-obscured galaxies are consistent with having an AGN presence? If starbursts are shut down by AGN activity, then we might expect strong starbursts such as submm-galaxies to be the precursors of AGN systems. In this case, the relative durations would be reflected by their relative number densities. The population of dust-obscured galaxies are a possible candidate for the end result of the submm galaxy starburst phase. These optical data are vital for the identification of dusty submillimetre galaxies and has been applied both to the selection of DOGs and as a discriminator in the selection of potential submillimetre gravitational lens candidates. Due to their optical faintness and high infrared emission, DOGs are selected using both 24 μm *and R-band data (Dey et al., 2008). The AKARI Deep Field South (ADF-S) field is a unique multi-wavelength field with deep Spitzer-24* μm *data, but with a lack of optical data. This chapter reports on the production of an optical R-band catalogue that has been constructed from observations made on the CTIO telescope. This work was submitted to a MNRAS (Barrufet L., 2016) and the optical catalogue is publicly available on-line at www.vizier.com*

5.1 Introduction

Some of the most important advances to our understanding of galaxy evolution have come from coordinated multi-wavelength surveys. In particular, the *AKARI* Deep Field South (ADF-S), which is a region situated close to the South Ecliptic Pole (SEP), was selected as a legacy cosmological field as part of the *AKARI* mission (Murakami et al., 2007). The ADF-S is a natural extragalactic deep field location due to its excellent visibility for a wide class of space missions (e.g. *Herschel, AKARI, WISE, Planck, Euclid, eRosita*, etc.) and the fact that it is located in a region of exceptionally low extinction and a correspondingly low hydrogen column density ($\sim 5 \cdot 10^{19}\mathrm{cm}^{-2}$) (Schlegel, Finkbeiner & Davis, 1998; Bracco et al., 2011). The field was observed by *AKARI* several times per day, producing a deep far-infrared image of this area of the sky. These properties make the ADF-S an excellent field for the multi-wavelength study of distant galaxies. Although this field has been covered at many different wavelengths (see Figure 5.1), many of the catalogues have not yet been published and, most significantly, there is a still notable lack of optical data (see Table 5.1).

Optical identifications are crucial in order to confirm the nature of the sources, to estimate accurate photometric redshifts, and to derive the stellar masses M_*. In this sense, optical surveys are a fundamental means for interpreting multi-wavelength surveys.

Optical data are essential for the selection of infrared galaxy populations. In this chapter two specific populations and science cases are addressed: the analysis of strong gravitational lenses, where the optical data are required in order to discriminate contamination from local sources, and in the selection and identification of Dust Obscured Galaxies (DOGs; Dey et al. (2008)).

The angular and flux magnification due to strong lensing are very useful for the detection of intrinsically fainter objects and for resolving the physical processes operating in high-redshift galaxies (Swinbank et al., 2014). Although single-dish submillimetre telescopes have limited spatial resolution, combining these wavelengths with optical

data in order to rule out the contamination from nearby galaxies makes it possible to detect these high-z sources using a simple submillimetre flux criterion (Negrello, 2010). DOGs are extremely red galaxies, a particular subset of Ultra Luminous Infrared Galaxies (ULIRGs) showing faint optical emission (Sanders & Mirabel, 1996). Due to their optical faintness, these galaxies have been previously missed in traditional optical studies of the distant Universe. In this work, a simple flux criterion following Dey et al. (2008) and Pope et al. (2008), that combines IR and optical wavelengths, has been used to select DOG candidates.

Submillimetre galaxies (SMGs) and DOGs have similar properties (i.e. a similar redshift $z \sim 2 \pm 0.5$) (Chapman et al., 2005), which suggests that they might be related in an evolutionary sequence similar to that of ULIRGs in the local Universe (e.g. Sanders et al., 1988; Bussmann et al., 2012). Although their role in the story of galaxy evolution is not completely understood, it is likely that their high luminosities are the result of an extremely active phase, during which these systems form stars and/or grow their central black holes at a rapid rate (Sanders et al., 1988). Studying these populations therefore allows for the investigation of the evolutionary sequence of star-formation with cosmic time.

In this Chapter, R-band optical observations carried out with the Mosaic-I camera on the Blanco CTIO telescope in Chile are reduced and analysed to produce a new source catalogue at the SEP. The observations covered a region of $\sim$11 deg^2 centered at the ADF-S (RA$= 4^h44^m00^s$ and Dec$= -53^\circ20'00''$). In Section 5.2 the various observations obtained in this field are summarised. In Section 5.3 the data reduction processing techniques used to produce the final image mosaic of the field are described. The source extraction and photometry is explained in Section 5.4. In Section 5.5 the results and data products (all publicly available) are described. Section 5.6 details the criteria used to search for gravitational lens candidates and DOGs and reports on the detailed analysis of these populations. Finally, in Section 5.7 a summary of the results is given together with the proposed future work.

Throughout this Chapter, J2000 coordinates are used. A standard concordance

cosmology with $H_0 = 70$ kms^{-1}Mpc^{-1}, $\Omega_m = 0.3$ and $\Omega_\Lambda = 0.7$ is assumed. All photometry is on the AB magnitude system where 23.9 $m_{AB} = 1\mu$Jy.

5.2 Observations

5.2.1 Optical observations

The observations were made in the R-band, using the 4-metre Blanco telescope (Cerro Tololo Inter-American Observatory, Chile), in combination with the Mosaic-I camera in 2004 over the extended area and in 2007 over the central area (see Figure 5.10). The data were obtained over 3 and 4 individual nights respectively. Each telescope pointing (25 in total, see Figure 5.1) and Figure 5.10 shows the distinction between the extended and central region, which was covered by a set of 3-to-5 dithered exposures, for a total exposure time ranging from 400s to 3600s.

The Mosaic-I camera contains an array of 8 detectors - each of them is composed of two chips, therefore the camera contains 16 chips - with a $0.27''$ pixel scale. The detectors are separated by a $15''$ gap in both the X and Y axes with a projected pixel size of $0.258''$ (Muller et al., 1998). In total, the camera covers a field of view of 36×36 arcmin^2 area.

Given the filters available between 2004 and 2007, the filter used in the central area (R-band filter, R Harris c6004) is slightly different from that used in the extended area (R-band filter, r SDSS c6018) (see Figure 5.2).

The observations were nominally centered at the SEP at RA$= 4^h44^m00^s$ and Dec$=-53^\circ23'00''$. The central region (circa 2004) covers 1 deg^2 around these coordinates whereas the external region (circa 2007) covers approximately 10 deg^2 with a fan-shape. Note that some images were unsuitable (bad image, bad seeing, or other defects) resulting in gaps in the co-added final image (see Figure 5.10). These image tiles were not used in the production of the final source catalogue.

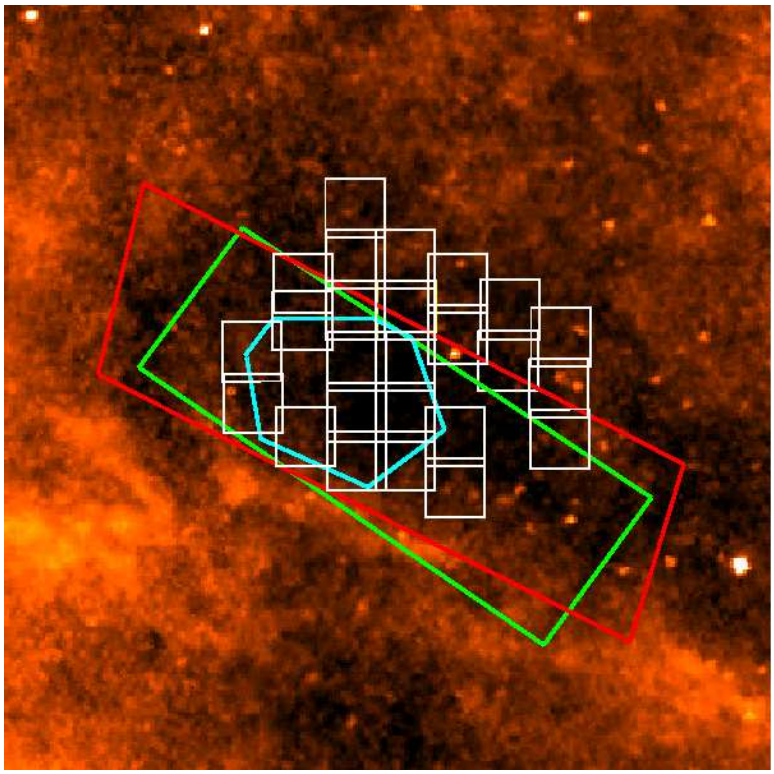

Figure 5.1: Footprint observations at the SEP. The background image is the IRAS 100μm map of the area (a size of 7.4 by 7.4 degrees). The white squares (25 in total) correspond to the R-band catalogue data; each pointing was covered by a set of 3-to-5 dithered exposures. The green lines represent the area covered by *H*erschel/SPIRE observations and the red area corresponds to the *S*pitzer/MIPS observations. Finally, the small central cyan area corresponds to the ATCA radio data (see Table 5.1). For distinction between extended and central region see Figure 5.10.

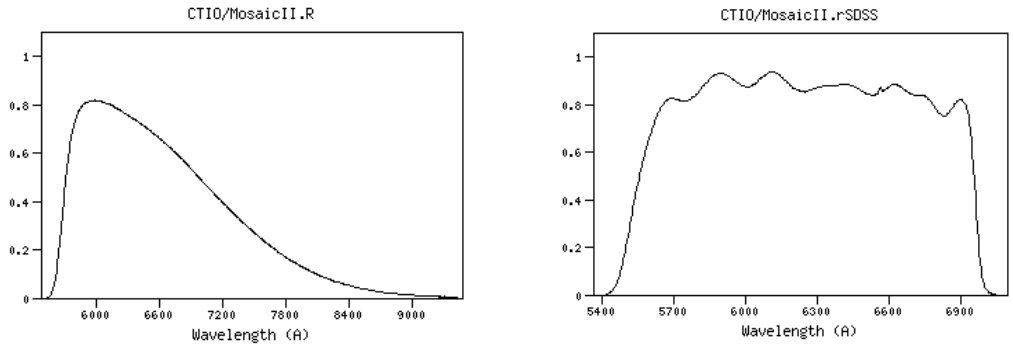

Figure 5.2: (Left) Transmission curve for the R band Harris filter used for the data taken in 2007 ($\lambda_{\rm eff} = 6441.99$ and FWHM=1510). (Right) Transmission curve SDDS R band filter used for the data taken in 2004. ($\lambda_{\rm eff} = 6162.76$ and FWHM=1468).

Telescope/instrument/band	Wavelength	Area [deg^2]	References
GALEX	NUV-FUV	All sky	(Bianchi, 2014)
CTIO/MOSAIC/UVBI	3590 4360 5410 6000	0.5	Baronchelli (in prep.)
CTIO/MOSAICII/griz	4826 6435 7825 9179	10	Public DES data
LaSilla/WFI/R	6300	1.0	(Baronchelli et al., 2016)
VST/OmegaCam / g i z	4700 7500 8880	1.0	Baronchelli (in prep.)
VISTA/J H Ks	1.25 1.65 2.15 μm	1.0	Vaccari (in prep.)
Spitzer/IRAC	3.6 4.5 μm	6.0	(Baronchelli et al., 2016)
AKARI/IRC	3.2 4.1 7 11 μm	1.0	(Davidge et al., 2017)
AKARI/IRC	15 24 μm	1.0	(Davidge et al., 2017)
Spitzer / MIPS	24 70 μm	11.0	(Clements et al., 2011)
AKARI / FIS	65 90 140 160 μm	12.0	Shirahata (in prep.)
Herschel / PACS	100 160 μm	1.0	Hatsukade (in prep.)
Herschel/SPIRE	250 350 500 μm	7.47	(Wang et al., 2014)
BLAST	250 350 500 μm	9.0	(Valiante et al., 2010)
ASTE / AzTEC	1.1 mm	0.25	(Hatsukade et al., 2011)
ATCA	20 cm	2.5	(White et al., 2010)

Table 5.1: Overview of observational data in *AKARI* Deep Field South (ADF-S) ordered from UV to radio wavelengths; all the data are publicly available.

5.3 Data Reduction

5.3.1 IRAF Pipeline Reduction

The data reduction was carried out using the Image Reduction and Analysis Facility (IRAF) software package, which is a general purpose software system for the reduction and analysis of astronomical data. A complete image for each pointing was created by mosaicking the 16 different detector chips together since, due to the characteristics of the Mosaic-I camera (see previous section 5.2), the data cannot be reduced using a common individual chip procedure. Data reduction was performed using the standard *mscred* IRAF packages (Valdes, 2003). These packages follow the common standard procedures for reduction of optical data but applied to the multi-chips they take into account the gaps between the chips.

The amount of data was considerable - seven nights of observations, 27 pointings for each of them with five sky images - so the first part of the reduction was to visualise all the images, in order to detect any unsuitable or unusable data. As is common, some

Step	Task	Function
1) Instrument Characteristics	*zerocombine*	Produce a master bias.
		Correct the zero level.
	darkcombine	Produce a master dark.
		Corrects the background.
	$flatcombine$	Produce a master flat-field.
		Correct the pixel respond.
	ccdproc	Apply the previous outputs to the observation image.
2) Astrometry	*mscgetcatalog*	Download reference catalogue in the field
	msczero	Correct the offset with reference catalogue
	msccmatch	Match the catalogue with the image
3) Alignment and stacking	*mcsimage*	Produce a new tangent-plane projection image
	mscimatch	Match the individual images of the same region
	mscstack	Stack individual observation images

Table 5.2: Main tasks and steps comprising the IRAF reduction process. The *mscred* package was used which takes into account the 16 chips making up each image. 1) General reduction to correct for instrumental effects carried out for each image and each pointing consisting of the creation of a *masterbias*, $masterflatfield$ and *masterzerocombine* for each image and subtraction from the observation image (five observation images per 25 pointings) 2) Astrometry is applied to five images per 25 pointings. 3) Merge the images - five for each pointing- by aligning via position and stacking them. Final result is 25 images, suitable for the extraction and subsequent photometry of astronomical sources.

bias and flats were bad and as such were not included in the reduction. Ultimately, two pointings were removed because of the bad quality of the images, therefore, the image (and corresponding source catalogue) was produced using 25 pointing observations (see Figure 5.10).

The first step in the data reduction process is to make the bias, background and flat-field correction pre-images which need to be applied to the observation images. These pre-images were taken every night before the astronomical observations commenced. Since the data were taken over seven different nights, this procedure was repeated for the seven different data sets. The bias are images taken with the camera closed in order to correct for the pedestal level from the camera. The IRAF task *zerocombine* produces the average of these images, the so-called 'master bias' (see Figure 5.3 right). In a similar way, the *darkcombine* and $flatcombine$ tasks produce an average product of the dark image (to correct the amount of background added during long exposures) and flat-field (to remove the gain and illumination variations across the chip - see Figure

5.3 left.) respectively. The master bias, master flat and the master dark images are then called by the IRAF task *ccdproc* - together with the corresponding observation image - in order to subtract them from the observation images (see Table 5.2).

Figure 5.3: (Left) Bias average image that corrects the noise from the camera. (Right) Flat-field average that correct the outcome of each pixel.

The second major pipeline step was to correct the astrometry. This was a key step in the reduction since accurate positions were required to enable future spectroscopic follow up, for example on the SALT facility where sub arc-second positions of the spectroscopic slits are essential. In order to correct the astrometry, the USNOB1 catalogue Monet et al. (2003) was used. The appropriate part of the catalogue can be downloaded using the World Coordinates System (WCS) contained in the image header with the *mscgetcatalog* task. The error from this catalogue is 0.02 arcseconds, which allowed a statistical improvement in position over the image error of more than 0.04 arcseconds. However, the most common task *mscsetwcs* - to correct the coordinates from the header - was not used since the offset was good enough. Instead, the task *msccmatch* was used to match the positions (see Figure 5.4). Using the task *msczero*, any offset between the image and catalogue was corrected for using a statistical method. The positions were then matched again using *msccmatch* iteratively until an error of 0.02 arcseconds was achieved. This procedure was repeated for every image.

The third step was to project and align the individual pointing images and to stack them in order to achieve a final deeper image. Before merging the individual images

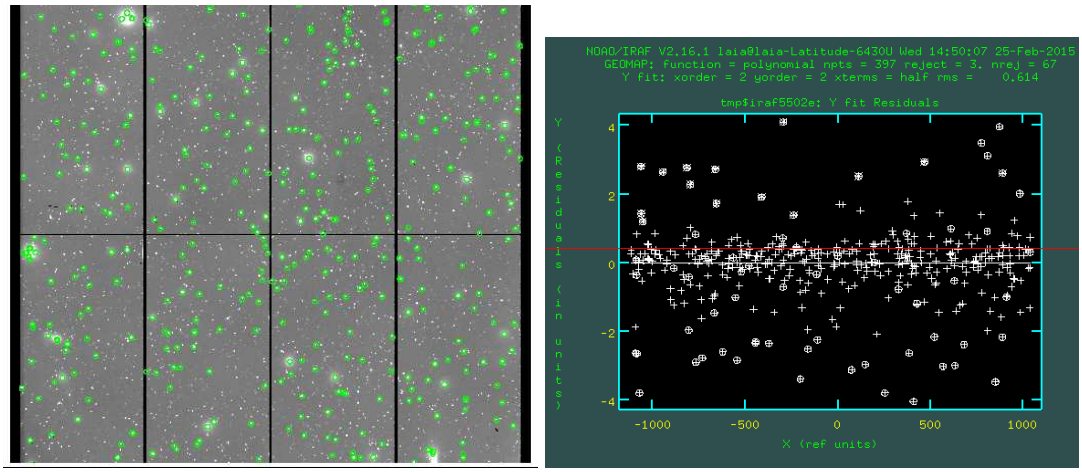

Figure 5.4: (Left) Image over plotting the USNOB1 catalogue with the task *mscgetcatalog* and *msctvmark*. Error 0.02 arcseconds from the catalog. (Right) *msccmatch* statistical improvement of the astrometry position.

to create a stacked image, it is necessary to produce a tangential-plane projection of all of them (5 x 25) using the *mcsimage* task. Then these individual project images are matched using the *mscimatch* task and stacked on the same region with the *mscstack* task; these tasks were run 25 times (once per pointing) with the corresponding set of five images. The final stacked image was obtained from the five individual images from the same region.

5.3.2 Archival Images

The data reduction using the IRAF pipeline tasks was also compared with the reduced images from the MOSAIC-I archival pipeline for products from the Blanco telescope and the MOSAIC-I camera. After checking the quality of the reduced images, they were used to produce the catalogue (see Figure 5.5). In general, the archival pipeline follows similar steps to those described in the section above, however, the final products were used instead to avoid repeating work already carried out.

The data reduction techniques required for mosaic CCD data can be challenging and require an additional procedure over that required for a single CCD image (see e.g. IRAF *mscred* package (Valdes, 2003)). Calibrated images were taken from the

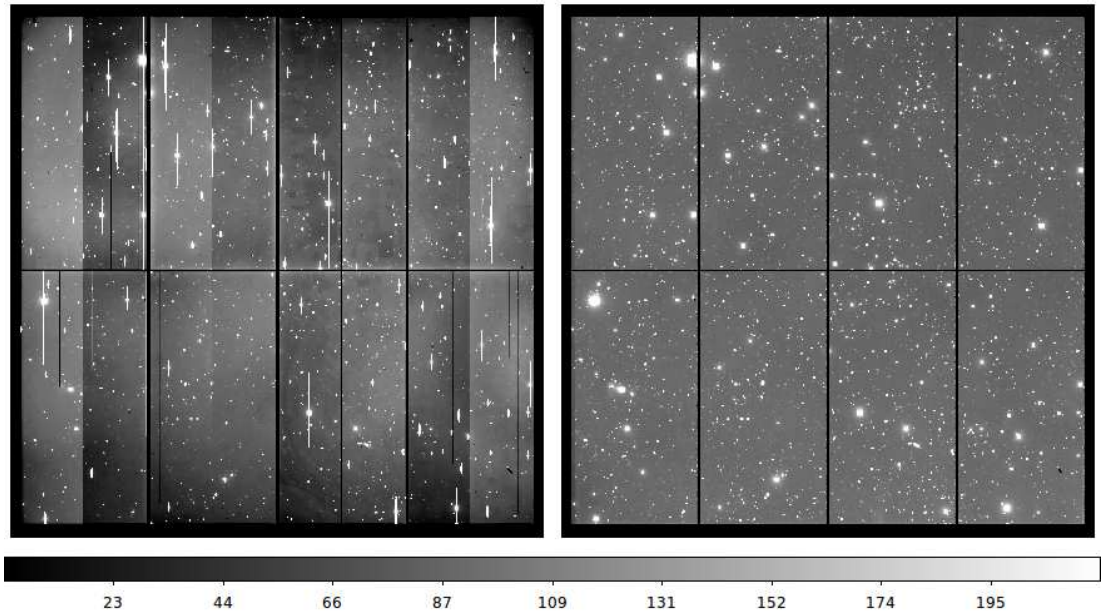

Figure 5.5: Example of a raw image (left) and (Right) final pipeline processed image

NOAO Science Archive (Smith et al., 2007) [1]. These images were processed using the Mosaic Camera Pipeline which is designed to produce calibrated MOSAIC-I data in the NOAO High-Performance Pipeline System (NHPPS) framework (Scott et al., 2007).

The NHPPS data reduction process is organised in a hierarchical structure of different IRAF scripts and deals with one aspect of the reduction process, from calibration (i.e. bias, dome flats, pupil ghost, fringe correction and dark sky flats) to the final data products (Swaters & Valdes, 2007). These procedures also determine the astrometry (similarly determined using the USNO-B catalogue). The pipeline also stacks the images in the same field, to obtain a deep final image, taking into account the projection of the image with a tangent plane projection function. This allows potential stacking of data products without additional resampling. The final stacked-single image is created with a greater depth and the elimination of gaps in the mosaic format (Valdes & Swaters, 2007).

Since the aim of the work was to build the deepest possible point source catalogue, the images were taken with long exposure times. Long exposures result in a large

[1] http://www.portal-nvo.noao.edu/

number of saturated stars in the field, producing the so called blooming effect, which generates stripes perpendicular to the saturated source (see Figure 5.6). After the reduction, (both the IRAF and the archival pipeline) the final images required further correction for this effect and some bad saturated pixels needed to be removed. The anti-blooming process considered the blooming effect through the saturated and inverted values (bad pixels) and masked them in the original image in order to exclude them from the photometry. The main parameters in the program are: the value of the CCD saturation in the image header, the contrast factor between the saturated strips and the closest pixel, and the minimum value (used to handle any potential blooming effects).

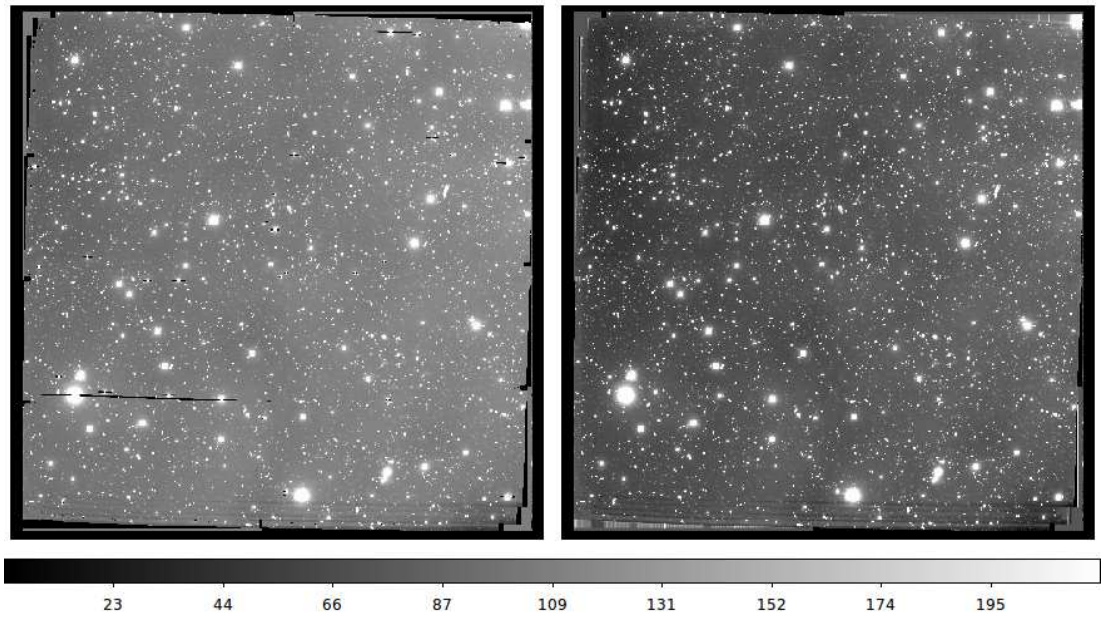

Figure 5.6: Image before (left) and after (right) running the anti-blooming program. The bad pixels are removed and do not take it into account for the photometry. The faints galaxies usable where at magnitude R=25 while the brightest were at R=18.

A final correction for the blooming effect is obtained by substituting the bad pixels (saturated or with values too different from the neighboring ones) with the average values of the adjacent pixels. The blooming removal allows for the elimination of many potential spurious sources during the source extraction phase. This correction was applied image by image, to obtain final images without any blooming effect. The corrected images are then used to extract the sources and to carry out the photometry

(see Figure 5.7).

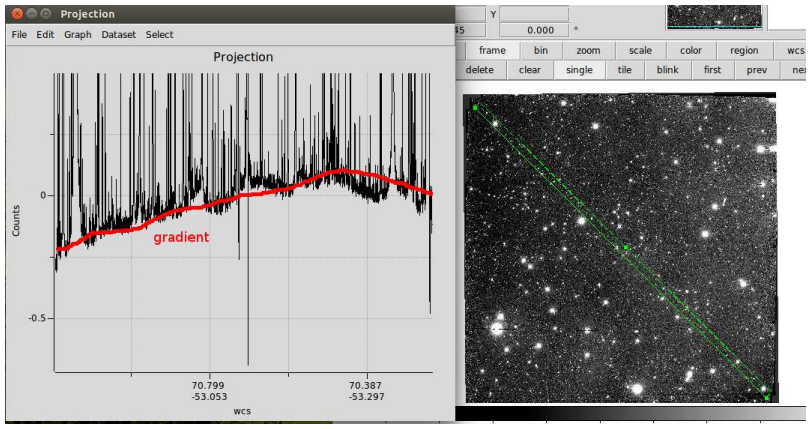

Figure 5.7: Image before and after the anti-blooming correction. The image shows a gradient that is not perfect but acceptably flat.

5.4 Source extraction and photometry

After the data reduction process, source extraction and photometry were carried out on every stacked image. An initial first attempt at the source extraction using IRAF was conducted, however the extraction of the sources was poor since the IRAF *Daofind* task was not identifying most sources due to their faintness. Therefore, the SExtractor software (Source-Extractor Bertin & Arnouts (2010)) was used to identify sources and compute the observed flux density in the final R-band mosaic by following the standard procedures outlined in Bertin (2003) and Holwerda (2003).

Essentially, the identification of the sources is made by defining the width and shape of those sources, followed by the extraction of these sources and the photometry assuming some statistical parameters for every image. These parameters were obtained with the *imexam* package in IRAF to calculate pixels mean, pixel average, maximum pixels average, etc to fit the background parameters in SExtractor. To this purpose, a minimum of 6 pixels above the 3σ of the local background was set. For each detected object, the total (AUTO) flux inside Kron (Kron, 1980) elliptical apertures was calculated. The aperture size was set to 2.5 R_K (Kron radius). This choice ensured that the apertures include more that the 90% of the total flux (Kron, 1980; Graham et al.,

2005). The use of elliptical variable apertures also ensures higher precision than fixed circular apertures when measuring the emission from any extended sources (see e.g. Baronchelli et al., 2016).

We verified that the extracted sources were detected above the 3σ level of the local background. The images were examined by eye to determine the most appropriate photometric apertures. Note that, as alluded to above, fixed aperture photometry was not well suited to the variety of the sources in the field. This was further confirmed through additional photometry using the DAOPHOT routine in IDL [2] which obtained consistent, but noisier, results. The SExtractor *MAG_AUTO* photometry (variable aperture) fits the source sample better because it takes different elliptic apertures depending on the source that fits well with the data (see Figure 5.8).

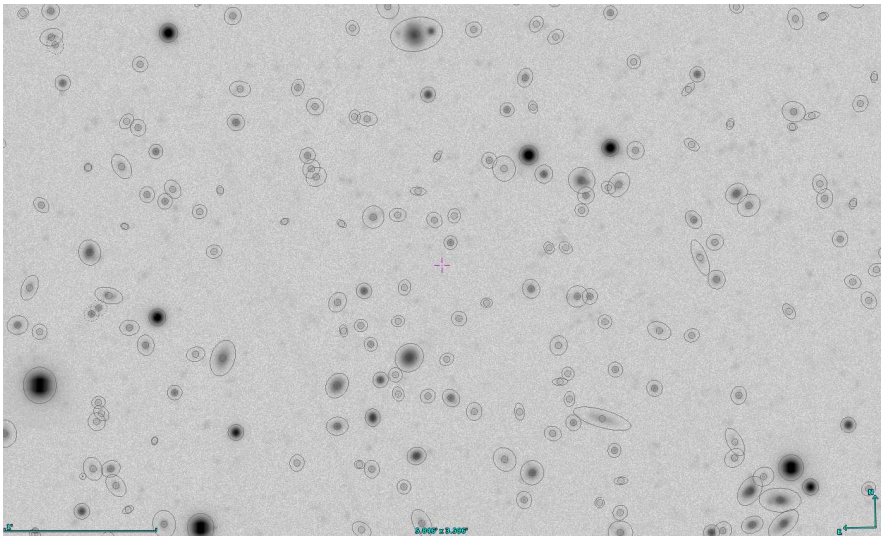

Figure 5.8: SExtractor variable apertures on a segment of the R-band image (the axis are RA and Dec $5.8'x3.6'$ size respectively). The detection of the sources correlate well with the image, as well as with the width and shape of the different apertures.

Finally, the *MAG_AUTO* photometry was compared with the independent shallower R-band (R=23) catalogue (Baronchelli et al., 2016) of the central region ($\sim 1\,\mathrm{deg}^2$). The data presented in this work extends the optically covered area in depth and width to a total of $\sim 11\,\mathrm{deg}^2$). This reference catalogue was produced by using the WFI camera in the MPG 2.2 meter-telescope at La Silla using a slightly different

[2] http://idlastro.gsfc.nasa.gov/

R-band filter. Despite the R-band filter being different (the images were taken with different exposure times and different telescopes) there is good agreement between the two catalogues (see Figure 5.9).

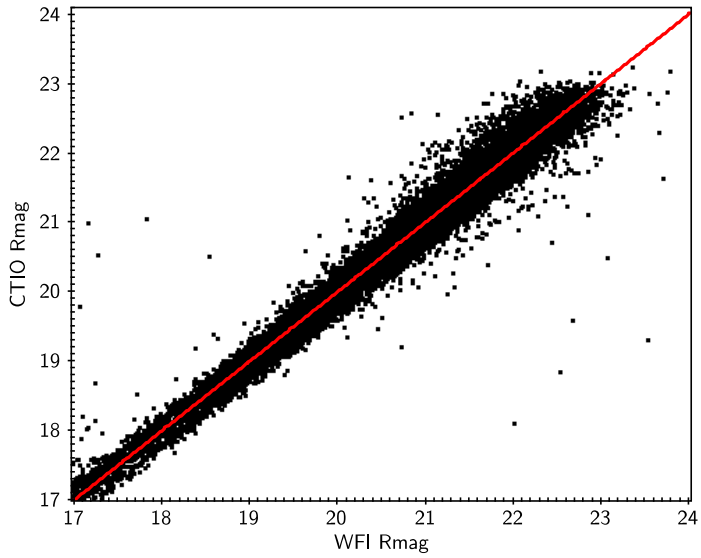

Figure 5.9: The Figure shows WFI magnitudes (Baronchelli et al., 2016) against CTIO magnitudes from my catalogue (two magnitudes deeper and wider than the former) in the central region assuming the final parameters used in SExtractor described in the text. The red line is the linear correlation, which shows that the photometry correlates well even though the catalogues corresponds to data from different telescopes and slightly different R-band filters.

In order to distinguish between stellar and extragalactic point sources, the *CLASS_STAR* parameter in SExtractor was used by defining as a star any source that followed one of the following criteria (Fadda et al., 2004):

- *CLASS_STAR* > 0.85 for R < 23
- *CLASS_STAR* > 0.9

Although the priority was to create a galaxy point source catalogue, the stars and the extended sources classified with the SExtractor flag 'STAR' and 'GALAXY(ES)' respectively, (see Table 5.3) were also included in order to obtain a more complete catalogue. For any overlapping regions of the covered field, the detections and the measured fluxes obtained in the deepest overlapping image were adopted.

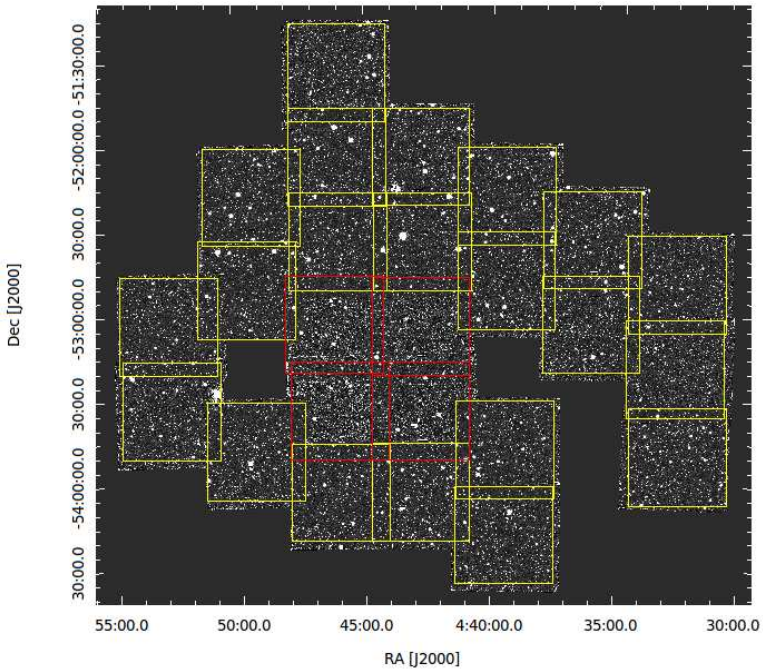

Figure 5.10: Co-added image of the field. The extended area (yellow) was observed in 2004 using an rSDSS filter whereas the central region data (red) was observed in 2007 using an RHarris filter.

Finally a co-added image was created using the Swarp software (Bertin, 2010), which allows resampling and co-adding of the different images into one final image of the total field (see Figure 5.10). For the co-addition the *COMBINE TYPE* was set to median. For the resampling, a *LANCZOS3* algorithm with automatic oversampling was used. Swarp takes into account the astrometry of the individual images, with both the background subtraction and the noise-level measurement for automatic weighting.

5.5 Catalogue

The final catalogue covers $\sim 11\,\mathrm{deg}^2$ with 462,523 sources to a depth of R=25 and source detection threshold of 3σ. The catalogue peaks at magnitude R=23 and their source distribution is showed in Figure 5.11.

The final point source catalogue contains 454,117 extragalactic point sources with an additional 12,378 and 5,487 entries classified as extended sources and stars respectively. The catalogue consists of 5 columns: the position (RA, Dec in J2000), the

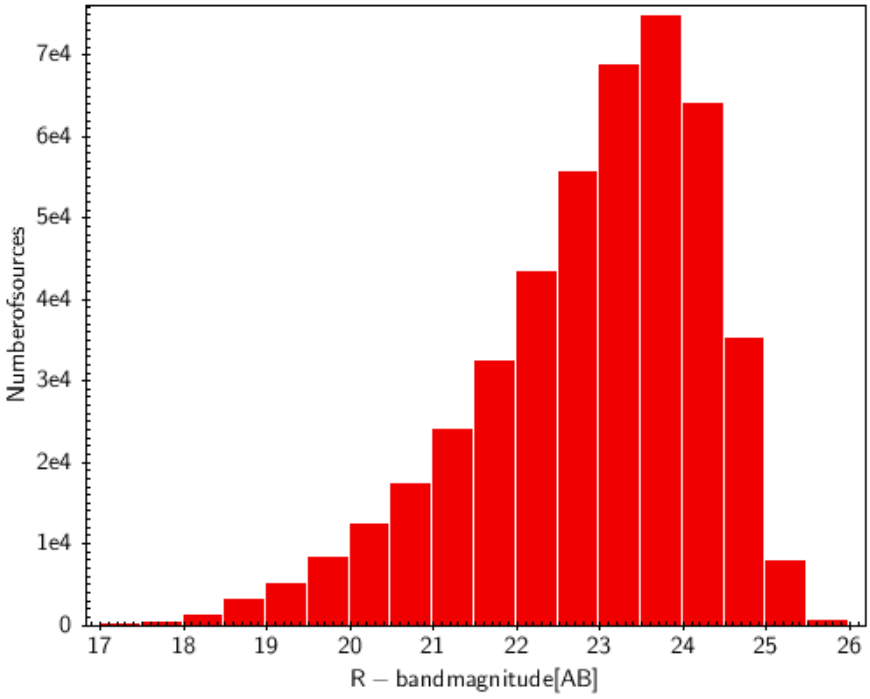

Figure 5.11: Histogram of the detected R-band sources as a function of brightness in AB magnitudes. The peak of the sources is around magnitude 23 but reaches to a depth of magnitude R=26, however, the sources between $26 > R > 25$ were removed after checking them by eye on the image because of their low reliability. The differential source counts are in excellent agreement with previous results (Barrufet L., 2016).

AB magnitude and respective error and a FLAG value that denotes if the source has been classified as a star ('STAR'), a point source galaxy ('GALAXY(PS)') or extended source galaxy ('GALAXY(ES)') (see an example in Table 5.3).

RA	Dec	Rmag	eRmag	Flag
72.7043524	-52.558814	25.0	0.2621	GALAXY(PS)
69.9093986	-52.2592086	24.0	0.207	GALAXY(PS)
69.9544288	-52.8177397	23.0129	0.1123	GALAXY(PS)
70.9945751	-54.0866881	22.4312	0.0838	GALAXY(PS)
67.9965667	-53.173181	22.3191	0.1191	GALAXY(PS)

Table 5.3: Example of the R-band catalogue for the 5 first sources of each object class Flag. The catalogue is made by 5 columns that correspond respectively to: Right ascension (J2000)[deg], Declination (J2000) [deg], R magnitude (Kron-like elliptical aperture [mag]) RMS uncertainty for R-band magnitudes, Flag corresponding to Star, point source galaxy (GALAXY(PS)) or extended source(GALAXY(ES)). The catalogue is publicly available at www.vizier.com

This R-band catalogue was used for obtaining the optical position for the spectroscopic observation proposal on the Southern African Large Telescope (SALT) (see

Chapter 4). SALT is an 11 meter optical telescope based in the southern hemisphere. The Open University was allocated 3 hours over 3 nights although the observations were eventually not taken due to bad weather. This time would have been used to carry out multi-object spectroscopy (MOS) to observe 30 objects at the same time. Using the catalogue, 3 different masks were produced, one for each night. The instrument used was the Robert Stobie Spectrograph (RSS), the main work-horse instrument on SALT.

The Phase I process consisted of submitting the observation proposal: scientific goals, area to observe and technical availability of the observations. This phase was successfully completed. The Phase II consists of elaborating an observation time plan and designing the different masks by using the specific SALT software. There were 3 different masks designed for the observations (see Figure 5.12).

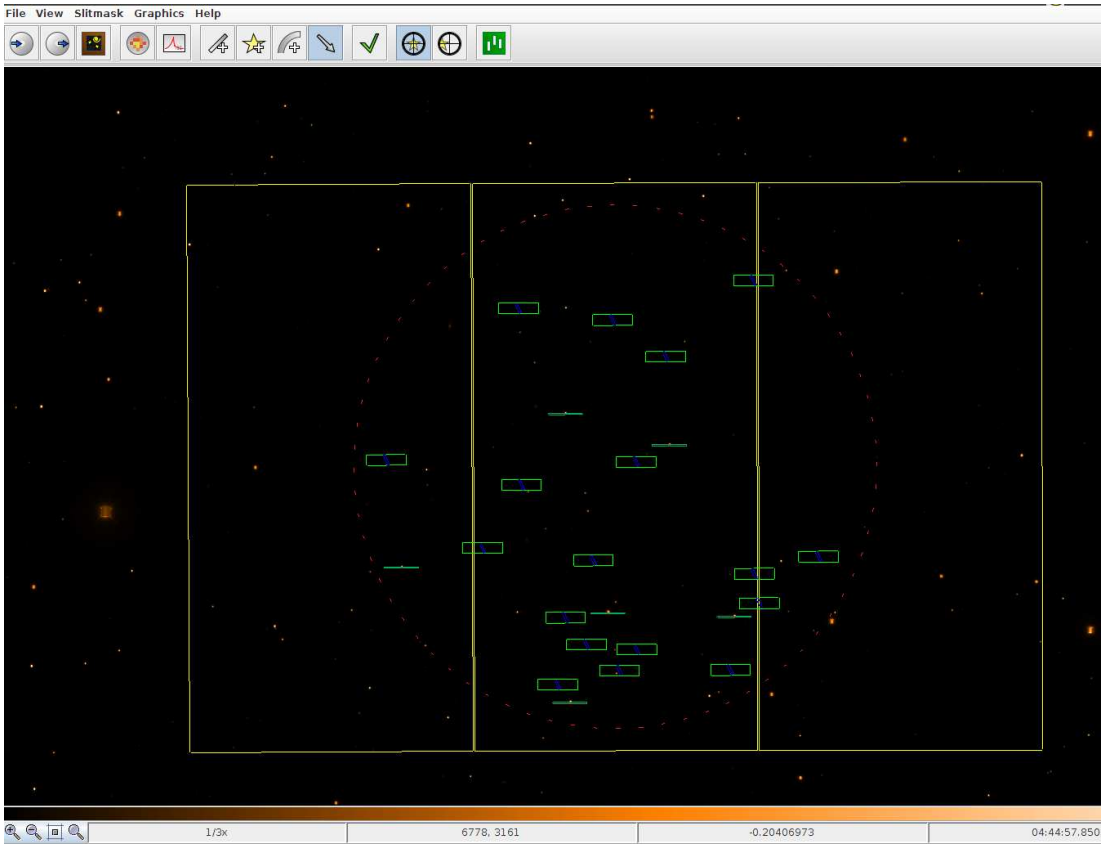

Figure 5.12: Image of 1 of the 3 masks designed with the program RSMT 1.99. The blue slits are the reference for the star reference position and the red slits are the AGN candidates. The background image is the reduced CTIO image.

5.6 Optical properties of IR galaxies

The R-band catalogue was used for optical identifications in order to make a selection of DOGs and gravitational lens candidates. To this end, a band-merged multi-wavelength catalogue was constructed from all available infrared, submillimetre and radio data. The ADF-S region at the SEP was covered by observations ranging from the radio to the IR regime (see Table 5.1), covering a total of 11 deg^2 (see Figure 5.1).

The ADF-S has also been observed by the *Herschel Space Observatory* (HSO; Pilbratt et al. (2010)) Spectral and Photometric Imaging Receiver (SPIRE) instrument (Griffin et al., 2010) with the *Herschel* catalogues available from the HerMEs HEDAM archive [2]. A band merged catalogue was produced using the 3 different SUSSEXtractor (Bertin & Arnouts, 2010) catalogues at 250μm, 350μm and 500μm respectively. The ID250 position was taken as a reference and the 350μm and 500μm wavelengths were cross-matched with a matching distance of 9 arcseconds. Although the 500μm images have lower resolution than the 250 μm ones, Wardlow et al. (2013) shows that the source deblending does not significantly affect any lensed galaxy selection (see Section 5.6.2), which provides further justification for using this new merged catalogue for the selection of lens candidates.

5.6.1 Dust Obscured Galaxies

Dust Obscured Galaxies are extremely red galaxies detected predominantly in the mid-infrared, that become an increasing fraction of the extragalactic population at fainter 24 μm flux densities (e.g. Houck et al., 2005). The spectroscopically measured redshifts for this population imply high luminosities ($10^{12} - 10^{14} L_{\odot}$) and redder colors than any local ULIRGs (Dey et al., 2008). Furthermore, DOGs exhibit both star formation and AGN activity, with the brighter sources being more AGN-dominated, which makes them an interesting population to study the connection between AGN and star formation at any given redshift.

[2] http://hedam.lam.fr/HerMES/

The *Spitzer* Space Telescope (Werner et al., 2004b) has demonstrated the existence of a significant population of high-redshift z $\sim$ 2 DOGs (Dey et al., 2008), which is the peak of star formation history, key to study the star formation specially in infrared wavelengths (see Introduction 1.2.1). For candidate selection, the *Spitzer* catalogue *Spitzer*/MIPS 24 μm in the ADF-S field was used (Clements et al., 2011), which covers $\sim$ 12 deg^2 and overlaps with $\sim$ 8.33 deg^2 of the R-band catalogue region. The selection of these sources relies on the idea that the of the big ratio between mid-IR and the optical, since the light emitted in optical wavelengths is faint, due to the dust absorption, and it is re-emitted in longer infrared wavelengths, which therefore are brighter than the optical. The formal selection is defined in Dey et al. (2008) as galaxies which satisfy the following two criteria:

1. $F_{24\mu m} \geq 0.3$mJy
2. $(R - mag24) \geq 14$ (Vega magnitude)

This last statement corresponds to a flux density ratio of $F_{24\mu m}/F_R \geq 982$ (Pope et al., 2008), who later relaxed the first criteria to accept galaxies at lower flux densities, i.e. $F_{24\mu m} \geq 100\mu$Jy. These criteria were applied to the sample, producing 157 sources that follow both conditions (see Figure 5.13).

From a total of 157 DOG candidates, only 15 have enough wavelength coverage (photometric points) to perform SED fitting (see Table 5.4). DOGs represent only 7 % of the total population at $F_{24\mu m} > 1$mJy but increase to 13 % at $\sim$ 0.3 mJy.

The photometric redshift and the infrared luminosity were calculated by using the LePHARE SED fitting code [3] and the results were compared with spectroscopic studies (see Section 3.2.2 for a detailed explanation of LePHARE code). The SEDs were fitted using a set of different spectral libraries (see Section 5.6.2), including starburst galaxies, spirals and ellipticals galaxies, AGNs, obscured star forming galaxies, and red star forming galaxies Berta et al. (2013); Polletta et al. (2007). Templates of high redshift galaxies Siebenmorgen & Krügel (2007) were also incorporated in order to

[3] http://www.cfht.hawaii.edu/ arnouts/LEPHARE/

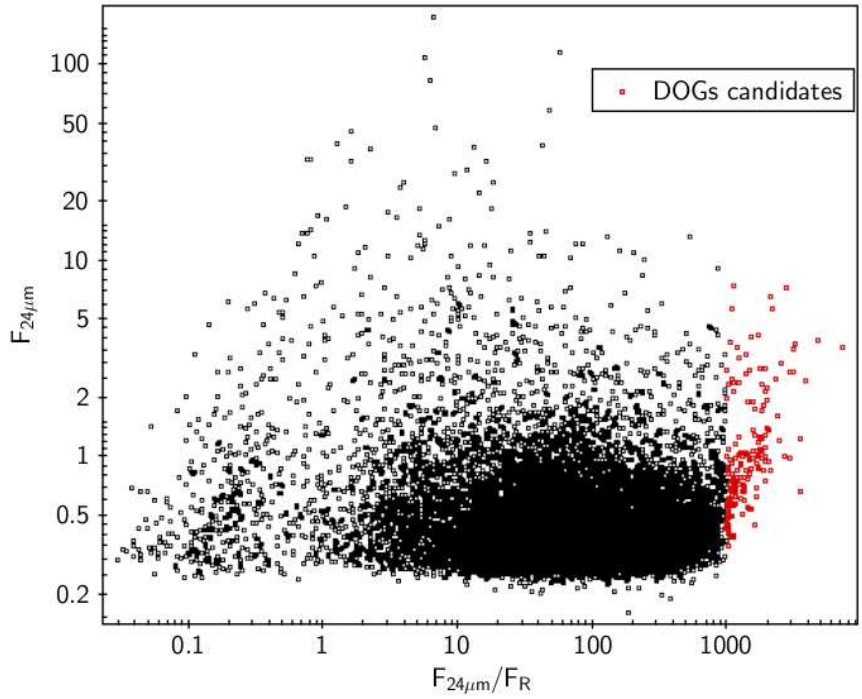

Figure 5.13: The figure shows all the sources in the R-band catalogue that match with the 24 μm catalogue (Clements et al., 2011). The 157 DOGs sources are shown as red dots representing objects with $F_{24\mu m} \geq 0.3$ mJy and $F_{24\mu m}$ / $F_R \geq 982$. DOGs lie in the right part of the diagram, since the dust does absorves the optical and remit in longer wavelengths, having a high ratio between the mid-IR and the optical band.

compare with sources that have a high luminosity but are not dusty sources. Among the 15 DOGs fitted, one (the 12th source in Table 5.6.1) is not well-fitted by templates and has been omitted from the analysis below. Fourteen DOGs SEDs are well fitted by the Berta et al. (2013); Polletta et al. (2007) templates, which include dust features. Of these fourteen, five of the sources can be fitted with an AGN dust torus, four fitted by warm star forming galaxies and five with star forming galaxies with an AGN contribution extending into the optical. This shows the expected AGN presence, together with high star formation, of these sources.

The calculated photometric redshift of our sample ranges from $0.52 < z_{phot} < 2.42$, fitting with the Berta et al. 2013 templates. These were further compared with the results of the photometric redshifts from the Baronchelli (in prep.) catalogue. For two sources (number eight and 12, see Appendix) the Baronchelli fits are better (lower χ^2) so the Baronchelli (in prep.) redshifts were used for fitting the template and calculat-

RA	**Dec**	**Rmag**	$F_{24\mu m}$ **[mJy]**
71.9692	-53.0106	25.0±0.3	0.39±0.02
71.0499	-52.8829	24.4±0.2	0.72±0.02
70.7864	-52.9546	23.8±0.2	1.11±0.02
71.6530	-52.9027	23.9 ±0.1	1.83±0.02
71.9065	-52.9010	23.9±0.1	1.97±0.02
71.6108	-53.8286	23.9±0.2	2.70±0.02
71.8243	-53.2335	23.9±0.2	1.90±0.02
71.3555	-52.8182	23.9±0.1	1.01±0.02
71.8353	-53.4269	23.7±0.2	2.26±0.06
70.4934	-53.4988	23.5±0.2	2.83±0.03
71.6090	-52.9035	23.7±0.1	3.02±0.04
71.6926	-53.2785	22.8±0.1	7.23±0.02
70.4909	-53.3415	22.8±0.1	5.73±0.02
71.5169	-52.7758	23.14±0.07	2.42±0.05
71.7639	-53.0698	21.85±0.03	7.46±0.02

Table 5.4: The table shows the 15 sources which were studied in detail as they have sufficient wavelength coverage to allow SED fitting (see the Appendix for the complete 157 DOGs). Main parameters of the DOGs candidates: coordinates (RA and Dec in the optical R-band), R-band magnitude derived from the catalogue derived in this chapter and flux and error at 24μm from the *Spitzer* catalogue (Clements et al., 2011) .

ing the luminosity. The average redshift of our sample is $\bar{z} = 1.7 \pm 0.1$, which is in agreement with previous studies in other regions (e.g. Dey et al., 2008).

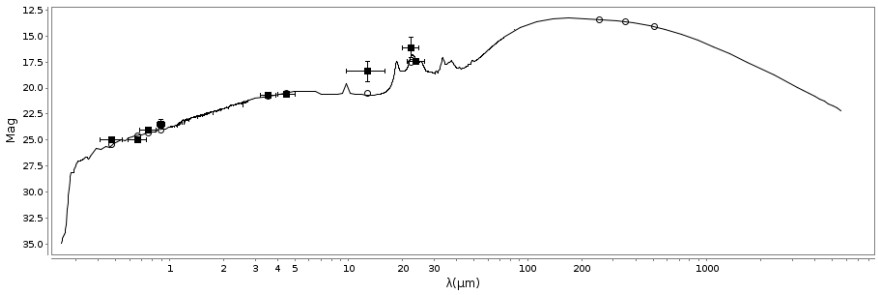

Figure 5.14: The SED of one of the candidates at z = 1.95 and $L_{IR} = 12.58 L_{\odot}$, where the black squares are the observations. The template that fits better (black line) is a warm star forming galaxy (Berta et al., 2013).

The resulting distribution of IR luminosities is $10^{13} L_{\odot}$ ($10^{11.98} < L_{IR}/L_{\odot} < 10^{13.4}$) where 33 % are Hyperluminous Luminous Galaxies (HLIRGs) with $L_{IR} > 10^{13} L_{\odot}$. This is in good agreement with the 30 % from spectroscopic studies (Melbourne et al., 2012). Furthermore, the 93 % of sources have $L_{IR} \geq 10^{12} L_{\odot}$ as in the spectroscopic

study of Dey et al. (2008). However, in this study the multi-wavelength coverage is bigger, specially in the FIR-submillimetre peak, which helps to constraint the SED fitting.

In order to calculate the Star Formation Rate of these sources the FIR luminosity indicator that takes into account the dusty nature of the DOGs regarding the star formation from (Hopkins, 2004) is used:

$$\frac{\mathrm{SFR}}{\mathrm{M_{\odot}yr^{-1}}} = 2.2 \times 10^{36} \frac{\mathrm{L_{FIR}}}{\mathrm{W}} \tag{5.1}$$

The mean SFR of the entire DOGs sample is SFR =1777 $\mathrm{M_{\odot}/yr}$ with an uncertainty on the mean of $\pm 350 \mathrm{M_{\odot}/yr}$.

This high SFR cannot be sustained for long periods, which suggests that these galaxies are going through a short-lived phase in their evolution and/or being powered by some mechanism such as AGN activity (Dey et al., 2008). The sample was divided into galaxies with and without an AGN presence by SED fitting.

By using the equation 5.1 for each source, the average SFR for the total DOGs sample with an AGN presence is 1519 $\mathrm{M_{\odot}/yr}$ whereas for the star forming galaxies it is 2422 $\mathrm{M_{\odot}/yr}$, with an uncertainty of the mean of $359 \mathrm{M_{\odot}/yr}$ and $834 \mathrm{M_{\odot}/yr}$ respectively. There is a difference between the SFR for the two types of sources, especially when taking into account that part of the luminosity from the DOGs with an AGN presence is coming from the AGN and not the host galaxy. However, these differences are at the $\sim 1\sigma$ level and a bigger sample is needed to obtain a more robust conclusion about the difference of SFR with the quenching of star formation via AGN feedback.

An exhaustive study of this population will be conducted using more multi-wavelength data allowing us to extend the number of candidates to $\sim$900 sources with a good multi-band coverage using further archival data. This will allow a thorough study of the nature of DOGs and it will determinate via SED fitting whether the high IR luminosity is produced by an AGN power-law SED or by star formation 'bump' SED

(Dey et al., 2008). It is very unlikely that the optical emission from DOGs is dominated by old stellar populations since most of the luminous regions of the galaxy are shrouded in dust. DOGs may represent an evolutionary phase in the formation of massive galaxies when the AGN is turned on, beginning the process of terminating the star formation (Dey et al., 2008). This extended analysis, which is already underway, will help to answer whether AGN were more bolometric dominant in DOGs at the peak epoch of the volume-averaged star formation density, compared to later epochs (see Future work 6.2.4).

5.6.2 Selection of gravitational lens candidates

The population of apparently bright galaxies at submillimetre wavelengths, e.g. 500μm (flux density, $F_{500\mu m}$), is expected to be dominated by either gravitationally lensed sources (high-z submillimetre galaxies) or low redshift late type galaxies and radio sources (Negrello, 2010). Since these two last 'contaminants' can be easily removed using optical and radio catalogues, a subsequent selection by submillimetre flux can be used efficiently to select lens candidates. The new R-band catalogue was used for a selection of lensing candidates at the SEP. In the SEP field, a total area of ~ 7.5 deg^2 is covered by Herschel-SPIRE observations at 250, 350 and 500 μm. The ADF-S SPIRE catalogue of Wang et al. (2014) - that overlaps ~ 2.4 deg^2 of the R-band catalogue region - to select lens candidates was used. In addition, complementary data from ATCA (Australia Telescope Compact Array) at 20 cm (White et al., 2012) was used in order to remove possible radio sources from the lens selection.

To identify lens systems, the R-band measurements presented in Section 5.3 were used. Since the expected surface density of lenses is about 1.5 per square degree, even when submillimetre colours are used to increase the sample size (González-Nuevo et al., 2012), a wide field is necessary to perform a survey of strong lenses. Moreover, the low resolution of the submillimetre single-dish telescopes yields positions insufficiently accurate for e.g. spectroscopic optical redshifts, but this can be solved with optical

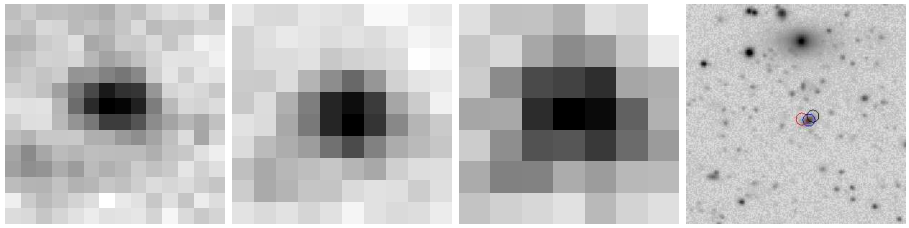

Figure 5.15: Lens candidate example, each row shows the same source at FIR wavelengths (250 μm, 350 μm, 500 μm respectively) and the R-band image. The coordinates of the R-band, 24 μm and 500 μm positions are over-plotted in blue, black and red circles respectively, with the cross-matches of all the lens candidates checked by eye (see A.11 in the A for thumbnail images of all 15 lens candidates). Since the resolution of the three SPIRE-bands is much lower than the optical band (see Figure 5.17), in order to be accurate with the cross-matching, the the *Spitzer* 24 μm data in the SEP was used to identify the optical match with the submillimetre source. Furthermore, this additional mid-infrared wavelength is useful to produce a better spectral fit to the SPIRE-bands (see Figure 5.18).

ground based imaging. Therefore, optical images are key in order to perform a visual inspection of the candidates.

Three different submillimetre based colour-colour criteria where initially exploited (Negrello, 2010; Wardlow et al., 2013; González-Nuevo et al., 2012) in order to select the lens candidates. These were further refined by visually checking the optical (R) image (see Figure 5.17), excluding local galaxies and extended submillimetre objects (an extended bright submillimetre source that is not a local galaxy can potentially be a cirrus cloud Rowan-Robinson, 2014).

Following the selection criteria described in Negrello (2010) candidates with 500 μm fluxes higher than 100 mJy were selected and possible contaminants as described above were excluded.

Lens candidate positions were then cross-correlated using a search radius of 4.5 arcseconds with our optical R-band catalogue. From the six sources identified at $F_{500\mu m} > 100$ mJy, three of them lie in the R-band overlapping region, of which one of them is a local galaxy and the other two are lens candidates (see Figure 5.17). Therefore, the density of $(0.8 \pm 0.6)/\mathrm{deg}^2$ is higher that the predicted source densities of less than 0.5 deg^2 for $F_{500\mu m} > 100$mJy (Negrello, 2010). However, strong field-to-field variation has been shown in (Negrello et al., 2017) which analysed a large area

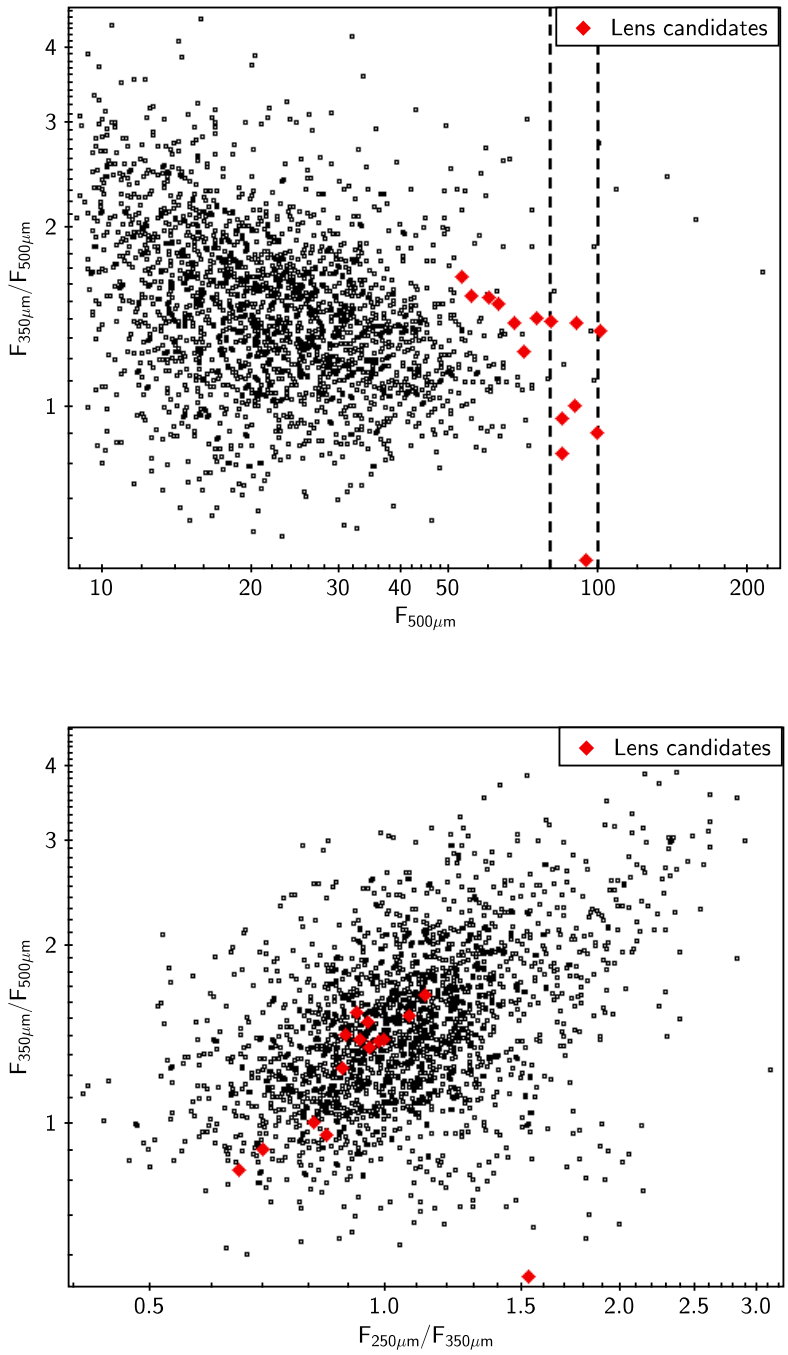

Figure 5.16: SPIRE colour-flux and colour-colour plots for sources detected in the SEP based on the criteria applied in Wardlow et al. (2013). (Top) The figure shows the colour $F_{350\mu m}/F_{500\mu m}$ against the 500 μm flux density. The lens candidates are plotted in red and the 2 vertical bars show the 80 mJy and 100 mJy flux limits. (Bottom) Colour-colour diagram $F_{350\mu m}/F_{500\mu m}$ against the $F_{250\mu m}/F_{350\mu m}$ flux with the same classification for the lens candidates. It shows that the lens candidates are redder than the background sources. The candidates removed were bluer as they are local galaxies or extended sources. The relative colours of the local galaxies and lens candidates also typically occupy different regions of the colour space. In both diagrams the lens candidates lie at the same positions as in previous work (e.g. (Nayyeri et al., 2017), (Wardlow et al., 2013)) which corroborates the classification.

of $\sim 600\,\mathrm{deg}^2$ in Herschel fields and found that the surface density at >100mJy is $131^{+17}_{-15} \times 10^{-3}/\mathrm{deg}^2$. The field-to-field variations can be as much as a factor of two even in survey areas as large as 50 square degrees, so the unexpectedly high number of lensed systems in our survey area could also represent real large scale structure rather than just small number statistics.

The same procedure was followed with sources 80 mJy $< \mathrm{F}_{500\mu\mathrm{m}} <$ 100 mJy (see Figure 5.16) to identify further lens candidates (Wardlow et al., 2013) Among the fourteen sources selected, nine of them lie in the optical covered area and five are actual lens candidates, after visual inspection.

Using the third selection method (González-Nuevo et al., 2012), 33 lens candidates were found that followed: $\mathrm{F}_{350\mu\mathrm{m}}$ >85 mJy, $\mathrm{F}_{250\mu\mathrm{m}} > 35$ mJy, $\mathrm{F}_{350\mu\mathrm{m}}/\mathrm{F}_{250\mu\mathrm{m}} > 0.6$ and $\mathrm{F}_{500\mu\mathrm{m}}/\mathrm{F}_{350\mu\mathrm{m}} > 0.4$ (González-Nuevo et al., 2012). Among them, 22 are not included in the previous criteria classifications with ($\mathrm{F}_{500\mu\mathrm{m}} <$ 80mJy). Finally 8 of them were selected as lens candidates, since the rest lie outside the optical region or were identified as extended sources. Therefore, in total there are 2 + 5 + 8 = 15 lens candidates (see Table 5.5). After cross-correlating these candidates with the ATCA radio catalogue, which covers $2.5\,\mathrm{deg}^2$ (White et al., 2012) and overlaps with $2.38\,\mathrm{deg}^2$ of the R-band catalogue, no radio detection for the selected candidates was found (note that for 4 of the candidates, there is no radio coverage available).

The final step was to use the R-band measurements to classify the lens candidates through SED fitting. Different SED templates were fitted with the aim of determining whether the detection in the R-band truly originates from the lensed object or from the foreground lens itself (see Figure 5.18). For a true lens candidate, the photometry should be consistent (i.e. well fit by a template SED) across all wavebands. In the case of a local foreground galaxy, the R-band point would be expected to be an anomaly in the SED.

For the SED fitting, the following templates were used:

- SWIRE templates (Berta et al., 2013) from the Polletta libraries (Polletta et al., 2007), which include common starburst galaxies (such as M82, Arp220) as well

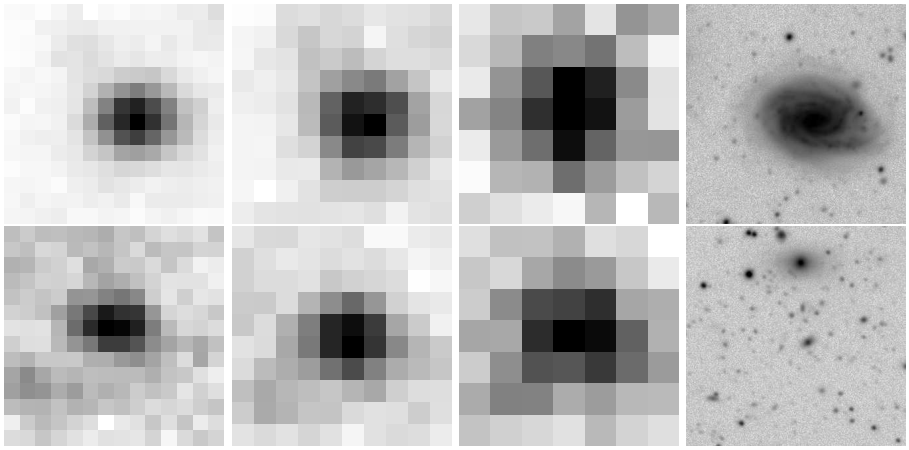

Figure 5.17: The plot shows two sources; each row shows the same source at FIR wavelengths of 250 μm, 350 μm and 500 μm respectively. The 4th image in each row corresponds to the R-band detection from our catalogue. Both sources follow the criteria $F_{500\mu m} > 100$mJy (Negrello, 2010). However, the first row shows a nearby galaxy which was subsequently removed from the candidate list, whereas the second is a reliable lens candidate.

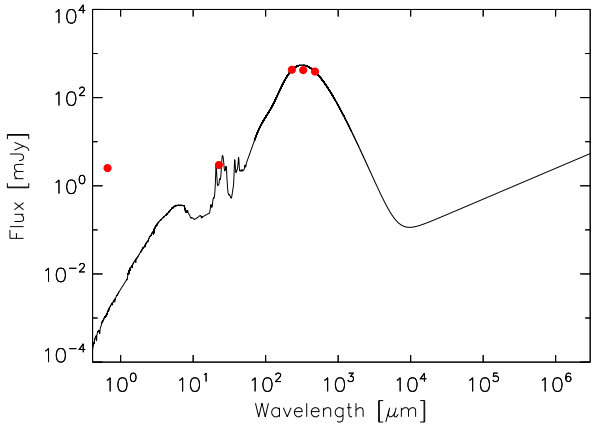

Figure 5.18: The Figure shows the SED fitting of the first lens candidate in Table 5.5. The R-band photometry does not fit with the rest of the data points, and is instead consistent with the R-band detection coming from a lower redshift galaxy.

as common spiral galaxies, ellipticals and AGN.

- Templates for red star-forming galaxies, obscured star-forming galaxies and AGN (Berta et al., 2013).

- SK06 templates (Siebenmorgen & Krügel, 2007) for high-z and high-luminosity sources.

For the three sources with $F_{500\mu m} > 100$mJy it was found that the first candidate is

RA	Dec	$F_{500\mu m}$	$F_{350\mu m}$	$F_{250\mu m}$	Rmag	z_{phot}
73.29603	-53.09905	100 ± 2	135 ± 2	129 ± 2	20.81 ± 0.03	2.413
72.12323	-54.05905	99 ± 2	89 ± 2	62 ± 2	22.56 ± 0.06	2.432
72.44603	-52.90909	94 ± 3	84 ± 2	108 ± 2	21.75 ± 0.07	2.462
72.13897	-54.04186	89 ± 3	123 ± 2	121 ± 2	21.74 ± 0.06	2.427
71.64437	-52.52412	89 ± 2	89 ± 2	73 ± 2	21.14 ± 0.07	2.427
73.04434	-52.87606	52 ± 2	87 ± 2	98 ± 2	22.9 ± 0.1	2.564
71.72428	-54.12940	84 ± 3	80 ± 2	67 ± 2	21.97 ± 0.06	2.359
69.62604	-54.30689	79 ± 2	110 ± 2	110 ± 2	23.8 ± 0.1	2.516
73.33087	-53.64143	74 ± 3	105 ± 2	93 ± 2	23.6 ± 0.1	2.494
70.47450	-54.06486	70 ± 8	87 ± 6	77 ± 7	23.7 ± 0.1	2.422
70.26307	-53.21083	67 ± 2	93 ± 2	86 ± 2	21.44 ± 0.04	2.418
73.06402	-53.34594	62 ± 2	93 ± 2	88 ± 2	23.9 ± 0.2	2.462
72.11264	-52.65849	60 ± 2	91 ± 2	98 ± 2	23.9 ± 0.2	2.457
68.41824	-54.06108	55 ± 2	85 ± 2	78 ± 2	21.33 ± 0.04	2.570
72.61251	-52.69087	84 ± 2	70 ± 2	45 ± 2	23.4 ± 0.1	2.452

Table 5.5: Final list of lens candidates: coordinates corresponding to the optical positions [degrees], the fluxes [mJy] for the SPIRE bands, the R-band magnitude [AB] and finally the photometric redshift.

not a lens, being the only source that is well fitted by a nearby a galaxy model. The optical image shows clearly the local nature of that galaxy (see Figure 5.17). The remaining two sources are good lens candidates. Finally a redshift was estimated (see Table 5.5), comparing with the Eyelash SED from González-Nuevo et al. (2012) which is at redshift 2.326. Figure 5.18 shows that the R-band flux is higher than expected for this submillimetre source, which is consistent with the scenario of a background galaxy being gravitationally lensed by a foreground system at lower redshift with the R-band flux originally from the foreground lens. The redshift is similar than the average redshift found it in Negrello et al. (2017) which is $z_{spec} = 2.5$. Therefore, the catalogue of gravitational lens I produced can contribute as the follow-up observations that Negrello et al. (2017) proposes in their work, comparing the sample in a different Herschel field, since the field-to-field difference in selecting gravitational lenses using the 500μm flux method is under discussion (Negrello et al., 2017).

5.7 Summary and conclusions

Deep observations with the CTIO/Blanco telescope in the R-band had been carried out to observe ~ 11 deg^2 area centered at RA $= 4^{\rm h}44^{\rm m}00^{\rm s}$ and Dec $= -53\,^{\circ}20'00''$ (J2000) in the SEP region. The final resulting catalogue includes point sources and extended sources (~ 472000 in total) with a 3 σ per pixel depth limiting magnitude of R=25. The catalogue is deep enough to perform a useful cross-correlation with multi-wavelength data from *Herschel, Spitzer* and *AKARI*. The R-band catalogue is a powerful tool for selecting Dust Obscured Galaxies due to their faintness in optical wavelengths. For the search of gravitational lenses, it is important to cover a large area particularly in fields such as the SEP, where there are wide-field ancillary data at IR and submillimetre wavelengths available.

A submillimetre classification scheme has been used to select lens candidates in parallel with the R-band catalogue in order to identify 15 candidates whose optical counterparts do not correspond to the submillimetre source. The density of sources ($0.8 \pm 0.6/\text{deg}^2$) is slightly higher than the predicted by Negrello (2010) using the same criterion ($0.5/\text{deg}^2$), which could be due to the field-to-field variation find in previous works (Negrello et al., 2017).

This catalogue was also used to classify and study Dust Obscured Galaxies. In total there are 157 DOGs in our catalogue, 14 of which have sufficient ancillary data to allow SED fitting. This sample has an average redshift $\bar{z} = 1.7 \pm 0.1$ and $10^{11.98} < L_{IR}/L_{\odot} < 10^{13.4}$, which is consistent with previous studies (Dey et al., 2008).

The multi-wavelength coverage in this field makes this sample ideal for and SED-based fitting approach to establish the AGN and star formation components of DOGs. The global SFR average is 1777 ± 350 M$_{\odot}$/yr, with a difference shown between the sources with an AGN presence and the sources without AGN, but a larger sample is need it to extract a conclusion and this question will be addressed in an extended analysis of the whole field, which is already underway. The star formation rates of the DOGs are comparable to those derived in the submm galaxy population (e.g. Hughes et al.

(1998), Negrello (2010)) and only 5/14 DOGs show evidence for any AGN component. This would therefore argue against the population being the end point of submm galaxy starbursts that have been quenched by AGN activity. Nevertheless, the mean redshift is consistent with that of submm galaxies. Another consideration is the relative number densities: DOGs have about 90 sources per square degree, which corresponds roughly to the surface density of 850um-selected galaxies with fluxes brighter than about 8-10mJy; these, like the DOGs, are also ultraluminous starbursts. Future work will model the SEDs of a larger sample, but in the meantime our provisional conclusion is we favour the alternative interpretation that DOGs are simply the starburst population with warmer colour temperatures, with the submm galaxy population being the corresponding cooler subset.

Chapter 6

Conclusions and Future work

6.1 Conclusions

This Thesis has used a multi-wavelength approach in the North and South Ecliptic Pole (NEP and SEP) in order to identify specific galaxy populations - specifically focusing on selection via infrared and submillimetre data. A thorough investigation of the available contemporary spectral energy distribution codes was made in order to identify the best algorithm for spectral fitting for the extracted galaxy samples. These fitting codes were then used to derive the physical properties of each galaxy population at different redshift ranges to analyse the star formation evolution over cosmic time. The main conclusions of this thesis are discussed below, however, this work has also produced important new samples / catalogues of intermediate to high redshift sources which will provide a legacy products for future (spectroscopic) follow up from ground based facilities in the near future.

High-redshift dusty star forming galaxies (DSFGs) provide an excellent sample with which to study the star formation properties through the dust emission. To date most of the large samples of these exotic sources, requiring wide areal coverage, have been selected using a few photometric detections in the submillimetre range (see e.g. Dowell et al., 2014; Asboth et al., 2016). On the other hand, thorough multi-wavelength studies of individual sources have revealed extreme star formation rates

(Riechers et al., 2013), although these may not be representative of the general DSFG population. Current studies have therefore not yet fully characterised the high-z DSFG population. This Thesis has studied this galaxy population, selecting large samples at redshifts between two and six from a multi-wavelength approach in well covered deep fields.

This thesis has made a thorough investigation and extended the work on high-z galaxy selection methodologies in order to produce a major legacy dataset for future follow up studies at ground based facilities. To summarise the methods:

- Submillimetre colour-colour diagrams (268 sources potentially at z > 2)
- Selection through submillimetre source position, by photometry at SCUBA-2 positions in *Herschel*-SPIRE maps (36 sources with $z_{phot} > 2$).
- Submillimetre flux 500 μm riser criterion, cross-matching independent source detections in individual *Herschel*-SPIRE (500, 350, 250μm) bands with $F_{500\mu m} > 30$ mJy and colours $F_{500\mu m}/F_{350\mu m} > 1.3$ (14 sources at potential redshift $4 < z < 6$).
- SPIRE dropouts technique: sources with a clear SCUBA-2 detection but lack of SPIRE detection in the three bands (46 sources with $1.70 < z_{phot} < 5.71$)

The product from this investigation is a new legacy catalogue containing 336 high-z sources at z > 2 with 186 sources having excellent multi-wavelength coverage.

The 186 sources with good multi-wavelength coverage were used as the basis of a sample with which to investigate several contemporary SED fitting codes: SMGs templates, LePHARE, MAGPHYS and CIGALE. The most basic fitting using simple SMG templates provides an indication of the photometric redshift by using mainly the FIR and submillimetre data to measure any "shift" in the spectrum, without taking any of the physical properties such as the dust temperature or redshift degeneracy into account.

The LePHARE code, although more sophisticated does not reproduce properly the properties of dusty galaxies and in addition has several limitations in the analysis of IR and longer wavelength data using a very limited number of templates. Similarly, MAGPHYS models the properties of DSFGs in a rather simplistic way, furthermore, having the handicap of requiring, a priori, an accurate spectroscopic redshift to ensure reliable results. The study in this thesis concluded that CIGALE wass the most successful code for studying dusty high-z galaxies since it not only takes into account the entire spectrum to model the properties of DSFGs, but is also able to estimate photometric redshifts.

CIGALE was therefore used to calculate the physical properties of the high-z sample - such as SFR and stellar masses. These properties were then used to evaluate the sample's positions on the Main Sequence (MS) of galaxies. The high-z population was found to have high SFRs, with in total 30% of them lying above the MS. For the specific redshift bin around $z \sim 2$, the percentage of galaxies above the MS rose to 51%, which is in good agreement with da Cunha et al. (2015) but around 10% less than Ikarashi et al. (2017) and Miettinen et al. (2017). It should be noted that other studies find no galaxies above the MS for the same redshift bin (Dunlop et al., 2017), however, in this case the selection of the sources was from a much smaller area produced by a deep pencil-beam survey, hence, the study is sensitive to lower SFRs at similar stellar masses and not rare exotic sources, favored by shallow wide area surveys. The big discrepancies in the results between these studies seems to indicate a biased effect since Ikarashi et al. (2017) and Miettinen et al. (2017) are longer wavelength submillimetre selected samples.

The galaxies lying on or above the MS are defined by two modes of star formation, continuous and burst. These modes were evaluated as a function of the star formation efficiency (SFE), relating the star formation and the gas reservoir within the galaxy. Searching for a parameter that correlates with the SFE could also relate to the triggering, or quenching of the star formation itself. I discovered a relation between the age of the starburst in the galaxy and the SFE: the earlier the starburst the more efficient

the star formation.

The SFE in the high-z DSFG population depends on the age of the burst in the galaxy (the earlier the burst, the greater the SFE), but not on the presence of any AGN or the age of the main population in the galaxy. This indicates that secular processes are less important - specifically in the high-z DSFGs - than external processes as mergers. The morphology of the galaxies can be related with mergers, which influence the SFR (Elbaz et al., 2017). The presence of the starburst may be caused by a merger, and the age of this starburst is in turn related to the state of that merger. This could therefore be the reason for the bimodality of star formation in SMGs and the cause of the greater number of ULIRGs at high redshift. There is spectroscopic evidence that mergers enhance the star formation in the early stages (Riechers et al., 2017), however, spectroscopic observations of this sample are required in order to investigate this phenomenon further.

It is noted that galaxies such as HFLS3 probably are not representative of this high-z SMG population, however, more galaxies like HFLS3 could be found by the proposed selection methods. Finally, I conclude that a multi-wavelength approach in deep fields, with a good coverage of photometric data as the NEP, is necessary for a better understanding of this population.

There is still much discussion as to what relationship the presence of an AGN in a galaxy can have with the star formation. Some authors support the theory that the presence of an AGN can suppress the star formation (Barger et al., 2015), whereas others infer the opposite (Juneau et al., 2013). This interplay between star-formation and AGN extends from the infrared to radio wavelengths where classically the star-forming and AGN populations were well defined (Windhorst, 2003), however, even radio emission at milli-micro-Jansky fluxes can indicate the presence of a low-luminosity AGN (such as Seyferts) as well as star formation. In order to investigate further this interplay between AGN and star-formation, a lower redshift sample based on radio surveys is ideal for studying the possible interaction of these two processes.

A method for calculating photometric redshifts in radio samples was developed using a multi-wavelength approach which obtains better results than simple cross-matching the catalogue with ancillary redshift data. This subsample is represented by a sub-mJy population with a moderate redshift distribution. This faint radio sample was divided by infrared luminosity in order to measure the IR emission, as an indicator of star formation. The results showed a high number of luminous sources: LIRGs representing 66% of the sample, whereas the ULIRGs are only 4% and sources with $L_{IR} < 10^{11} \cdot L_{\odot}$ are the remaining 30%.

The radio sample contained 56% of sources that require some AGN presence at some level derived from the SED fitting but only 7 sources are actually AGN dominated (defined as an AGN fraction > 20%). In most cases, the contribution of these AGN is low, 4% on average. Evaluating this property by L_{IR} shows that SED fits of ULIRGs require three times more AGN contribution than lower luminosity galaxies. In addition to the AGN fraction, on average ULIRGs appear to have only about half of the PAH strength of galaxies with lower IR luminosities. The study here finds an expected PAH deficit in the most luminous sources which also tend to be at higher redshift in the sample (Elbaz et al., 2011).

As expected ULIRGs clearly have a higher star formation rate than the lower luminosity galaxies, specifically, ULIRGs have 37 times higher SFR than galaxies with $L_{IR} < 10^{11} \cdot L_{\odot}$ and are three times more efficient at forming stars. The stellar and gas masses are also around one order of magnitude higher in both the LIRGs and ULIRGs than in the less luminous galaxies, which indicates that the high luminosity is proceeded by high star formation. However, this idea is not straightforward and the mass of the gas in the galaxy does not follow the same trend as the star formation efficiency, which means that there is another (or several) factor that influences the star formation. For the LIRGs there is an evolution of the AGN fraction with redshift indicating that at high IR luminosities the AGN presence is higher at higher redshifts. These results, together which the PAH deficit and the AGN fraction, indicate that a fraction of the luminosity could be contributed from AGN activity instead of star formation. Therefore,

I conclude that the main source of the high luminosity is the star formation, although it can be enhanced by an AGN presence.

In order to segregate the AGN population from the star-forming galaxies, it was found that mid-IR data was very effective in classifying AGN via colour-colour diagrams. In the case of the sample at the NEP, I found that the *AKARI* data could be used effectively for classifying AGN in a more reliable way than by using *WISE* data since *AKARI* provides 5 more extra bands over a similar wavelength coverage to *WISE*. An efficient colour-colour criteria to classify AGN with *AKARI* data was identified that could achieve around 90% completeness. The criteria consists of using four different *AKARI* bands (N2, N3, S7, S11) to create two colours that identify the power-law characteristic of AGN: N4-N2 > 0.1 and 1.5 > S7-S11 > 0. The use of two different colours in close wavelength proximity (4.4 μm - 2.4 μm and 10.9 μm - 7.3 μm) allows the detection of the prominent drop in galaxy emission and the power law spectrum in two different parts of the mid-IR regime, constraining the AGNs in a narrow region in the colour-colour parameter space.

Chapter 3 and Chapter 4 have dealt with star-formation at high (6 > z > 4) and low (z < 1.2) redshift respectively. However, the peak of the cosmic star-formation occurs at redshift $\sim$2. Connecting these studies in this thesis is the analysis of the dust obscured galaxies (DOGs) in and Chapter 5 The DOGs population are defined at z $\sim$ 2 and also contain both an AGN presence and strong star formation (Dey et al., 2008). Classically, DOGs have been selected on the basis of their 24 μm band and R-band fluxes.

For the SEP field, although deep *Spitzer* 24 μm coverage plus multi-wavelength data was available, historically there has always been a lack of a deep optical catalogue in this region which has hindered progress in this area of the sky. Therefore, the data from previous deep observations from the CTIO/Blanco telescope in the R band over $\sim$ 11 deg^2 at the SEP has been reduced and analysed and a new legacy R-band catalogue was created that includes a total of $\sim$ 472000 sources to a faint limiting magnitude of R=25. Such a depth is deep enough to perform essential cross-correlation with multi-

wavelength infrared data from *Herschel, Spitzer* and *AKARI*. This new catalogue was used to classify and study the Dust Obscured Galaxies in the SEP. Combining the new catalogue with the *Spitzer* 24 μm data a total of 157 DOGs were identified of which 14, having sufficient multi wavelength ancillary data were analysed via SED fitting. This sample has an average redshift $\bar{z} = 1.7 \pm 0.1$ spanning the luminosity range $10^{11.98} < L_{IR}/L_{\odot} < 10^{13.4}$. The global average SFR is 1777 $\pm$ 350 $M_{\odot}$/yr. A difference was also seen between DOGs with and without an AGN presence, which may indicate possible quenching of star formation in sources with an AGN presence.

This thesis has studied various different galaxy populations from redshift 0.1 to 6.2. I conclude that the star formation evolves with redshift and almost certainly with different star formation modes. For the dusty high redshift sample (z > 2) the epoch of the starburst in the galaxy enhances the star formation and is probably related to the merging of galaxies. However, at lower redshift ($\sim$ 2), the study of the dust obscured galaxies shows that the presence of AGN is greater than in the high-z dusty star forming galaxy sample implying a possible epoch of AGN in their role of modulating star-formation within galaxies. The study of the radio sample, at redshift lower than two, also confirms that the presence of AGN in LIRGS - high luminous galaxies with high star formation - increases with redshift. Secular processes appear more significant at lower redshift, whereas mergers are more prolific at high redshift. These different mechanisms of enhancing star formation at different redshifts could explain why the presence of ULIRGs is higher in the high redshift Universe than in the local Universe.

6.2 Future work

This thesis produced significant legacy products and has moreover laid the groundwork for extensively follow up of important objects with ground based facilities. Below a brief outline of proposed future work is presented.

6.2.1 Selection of high redshift galaxies

Future work will expand and extend the methods for the selection of high redshift sources. Moreover, the advent of new wider/deeper catalogues will provide new data mining opportunities for the selection methods explored in this thesis:

- New methods for the selection of high-z sources.

  The SPIRE maps method was successfully applied in Chapter 2, discovering sources at $4 < z < 6$. This method can be extended in concept to include the so-called 'D-maps' method (see e.g. Dowell et al., 2014; Asboth et al., 2016) This is a more sophisticated method that consists of creating a combination of the three SPIRE maps - each of them with a different weighting - in order to produce a D-map. Bright sources are extracted from the D-map and the photometry at these positions is made on the three original SPIRE maps.

  As an extension of my investigation into high-z selection techniques, I propose to construct D-maps in the specific fields where larger quantities of ancillary data are available: the NEP, the AKARI Deep Field South (ADFS) - which have already been studied from a multi-wavelength point of view for other purposes in Chapter 5 - and the SPIRE dark field, possibly the deepest submillimetre field on the sky. Altogether, Following an initial investigation I expect to obtain around 40 candidates with redshifts at least $z > 4$. The advantage of producing the maps in these fields compared to previous work in other fields is the amount of multi-wavelength data that can be used for a better estimation of the photometric redshift and therefore to derive the physical properties of these galaxies (see 3 for a detailed explanation of the SED fitting methods used to calculate physical properties).

- Data mining of new data sets

  In Chapter 3, robust methods for selecting high-z candidates have been introduced and applied. New data sets becoming available in the NEP will help to

improve the SED fitting and to expand the SCUBA-2 maps methods over the wider area (NEP Wide field).

In particular, we have recently acquired Spitzer/IRAC data at 3.6 and 4.5 μm over an area of ~ 7 deg^2 in the NEP (Nayyeri et al., 2018). Furthermore, the incorporation of the Herschel/PACS data (100 μm and 160 μm) for the high-z candidates will improve the SED fitting via better sampling of the dust emission peak. This additional ancillary data will improve the photometric redshift precision and the estimation of the dust properties of these sources. Finally, new SCUBA-2 data over the entire NEP-Wide area will allow us to expand the SPIRE-dropout method to the wide field area. This new updated SCUBA-s catalogue of Geach et al. (2016) that contains 330 sources will be used to confirm and extend the early catalogue used in Section 2.3.4 which was limited to 136 sources (with an apparent systematic positional offset). This is necessary - together with spectroscopic confirmation - to confirm the nature of the SPIRE dropouts, which will allow us to address and answer the question of the nature of the DSFGs at high redshift and the evolutionary link to the local Universe.

6.2.2 Physical properties of the high-z population at the NEP

Future work on exploiting the high-redshift sources discovered in this thesis will centre on making spectroscopic observations of individual sources using ground based facilities.

At the dawn of the discovery of the SMG population, it was suggested that a powerful tool to obtain accurate spectroscopic redshifts would be the CO lines (Blain et al., 2002). The future has arrived and the Large Millimetre Telescope (LMT; Schloerb, Carrasco & Brinks (2007)) will finish its early science phase soon, allowing external users to apply for time on the facility. I will propose to include a list of the 13 sources at photometric redshift between $4 < z < 6$ together with examples of high-z galaxy candidates with high star formation efficiency in order to study their gas properties. The main aim

of this future proposal will be to obtain spectroscopic redshifts, to confirm the photometric redshift, with the strategy to observe using two instruments on the telescope in order to optimize the time while submitting a large list ($\sim$20) objects. Snapshot photometry will simultaneously be made with the AzTEC camera at 1.1 mm, then, if a detection is confirmed, follow up spectroscopy will be made with the Redshift Spectroscopic Receiver (RSR) to detect the CO lines using the AzTEC position. This will allow observation of a large number of sources and guarantee that hours of spectroscopic observation are not wasted without detection. Furthermore, the position derived from AzTEC will be more accurate for spectroscopy that the current SPIRE position due to the smaller beam size of the former and the closer band position. In the case where there is no detection at 1.1 mm the observation can still provide an upper-limit as input to the CIGALE SED fitting code in order to improve the photometric redshift. Regarding the spectroscopy, the RSR was made specifically for the detection of high-z SMGs since it covers a wide range of the submillimetre spectrum, a 90 GHz atmospheric window (73-111 GHz) in a single tuning. The resolution is good enough to detect CO lines and calculate the spectroscopic redshift. Clearly millimetric spectroscopic observations have the advantage of not requiring multi-wavelength counterpart identification and since these galaxies have been already detected in the submillimetre, they are expected to have luminous millimetre counterparts, which will facilitate the identification.

Two sources from my sample (see Figure 3.26) have already been submitted as a spectroscopic proposal to the SMA under the name of "Building a sample of the highest redshift SMGs". The proposal is a blind search for the [CII] line in order to confirm a spectroscopic redshift which if detected, will enforce the idea of selecting sources in multi-wavelength coverage fields and it will allow us to expand the study to other fields as proposed in Chapter 2. It is expected to be a relatively easy detection, since the [CII] line is very bright and can contain up to 1 % of the total bolometric luminosity of a source, tending to be one of the brightest lines in SMGs. The [CII] can be a good indicator of the star formation Sargsyan et al. (2012), although other authors

defend that although report an empirical calibration between [CII] and the SFR, [CII] is not a good indicator of star formation (Farrah et al., 2013). Indeed, the role of [CII] as a SFR tracer in DSFGs is under debate (see Casey, Narayanan & Cooray (2014) for review) and a thorough analysis in the high-z sample that this thesis presents can through some light on this topic. This follow up spectroscopy will also allow me to address additional outstanding issues of high redshift galaxies and their relationship to populations in the local-intermediate redshift Universe such as the [CII] deficit between ULIRGs (Zavala et al., 2018) and the relationship between the SFR and compactness of galaxies on and off the Main Sequence (Elbaz et al., 2011) The former will be investigated through the proposed SMA observations of selected $z_{phot} \sim 5$ galaxies, to determine whether these galaxies are representative of the high-z population, the latter will be investigated using the optical images from the SUBARU Hyper-SuprimeCam (data already taken). A combination of these observations will reveal any link between the [CII] deficit in the high-z star forming galaxies and their SF-compactness (see Díaz-Santos et al., 2013).

Further photometric data at longer wavelengths can also be accrued in order to better constrain the photometric redshift. One of the possibilities is to get photometry for my sources with the NIKA2 instrument on IRAM telecope at 1.3 mm and 2 mm. Obtaining these two data points would be key to robust SED fitting, since in some cases there are only SPIRE detections. Furthermore, the extension of new data in the NEP, which includes *Spitzer*, SCUBA-2, and improved exploitation of the PACS data (see Future work in Chapter 2), will allow me to constrain the FIR peak and improve the photometric redshift and dust properties of the star-forming population.

6.2.3 Radio properties of galaxies

Chapter 4 contained a variety of pilot studies that should be further developed. Moreover, much of the work described in this Chapter was made using the initial versions of the radio catalogues that have since been updated (e.g. White, in prep.).

Utilising the new catalogues, future work will include:

- Improved AGN classification

The NEP is a unique field with extensive high quality photometric and growing spectroscopic data which will allow us to check the reliability of the AGN classification Furthermore, the recent incorporation of Spitzer data in the NEP makes the combination of the two data sets to classify AGN even more reliable (see Figure 6.1). A thorough study of AGN classification in the NEP field by combining colour-colour diagrams and SED fitting methods will be made. The reliability of the classification schemes can be confirmed using direct spectroscopy, then photometric classification will be used to select AGN for future follow-up.

The reliability of the AGN classification will be checked with the LePhare fitting code since it allows a comparison of the data with an extended set of templates that are AGN dominated. However, the photometric redshift must first be calculated with another code. CIGALE is tailor made for this purpose since it allows us to introduce AGN models and both methods combined will allow us to check the results with different codes and see if they are consistent.

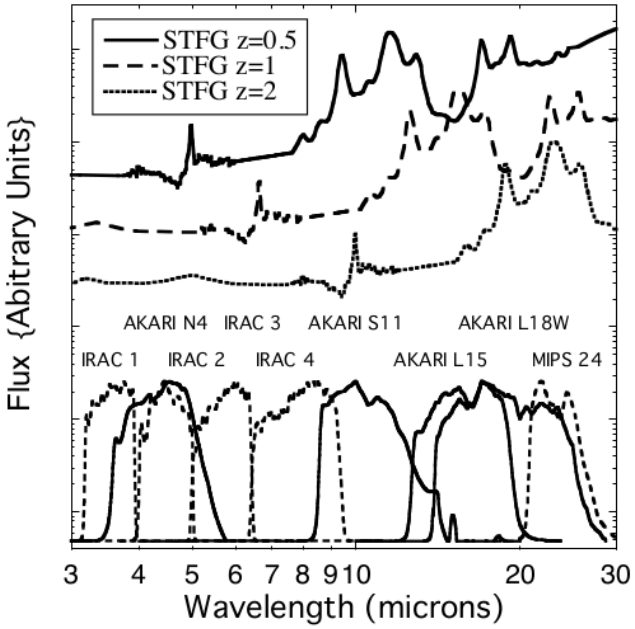

Figure 6.1: This Figure from Pearson et al. (2010) shows the SED of three star forming galaxies (STFG) in the PAHs region of the spectrum at redshifts z= 0.5 , 1 and 2 respectively (upper part). In the lower part of the diagram AKARI and Spitzer filters are represented which perfectly cover this part of the spectrum for SFGs at different redshifts.

6.2.4 Optical catalogue of IR sources at the South Ecliptic Pole.

A major legacy data product from this thesis was the R-band optical catalogue. Much time was spent on the data reduction and analysis in order to produce a lasting and valuable product for future scientific exploitation. Work on this legacy product will continue with the aim of producing a fully comprehensive, multi-wavelength public catalogue in the SEP field.

The work carried out in Chapter 5 significantly contributes to this task. Furthermore, by gathering these data, it will allow me to produce a much more thorough study of DOGs, which will be conducted combining optical data from the DECam catalogue (see Table 5.1). This will extend the number of DOGs candidates to $\sim$900 sources with good multi-band coverage using further archival data. This will enable a thorough study of the nature of DOGs allowing determination via SED fitting as to whether the high IR luminosity is produced by an AGN (power-law) SED or by star formation ('bump') SED (Dey et al., 2008). It is very unlikely that the optical emission

from DOGs is dominated by old stellar populations since most of the luminous regions of the galaxy are shrouded in dust. DOGs may represent an evolutionary phase in the formation of massive galaxies when the AGN turns on and begins the process of terminating the star formation (Dey et al., 2008). This extended analysis, already underway, will help answer whether AGN were bolometrically more dominant in DOGs at the peak epoch of the volume-averaged star formation density, compared to later epochs.

Moreover, the use of the code CIGALE (already used extensively in this thesis research) will be used to calculate the photometric redshift and other physical parameters, such as the luminosities, SFRs, AGN presence, etc.

Appendix A

Appendix

A.1 High redshift candidates

ID	RA [deg]	Dec [deg]	$F_{250\mu m}$ [mJy]	$F_{350\mu m}$ [mJy]	$F_{500\mu m}$ [mJy]
3871	266.76	66.50	34.24±8.38	37.84±6.59	42.36±7.99
3257	266.79	66.28	29.24±8.72	33.94±7.37	35.13±9.43
1965	267.00	66.14	45.87±8.86	40.82±7.13	43.39±8.71
2512	267.07	65.92	39.35±8.28	57.28±7.07	43.45±7.79
3475	267.11	66.70	38.10±8.98	43.17±6.75	51.24±8.96
3915	267.14	65.87	29.62±7.85	38.05±7.11	24.16±8.69
2614	267.17	66.64	46.34±9.94	50.10±7.35	39.55±9.30
2763	267.25	66.54	36.49±8.65	67.39±7.74	36.86±7.84
3550	267.28	66.84	36.97±8.77	64.50±7.95	69.48±8.52
3623	267.36	65.76	32.04±7.74	46.70±6.31	33.60±7.59
1636	267.42	66.11	50.46±8.62	76.86±6.69	46.79±9.69
2774	267.43	66.88	35.85±8.04	47.68±7.16	40.27±8.13

Table A.1: List of the 186 high-z candidates in the NEP sort it out by deacrising readshift. The first column is the ID we gave to the source and the rest of their columns are as follows: redshift, SFR, solar masses, gass masses, AGN fraction and χ^2.

ID	RA [deg]	Dec [deg]	$F_{250\mu m}$ [mJy]	$F_{350\mu m}$ [mJy]	$F_{500\mu m}$ [mJy]
1960	267.74	65.70	46.15±8.84	42.19±7.65	38.00±7.83
969	267.75	67.20	54.92±8.58	50.09±7.52	41.78±8.05
1261	267.80	66.40	51.04±8.56	65.59±6.44	47.37±7.98
4547	267.81	66.15	35.78±9.36	41.58±7.40	40.54±8.48
2715	267.82	67.39	27.76±8.48	37.07±7.14	22.19±8.28
1068	267.91	66.80	61.68±9.68	64.38±7.60	49.31±8.49
4321	267.93	65.71	24.16±8.43	26.24±6.82	28.18±8.84
2533	267.96	65.91	30.51±8.05	36.15±7.19	24.59±7.63
2039	268.00	67.11	38.07±9.19	49.42±7.47	41.71±8.45
2202	268.05	66.01	35.07±8.16	61.61±7.23	29.82±8.62
4237	268.09	65.44	33.49±8.55	39.10±7.55	32.47±8.42
1386	268.12	65.68	49.86±8.56	53.93±6.75	40.18±8.84
1214	268.16	67.25	50.12±8.35	72.06±7.12	41.53±8.64
3878	268.18	66.14	33.08±8.03	62.22±6.92	60.49±8.08
750	268.23	67.51	60.97±8.44	79.95±7.65	61.04±8.98
3491	268.30	66.98	38.25±9.01	41.85±7.63	41.24±8.23
912	268.39	65.61	58.28±8.59	41.17±7.28	45.74±7.85
3447	268.50	65.97	37.96±8.88	56.05±6.63	59.26±9.24
3782	268.50	65.53	35.22±8.34	38.43±7.30	42.01±8.52
2163	268.60	67.30	38.67±7.69	48.90±7.92	43.03±8.27
3017	268.67	67.24	40.68±9.05	36.11±7.32	41.37±9.59
4377	268.77	65.80	32.64±9.33	53.79±7.42	42.50±8.37
3715	268.78	65.67	37.84±9.18	50.57±7.22	30.23±8.74
1215	268.78	67.25	49.99±8.24	47.58±7.01	39.94±7.85
4804	268.82	67.61	34.06±8.98	39.63±7.19	39.87±7.97
3976	268.99	67.13	34.22±8.40	45.66±6.96	32.24±8.32
4330	269.02	65.90	34.84±8.86	41.82±7.21	44.76±8.40
4788	269.12	65.61	33.91±9.00	57.09±7.20	39.10±9.35
2227	269.14	65.38	42.23±8.54	48.86±6.83	33.05±8.20
2198	269.17	65.26	41.37±8.45	37.44±7.45	31.32±8.22
1698	269.25	67.29	45.75±8.48	41.18±7.74	35.40±9.27
4673	269.26	65.72	30.61±8.08	41.69±6.94	25.50±9.26
4539	269.37	65.35	36.23±9.36	40.62±6.99	47.47±8.20
2822	269.42	66.03	41.43±8.85	47.71±7.19	31.20±8.39
3697	269.43	67.64	34.27±8.39	43.86±7.24	36.72±8.46
3589	269.44	67.05	16.59±4.40	38.05±3.58	28.06±4.37
3009	269.55	65.92	32.28±8.25	39.42±7.63	49.41±8.60
1891	269.57	65.46	46.14±8.91	35.87±7.30	35.48±8.90
1937	269.63	67.66	46.89±8.92	39.87±6.92	37.36±8.47
2492	269.65	67.04	6.820±4.14	14.68±4.07	20.45±4.47

Table A.2: Same as Table A.1

ID	RA [deg]	Dec [deg]	$F_{250\mu m}$ [mJy]	$F_{350\mu m}$ [mJy]	$F_{500\mu m}$ [mJy]
3906	270.05	65.71	38.64±8.71	44.52±8.20	34.87±8.05
935	270.07	66.34	16.80±4.55	18.88±3.84	26.62±4.52
2342	270.07	65.82	45.41±9.42	42.17±6.82	39.16±8.56
3261	270.09	67.11	35.12±8.28	39.65±7.31	32.88±8.29
3451	270.10	67.35	33.22±7.83	47.10±6.67	28.17±7.97
2574	270.13	66.97	18.54±5.03	19.82±4.71	24.74±4.79
377	270.15	66.36	36.01±3.96	54.37±3.43	29.99±4.29
1733	270.15	66.29	30.81±5.73	40.02±4.30	24.94±5.03
3064	270.20	65.22	40.78±9.20	51.69±7.14	36.87±9.18
1985	270.21	66.78	19.03±3.72	20.00±3.19	21.18±3.73
578	270.23	66.74	29.91±3.74	38.75±3.15	25.76±3.54
2219	270.27	65.98	42.35±8.59	48.70±7.06	38.80±9.06
939	270.30	66.70	27.00±4.06	31.27±3.43	31.98±3.82
110	270.30	66.65	50.04±3.68	56.12±3.03	38.80±3.91
3018	270.37	65.76	39.57±8.77	36.98±7.08	30.90±8.07
4038	270.43	66.93	19.76±7.48	23.67±4.93	26.68±6.47
3026	270.46	67.13	39.10±8.47	40.40±6.57	36.40±8.67
1319	270.48	67.29	51.44±8.66	74.53±6.65	48.00±8.54
4227	270.49	67.35	28.20±8.88	30.21±6.91	36.45±8.33
4047	270.54	66.83	7.261±4.74	8.340±4.05	11.09±5.34
4279	270.59	66.10	33.57±8.59	35.69±7.14	33.53±9.21
3650	270.62	66.57	23.55±5.36	43.44±4.08	43.18±5.14
2493	270.63	66.24	44.26±9.36	48.58±7.54	44.22±8.23
2192	270.63	67.46	42.93±8.48	57.27±7.64	35.94±8.74
2357	270.64	66.73	25.13±5.24	36.60±4.69	25.74±5.51
1668	270.66	65.37	48.12±8.77	61.33±6.76	45.19±9.53
4612	270.70	65.92	33.36±8.66	47.05±7.17	42.67±8.11
553	270.72	66.57	34.93±4.42	38.59±3.93	30.33±5.22
2985	270.73	66.19	37.97±8.51	45.32±7.13	42.21±8.78
2539	270.81	65.27	40.70±8.56	62.26±6.84	38.74±9.06
1990	270.83	65.66	46.30±8.99	71.66±6.69	58.47±9.48
2835	270.83	67.07	39.31±8.72	40.96±7.15	39.77±8.38
1079	270.85	66.56	30.70±4.80	38.32±4.08	30.35±4.80
3980	270.88	65.54	38.58±9.39	58.60±7.42	46.97±8.75
2787	270.89	65.46	42.31±9.26	36.81±7.26	35.76±8.89
1486	271.03	65.61	46.88±8.29	50.36±6.98	41.27±8.16
2679	271.05	66.74	40.00±8.51	39.17±7.12	41.71±8.15
3141	271.07	67.63	36.35±8.28	38.17±7.05	28.07±9.06
914	271.12	66.91	55.57±8.23	38.56±7.77	43.00±8.17
2257	271.15	66.84	47.27±9.58	50.01±7.29	41.80±7.70
728	271.20	65.64	57.51±7.85	62.32±7.03	51.40±8.46
4696	271.21	65.97	32.51±8.49	44.73±6.84	38.17±8.45
3446	271.29	67.10	26.16±8.37	36.13±6.86	22.33±7.89
1205	271.35	67.37	53.57±8.75	75.75±7.48	50.33±9.49
3753	271.50	67.12	42.54±8.61	37.98±8.07	37.87±8.17
1344	271.54	65.61	52.46±8.97	64.70±7.00	42.21±8.94

Table A.3: Same as Table A.1

ID	RA [deg]	Dec [deg]	$F_{250\mu m}$ [mJy]	$F_{350\mu m}$ [mJy]	$F_{500\mu m}$ [mJy]
2191	271.68	65.61	45.02±8.99	55.66±6.85	48.43±8.89
590	271.79	66.67	64.60±8.21	89.88±7.42	65.31±9.48
2450	271.80	67.22	37.59±8.99	37.08±6.51	36.50±7.85
3466	271.89	67.03	34.19±8.75	54.95±7.22	25.80±8.88
1396	271.91	66.85	50.06±8.64	35.17±6.90	43.64±8.34
2029	271.96	66.69	50.69±8.93	64.61±7.46	48.47±8.06
729	272.03	66.21	59.68±8.22	65.98±6.72	47.31±8.25
1932	272.13	65.95	24.28±9.34	38.89±7.09	29.08±8.63
3634	272.14	67.06	36.74±9.28	42.68±7.02	45.03±8.50
3727	272.17	67.37	35.81±8.42	39.03±6.79	34.82±8.12
951	272.20	67.40	61.70±9.33	58.55±7.54	46.87±9.25
1843	272.20	66.55	42.44±8.13	64.03±6.95	35.97±9.03
2589	272.44	67.19	40.52±8.58	51.98±7.11	41.43±8.54
1024	272.45	65.75	52.43±8.06	59.63±7.11	62.74±8.44
930	272.51	66.99	56.75±8.54	55.57±7.11	45.20±9.28
2184	272.54	65.91	43.01±8.63	61.49±7.57	42.71±7.71
1542	272.64	66.41	47.73±8.43	60.30±6.80	55.34±7.59
2747	272.69	67.05	43.28±8.34	42.16±6.84	34.50±9.26
1835	272.73	67.35	43.60±8.12	43.18±7.11	33.63±8.40
2918	272.74	67.03	36.15±8.06	38.72±7.22	30.22±8.16
1986	272.85	67.34	45.37±8.80	41.51±7.73	38.07±9.62
4115	272.91	67.12	29.55±8.48	30.69±7.17	43.42±8.10
3882	272.99	66.35	33.81±8.50	35.83±6.95	26.41±8.86
1935	273.11	66.82	44.81±8.67	47.52±6.43	39.31±8.03
2435	273.11	66.80	41.15±8.58	42.41±6.90	37.39±8.62
2735	273.23	66.87	42.22±9.29	36.77±7.63	31.75±7.84
4398	266.44	67.22	18.99±8.16	25.07±6.79	31.08±8.33
2100	270.29	66.43	22.18±4.40	23.74±3.62	30.08±4.28
1400	274.07	65.79	10.49±7.18	20.79±6.62	26.46±7.38
27	274.27	66.02	199.0±8.60	235.4±8.70	192.9±8.92
127	266.82	66.65	111.1±8.53	107.7±7.90	95.81±8.06
131	273.80	66.49	110.9±8.59	97.59±7.05	84.24±8.95
462	269.17	67.72	72.36±8.33	69.71±6.81	62.57±8.85
489	271.79	65.37	74.74±8.88	90.62±7.42	83.84±8.52
576	270.62	65.19	69.28±8.79	103.1±7.14	78.33±9.93
605	265.89	67.09	70.22±9.08	71.61±6.84	63.06±8.30
757	265.47	66.88	56.55±7.82	67.89±6.86	50.67±8.62
771	269.69	68.02	60.96±8.49	50.22±7.13	50.16±8.18
841	267.29	66.86	63.96±9.12	53.38±6.58	52.93±9.56
905	265.99	66.54	54.85±8.09	66.98±6.66	51.79±7.35
1054	272.17	66.21	53.71±8.37	46.96±7.75	43.62±8.27
1100	273.59	66.97	60.97±9.61	79.96±11.4	67.99±11.2
1156	271.56	68.11	45.82±8.00	41.21±7.18	35.10±8.15
1171	270.14	65.12	48.94±7.85	46.75±7.47	39.97±8.83
1219	273.49	65.69	53.50±8.83	68.61±7.17	70.80±8.84
1243	266.38	67.31	51.64±8.62	60.38±7.08	52.12±8.82

Table A.4: Same as Table A.1

ID	RA [deg]	Dec [deg]	$F_{250\mu m}$ [mJy]	$F_{350\mu m}$ [mJy]	$F_{500\mu m}$ [mJy]
1248	269.26	67.96	52.00±10.3	59.98±7.58	44.32±9.29
1255	270.88	65.38	51.41±8.56	43.67±6.96	42.21±8.12
1296	273.34	67.01	48.88±8.26	66.70±7.14	47.79±8.99
1310	273.69	66.01	56.09±9.69	54.31±8.05	64.27±9.25
1343	268.64	67.71	47.64±8.12	41.57±7.00	51.15±8.58
1368	270.82	67.14	48.88±8.30	54.76±7.11	41.36±9.21
1413	268.29	64.84	70.52±12.2	84.50±11.4	62.56±11.8
1417	271.71	67.58	39.89±8.08	58.98±8.26	33.98±8.99
1447	266.18	67.18	50.96±8.83	47.35±7.44	44.81±8.56
1452	268.27	64.96	62.66±10.3	81.46±8.33	54.11±11.7
1516	271.31	67.68	46.27±8.19	55.61±7.07	42.71±8.83
1544	267.27	66.35	50.48±8.95	48.91±7.47	41.44±8.40
1560	272.87	67.26	47.25±8.29	57.08±7.16	42.20±7.98
1586	266.54	67.08	50.22±8.98	43.72±7.53	38.98±8.55
1634	273.44	66.95	47.62±8.64	36.28±6.86	48.90±8.25
1715	270.98	68.10	47.14±8.70	76.57±8.18	46.82±8.40
1717	269.21	65.19	45.49±8.41	45.08±7.68	34.17±8.58
1729	269.13	65.24	42.90±7.96	68.02±7.12	61.65±9.40
1760	269.65	65.02	46.06±8.59	54.03±7.82	58.55±9.26
1862	269.07	67.24	45.60±8.65	55.83±7.62	41.71±8.79
1867	272.16	65.56	45.94±8.76	47.58±7.61	53.37±9.61
1886	265.90	66.82	45.36±8.70	53.89±7.47	53.45±9.04
1899	274.09	66.33	38.83±7.16	44.82±5.85	52.16±7.40
1910	269.17	67.09	44.33±8.49	39.31±6.68	35.71±9.31
1915	270.84	65.07	51.69±9.94	51.95±9.73	41.09±9.66
1972	273.73	66.72	45.37±8.75	59.99±6.50	55.60±8.47
1995	268.89	67.88	47.92±9.31	45.04±7.64	45.86±8.56
2021	268.96	65.05	45.71±8.87	44.88±6.71	42.01±8.99
2031	271.14	68.02	39.53±8.02	53.32±6.79	37.51±8.31
2052	273.63	66.67	47.17±9.23	55.48±7.06	39.23±8.10
2077	272.80	65.66	49.46±9.87	47.45±7.35	64.78±8.42
2105	271.02	65.79	43.56±8.70	36.75±8.04	34.20±8.36
2113	272.70	66.56	48.15±9.34	86.84±7.22	99.25±8.49
2122	267.81	65.14	53.00±10.5	59.37±8.34	44.91±10.6
2174	270.24	67.78	41.78±8.33	48.72±6.87	33.37±9.26
2209	270.90	65.94	43.18±8.63	51.55±6.95	41.98±8.60
2228	267.40	67.57	41.80±8.51	62.11±6.75	47.28±8.18
2241	268.68	65.22	43.50±8.84	68.05±7.89	46.41±8.35
2296	273.02	67.40	41.94±8.93	48.01±7.11	37.24±8.32
2302	271.69	65.40	46.51±9.49	42.80±6.90	37.54±8.27
2327	273.67	66.25	40.05±8.13	40.43±7.11	30.35±8.65
2336	268.91	65.01	39.32±8.10	40.03±6.95	35.74±8.90
2379	271.71	68.33	63.63±13.2	85.37±10.1	74.05±13.0
2517	271.35	68.28	42.54±8.90	41.18±7.56	43.90±8.41
2630	267.95	67.46	45.12±9.72	69.60±7.15	52.98±8.76
2633	271.72	68.22	39.04±8.41	46.64±7.86	30.46±8.41

Table A.5: Same as Table A.1

ID	RA [deg]	Dec [deg]	$F_{250\mu m}$ [mJy]	$F_{350\mu m}$ [mJy]	$F_{500\mu m}$ [mJy]
2663	270.18	65.07	42.75±9.14	37.56±7.33	38.52±9.14
2671	270.79	67.86	27.92±8.86	48.16±6.86	21.64±8.21
2672	273.45	66.39	41.96±8.96	60.93±7.41	56.13±8.72
2674	269.57	67.90	40.01±8.62	53.32±6.70	48.17±7.92
2687	267.71	65.22	60.35±12.9	47.15±7.48	50.33±11.5
2732	269.33	65.92	36.91±7.92	50.11±6.76	52.86±8.51
2803	269.62	64.83	39.13±8.71	44.82±7.52	40.51±8.77
2830	272.31	67.56	43.60±9.60	58.65±7.73	35.18±9.82
2841	273.93	65.95	40.03±8.79	36.49±7.60	41.58±8.43
2844	268.16	65.93	39.42±8.58	40.34±6.91	35.03±8.50
2888	272.01	68.37	42.89±9.71	41.39±9.02	32.63±10.7
2906	274.12	66.27	33.09±8.47	38.77±6.62	28.28±7.42
2969	270.76	67.81	34.02±8.52	35.30±6.76	31.71±9.53
2976	273.72	66.56	38.79±8.74	50.17±7.10	47.79±8.48
2995	273.45	66.18	41.70±9.41	61.29±7.25	50.71±9.20
3010	272.82	65.50	39.25±9.04	52.19±6.90	29.97±9.50
3022	266.21	67.11	39.36±8.81	47.84±7.58	51.32±8.34
3033	268.62	65.97	40.14±9.03	46.85±7.71	37.19±8.87
3159	272.20	67.44	46.49±10.6	35.89±7.48	36.10±8.26
3191	265.67	67.05	38.99±8.90	45.67±6.71	36.35±7.83
3199	270.96	67.79	38.90±8.99	48.22±7.34	38.40±9.67
3211	267.00	67.05	43.43±9.00	42.93±7.69	39.53±9.40
3269	271.08	65.45	39.60±9.07	39.91±7.39	34.50±9.22
3308	271.19	68.23	31.94±9.10	42.79±6.91	25.24±8.56
3318	270.73	67.42	37.18±8.66	41.88±8.71	36.53±8.34
3356	265.64	67.23	32.84±7.82	44.94±6.23	39.61±7.53
3411	268.46	65.04	35.25±8.25	38.46±6.59	27.86±8.17
3437	271.91	65.32	49.35±11.6	49.01±8.30	41.92±12.1
3440	269.89	65.05	35.04±8.28	35.49±7.70	33.16±9.24
3461	268.82	67.78	37.70±8.86	52.97±6.97	37.17±7.95
3463	273.78	65.99	38.34±8.16	43.94±7.26	29.71±8.11
3480	271.01	67.73	36.43±8.72	37.54±6.83	35.16±8.94
3508	267.23	67.17	36.02±8.44	38.07±7.47	27.83±7.78
3530	266.63	67.19	40.92±9.84	51.41±6.98	33.20±8.88
3575	268.43	67.67	35.34±8.39	43.45±6.60	29.05±8.35
3617	272.46	65.43	44.34±10.7	40.57±7.93	53.28±10.3
3645	272.75	65.63	34.54±8.35	42.05±7.44	31.73±9.37
3654	270.44	67.90	35.37±8.70	49.42±8.30	32.20±8.06
3776	267.98	65.00	37.98±9.21	35.77±8.28	33.87±9.21
3785	273.77	66.06	30.88±9.14	50.98±6.71	41.48±8.40
3876	271.55	65.21	50.34±13.4	53.00±8.96	42.16±13.9
3889	270.75	65.10	40.69±9.91	43.61±7.21	42.18±10.2
3940	269.71	67.64	37.49±9.44	38.58±7.36	32.44±8.42
4103	271.16	67.62	34.04±8.57	35.46±7.03	43.05±8.93
4157	274.06	66.21	32.24±8.06	36.73±7.23	30.72±8.18
4168	268.38	65.33	24.12±8.67	49.74±6.50	24.57±8.36

Table A.6: Same as Table A.1

ID	RA [deg]	Dec [deg]	$F_{250\mu m}$ [mJy]	$F_{350\mu m}$ [mJy]	$F_{500\mu m}$ [mJy]
4178	271.66	67.88	35.11±8.81	36.85±7.26	27.47±8.78
4202	270.29	67.82	34.12±8.62	41.87±7.10	27.24±7.92
4251	270.61	65.02	51.22±13.8	60.46±11.0	39.61±12.3
4341	273.58	67.07	43.54±11.0	36.56±9.68	50.97±10.8
4351	273.76	66.21	35.87±9.17	36.23±7.47	27.98±8.52
4400	268.09	65.34	43.47±8.99	43.41±7.64	38.49±8.13
4438	270.52	67.74	34.78±8.92	53.17±6.97	47.91±8.47
4455	270.05	68.24	34.80±11.9	40.81±8.80	52.48±10.0
4527	267.26	66.32	33.12±8.22	47.05±6.31	29.30±9.01
4536	270.87	66.24	34.16±8.84	51.64±6.84	45.38±8.09
4552	273.59	66.95	42.91±11.1	42.92±10.1	36.97±12.9
4575	270.51	67.99	35.29±9.36	49.48±7.35	30.42±8.75
4619	266.67	66.10	34.55±8.95	37.11±7.63	26.15±8.66
4807	274.04	65.78	30.22±7.98	43.11±6.62	40.82±8.55
241	269.87	66.87	36.81±3.47	44.37±2.89	35.60±3.60
161	268.82	66.42	61.37±5.10	23.02±5.02	5.076±5.03
240	269.13	66.55	36.54±3.45	44.05±2.85	30.77±3.62
259	269.07	66.76	39.33±3.84	49.75±3.22	34.58±3.79
266	268.70	66.58	48.94±4.82	51.83±3.97	39.53±4.93
277	269.21	66.66	31.36±3.22	37.03±2.93	30.35±3.38
289	269.28	66.68	33.45±3.44	38.42±2.83	27.55±3.54
373	269.90	66.61	30.14±3.32	38.72±2.84	31.44±3.66
447	269.49	66.61	30.94±3.58	44.14±2.98	34.28±3.84
562	269.23	66.90	32.62±4.07	39.71±3.32	25.92±4.41
618	268.81	66.73	34.79±4.50	48.99±3.63	28.20±4.89
753	269.04	66.66	26.60±3.68	36.64±2.83	35.81±3.87
762	269.76	66.65	15.47±3.46	25.04±2.88	32.24±3.56
861	269.50	66.34	25.30±3.72	37.02±3.00	28.28±3.87
994	269.42	66.90	14.91±3.47	19.77±2.85	5.380±3.53
1707	270.06	66.56	19.75±3.72	29.38±2.96	29.99±3.46
1838	268.05	66.65	51.51±9.71	36.78±6.70	41.79±8.87
2258	269.26	66.22	29.65±6.00	25.06±4.78	7.900±5.57
2267	270.04	66.33	12.75±4.48	27.75±3.62	28.31±4.03
2627	270.03	66.59	10.73±3.29	12.63±2.76	18.26±3.50
2652	268.81	66.84	13.69±5.43	38.45±4.11	28.84±5.15
2725	269.18	66.57	16.10±3.48	12.45±2.75	3.543±3.40
2812	269.22	66.75	15.32±3.43	9.48E±2.78	1.255±3.38
2968	269.90	66.61	11.77±3.47	10.56±2.73	1.528±3.60
2996	269.16	66.65	13.95±3.36	18.60±2.79	26.59±3.37
3133	268.35	66.53	39.32±8.86	44.85±6.53	30.39±8.54
3321	269.28	66.25	23.40±5.51	27.82±4.31	29.79±5.03
3370	268.95	66.15	37.75±8.92	42.29±8.08	38.90±8.84
3725	270.01	66.69	13.91±3.36	3.682±2.89	1.912±3.44
3747	267.96	66.58	36.06±8.72	11.41±8.01	2.832±8.56

Table A.7: Same as Table A.1

ID	RA [deg]	Dec [deg]	$F_{250\mu m}$ [mJy]	$F_{350\mu m}$ [mJy]	$F_{500\mu m}$ [mJy]
3829	269.40	66.27	20.31±4.95	14.14±3.72	4.077±4.95
3911	269.33	66.47	19.38±3.29	13.71±2.63	3.418±3.65
3970	268.99	66.89	23.94±5.77	26.78±4.03	31.68±6.07
4142	268.11	66.35	33.59±8.43	39.62±7.48	29.02±7.55
4175	269.07	66.39	16.73±4.42	17.96±4.32	19.30±5.14
4191	269.21	66.29	23.26±6.56	45.83±4.89	31.78±6.17
4193	269.67	67.04	15.75±4.03	26.80±3.67	32.58±4.75
3213	269.68	67.74	34.37±7.90	46.60±7.32	39.64±9.19
1227	269.68	67.60	52.88±9.50	55.91±7.41	48.24±8.06
1045	269.72	65.54	55.09±8.58	77.89±8.07	54.85±9.40
2545	269.82	66.19	28.83±6.12	35.16±4.27	32.90±5.59
1211	269.86	67.00	27.82±4.57	39.12±3.79	22.80±5.05
4120	269.87	65.60	36.57±9.15	39.74±7.03	29.49±7.89
3852	270.00	67.56	34.44±8.34	79.28±7.33	88.09±8.99
2452	270.01	67.31	41.78±8.72	36.96±7.15	33.90±9.23
2064	270.02	67.65	36.86±7.59	35.54±6.73	29.39±8.17
4525	267.53	66.05	34.78±8.99	58.08±7.70	36.52±7.99
3060	267.55	66.98	38.59±8.62	40.80±6.39	29.79±7.87
3811	267.62	66.91	36.42±8.85	41.78±6.79	30.04±9.13
2940	267.64	66.08	32.37±8.99	55.00±7.38	47.01±9.38
67	267.71	66.08	133.0±8.05	155.0±7.44	115.2±8.14

Table A.8: Same as Table A.1

ID	z_{phot}	SFR $[M_\odot/yr]$	M_* $[M_\odot]$	M_{gas} $[M_\odot]$	Ageburst [Myrs]	AGN fraction [%]	χ^2
3623	6.2 ± 0.3	12392 ± 6278	2.1332E12 $\pm$ 7.80E11	8.22E11 $\pm$ 3.22E11	118	0.06	0.53
2202	5.9 ± 0.3	7083 ± 1169	1.5326E12 $\pm$ 5.365E11	6.34E11 $\pm$ 2.84E11	120	0.1	1.34
762	5.7 ± 0.3	3979 ± 473	2.0684E12 $\pm$ 4.435E11	1.035E12 $\pm$ 2.632E11	155	0.15	0.9
4377	5.6 ± 0.3	30820 ± 5612	4.1966E12 $\pm$ 1.293E12	1.61E12 $\pm$ 6.94E11	91	0.01	2.15
1319	5.6 ± 0.3	37789 ± 3793	5.359E12 $\pm$ 1.6723E12	2.063E12 $\pm$ 9.00E11	94	0.0	5.02
NEP0163	5.5 ± 0.3	3623 ± 576	7.94E11 $\pm$ 1.6866E11	3.286E11 $\pm$ 1.074E11	133	0.11	3.01
3915	5.1 ± 0.3	5746 ± 806	2.515E12 $\pm$ 5.1445E11	1.249E12 $\pm$ 3.14E11	133	0.0	1.15
1542	4.9 ± 0.2	9519 ± 4223	4.979E12 $\pm$ 6.371E11	2.536E12 $\pm$ 3.91E11	151	0.1	3.36
1636	4.7 ± 0.2	65294 ± 3265	4.2105E13 $\pm$ 2.1054E12	2.18E13 $\pm$ 1.095E12	182	0.0	16.19
NEP0051	4.7 ± 0.2	3225 ± 841	6.715E11 $\pm$ 3.133E11	2.863E11 $\pm$ 1.72E11	113	0.01	0.59
914	4.5 ± 0.2	7694 ± 567	1.067E12 $\pm$ 1.4613E11	3.714E11 $\pm$ 7.05E10	111	0.1	15.45
3811	4.5 ± 0.2	6523 ± 720	1.4295E12 $\pm$ 2.826E11	5.71E11 $\pm$ 1.748E11	148	0.0	9.36
259	4.2 ± 0.2	6069 ± 494	6.925E11 $\pm$ 9.822E10	2.367E11 $\pm$ 4.896E10	82	0.0	11.43
1985	4.0 ± 0.2	2126 ± 106	1.0631E12 $\pm$ 1.872E11	5.30E11 $\pm$ 1.185E11	156	0.25	4.52
NEP0018	4.0 ± 0.2	3805 ± 1871	5.916E11 $\pm$ 1.2732E11	2.373E11 $\pm$ 8.19E10	105	0.12	5.02
2198	3.9 ± 0.2	38988 ± 1949	2.5576E13 $\pm$ 1.2787E12	1.324E13 $\pm$ 6.63E11	189	0.0	13.16
3550	3.8 ± 0.2	3269 ± 400	5.431E11 $\pm$ 2.4768E11	2.17E11 $\pm$ 1.332E11	103	0.12	0.45
935	3.5 ± 0.2	1108 ± 156	2.643E11 $\pm$ 1.1858E11	1.163E11 $\pm$ 6.74E10	119	0.12	0.35
3009	3.5 ± 0.2	1859 ± 193	3.284E11 $\pm$ 1.5006E11	1.334E11 $\pm$ 8.28E10	106	0.1	0.27
4612	3.5 ± 0.2	2300 ± 198	4.394E11 $\pm$ 2.102E11	1.838E11 $\pm$ 1.16E11	108	0.25	0.73
4330	3.4 ± 0.2	1572 ± 268	4.6297E11 $\pm$ 2.1362E11	2.135E11 $\pm$ 1.212E11	123	0.24	0.88
3447	3.3 ± 0.2	2610 ± 313	5.373E11 $\pm$ 2.0775E11	2.254E11 $\pm$ 1.199E11	117	0.1	1.69
3133	3.3 ± 0.2	2404 ± 120	1.5318E12 $\pm$ 1.0077E11	7.91E11 $\pm$ 5.80E10	177	0.1	7.55
NEP0215	3.3 ± 0.2	2082 ± 104	1.2066E12 $\pm$ 1.1977E11	6.15E11 $\pm$ 7.72E10	162	0.25	4.73
2574	3.3 ± 0.2	1778 ± 89	1.1967E12 $\pm$ 5.9635E10	6.19E11 $\pm$ 3.09E10	200	0.25	7.46
2679	3.3 ± 0.2	4144 ± 207	3.8237E11 $\pm$ 5.3526E10	1.252E11 $\pm$ 2.72E10	68	0.1	3.67
3018	3.3 ± 0.2	1638 ± 190	6.843E11 $\pm$ 1.6373E11	3.344E11 $\pm$ 9.9810	133	0.1	0.89
4115	3.3 ± 0.2	2764 ± 567	7.082E11 $\pm$ 2.4503E11	3.15E11 $\pm$ 1.48E11	124	0.14	0.47

Table A.9: List of the 186 high-z candidates in the NEP sort it out by deacrising readshift. The first column is the ID we gave to the source and the rest of their columns are as follows: redshift, SFR, solar masses, gass masses, AGN fraction and χ^2.

ID	z_{phot}	SFR $[M_\odot/yr]$	M_* $[M_\odot]$	M_{gas} $[M_\odot]$	Ageburst [Myrs]	AGN fraction [%]	χ^2
NEP0329	3.3 ± 0.2	3723 ± 186	8.113E11 $\pm$ 1.799E11	3.46E11 $\pm$ 1.10E11	115	0.1	4.53
2835	3.2 ± 0.2	1602 ± 174	3.186E11 $\pm$ 1.4403E11	1.334E11 $\pm$ 8.15E10	111	0.1	0.76
553	3.2 ± 0.2	1600 ± 137	2.9563E11 $\pm$ 1.3797E11	1.213E11 $\pm$ 7.6510	107	0.25	1.24
1396	3.2 ± 0.2	6041 ± 302	3.925E12 $\pm$ 1.9628E11	2.032E12 $\pm$ 1.011E11	186	0.25	11.0
2545	3.2 ± 0.2	1646 ± 286	3.2683E11 $\pm$ 1.1968E11	1.365E11 $\pm$ 6.90E10	115	0.23	0.43
2652	3.2 ± 0.2	1021 ± 51	1.812E11 $\pm$ 2.008E10	6.75E10 $\pm$ 1.174E10	144	0.1	7.24
3697	3.2 ± 0.2	1544 ± 179	3.4845E11 $\pm$ 1.495E11	1.505E11 $\pm$ 8.61E10	117	0.1	2.2
4193	3.2 ± 0.2	1037 ± 93	2.0127E11 $\pm$ 4.039E10	7.95E10 $\pm$ 2.47E10	135	0.1	0.7
4227	3.2 ± 0.2	1554 ± 167	4.927E11 $\pm$ 1.9633E11	2.294E11 $\pm$ 1.146E11	127	0.1	2.47
NEP0030	3.2 ± 0.2	947 ± 237	1.2501E11 $\pm$ 2.379E10	4.4510 $\pm$ 1.08E10	107	0.12	9.59
4279	3.1 ± 0.2	2087 ± 104	1.4744E11 $\pm$ 1.1485E10	4.75E10 $\pm$ 7.79E9	50	0.1	5.85
2940	3.1 ± 0.2	1643 ± 218	2.0315E11 $\pm$ 6.592E10	7.45E10 $\pm$ 3.242E10	88	0.11	0.98
4038	3.1 ± 0.2	857 ± 132	1.4466E11 $\pm$ 5.853E10	5.78E10 $\pm$ 3.214E10	106	0.11	2.05
3878	3.0 ± 0.2	1845 ± 113	1.1249E12 $\pm$ 9.032E10	5.80E11 $\pm$ 5.20E10	164	0.11	2.16
4142	3.0 ± 0.2	1089 ± 255	2.1853E11 $\pm$ 1.1673E11	9.17E10 $\pm$ 6.28E10	113	0.23	3.06
4321	3.0 ± 0.2	919 ± 169	1.8248E11 $\pm$ 9.472E10	7.67E10 $\pm$ 5.19E10	110	0.12	0.12
NEP0040	3.0 ± 0.2	816 ± 107	1.6332E11 $\pm$ 6.624E10	6.836E10 $\pm$ 3.78E10	114	0.1	0.6
2985	3.0 ± 0.2	1495 ± 257	3.018E11 $\pm$ 1.5675E11	1.272E11 $\pm$ 8.54E10	110	0.02	0.06
3650	3.0 ± 0.2	1493 ± 75	1.0782E11 $\pm$ 9.667E9	3.594E10 $\pm$ 6.11E9	50	0.12	2.31
3871	2.9 ± 0.2	1365 ± 187	2.8166E11 $\pm$ 1.3353E11	1.194E11 $\pm$ 7.5010	113	0.12	0.22
4804	2.9 ± 0.2	1318 ± 206	2.627E11 $\pm$ 1.2845E11	1.1011 $\pm$ 7.10E10	110	0.12	0.08
2163	2.9 ± 0.1	1363 ± 169	2.5665E11 $\pm$ 1.1434E11	1.05E11 $\pm$ 6.38E10	111	0.0	0.23
4788	2.9 ± 0.1	1562 ± 206	3.183E11 $\pm$ 1.4778E11	1.346E11 $\pm$ 8.26E10	112	0.1	0.3
3976	2.9 ± 0.1	1352 ± 249	2.991E11 $\pm$ 1.4857E11	1.293E11 $\pm$ 8.29E10	115	0.03	0.06
NEP0081	2.9 ± 0.1	858 ± 125	1.965E11 $\pm$ 9.793E10	8.5710 $\pm$ 5.48E10	114	0.0	1.23
3370	2.9 ± 0.1	2215 ± 290	1.4056E12 $\pm$ 1.379E11	7.22E11 $\pm$ 7.50E10	181	0.1	5.67
1990	2.9 ± 0.1	13526 ± 676	8.40E12 $\pm$ 4.863E11	4.33E12 $\pm$ 3.07E11	173	0.0	25.1
2029	2.8 ± 0.1	1778 ± 228	3.4915E11 $\pm$ 1.6887E11	1.46E11 $\pm$ 9.32	110	0.05	0.02

Table A.10: Same as Table A.9

ID	z_{phot}	SFR $[M_\odot/yr]$	M_* $[M_\odot]$	M_{gas} $[M_\odot]$	Ageburst [Myrs]	AGN fraction [%]	χ^2
NEP0085	2.8 ± 0.1	653 ± 230	$1.4647E11 \pm 9.759E10$	$6.336E10 \pm 5.12E10$	114	0.12	1.09
3466	2.8 ± 0.1	1256 ± 145	$3.9885E11 \pm 1.5036E11$	$1.85E11 \pm 8.81E10$	127	0.1	1.42
NEP0241	2.8 ± 0.1	579 ± 180	$8.202E10 \pm 1.2905E10$	$3.025E10 \pm 7.585E9$	111	0.08	1.86
2763	2.8 ± 0.1	1422 ± 211	$2.1668E11 \pm 8.585E10$	$8.44E10 \pm 4.57E10$	100	0.1	0.72
3213	2.8 ± 0.1	1779 ± 408	$4.357E11 \pm 1.763E11$	$1.927E11 \pm 1.026E11$	120	0.11	0.04
930	2.8 ± 0.1	1568 ± 166	$5.081E11 \pm 1.9983E11$	$2.38E11 \pm 1.173E11$	127	0.1	3.42
NEP0023	2.8 ± 0.1	507 ± 46	$3.7206E10 \pm 3.9272E9$	$1.211E10 \pm 2.327E9$	52	0.12	2.44
3882	2.7 ± 0.1	1216 ± 145	$4.935E11 \pm 1.3888E11$	$2.403E11 \pm 8.36E10$	135	0.1	1.62
4525	2.7 ± 0.1	1393 ± 230	$2.765E11 \pm 1.3545E11$	$1.162E11 \pm 7.51E10$	111	0.02	0.54
4696	2.7 ± 0.1	1352 ± 202	$3.199E11 \pm 1.3629E11$	$1.398E11 \pm 7.8610$	119	0.12	0.01
2039	2.7 ± 0.1	1367 ± 197	$2.715E11 \pm 1.1226E11$	$1.133E11 \pm 6.375E10$	114	0.11	0.07
3261	2.7 ± 0.1	1002 ± 127	$1.766E11 \pm 7.89E10$	$7.17E10 \pm 4.35E10$	106	0.0	0.58
1205	2.7 ± 0.1	1706 ± 236	$3.315E11 \pm 1.6067E11$	$1.384E11 \pm 8.8210$	109	0.11	0.29
3475	2.7 ± 0.1	1197 ± 134	$2.641E11 \pm 1.1193E11$	$1.137E11 \pm 6.40E10$	117	0.1	0.74
729	2.7 ± 0.1	1677 ± 186	$2.312E11 \pm 3.3028E10$	$8.39E10 \pm 1.847E10$	101	0.0	9.29
912	2.7 ± 0.1	1381 ± 225	$2.89E11 \pm 1.458E11$	$1.236E11 \pm 8.08E10$	112	0.03	0.87
NEP0019	2.7 ± 0.1	796 ± 273	$1.7814E11 \pm 1.1715E11$	$7.72E10 \pm 6.19E10$	114	0.12	2.46
562	2.7 ± 0.1	1430 ± 72	$6.754E11 \pm 1.0512E11$	$3.315E11 \pm 6.8810$	148	0.0	7.05
1932	2.6 ± 0.1	985 ± 152	$2.1272E11 \pm 9.351E10$	$9.0810 \pm 5.32E10$	116	0.09	0.08
2219	2.6 ± 0.1	1457 ± 191	$2.6264E11 \pm 9.483E10$	$1.061E11 \pm 5.27E10$	112	0.0	0.08
NEP0027	2.6 ± 0.1	637 ± 232	$1.4203E11 \pm 9.637E10$	$6.176E10 \pm 5.0410$	114	0.12	0.46
3017	2.6 ± 0.1	1138 ± 185	$2.555E11 \pm 1.148E11$	$1.163E11 \pm 7.50E10$	116	0.11	0.5
3026	2.6 ± 0.1	1078 ± 167	$2.2406E11 \pm 1.2485E11$	$1.028E11 \pm 8.23E10$	110	0.11	0.1
1227	2.6 ± 0.1	1618 ± 238	$2.0663E11 \pm 6.761E10$	$8.050 \pm 3.82E10$	89	0.1	2.57
1486	2.6 ± 0.1	1531 ± 231	$5.225E11 \pm 2.946E11$	$2.73E11 \pm 2.092E11$	123	0.0	0.17
2357	2.6 ± 0.1	861 ± 130	$2.3726E11 \pm 1.4973E11$	$1.193E11 \pm 1.033E11$	117	0.13	0.15
2450	2.5 ± 0.1	955 ± 139	$1.7786E11 \pm 8.606E10$	$7.76E10 \pm 5.49E10$	108	0.24	0.49
NEP0145	2.5 ± 0.1	691 ± 43	$4.104E11 \pm 7.398E10$	$2.176E11 \pm 5.964E10$	151	0.0	5.64

Table A.11: Same as Table A.9

ID	z_{phot}	SFR $[M_\odot/yr]$	M_* $[M_\odot]$	M_{gas} $[M_\odot]$	Ageburst [Myrs]	AGN fraction [%]	χ^2
1668	2.5 ± 0.1	1277 ± 178	2.2748E11 $\pm$ 1.2621E11	9.92E10 $\pm$ 7.9310	103	0.07	0.3
2539	2.5 ± 0.1	1362 ± 214	3.6154E11 $\pm$ 1.7865E11	1.75E11 $\pm$ 1.223E11	119	0.11	0.35
266	2.5 ± 0.1	1615 ± 81	1.2344E11 $\pm$ 1.5654E10	5.02E10 $\pm$ 1.226E10	50	0.1	3.5
2787	2.5 ± 0.1	914 ± 143	5.195E11 $\pm$ 2.19E11	3.04E11 $\pm$ 1.657E11	132	0.1	0.42
NEP0007	2.5 ± 0.1	432 ± 71	5.387E10 $\pm$ 1.8723E10	2.356E10 $\pm$ 1.3210	72	0.11	2.07
1045	2.5 ± 0.1	1595 ± 190	2.861E11 $\pm$ 1.593E11	1.259E11 $\pm$ 1.009E11	103	0.0	0.86
1215	2.5 ± 0.1	1285 ± 173	2.853E11 $\pm$ 1.8802E11	1.34E11 $\pm$ 1.269E11	109	0.0	0.22
1733	2.5 ± 0.1	1042 ± 148	3.4444E11 $\pm$ 2.1072E11	1.792E11 $\pm$ 1.496E11	123	0.1	2.1
2227	2.5 ± 0.1	1183 ± 155	4.607E11 $\pm$ 2.2577E11	2.487E11 $\pm$ 1.63E11	125	0.1	0.8
2918	2.5 ± 0.1	835 ± 121	2.9604E11 $\pm$ 1.7654E11	1.588E11 $\pm$ 1.267E11	121	0.1	1.02
3852	2.5 ± 0.1	1406 ± 137	2.8835E11 $\pm$ 1.6595E11	1.329E11 $\pm$ 1.078E11	106	0.1	2.06
NEP0082	2.5 ± 0.1	608 ± 118	1.4246E11 $\pm$ 7.059E10	6.6910 $\pm$ 4.73E10	116	0.0	0.52
2512	2.4 ± 0.1	1168 ± 160	2.2872E11 $\pm$ 1.3717E11	1.039E11 $\pm$ 8.89E10	106	0.09	0.09
3906	2.4 ± 0.1	930 ± 153	2.119E11 $\pm$ 1.4407E11	1.012E11 $\pm$ 9.65E10	110	0.12	0.0
1344	2.4 ± 0.1	1286 ± 191	2.8396E11 $\pm$ 1.8635E11	1.336E11 $\pm$ 1.241E11	108	0.12	0.19
2589	2.4 ± 0.1	1498 ± 270	3.547E11 $\pm$ 1.642E11	1.66E11 $\pm$ 1.10E11	116	0.23	0.56
1068	2.4 ± 0.1	1129 ± 140	2.4396E11 $\pm$ 1.5156E11	1.136E11 $\pm$ 9.99E10	108	0.0	0.75
1261	2.4 ± 0.1	1217 ± 164	1.978E11 $\pm$ 1.0185E11	8.37E10 $\pm$ 6.194E10	99	0.05	0.62
1386	2.4 ± 0.1	1053 ± 248	2.3784E11 $\pm$ 1.653E11	1.123E11 $\pm$ 1.0711	109	0.0	0.91
1698	2.4 ± 0.1	852 ± 225	1.855E11 $\pm$ 1.2351E11	8.67E10 $\pm$ 7.87E10	109	0.0	0.82
2191	2.4 ± 0.1	1074 ± 127	1.8523E11 $\pm$ 7.995E10	7.90E10 $\pm$ 5.026E10	106	0.0	1.07
2342	2.4 ± 0.1	867 ± 133	2.0828E11 $\pm$ 1.2649E11	1.007E11 $\pm$ 8.58E10	113	0.25	1.86
578	2.4 ± 0.1	721 ± 48	4.211E11 $\pm$ 5.214E10	2.174E11 $\pm$ 3.75E10	161	0.1	3.3
NEP0069	2.4 ± 0.1	949 ± 145	9.299E10 $\pm$ 2.3675E10	3.59E10 $\pm$ 1.472E10	67	0.06	0.75
2064	2.3 ± 0.1	810 ± 136	1.6338E11 $\pm$ 9.397E10	7.44E10 $\pm$ 6.13E10	108	0.1	0.08
2435	2.3 ± 0.1	1058 ± 170	2.3304E11 $\pm$ 1.0641E11	1.066E11 $\pm$ 6.99E10	116	0.1	0.14
NEP0061	2.3 ± 0.1	596 ± 220	1.6037E11 $\pm$ 1.4007E11	7.97E10 $\pm$ 9.0510	114	0.12	0.16
3782	2.3 ± 0.1	780 ± 93	1.3741E11 $\pm$ 5.052E10	5.74E10 $\pm$ 3.1010	110	0.1	0.53

Table A.12: Same as Table A.9

ID	z_{phot}	SFR $[M_\odot/yr]$	M_* $[M_\odot]$	M_{gas} $[M_\odot]$	Ageburst [Myrs]	AGN fraction [%]	χ^2
1935	2.3 ± 0.1	931 ± 138	1.563E11 $\pm$ 7.48E10	6.65E10 $\pm$ 4.64E10	102	0.05	0.62
1937	2.3 ± 0.1	917 ± 158	2.3757E11 $\pm$ 1.6224E11	1.173E11 $\pm$ 1.104E11	113	0.16	0.21
2614	2.3 ± 0.1	1040 ± 173	2.19E11 $\pm$ 1.0391E11	1.009E11 $\pm$ 6.75E10	112	0.07	2.44
3064	2.3 ± 0.1	1010 ± 187	4.584E11 $\pm$ 2.473E11	2.61E11 $\pm$ 1.798E11	124	0.14	0.45
3451	2.3 ± 0.1	868 ± 133	2.845E11 $\pm$ 1.406E11	1.453E11 $\pm$ 9.94E10	124	0.0	1.01
3634	2.3 ± 0.1	872 ± 107	6.958E11 $\pm$ 2.3286E11	4.35E11 $\pm$ 1.72E11	139	0.25	0.44
447	2.3 ± 0.1	896 ± 282	2.4005E11 $\pm$ 2.0285E11	1.19E11 $\pm$ 1.31E11	114	0.12	1.1
NEP0073	2.2 ± 0.1	573 ± 206	1.5464E11 $\pm$ 1.3359E11	7.66E10 $\pm$ 8.65E10	114	0.12	0.4
2747	2.2 ± 0.1	1106 ± 197	2.725E11 $\pm$ 1.276E11	1.284E11 $\pm$ 8.65E10	118	0.11	0.02
3141	2.2 ± 0.1	814 ± 144	2.4564E11 $\pm$ 1.3972E11	1.245E11 $\pm$ 9.81E10	121	0.14	0.0
NEP0042	2.2 ± 0.1	700 ± 245	1.8873E11 $\pm$ 1.6277E11	9.36E10 $\pm$ 1.053E11	114	0.12	0.07
NEP0298	2.2 ± 0.1	395 ± 150	8.396E10 $\pm$ 5.883E10	3.894E10 $\pm$ 3.63E10	109	0.01	0.67
1214	2.2 ± 0.1	1043 ± 140	1.5043E11 $\pm$ 5.659E10	6.08E10 $\pm$ 3.27E10	96	0.03	1.12
1835	2.2 ± 0.1	1292 ± 280	3.871E11 $\pm$ 2.1025E11	1.98E11 $\pm$ 1.52E11	121	0.12	0.01
2184	2.2 ± 0.1	1226 ± 161	1.9067E11 $\pm$ 6.4486E10	7.72E10 $\pm$ 3.810	103	0.0	1.33
3321	2.2 ± 0.1	431 ± 27	4.102E10 $\pm$ 1.1141E10	1.742E10 $\pm$ 7.769	55	0.1	1.69
67	2.2 ± 0.1	2410 ± 261	4.1823E11 $\pm$ 1.7824E11	1.78E11 $\pm$ 1.083E11	105	0.0	0.39
753	2.2 ± 0.1	550 ± 68	4.83E10 $\pm$ 1.3251E10	2.148E10 $\pm$ 9.06E9	50	0.01	4.68
110	2.1 ± 0.1	1020 ± 143	2.5582E11 $\pm$ 1.6818E11	1.251E11 $\pm$ 1.14E11	113	0.15	0.06
2493	2.1 ± 0.1	498 ± 45	4.96E11 $\pm$ 5.276E10	3.236E11 $\pm$ 3.57E10	128	0.1	3.34
4191	2.1 ± 0.1	843 ± 87	8.655E10 $\pm$ 2.1465E10	4.01E10 $\pm$ 1.632E10	53	0.0	4.48
NEP0247	2.1 ± 0.1	188 ± 52	1.1183E11 $\pm$ 2.2873E10	7.07E10 $\pm$ 1.653E10	85	0.0	1.21
2192	2.1 ± 0.1	894 ± 103	1.2857E11 $\pm$ 3.986E10	5.05E10 $\pm$ 2.30E10	99	0.1	3.73
289	2.1 ± 0.1	734 ± 38	1.4928E11 $\pm$ 4.987E10	6.09E10 $\pm$ 2.985E10	141	0.1	2.16
3060	2.1 ± 0.1	755 ± 102	4.554E11 $\pm$ 1.8925E11	2.718E11 $\pm$ 1.414E11	132	0.1	2.83
3446	2.1 ± 0.1	1099 ± 315	4.759E11 $\pm$ 1.9296E11	2.607E11 $\pm$ 1.496E11	132	0.18	0.42
3715	2.1 ± 0.1	785 ± 90	1.8585E11 $\pm$ 9.19E10	8.67E10 $\pm$ 6.1410	117	0.25	1.46
2822	2.0 ± 0.1	774 ± 134	2.0455E11 $\pm$ 1.4198E11	1.02E11 $\pm$ 9.63E10	113	0.2	0.05

Table A.13: Same as Table A.9

ID	z_{phot}	SFR $[M_\odot/yr]$	M_* $[M_\odot]$	M_{gas} $[M_\odot]$	Ageburst [Myrs]	AGN fraction [%]	χ^2
1024	2.0 ± 0.1	1042 ± 117	1.4097E11 $\pm$ 4.572E10	5.52E10 $\pm$ 2.577E10	94	0.0	1.31
4175	2.0 ± 0.1	207 ± 37	2.4597E10 $\pm$ 1.3265E10	1.087E10 $\pm$ 9.029	67	0.1	1.41
618	2.0 ± 0.1	820 ± 249	2.202E11 $\pm$ 1.8356E11	1.093E11 $\pm$ 1.207E11	114	0.13	1.9
NEP0297	2.0 ± 0.1	373 ± 139	1.0046E11 $\pm$ 8.788E10	4.985E10 $\pm$ 5.67E10	114	0.12	0.49
1707	2.0 ± 0.1	412 ± 30	5.8325E10 $\pm$ 8.06E9	2.075E10 $\pm$ 4.505E9	116	0.0	2.5
2257	1.9 ± 0.1	638 ± 65	7.046E11 $\pm$ 7.061E10	4.60E11 $\pm$ 4.756E10	147	0.0	4.84
2735	1.9 ± 0.1	934 ± 195	2.999E11 $\pm$ 1.3664E11	1.54E11 $\pm$ 9.92E10	124	0.0	2.75
373	1.9 ± 0.1	496 ± 56	1.566E11 $\pm$ 8.702E10	8.1110 $\pm$ 6.13E10	119	0.0	1.7
861	1.9 ± 0.1	339 ± 29	1.4807E11 $\pm$ 3.084E10	7.72E10 $\pm$ 2.485E10	110	0.1	4.72
NEP0162	1.9 ± 0.1	463 ± 165	1.2447E11 $\pm$ 1.0779E11	6.19E10 $\pm$ 6.97E10	114	0.12	0.24
1891	1.9 ± 0.1	2488 ± 124	3.427E12 $\pm$ 1.7135E11	2.245E12 $\pm$ 1.123E11	200	0.0	7.65
4120	1.9 ± 0.1	590 ± 95	8.523E10 $\pm$ 2.8967E10	3.408E10 $\pm$ 1.662E10	98	0.09	1.49
NEP0074	1.9 ± 0.1	254 ± 44	3.0234E11 $\pm$ 3.868E10	1.973E11 $\pm$ 2.576E10	167	0.0	3.2
939	1.8 ± 0.1	429 ± 54	6.043E10 $\pm$ 1.6516E10	2.523E10 $\pm$ 1.062E10	90	0.01	4.65
NEP0300	1.8 ± 0.1	523 ± 269	1.596E11 $\pm$ 1.53E11	8.17E10 $\pm$ 9.82E10	117	0.01	0.85
NEP0013	1.7 ± 0.1	259 ± 16	3.4456E11 $\pm$ 2.1293E10	2.25E11 $\pm$ 1.419E10	190	0.0	2.31
240	1.7 ± 0.1	372 ± 19	5.122E11 $\pm$ 2.561E10	3.35E11 $\pm$ 1.67E10	200	0.0	4.16
3970	1.7 ± 0.1	240 ± 16	1.4422E11 $\pm$ 1.4166E10	7.44E10 $\pm$ 9.75E9	162	0.1	3.19
969	1.7 ± 0.1	561 ± 83	8.844E10 $\pm$ 4.259E10	3.68E10 $\pm$ 2.5410	99	0.0	1.75
1838	1.6 ± 0.1	550 ± 56	2.22E11 $\pm$ 4.7806E10	1.14E11 $\pm$ 4.384E10	130	0.0	3.39
277	1.6 ± 0.1	465 ± 23	3.623E10 $\pm$ 6.402E9	1.658E10 $\pm$ 4.95E9	50	0.1	6.93
377	1.5 ± 0.1	447 ± 27	3.639E10 $\pm$ 6.382E9	1.471E10 $\pm$ 5.16E9	54	0.0	1.77
1079	1.5 ± 0.1	1765 ± 190	1.2083E12 $\pm$ 3.386E11	6.89E11 $\pm$ 3.085E11	161	0.0	6.35
4539	1.5 ± 0.1	459 ± 88	2.096E11 $\pm$ 1.1834E11	1.254E11 $\pm$ 9.34E10	126	0.25	1.08
590	1.5 ± 0.1	622 ± 69	1.7037E11 $\pm$ 3.5166E10	8.24E10 $\pm$ 2.97E10	119	0.0	2.78
951	1.5 ± 0.1	486 ± 63	6.4506E10 $\pm$ 2.4055E10	2.68E10 $\pm$ 1.466E10	90	0.0	1.16
728	1.5 ± 0.1	560 ± 96	1.1536E11 $\pm$ 4.3075E10	5.27E10 $\pm$ 3.186E10	116	0.0	3.34

Table A.14: Same as Table A.9

ID	z_{phot}	SFR $[M_\odot/yr]$	M_* $[M_\odot]$	M_{gas} $[M_\odot]$	Ageburst [Myrs]	AGN fraction [%]	χ^2
NEP0265	1.4 ± 0.1	107 ± 5	1.566E11 $\pm$ 1.823E10	1.046E11 $\pm$ 1.77E10	200	0.0	7.4
750	1.4 ± 0.1	1103 ± 118	2.0944E11 $\pm$ 4.9975E10	8.77E10 $\pm$ 3.71E10	130	0.0	6.51
3727	1.3 ± 0.1	450 ± 81	9.03E10 $\pm$ 3.6084E10	4.156E10 $\pm$ 2.66E10	117	0.0	2.6
4547	1.3 ± 0.1	364 ± 27	6.187E10 $\pm$ 1.5907E10	2.866E10 $\pm$ 1.320	109	0.1	2.49
NEP0103	1.3 ± 0.1	264 ± 22	1.3846E11 $\pm$ 2.8954E10	9.73E10 $\pm$ 2.383E10	60	0.0	1.93
2715	1.3 ± 0.1	1105 ± 56	1.0486E11 $\pm$ 2.3967E10	4.32E10 $\pm$ 1.816E10	61	0.25	1.49
NEP0015	1.2 ± 0.1	169 ± 8	1.2473E10 $\pm$ 1.1214E9	5.42E9 $\pm$ 9.36E8	50	0.0	6.5
NEP0054	1.2 ± 0.1	205 ± 14	1.744E10 $\pm$ 3.836E9	7.52E9 $\pm$ 3.174E9	53	0.1	2.66
2627	1.2 ± 0.1	62 ± 6	6.289E10 $\pm$ 2.16E10	4.05E10 $\pm$ 1.77E10	161	0.01	2.36
3753	1.2 ± 0.1	269 ± 83	1.0613E11 $\pm$ 6.406E10	6.194E10 $\pm$ 4.97E10	124	0.0	4.03
NEP0115	1.1 ± 0.1	172 ± 15	3.556E10 $\pm$ 6.842E9	1.456E10 $\pm$ 4.65E9	144	0.0	1.31
3980	1.1 ± 0.1	199 ± 48	9.97E10 $\pm$ 5.8276E10	6.384E10 $\pm$ 4.894E10	126	0.0	1.86
NEP0164	1.1 ± 0.1	127 ± 12	8.724E10 $\pm$ 5.337E10	5.86E10 $\pm$ 4.39E10	119	0.1	1.74
1986	1.0 ± 0.1	324 ± 47	1.839E11 $\pm$ 6.992E10	1.085E11 $\pm$ 6.5710	143	0.0	5.61
1211	1.0 ± 0.1	104 ± 12	3.766E10 $\pm$ 7.787E9	1.815E10 $\pm$ 5.67E9	132	0.0	1.31
3491	1.0 ± 0.1	135 ± 21	5.736E10 $\pm$ 8.047E9	2.77E10 $\pm$ 5.71E9	140	0.0	1.53
1960	0.9 ± 0.1	164 ± 24	5.018E10 $\pm$ 3.0125E10	2.84E10 $\pm$ 2.484E10	119	0.0	0.56
1965	0.9 ± 0.1	160 ± 14	7.496E10 $\pm$ 2.6645E10	4.33E10 $\pm$ 2.516E10	131	0.0	1.46
2452	0.7 ± 0.1	88 ± 15	2.0704E10 $\pm$ 1.219E10	1.148E10 $\pm$ 1.037E10	116	0.0	1.94
1024	2.0 ± 0.1	1042 ± 117	1.4097E11 $\pm$ 4.572E10	5.52E10 $\pm$ 2.577E10	94	0.0	1.31
4175	2.0 ± 0.1	207 ± 37	2.4597E10 $\pm$ 1.3265E10	1.087E10 $\pm$ 9.029	67	0.1	1.41
618	2.0 ± 0.1	820 ± 249	2.202E11 $\pm$ 1.8356E11	1.093E11 $\pm$ 1.207E11	114	0.13	1.9
NEP0297	2.0 ± 0.1	373 ± 139	1.0046E11 $\pm$ 8.788E10	4.985E10 $\pm$ 5.67E10	114	0.12	0.49
1707	2.0 ± 0.1	412 ± 30	5.8325E10 $\pm$ 8.06E9	2.075E10 $\pm$ 4.505E9	116	0.0	2.5
2257	1.9 ± 0.1	638 ± 65	7.046E11 $\pm$ 7.061E10	4.60E11 $\pm$ 4.756E10	147	0.0	4.84
2735	1.9 ± 0.1	934 ± 195	2.999E11 $\pm$ 1.3664E11	1.54E11 $\pm$ 9.92E10	124	0.0	2.75
373	1.9 ± 0.1	496 ± 56	1.566E11 $\pm$ 8.702E10	8.1110 $\pm$ 6.13E10	119	0.0	1.7
861	1.9 ± 0.1	339 ± 29	1.4807E11 $\pm$ 3.084E10	7.72E10 $\pm$ 2.485E10	110	0.1	4.72

Table A.15: Same as Table A.9

ID	z_{phot}	SFR $[M_\odot/yr]$	M_* $[M_\odot]$	M_{gas} $[M_\odot]$	Ageburst [Myrs]	AGN fraction [%]	χ^2
NEP0162	1.9 ± 0.1	463 ± 165	1.2447E11 ± 1.0779E11	6.19E10 ± 6.97E10	114	0.12	0.24
1891	1.9 ± 0.1	2488 ± 124	3.427E12 ± 1.7135E11	2.245E12 ± 1.123E11	200	0.0	7.65
4120	1.9 ± 0.1	590 ± 95	8.523E10 ± 2.8967E10	3.408E10 ± 1.662E10	98	0.09	1.49
NEP0074	1.9 ± 0.1	254 ± 44	3.0234E11 ± 3.868E10	1.973E11 ± 2.576E10	167	0.0	3.2
939	1.8 ± 0.1	429 ± 54	6.043E10 ± 1.6516E10	2.523E10 ± 1.062E10	90	0.01	4.65
NEP0300	1.8 ± 0.1	523 ± 269	1.596E11 ± 1.53E11	8.17E10 ± 9.82E10	117	0.01	0.85
NEP0013	1.7 ± 0.1	259 ± 16	3.4456E11 ± 2.1293E10	2.25E11 ± 1.419E10	190	0.0	2.31
240	1.7 ± 0.1	372 ± 19	5.122E11 ± 2.561E10	3.35E11 ± 1.67E10	200	0.0	4.16
3970	1.7 ± 0.1	240 ± 16	1.4422E11 ± 1.4166E10	7.44E10 ± 9.75E9	162	0.1	3.19
969	1.7 ± 0.1	561 ± 83	8.844E10 ± 4.259E10	3.68E10 ± 2.5410	99	0.0	1.75
1838	1.6 ± 0.1	550 ± 56	2.22E11 ± 4.7806E10	1.14E11 ± 4.384E10	130	0.0	3.39
277	1.6 ± 0.1	465 ± 23	3.623E10 ± 6.402E9	1.658E10 ± 4.95E9	50	0.1	6.93
377	1.5 ± 0.1	447 ± 27	3.639E10 ± 6.382E9	1.471E10 ± 5.16E9	54	0.0	1.77
1079	1.5 ± 0.1	1765 ± 190	1.2083E12 ± 3.386E11	6.89E11 ± 3.085E11	161	0.0	6.35
4539	1.5 ± 0.1	459 ± 88	2.096E11 ± 1.1834E11	1.254E11 ± 9.34E10	126	0.25	1.08
590	1.5 ± 0.1	622 ± 69	1.7037E11 ± 3.5166E10	8.24E10 ± 2.97E10	119	0.0	2.78
951	1.5 ± 0.1	486 ± 63	6.4506E10 ± 2.4055E10	2.68E10 ± 1.466E10	90	0.0	1.16
728	1.5 ± 0.1	560 ± 96	1.1536E11 ± 4.3075E10	5.27E10 ± 3.186E10	116	0.0	3.34
NEP0265	1.4 ± 0.1	107 ± 5	1.566E11 ± 1.823E10	1.046E11 ± 1.77E10	200	0.0	7.4
750	1.4 ± 0.1	1103 ± 118	2.0944E11 ± 4.9975E10	8.77E10 ± 3.71E10	130	0.0	6.51
3727	1.3 ± 0.1	450 ± 81	9.03E10 ± 3.6084E10	4.156E10 ± 2.66E10	117	0.0	2.6
4547	1.3 ± 0.1	364 ± 27	6.187E10 ± 1.5907E10	2.866E10 ± 1.320	109	0.1	2.49
NEP0103	1.3 ± 0.1	264 ± 22	1.3846E11 ± 2.8954E10	9.73E10 ± 2.383E10	60	0.0	1.93
2715	1.3 ± 0.1	1105 ± 56	1.0486E11 ± 2.3967E10	4.32E10 ± 1.816E10	61	0.25	1.49
NEP0015	1.2 ± 0.1	169 ± 8	1.2473E10 ± 1.1214E9	5.42E9 ± 9.36E8	50	0.0	6.5
NEP0054	1.2 ± 0.1	205 ± 14	1.744E10 ± 3.836E9	7.52E9 ± 3.174E9	53	0.1	2.66
2627	1.2 ± 0.1	62 ± 6	6.289E10 ± 2.16E10	4.05E10 ± 1.77E10	161	0.01	2.36
3753	1.2 ± 0.1	269 ± 83	1.0613E11 ± 6.406E10	6.194E10 ± 4.97E10	124	0.0	4.03

Table A.16: Same as Table A.9

ID	z_{phot}	SFR $[M_\odot/yr]$	M_* $[M_\odot]$	M_{gas} $[M_\odot]$	Ageburst [Myrs]	AGN fraction [%]	χ^2
NEP0115	1.1 ± 0.1	172 ± 15	$3.556E10 \pm 6.842E9$	$1.456E10 \pm 4.65E9$	144	0.0	1.31
3980	1.1 ± 0.1	199 ± 48	$9.97E10 \pm 5.8276E10$	$6.384E10 \pm 4.894E10$	126	0.0	1.86
NEP0164	1.1 ± 0.1	127 ± 12	$8.724E10 \pm 5.337E10$	$5.86E10 \pm 4.39E10$	119	0.1	1.74
1986	1.0 ± 0.1	324 ± 47	$1.839E11 \pm 6.992E10$	$1.085E11 \pm 6.5710$	143	0.0	5.61
1211	1.0 ± 0.1	104 ± 12	$3.766E10 \pm 7.787E9$	$1.815E10 \pm 5.67E9$	132	0.0	1.31
3491	1.0 ± 0.1	135 ± 21	$5.736E10 \pm 8.047E9$	$2.77E10 \pm 5.71E9$	140	0.0	1.53
1960	0.9 ± 0.1	164 ± 24	$5.018E10 \pm 3.0125E10$	$2.84E10 \pm 2.484E10$	119	0.0	0.56
1965	0.9 ± 0.1	160 ± 14	$7.496E10 \pm 2.6645E10$	$4.33E10 \pm 2.516E10$	131	0.0	1.46
2452	0.7 ± 0.1	88 ± 15	$2.0704E10 \pm 1.219E10$	$1.148E10 \pm 1.037E10$	116	0.0	1.94

Table A.17: Same as Table A.9

A.2 SED fitting for the complete sample of radio galaxies.

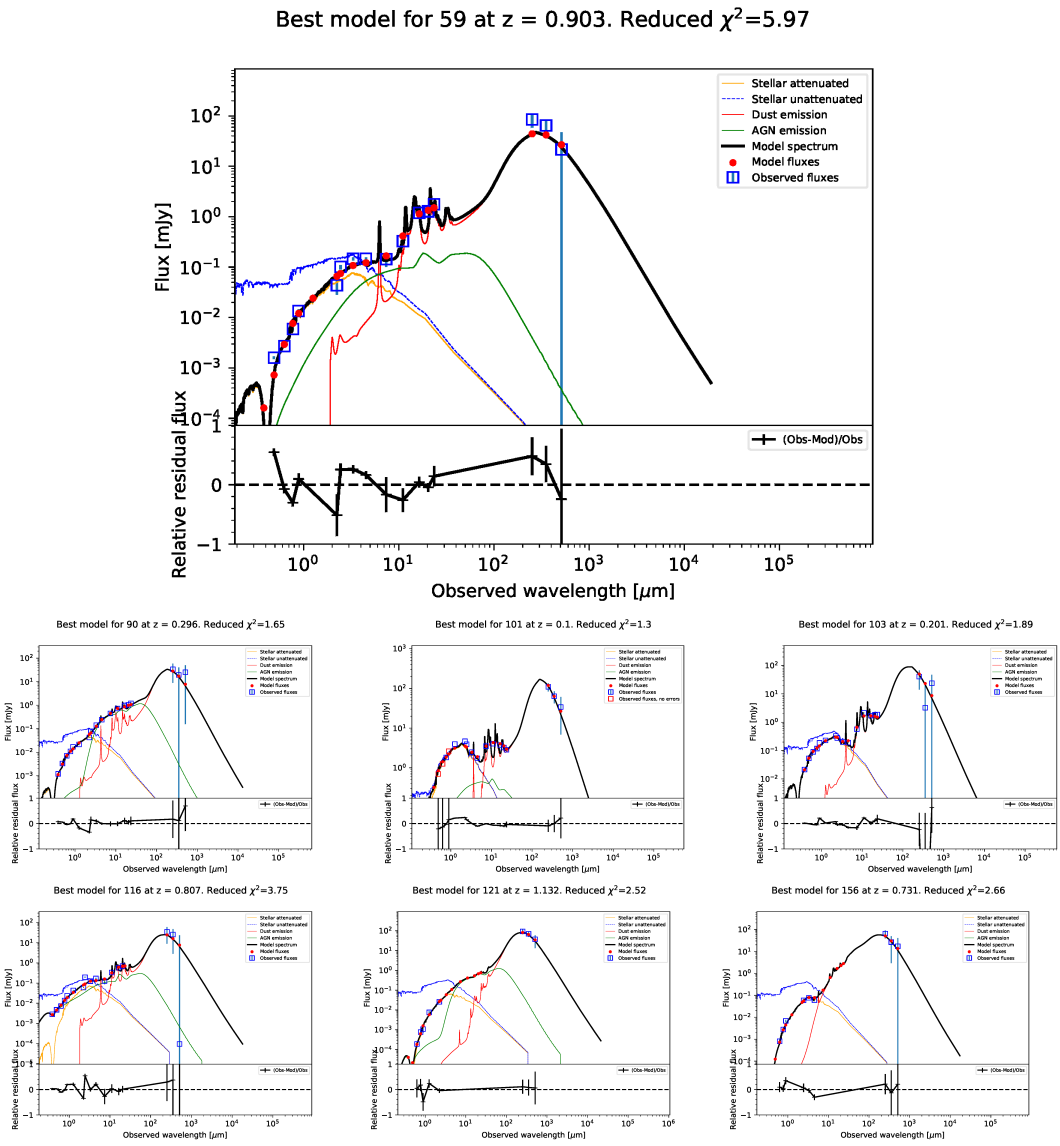

Figure A.1: SED for the 169 radio sources sorted out by ID. The blue squares are the observed fluxes [mJy] whereas the red dots show the predicted fluxes by the best model that fits the observations (black line). Cigale modules are represented in the legend: the blue line is the stellar emission (Bruzual & Charlot, 2003), the yellow line defines the dust attenuation whereas (Charlot & Fall, 2000) the dust emission is defined by the red line (Draine & Li, 2007) and the green line defines the AGN emission (Fritz, Franceschini & Hatziminaoglou, 2006).

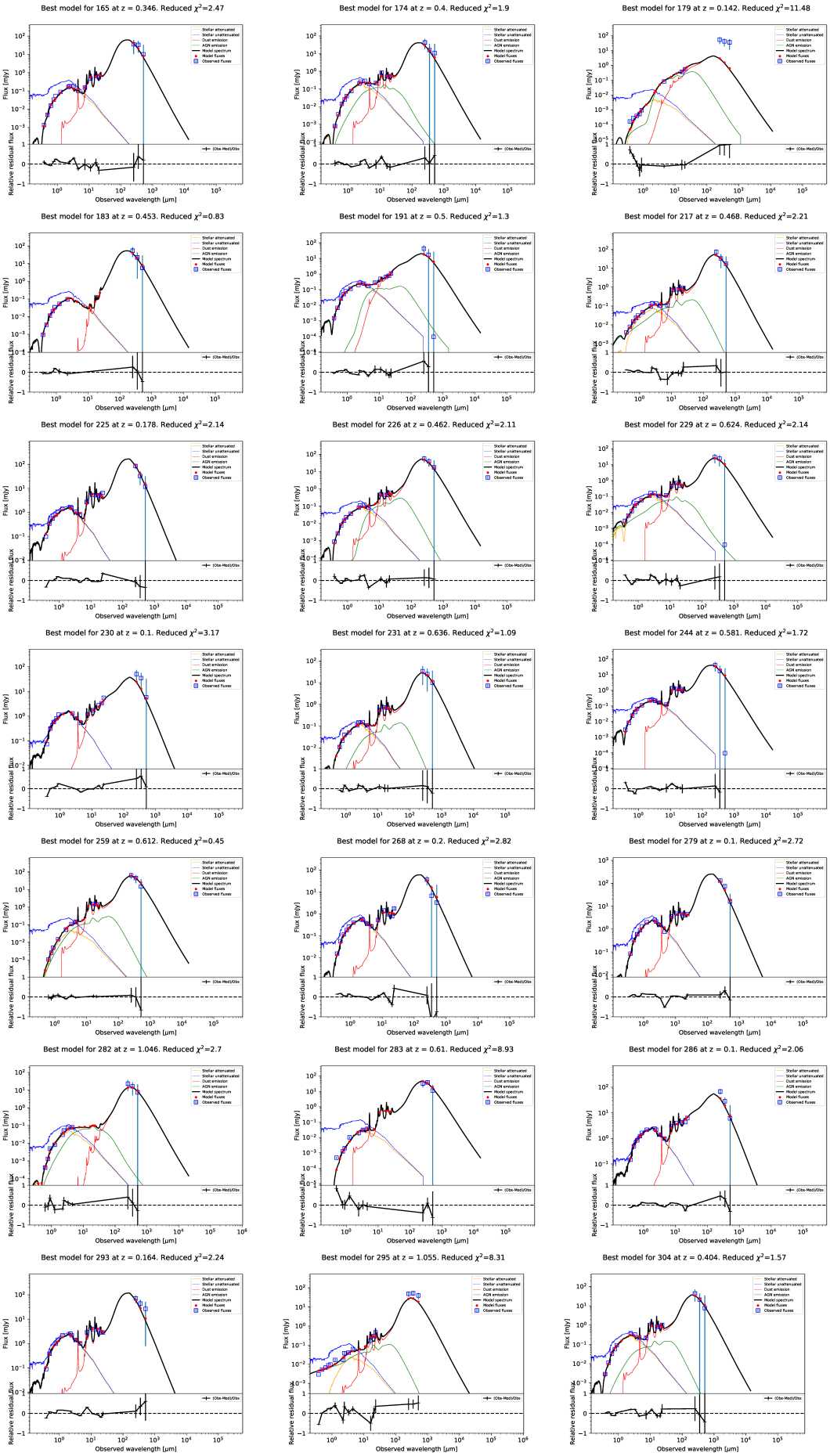

Figure A.2: Same as Figure A.1

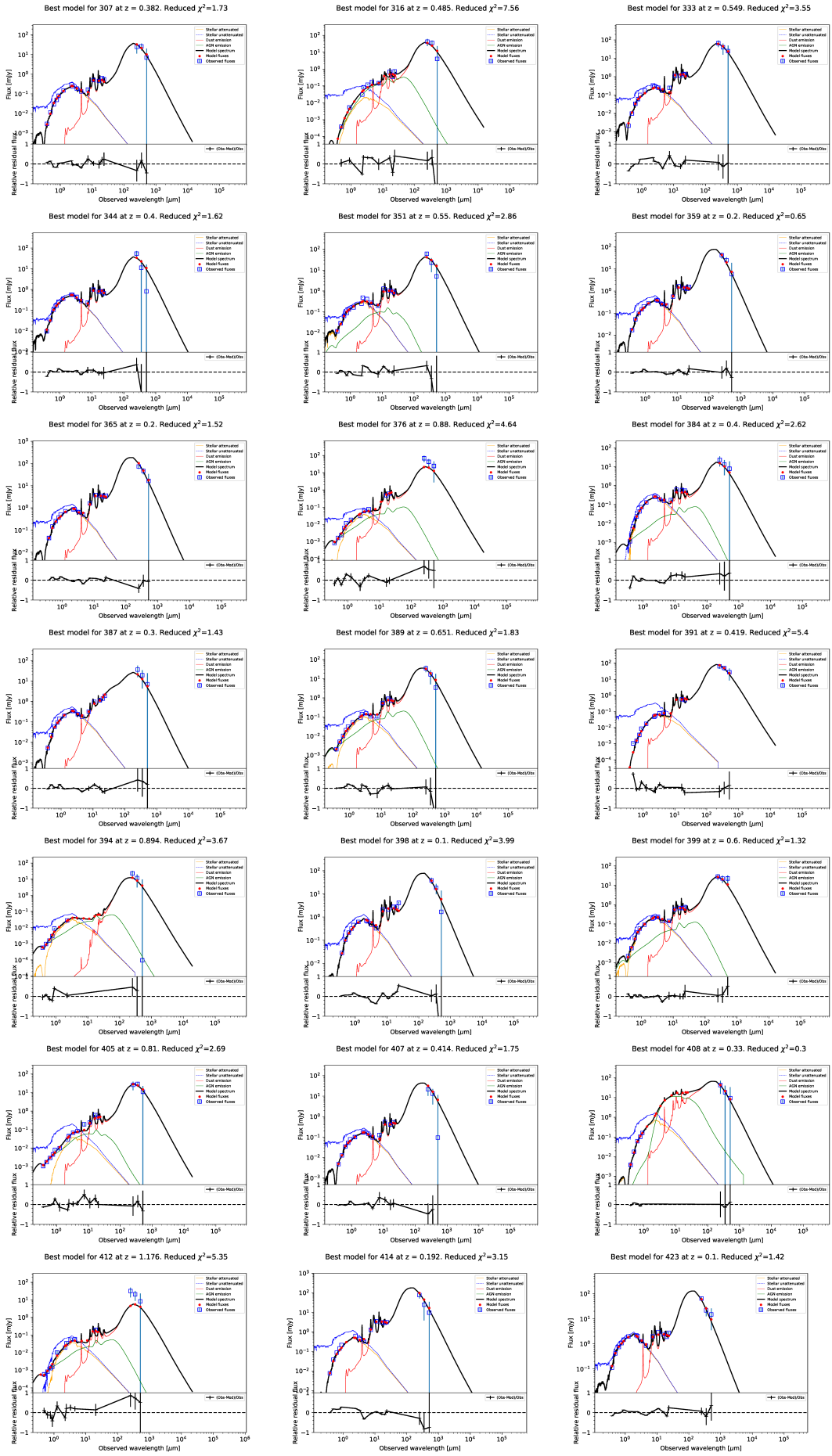

Figure A.3: Same as Figure A.1

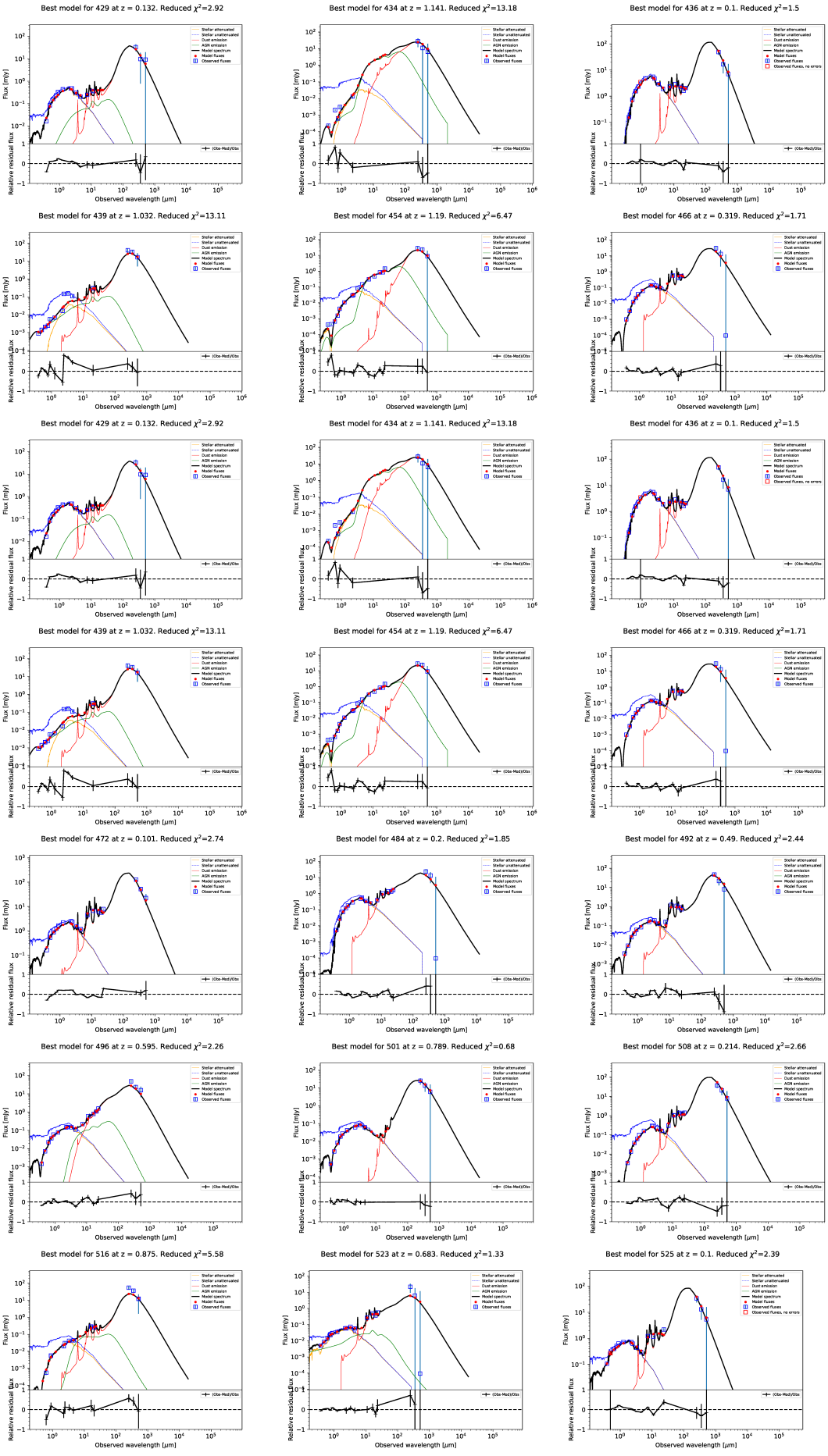

Figure A.4: Same as Figure A.1

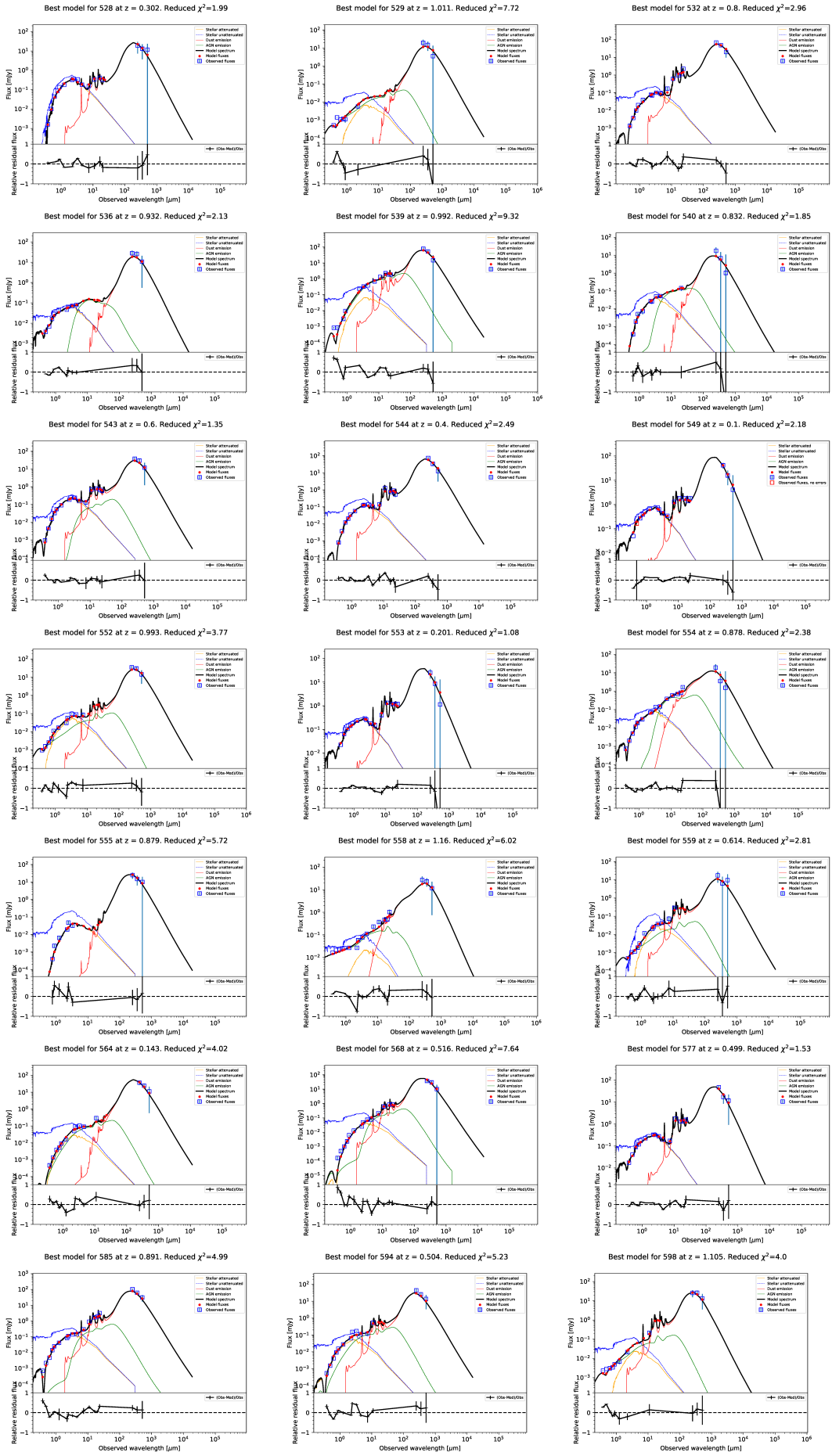

Figure A.5: Same as Figure A.1

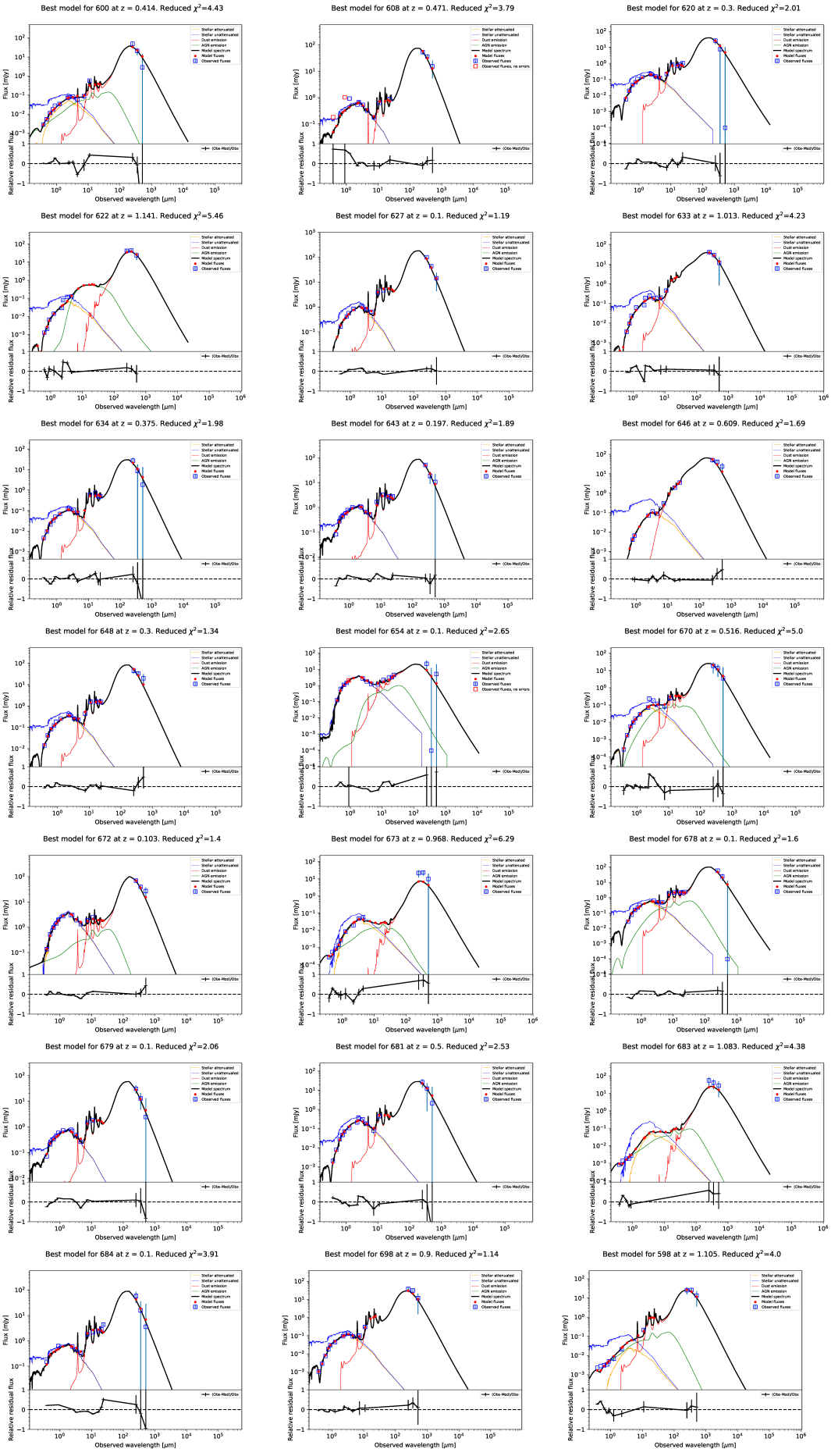

Figure A.6: Same as Figure A.1

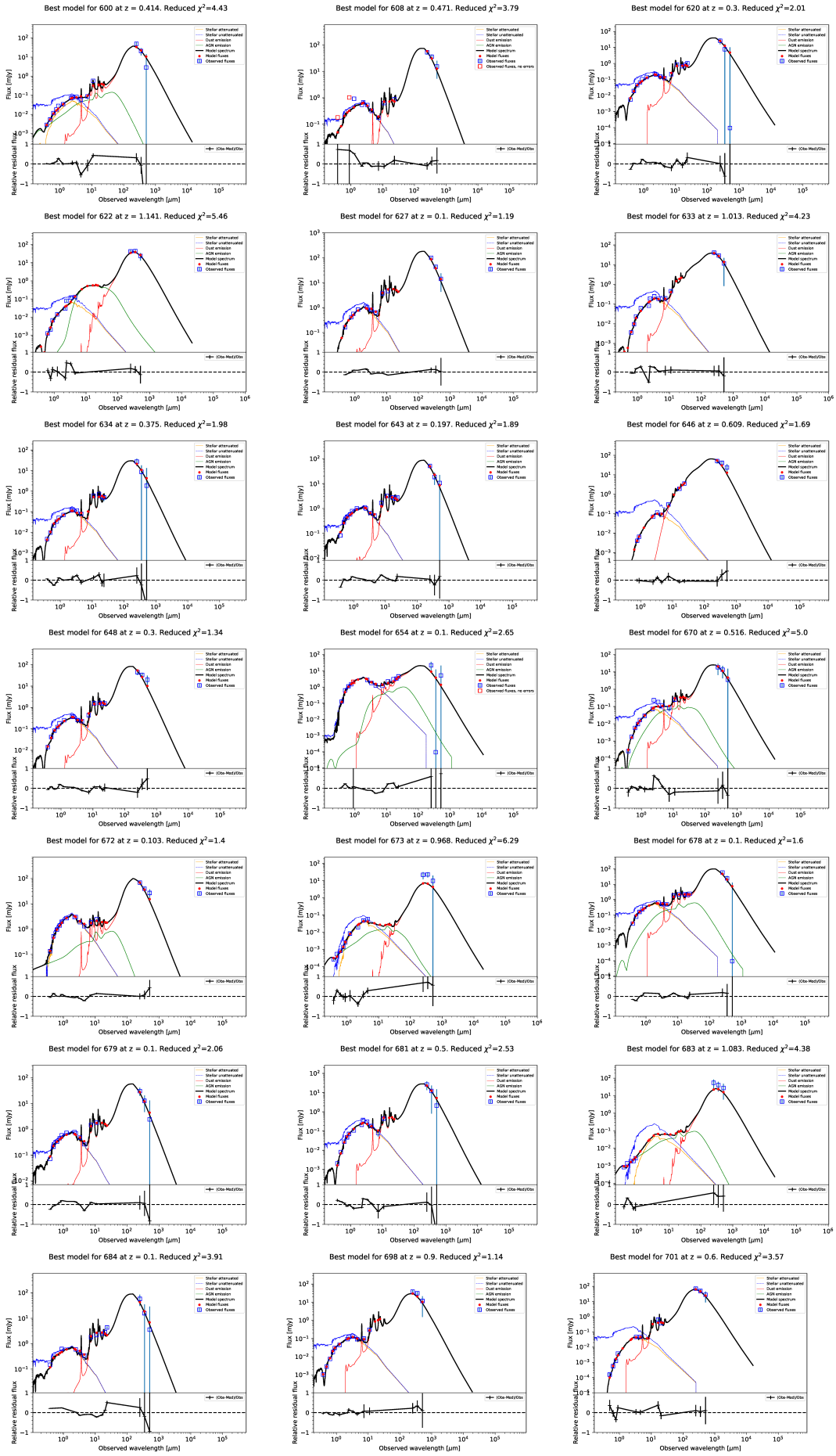

Figure A.7: Same as Figure A.1

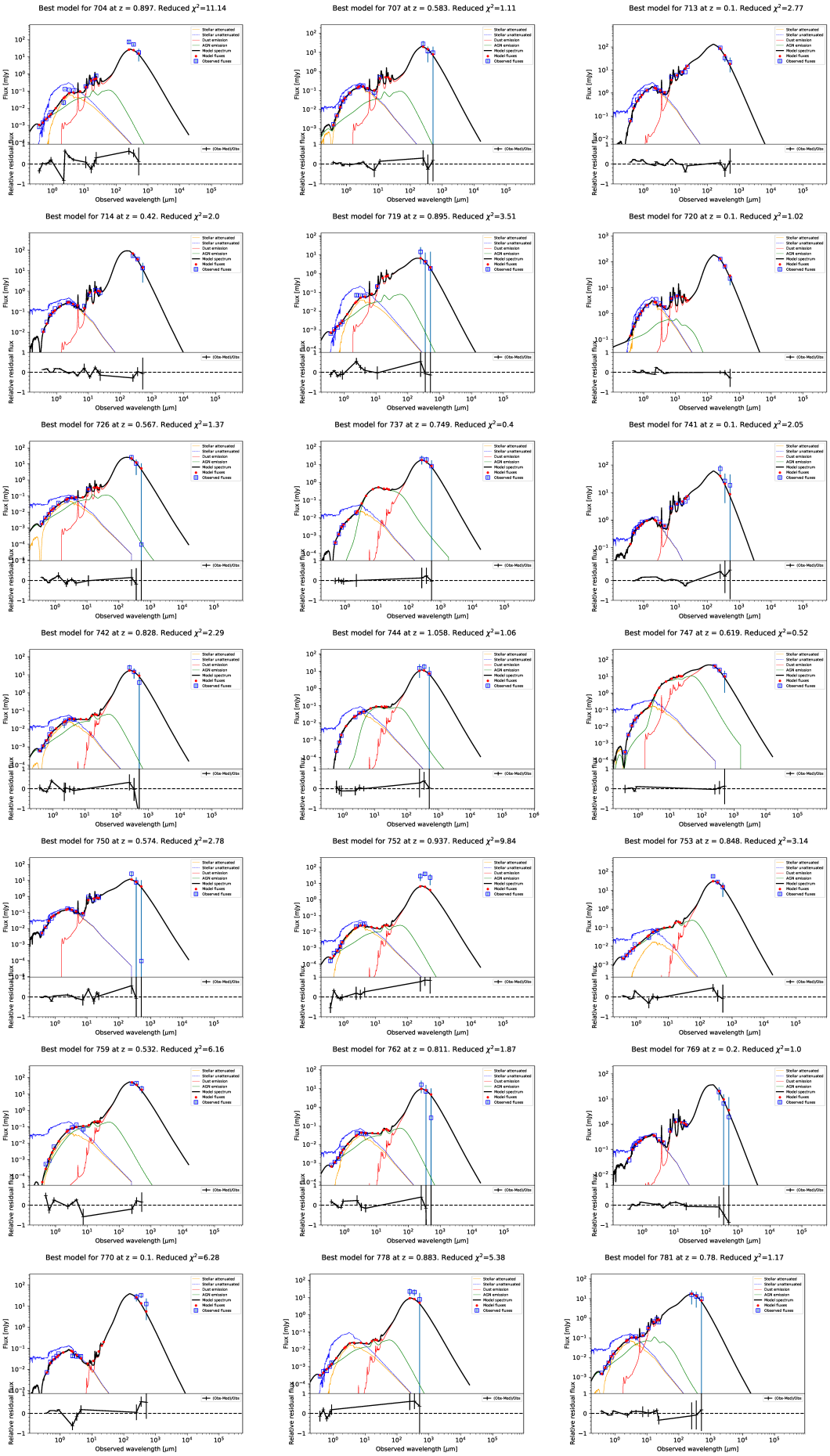

Figure A.8: Same as Figure A.1

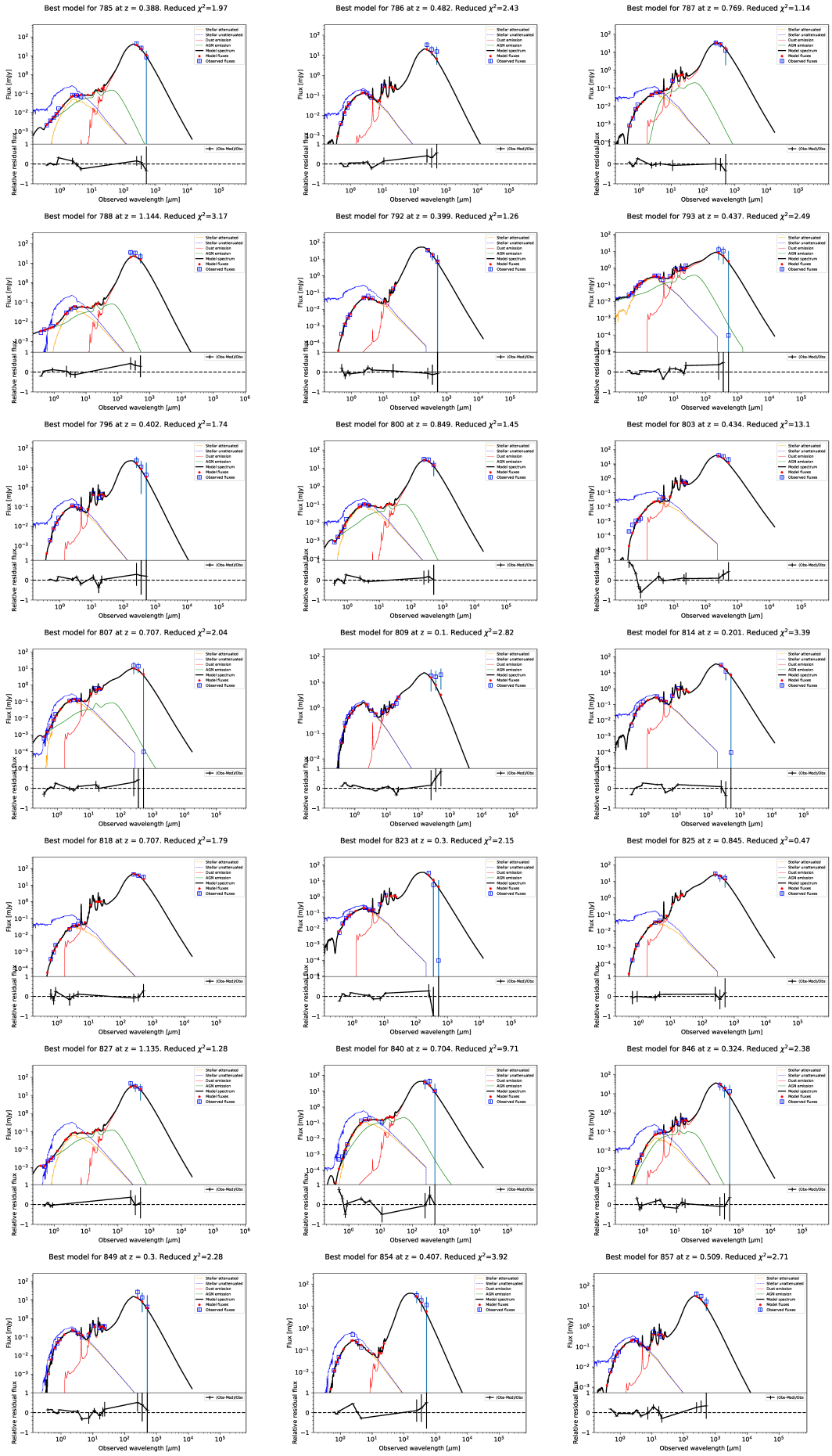

Figure A.9: Same as Figure A.1

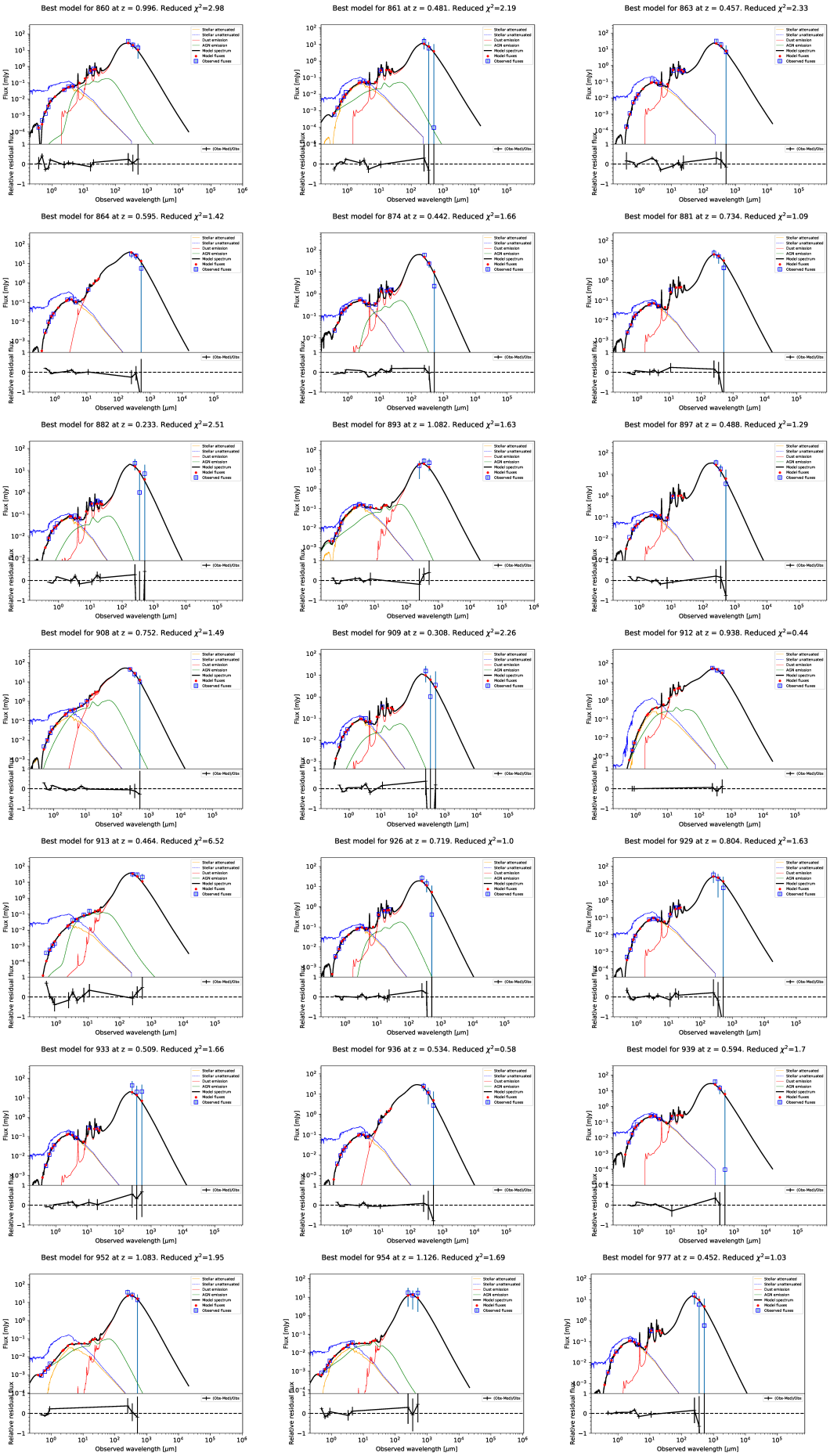

Figure A.10: Same as Figure A.1

A.3 Lens candidates postage stamps and SEDs

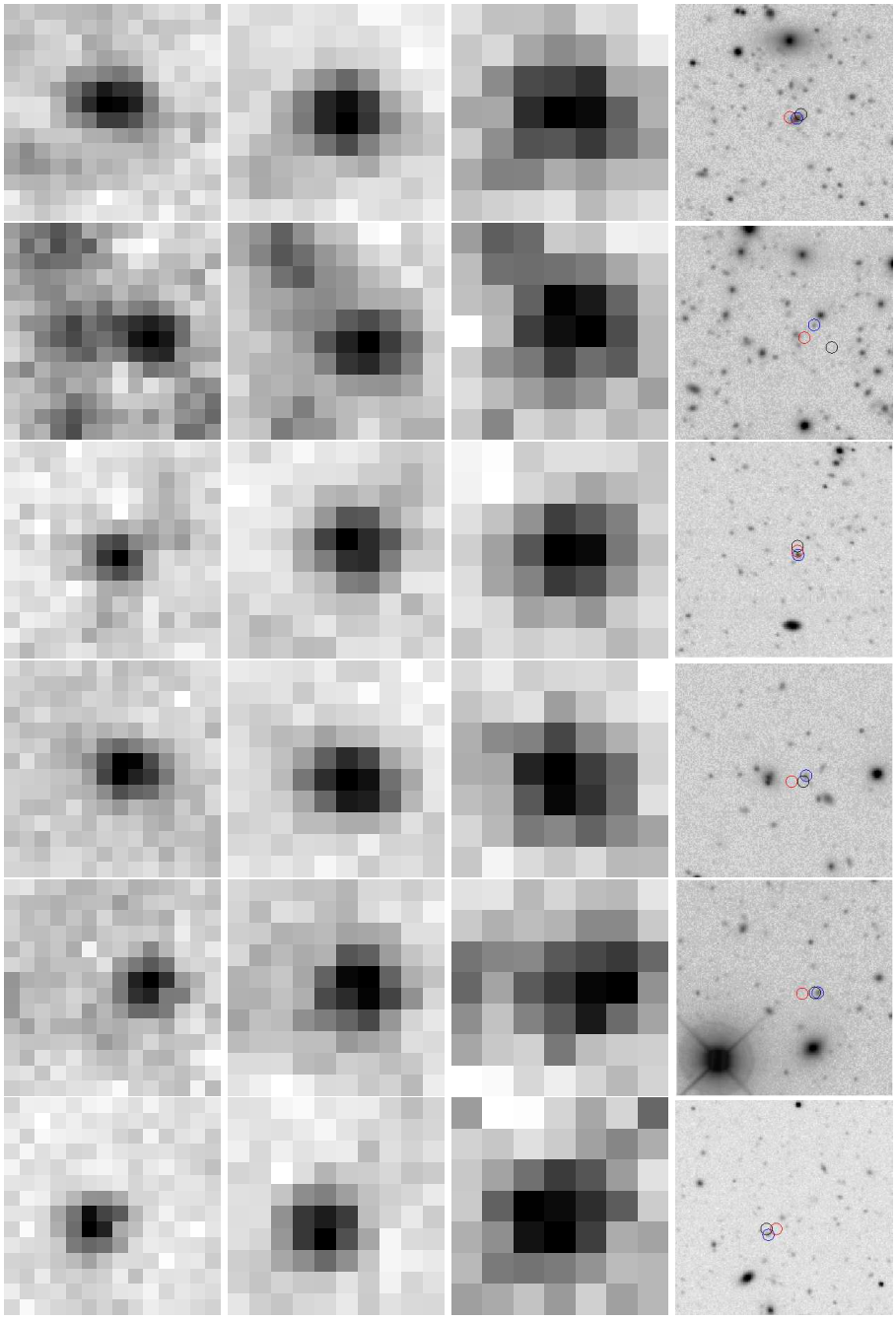

Figure A.11: Lens candidates images for the sources in the same order as Table 5.5 and centered at the table coordinates with a size of 1.4x1.4 arcmin. Each row shows the same source at FIR wavelengths (250 μm, 350 μm and 500 μm respectively) and the 4th image in each row corresponds to the R-band detection from our catalogue. The coordinates of the R-band, 24 μm and 500 μm positions are over-plotted in blue, black and red circles respectively.

A.4 List of DOGs candidates and SEDs.

RA	Dec	Rmag	$F_{24\mu m}$ [mJy]	RA	Dec	Rmag	$F_{24\mu m}$ [mJy]
72.144	-53.990	25.7±0.4	0.668±0.02	72.703	-52.093	24.7±0.22	0.456±0.02
72.034	-52.276	25.2±0.3	0.447±0.02	73.357	-53.256	24.5±0.22	0.988±0.02
71.331	-52.489	25.0±0.3	0.985±0.02	72.613	-52.326	24.7±0.22	0.446±0.02
72.112	-53.607	25.0±0.3	0.393±0.02	72.263	-53.854	24.5±0.22	0.563±0.02
72.822	-52.932	24.9±0.3	0.544±0.02	72.627	-52.047	24.6±0.22	1.212±0.02
72.802	-53.016	25.0±0.3	0.352±0.02	72.232	-52.258	24.7±0.22	0.459±0.02
72.222	-52.865	25.0±0.3	1.231±0.02	72.058	-53.588	24.6±0.22	0.670±0.02
72.756	-52.980	24.9±0.3	1.018±0.02	71.555	-52.691	24.6±0.22	0.879±0.02
72.442	-52.409	25.0±0.3	0.398±0.02	72.522	-53.566	24.5±0.22	0.704±0.02
71.969	-53.010	25.0±0.3	0.393±0.02	71.389	-54.028	24.4±0.22	1.018±0.02
72.677	-53.049	24.9±0.3	0.403±0.02	72.668	-52.969	24.5±0.22	1.019±0.02
71.975	-52.438	24.9±0.3	0.399±0.02	72.355	-53.814	24.4±0.22	1.129±0.02
72.267	-53.057	24.9±0.3	0.515±0.02	71.788	-52.323	24.5±0.22	0.733±0.02
72.549	-53.120	24.9±0.3	0.542±0.02	72.648	-52.455	24.6±0.12	0.489±0.02
72.703	-53.889	24.8±0.3	0.848±0.02	72.763	-52.716	24.5±0.22	0.924±0.02
72.179	-52.315	24.9±0.2	0.630±0.02	72.377	-53.783	24.5±0.22	0.580±0.02
72.482	-52.137	24.8±0.2	0.759±0.02	71.835	-53.959	24.1±0.12	1.008±0.02
72.527	-52.852	24.9±0.2	0.555±0.02	72.934	-52.959	24.2±0.12	0.930±0.02
72.484	-52.496	24.8±0.2	0.405±0.02	73.460	-52.763	24.1±0.12	0.826±0.02
72.723	-52.599	24.8±0.2	0.696±0.02	72.170	-52.832	24.1±0.12	0.814±0.02
72.357	-53.647	24.7±0.3	0.602±0.02	72.185	-54.042	24.1±0.12	1.058±0.02
72.667	-52.414	24.8±0.3	0.426±0.02	72.625	-52.851	24.2±0.12	0.919±0.02
72.656	-53.968	24.7±0.3	0.949±0.02	71.977	-52.662	24.0±0.12	1.062±0.02
72.453	-52.170	24.7±0.2	0.939±0.02	71.145	-52.685	24.4±0.12	0.613±0.02
72.478	-52.617	24.7±0.2	0.850±0.02	72.745	-52.146	24.7±0.22	0.499±0.02
72.030	-53.888	24.7±0.3	0.503±0.02	72.668	-53.043	24.6±0.2	0.575±0.02
71.913	-53.893	24.6±0.3	0.506±0.02	73.082	-53.088	24.1±0.2	1.062±0.02
72.266	-52.600	24.6±0.3	3.648±0.04	72.614	-53.879	24.8±0.2	0.434±0.02
68.636	-53.279	22.9±0.1	2.357±0.055	69.945	-54.205	24.0±0.2	0.990±0.02
69.247	-53.084	22.8±0.1	4.110±0.02	72.099	-52.276	24.0±0.2	0.921±0.02
70.952	-53.719	22.8±0.1	2.793±0.043	72.307	-52.366	24.3±0.2	0.737±0.02
70.490	-53.341	22.8±0.1	5.733±0.02	72.219	-52.782	24.3±0.2	0.752±0.02
72.518	-52.364	24.2±0.1	1.267±0.02	72.136	-52.835	24.6±0.2	0.616±0.02
73.242	-53.781	24.0±0.1	1.372±0.02	72.270	-52.249	24.5±0.2	0.829±0.02
72.487	-52.510	24.3±0.1	1.378±0.02	72.675	-52.143	24.4±0.2	0.867±0.02
71.153	-52.466	24.0±0.1	3.933±0.038	70.936	-52.890	24.4±0.2	0.670±0.02
70.786	-52.954	23.8±0.2	1.105±0.02	73.141	-53.112	24.3±0.2	2.436±0.04
72.286	-53.078	24.0±0.1	1.022±0.02	72.327	-52.191	24.5±0.2	0.544±0.02
72.028	-53.837	22.5±0.1	3.848±0.068				

Table A.18: The table shows the total 157 DOGs candidates. Main parameters of the DOGs candidates: coordinates (RA and Dec in the optical R-band), the R-magnitude and error, flux and error at $24\mu m$ from the Spitzer catalogue (Clements et al., 2011).

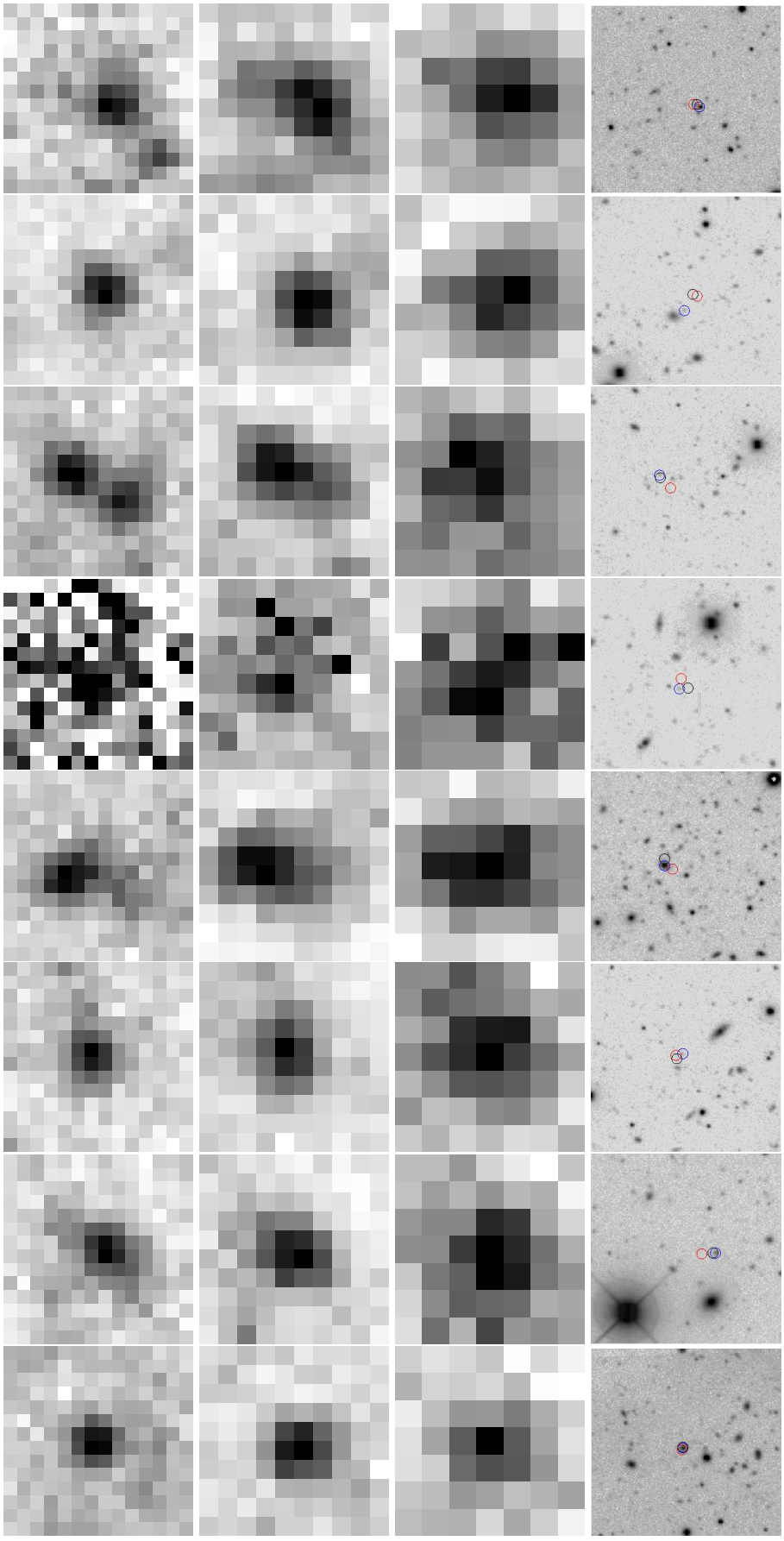

Figure A.12: Same as Figure A.11

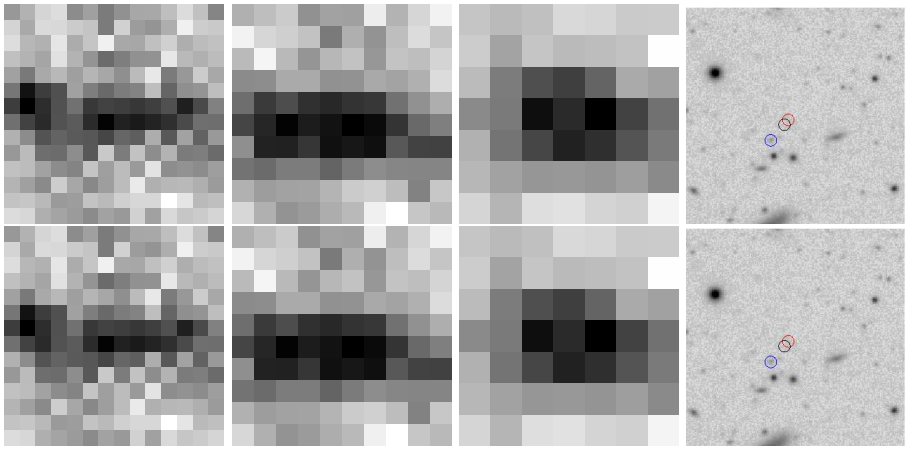

Figure A.13: Same as Figure A.11

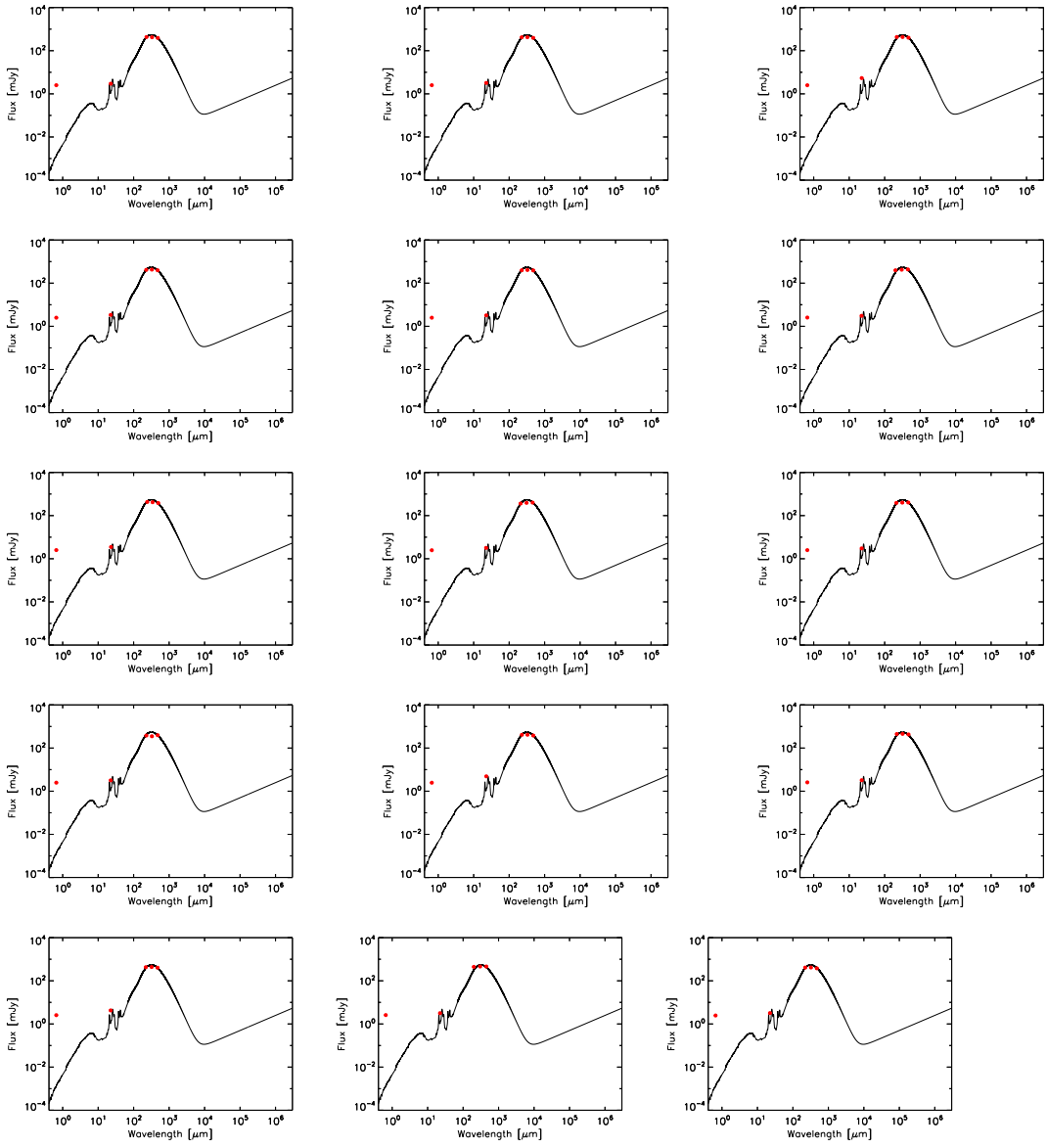

Figure A.14: The figure shows the SEDs of the total 15 final lens candidates after checking by eye and removing the sources that are nearby galaxies.

RA	Dec	Rmag	$F_{24\mu m}$ [mJy]	RA	Dec	Rmag	$F_{24\mu m}$ [mJy]
73.036	-53.403	24.0±0.2	0.890±0.02	72.755	-53.626	24.4±0.2	0.672±0.02
73.086	-53.101	24.0±0.2	2.715±0.044	71.846	-52.421	24.5±0.2	0.627±0.02
72.079	-52.440	24.4±0.1	1.097±0.02	71.065	-52.542	24.6±0.2	0.669±0.02
72.118	-52.516	24.2±0.1	1.036±0.02	71.086	-52.672	24.4±0.2	0.725±0.02
71.653	-52.902	23.8±0.1	1.833±0.02	71.501	-52.659	24.3±0.2	0.709±0.02
73.086	-52.787	24.0±0.2	0.869±0.02	72.611	-52.741	24.4±0.2	0.640±0.02
72.775	-52.977	24.4±0.1	1.105±0.02	72.598	-52.576	24.5±0.2	1.033±0.02
71.161	-52.842	24.2±0.1	1.073±0.02	71.215	-54.069	24.2±0.2	1.393±0.02
71.906	-52.901	23.8±0.1	1.971±0.02	71.835	-53.426	23.7±0.2	2.262±0.063
72.488	-52.816	24.1±0.1	1.298±0.02	72.952	-53.002	23.7±0.1	2.512±0.02
71.610	-53.828	23.9±0.2	2.697±0.02	71.824	-53.233	23.6±0.2	1.902±0.02
73.503	-52.784	23.9±0.2	1.725±0.02	71.355	-52.818	23.8±0.1	1.014±0.02
71.906	-52.611	23.8±0.1	1.172±0.02	72.751	-52.214	23.8±0.1	1.270±0.02
72.666	-52.309	24.4±0.1	0.782±0.02	73.647	-53.387	24.3±0.2	1.074±0.02
73.540	-52.831	23.7±0.1	3.530±0.02	71.969	-52.500	24.6±0.2	0.561±0.02
71.451	-54.367	23.0±0.1	2.423±0.046	72.152	-53.103	24.4±0.2	0.616±0.02
68.286	-53.560	22.6±0.1	6.602±0.02	71.455	-53.988	24.3±0.2	0.993±0.02
71.516	-52.775	23.1±0.1	2.422±0.045	72.190	-53.772	24.3±0.2	0.984±0.02
69.895	-54.194	22.0±0.1	5.756±0.02	70.972	-52.589	24.2±0.2	0.767±0.02
73.196	-53.390	22.6±0.1	3.604±0.038	72.353	-52.924	24.5±0.2	0.566±0.02
71.763	-53.069	21.8±0.1	7.455±0.02	71.819	-54.171	24.3±0.2	1.625±0.02
71.258	-52.775	24.5±0.1	0.682±0.02	72.559	-52.696	24.5±0.2	0.778±0.02
71.341	-52.713	23.8±0.1	2.156±0.02	72.353	-52.505	24.6±0.2	0.949±0.02
71.373	-52.655	24.0±0.1	0.975±0.02	71.913	-52.612	24.4±0.2	0.664±0.02
70.493	-53.498	23.5±0.2	2.831±0.034	73.114	-53.052	24.2±0.2	0.762±0.02
70.617	-54.314	23.7±0.2	3.791±0.02	72.152	-52.190	24.3±0.2	0.722±0.02
72.919	-52.765	23.8±0.1	1.759±0.02	72.575	-52.545	24.2±0.2	1.195±0.02
71.609	-52.903	23.7±0.1	3.016±0.042	71.934	-52.306	24.4±0.2	0.681±0.02
71.770	-54.183	23.2±0.1	2.657±0.02	73.346	-53.623	24.3±0.2	0.781±0.02
72.462	-53.730	23.2±0.1	1.986±0.02	71.632	-52.296	24.3±0.2	1.241±0.02
72.569	-52.358	23.2±0.1	2.752±0.049	72.150	-52.914	24.4±0.2	0.608±0.02
72.277	-52.246	23.4±0.1	2.808±0.051	72.560	-52.658	24.3±0.2	0.975±0.02
73.199	-53.082	23.6±0.1	1.915±0.02	72.376	-54.110	24.3±0.2	1.287±0.02
71.980	-52.248	23.0±0.1	2.487±0.039	71.579	-52.864	24.4±0.2	1.021±0.02
73.329	-52.784	22.9±0.1	3.335±0.02	72.421	-52.938	24.3±0.2	0.795±0.02
73.117	-53.677	23.6±0.1	2.329±0.061	71.922	-52.282	24.2±0.2	0.849±0.02
69.320	-54.139	22.8±0.1	3.168±0.02	71.853	-52.252	24.6±0.2	0.894±0.02
71.692	-53.278	22.8±0.1	7.229±0.02	71.111	-52.478	24.3±0.2	0.684±0.02
73.597	-52.852	23.2±0.1	2.153±0.056	71.049	-52.882	24.3±0.2	0.723±0.02
70.699	-54.155	22.9±0.1	4.174±0.02	71.981	-52.516	24.3±0.2	0.862±0.02

Table A.19: Same as in Table A.18.

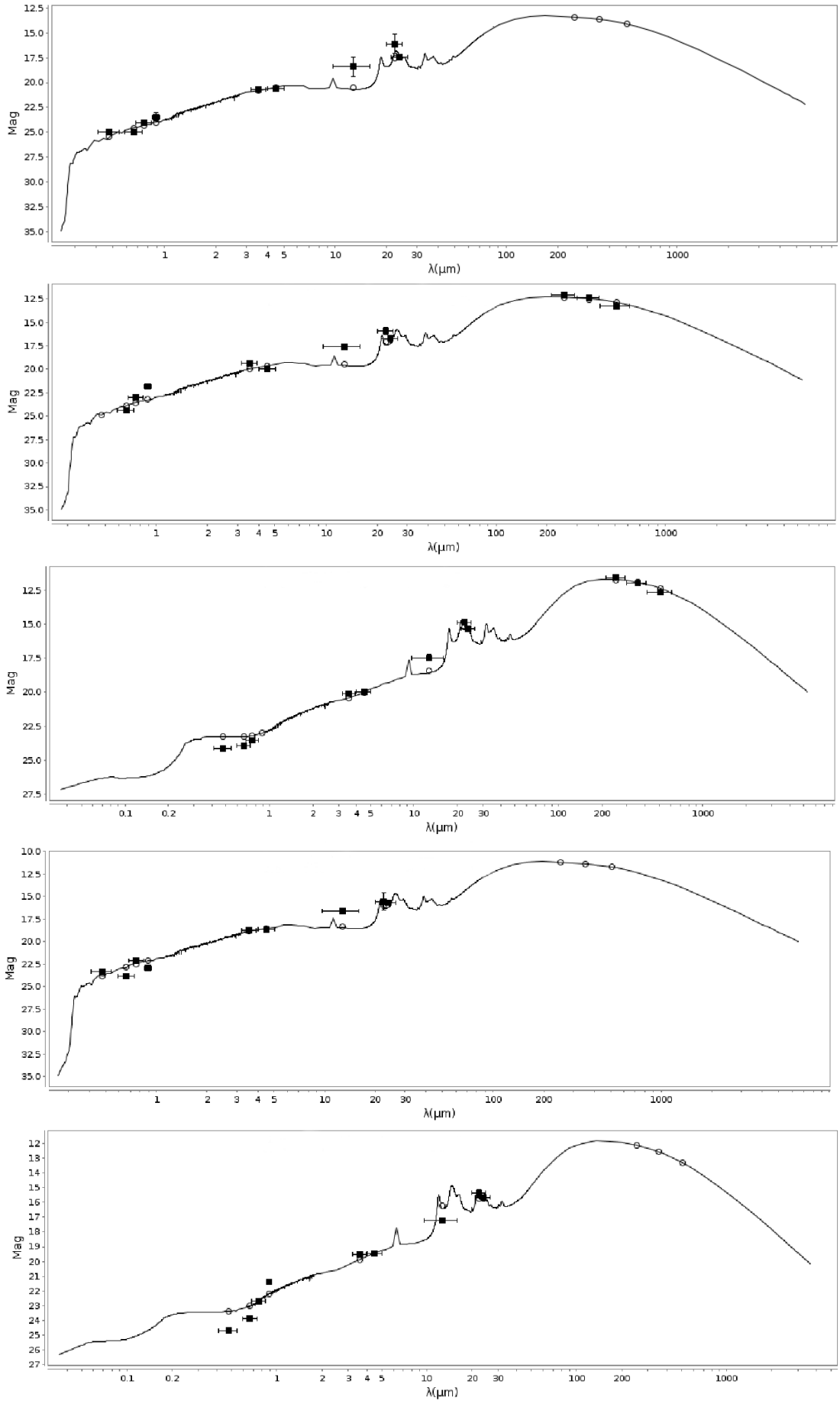

Figure A.15: The plot shows the SED of the 15 DOGs candidates. The filled squares show the observation and the empty dots show the theoretical values of the template.

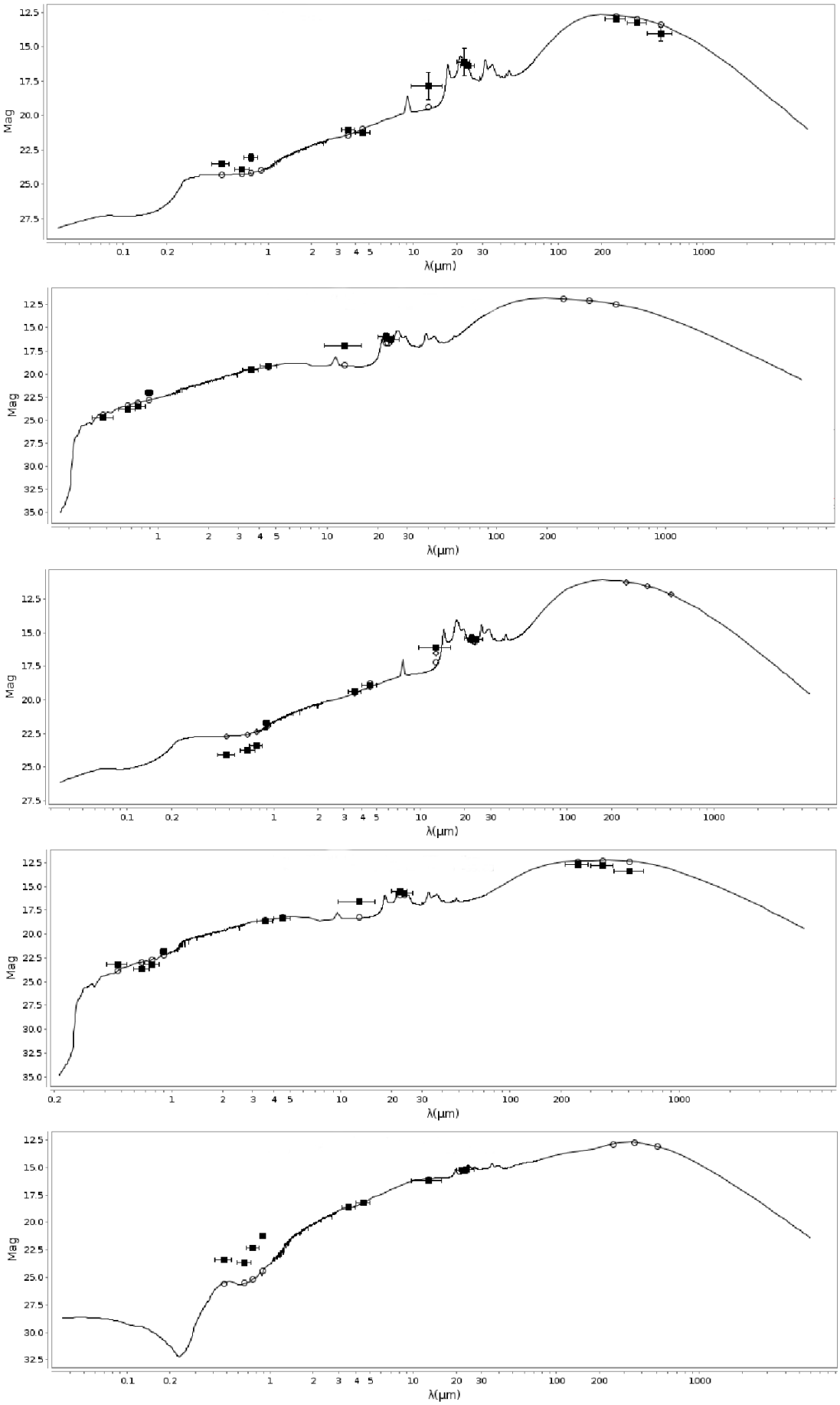

Figure A.16: Same as in Figure A.15

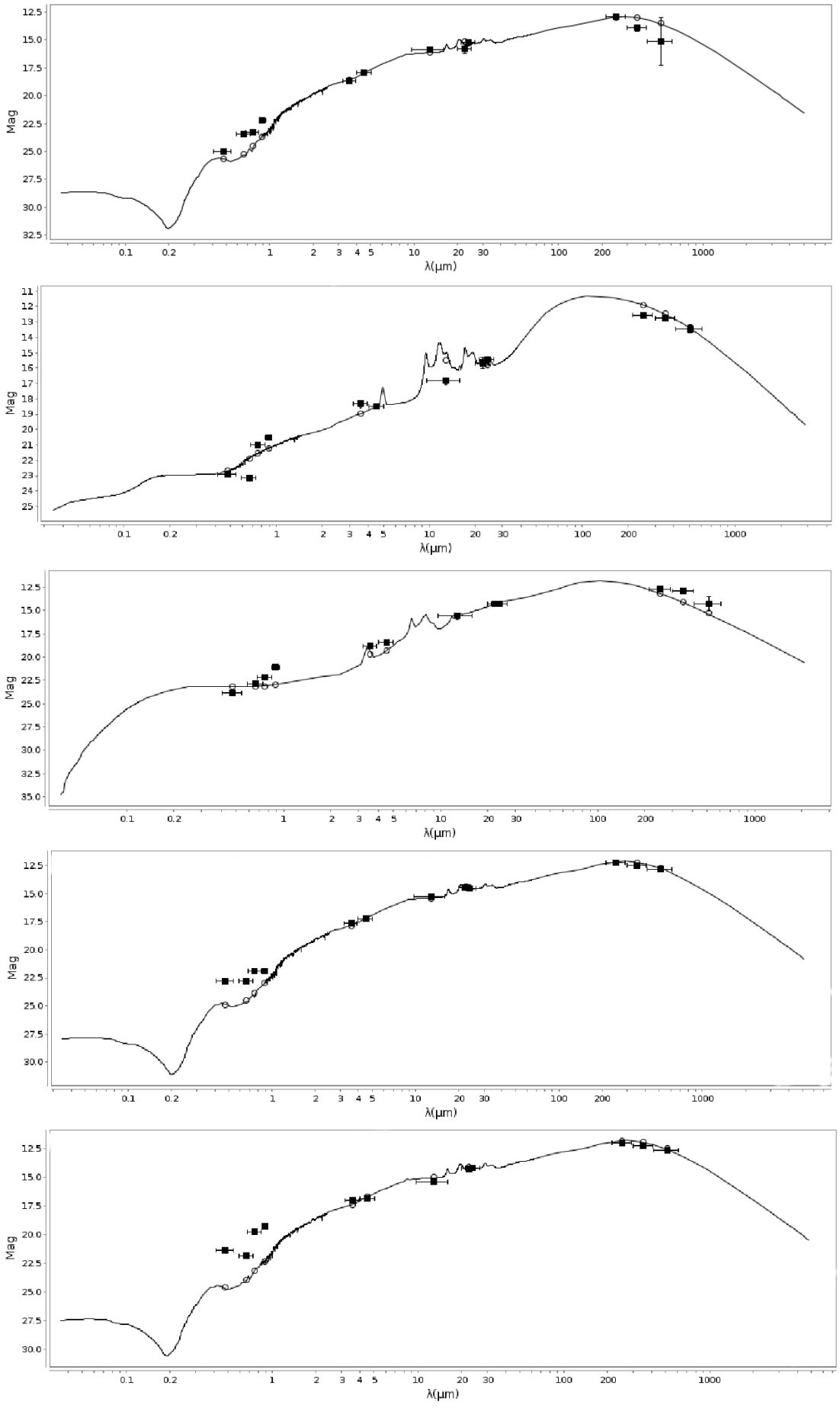

Figure A.17: Same as in Figure A.15

Bibliography

Amblard A. et al., 2010, Astronomy and Astrophysics, 518, L9

Antonucci R., 1993, Anual Review, 31, 473

Appleton P. N. et al., 2004, The Astrophysical Journal, 154, 147

Aravena M. et al., 2016, Astrophysical Journal, 833, 68

Arnouts S., Ilbert O., 2011, LePHARE: Photometric Analysis for Redshift Estimate. Astrophysics Source Code Library

Asboth V. et al., 2016, Monthly Notices of the RAS, 462, 1989

Assef R. J. et al., 2010, Astrophysical Journal, 713, 970

Barger A. J., Cowie L. L., Owen F. N., Chen C.-C., Hasinger G., Hsu L.-Y., Li Y., 2015, Astrophysical Journal, 801, 87

Barger A. J., Cowie L. L., Sanders D. B., Fulton E., Taniguchi Y., Sato Y., Kawara K., Okuda H., 1998, Nature, 394, 248

Baronchelli I., 2015, PhD thesis, Padova University

Baronchelli I. et al., 2018, Astrophysical Journal, 857, 64

Baronchelli I. et al., 2016, Astrophysical Journal, Supplement, 223, 1

Barrufet L. et al., 2017, Publication of Korean Astronomical Society, 32, 267

Barrufet L., Pearson C. S. S. B. I. . W. G., 2016, MNRAS

Berta S. et al., 2013, Astronomy and Astrophysics, 551, A100

Bertin E., 2003, SExtractor. Institut d'Astrophysique & Observatoire de Paris

Bertin E., 2010, SWarp: Resampling and Co-adding FITS Images Together. Astrophysics Source Code Library

Bertin E., Arnouts S., 2010, SExtractor: Source Extractor. Astrophysics Source Code Library

Bianchi L., 2014, Astrophysics and Space Science, 354, 103

Blain A. W., Smail I., Ivison R. J., Kneib J.-P., Frayer D. T., 2002, Physics Reports, 369, 111

Bonzini M. et al., 2015, Monthly Notices of the RAS, 453, 1079

Bonzini M., Padovani P., Mainieri V., Kellermann K. I., Miller N., Rosati P., Tozzi P., Vattakunnel S., 2013, MNRAS, 436, 3759

Boulanger F., Boisssel P., Cesarsky D., Ryter C., 1998, Astronomy and Astrophysics, 339, 194

Bouwens R. J. et al., 2011, Astrophysical Journal, 737, 90

Bower R. G., Benson A. J., Malbon R., Helly J. C., Frenk C. S., Baugh C. M., Cole S., Lacey C. G., 2006, Monthly Notices of the RAS, 370, 645

Bracco A. et al., 2011, Monthly Notices of the RAS, 412, 1151

Brammer G. B., van Dokkum P. G., Coppi P., 2008, Astrophysical Journal, 686, 1503

Brand K. et al., 2006, Astrophysical Journal, 644, 143

Bruzual G., Charlot S., 2003, Monthly Notices of the RAS, 344, 1000

Buat V. et al., 2014, Astronomy and Astrophysics, 561, A39

Bussmann R. S. et al., 2012, Astrophysical Journal, 744, 150

Calzetti D., 2001, Publications of the ASP, 113, 1449

Calzetti D., Armus L., Bohlin R. C., Kinney A. L., Koornneef J., Storchi-Bergmann T., 2000, Astrophysical Journal, 533, 682

Carilli C. L., Yun M. S., 1999, The Astrophysical Journal, 513, L13

Casey C. M., 2012, Monthly Notices of the RAS, 425, 3094

Casey C. M. et al., 2012, Astrophysical Journal, 761, 140

Casey C. M., Narayanan D., Cooray A., 2014, Physics Reports, 541, 45

Chabrier G., 2003, Publications of the ASP, 115, 763

Chapman S. C., Blain A. W., Smail I., Ivison R. J., 2005, Astrophysical Journal, 622, 772

Charlot S., Fall S. M., 2000, Astrophysical Journal, 539, 718

Ciesla L. et al., 2016, Astronomy and Astrophysics, 585, A43

Ciesla L., Elbaz D., Fensch J., 2017, Astronomy and Astrophysics, 608, A41

Clements D. L., 2017, Publication of Korean Astronomical Society, 32, 275

Clements D. L., Bendo G., Pearson C., Khan S. A., Matsuura S., Shirahata M., 2011, VizieR Online Data Catalog, 741

Condon J. J., 1992, Annual Review, 30, 575

da Cunha E., Charlot S., Elbaz D., 2008, Monthly Notices of the RAS, 388, 1595

da Cunha E. et al., 2015, Astrophysical Journal, 806, 110

Daddi E. et al., 2007, Astrophysical Journal, 670, 156

Davidge H., Serjeant S., Pearson C., Matsuhara H., Wada T., Dryer B., Barrufet L., 2017, Monthly Notices of the RAS, 472, 4259

de Graauw T. et al., 2010, Astronomy and Astrophysics, 518, L6

Dey A. et al., 2008, Astrophysical Journal, 677, 943

Díaz-Santos T. et al., 2013, Astrophysical Journal, 774, 68

Dole H. et al., 2006, Astronomy and Astrophysics, 451, 417

Donley, 2012, The Astrophysical Journal , 748:142 (22pp), 748, 142

Dowell C. D. et al., 2014, Astrophysical Journal, 780, 75

Draine B. T., Lee H. M., 1984, Astrophysical Journal, 285, 89

Draine B. T., Li A., 2007, Astrophysical Journal, 657, 810

Duivenvoorden S. et al., 2018, Monthly Notices of the RAS, 477, 1099

Dunlop J. S. et al., 2017, Monthly Notices of the RAS, 466, 861

Dunne L., Eales S., Edmunds M., Ivison R., Alexander P., Clements D. L., 2000, Monthly Notices of the RAS, 315, 115

Elbaz D. et al., 2007, Astronomy and Astrophysics, 468, 33

Elbaz D. et al., 2011, Astronomy and Astrophysics, 533, A119

Elbaz D. et al., 2017, Submitted A&A

Fadda D., Lari C., Rodighiero G., Franceschini A., Elbaz D., Cesarsky C., Perez-Fournon I., 2004, VizieR Online Data Catalog, 342, 70023

Farrah D. et al., 2013, Astrophysical Journal, 776, 38

Fazio G. G. et al., 2004, Astrophysical Journal, Supplement, 154, 10

Fritz J., Franceschini A., Hatziminaoglou E., 2006, Monthly Notices of the RAS, 366, 767

Fudamoto Y. et al., 2017, Monthly Notices of the RAS, 472, 2028

Geach J. E. et al., 2016, Astrophysical Journal, 832, 37

González-Nuevo J. et al., 2012, The Astronomical Journal, 749, 65

Graham A. W., Driver S. P., Petrosian V., Conselice C. J., Bershady M. A., Crawford S. M., Goto T., 2005, Astronomical Journal, 130, 1535

Griffin M. J. et al., 2010, Astronomy and Astrophysics, 518, L3

Hatsukade B. et al., 2011, VizieR Online Data Catalog, 741

Holland W. et al., 2006, in Proceedings of the SPIE, Vol. 6275, Society of Photo-Optical Instrumentation Engineers (SPIE) Conference Series, p. 62751E

Holwerda B. W., 2003, Source Extractor dor Dummies. Space Telescope Science Institute, Baltimore USA

Hopkins A. M., 2004, Astrophysical Journal, 615, 209

Houck J. R. et al., 2005, Astrophysical Journal, Letters, 622, L105

Hughes D. H. et al., 1998, Nature, 394, 241

Ikarashi S. et al., 2017, Astrophysical Journal, Letters, 849, L36

Ivison, 2012, Monthly Notices of the Royal Astronomical Society, 1320

Ivison R. J. et al., 2010, Astronomy and Astrophysics, 518, L31

Juneau S. et al., 2013, Astrophysical Journal, 764, 176

Kawada M. et al., 2007, Publications of the ASJ, 59, S389

Kennicutt, Jr. R. C., 1983, The Astronomical Journal, 272, 54

Kennicutt, Jr. R. C., 1998, Annual Review of Astron and Astrophys, 36, 189

Kessler M. F. et al., 1996, Astronomy and Astrophysics, 315, L27

Kim S. J. et al., 2012, Astronomy and Astrophysics, 548, A29

Koprowski M. P. et al., 2016, Monthly Notices of the RAS, 458, 4321

Kovács A., Chapman S. C., Dowell C. D., Blain A. W., Ivison R. J., Smail I., Phillips T. G., 2006, Astronomical Journal, 650, 592

Kron R. G., 1980, Astrophysical Journal, Supplement, 43, 305

Krumpe M. et al., 2015, VizieR Online Data Catalog, 744

Lacy, 2004, The Astrophysical Journal Supplement Series, 166

Lacy, 2007, The Astronomical Journal, 186Y205

Lake S. E., Wright E. L., Petty S., Assef R. J., Jarrett T. H., Stanford S. A., Stern D., Tsai C.-W., 2012, Astronomical Journal, 143, 7

Laurent O., Mirabel I. F., Charmandaris V., Gallais P., Madden S. C., Sauvage M., Vigroux L., Cesarsky C., 2000, Astronomy and Astrophysics, 359, 887

Le Floc'h E. et al., 2005, Astrophysical Journal, 632, 169

Lonsdale C. et al., 2004, Astrophysical Journal, Supplement, 154, 54

Lonsdale C. J., Farrah D., Smith H. E., 2006, Ultraluminous Infrared Galaxies, Mason J. W., ed., p. 285

Madau P., Pozzetti L., Dickinson M., 1998, Astrophysical Journal, 498, 106

Magnelli B. et al., 2015, A&A, 573, A45

Magnelli B. et al., 2014, A&A, 561, A86

Maraston C., 2005, Monthly Notices of the RAS, 362, 799

Martin D. C. et al., 2005, Astrophysical Journal, Letters, 619, L1

Matsuhara H. et al., 2006, Astronomical Society of Japan, 58, 673

Melbourne J. et al., 2012, Astronomical Journal, 143, 125

Michałowski M., Hjorth J., Watson D., 2010, Astronomy and Astrophysics, 514, A67

Miettinen O. et al., 2017, Astronomy and Astrophysics, 597, A5

Mingo B. et al., 2016, Monthly Notices of the RAS, 462, 2631

Monet D. G. et al., 2003, Astronomical Journal, 125, 984

Mortier A. M. J. et al., 2005, Monthly Notices of the RAS, 363, 563

Moshir M., 1991, Journal of the British Interplanetary Society, 44, 495

Muller G. P., Reed R., Armandroff T., Boroson T. A., Jacoby G. H., 1998, in Society of Photo-Optical Instrumentation Engineers (SPIE) Conference Series, Vol. 3355, Optical Astronomical Instrumentation, D'Odorico S., ed., pp. 577–585

Murakami H. et al., 2007, Publications of the ASJ, 59, S369

Murata K. et al., 2013, A&A, 559, A132

Nayyeri H. et al., 2017, Astrophysical Journal, 844, 82

Nayyeri H. et al., 2018, Astrophysical Journal, Supplement, 234, 38

Negrello, 2010, Science, 300, 800

Negrello M. et al., 2017, Monthly Notices of the RAS, 465, 3558

Netzer H., 2015, Annual Review of Astron and Astrophys, 53, 365

Neugebauer G. et al., 1984, Astrophysical Journal, Letters, 278, L1

Nguyen H. T. et al., 2010, Astronomy and Astrophysics, 518, L5

Noeske K. G. et al., 2007, Astrophysical Journal, Letters, 660, L43

Noll S., Burgarella D., Giovannoli E., Buat V., Marcillac D., Mu∼noz-Mateos J. C., 2009, Astronomy and Astrophysics, 507, 1793

Oi, 2014, Astronomy and Astrophysics, A60

Oliver S. et al., 2000, Monthly Notices of the RAS, 316, 749

Oliver S. J. et al., 2012, Monthly Notices of the RAS, 424, 1614

Onaka T. et al., 2007, Publications of the ASJ, 59, S401

Padovani, 2009, The Astrophysical Journal, 235–246

Padovani, 2014, Proceedings IAU Symposium

Padovani P. et al., 2017, Astronomy and Astrophysics Reviews, 25, 2

Page M. J. et al., 2012, Nature, 485, 213

Pearson, 2018, Monthly Notices of the Royal Astronomical Society, 175P

Pearson C. P. et al., 2010, Astronomy and Astrophysics, 514, A9

Peeters E., Spoon H. W. W., Tielens A. G. G. M., 2004, Astrophysical Journal, 613, 986

Pilbratt G. L. et al., 2010, Astronomy and Astrophysics, 518, L1

Poglitsch A. et al., 2010, Astronomy and Astrophysics, 518, L2

Polletta M. et al., 2007, Astrophysical Journal, 663, 81

Pope A. et al., 2008, Astrophysical Journal, 675, 1171

Riechers D. A. et al., 2013, Nature, 496, 329

Riechers D. A. et al., 2017, Astrophysical Journal, 850, 1

Rieke G. H. et al., 2004, Astrophysical Journal, Supplement, 154, 25

Rigopoulou D., Spoon H. W. W., Genzel R., Lutz D., Moorwood A. F. M., Tran Q. D., 1999, Astronomical Journal, 118, 2625

Rowan-Robinson, 2014, Monthly. Notices of the Royal Astronnomical Society, 445, 3848

Rowan-Robinson M., 1992, Monthly Notices of the RAS, 258, 787

Rowan-Robinson M. et al., 1991, Nature, 351, 719

Rowan-Robinson M., Crawford J., 1989, Monthly Notices of the RAS, 238, 523

Rowan-Robinson M. et al., 2016, Monthly Notices of the RAS, 461, 1100

Salpeter E. E., 1955, Astrophysical Journal, 121, 161

Sanders D. B., Mirabel I. F., 1996, Annual Review of Astron and Astrophys, 34, 749

Sanders D. B., Soifer B. T., Elias J. H., Madore B. F., Matthews K., Neugebauer G., Scoville N. Z., 1988, Astrophysical Journal, 325, 74

Sargent M. T. et al., 2014, Astrophysical Journal, 793, 19

Sargsyan L. et al., 2012, Astrophysical Journal, 755, 171

Saunders W. et al., 2000, Monthly Notices of the RAS, 317, 55

Sawicki M., 2002, Astronomical Journal, 124, 3050

Schlegel D. J., Finkbeiner D. P., Davis M., 1998, Astrophysical Journal, 500, 525

Schloerb F. P., Carrasco L., Brinks E., 2007, The Large Millimeter Telescope, Lobanov A. P., Zensus J. A., Cesarsky C., Diamond P. J., eds., Springer-Verlag, p. 47

Schneider P., 2006, Extragalactic Asstronomy ans Cosmology, York S. B. H. N., ed.

Schreiber C., Elbaz D., Pannella M., Ciesla L., Wang T., Koekemoer A., Rafelski M., Daddi E., 2016, Astronomy and Astrophysics, 589, A35

Scott D., Pierfederici F., Swaters R. A., Thomas B., Valdes F. G., 2007, in Astronomical Society of the Pacific Conference Series, Vol. 376, Astronomical Data Analysis Software and Systems XVI, Shaw R. A., Hill F., Bell D. J., eds., p. 265

Serjeant S., Gruppioni C., Oliver S., 2002, Monthly Notices of the RAS, 330, 621

Seymour N., Huynh M., Dwelly T., Symeonidis M., Hopkins A., McHardy I. M., Page M. J., Rieke G., 2009, Monthly Notices of the Royal Astronomical Society, 398, 1573

Shankar F., Weinberg D. H., Miralda-Escudé J., 2009, Astrophysical Journal, 690, 20

Shim H. et al., 2013, VizieR Online Data Catalog, 220

Siebenmorgen R., Krügel E., 2007, Astronomy and Astrophysics, 461, 445

Silk J., Rees M. J., 1998, Astronomy and Astrophysics, 331, L1

Smail I., Ivison R. J., Blain A. W., 1997, Astrophysical Journal, Letters, 490, L5

Smith R. C., Dickinson M., Lowry S., Miller C. J., Trueblood M., Valdes F., 2007, in Astronomical Society of the Pacific Conference Series, Vol. 376, Astronomical Data Analysis Software and Systems XVI, Shaw R. A., Hill F., Bell D. J., eds., p. 615

Speagle J. S., Steinhardt C. L., Capak P. L., Silverman J. D., 2014, Astrophysical Journal, Supplement, 214, 15

Spoon H. W. W. et al., 2004, Astrophysical Journal, Supplement, 154, 184

Stern, 2012, The Astrophysical Journal, 753, 30

Stern D. et al., 2005, Astrophysical Journal, 631, 163

Stickel M. et al., 2000, Astronomy and Astrophysics, 359, 865

Strandet M. L. et al., 2017, Astrophysical Journal, Letters, 842, L15

Swaters R. A., Valdes F. G., 2007, in Astronomical Society of the Pacific Conference Series, Vol. 376, Astronomical Data Analysis Software and Systems XVI, Shaw R. A., Hill F., Bell D. J., eds., p. 269

Swinbank A. M. et al., 2014, Monthly Notices of the RAS, 438, 1267

Valdes F., 2003, The reduction of CCD Mosaic Data. Nationa Optical Astronomy Observatories

Valdes F. G., Swaters R. A., 2007, in Astronomical Society of the Pacific Conference Series, Vol. 376, Astronomical Data Analysis Software and Systems XVI, Shaw R. A., Hill F., Bell D. J., eds., p. 273

Valiante E. et al., 2010, Astrophysical Journal, Supplement, 191, 222

Vlahakis C., Eales S., Dunne L., 2007, Monthly Notices of the RAS, 379, 1042

Walcher C. J. et al., 2008, Astronomy and Astrophysics, 491, 713

Walcher J., Groves B., Budavári T., Dale D., 2011, Astrophysics and Space Science, 331, 1

Walter F. et al., 2012, Astrophysical Journal, 752, 93

Wang L. et al., 2014, Monthly Notices of the RAS, 444, 2870

Wardlow J. L. et al., 2013, Astrophysical Journal, 762, 59

Werner M. W. et al., 2004a, Astrophysical Journal, Supplement, 154, 1

Werner M. W. et al., 2004b, Astrophysical Journal, Supplement, 154, 1

White, in prep.

White G. J. et al., 2017, Publication of Korean Astronomical Society, 32, 231

White G. J. et al., 2012, Monthly Notices of the RAS, 427, 1830

White G. J. et al., 2010, Astronomy and Astrophysics, 517, A54

Wilkinson A. et al., 2017, Monthly Notices of the RAS, 464, 1380

Windhorst R. A., 2003, New Astronomy Review, 47, 357

Wright E. L. et al., 2010, Astronomical Journal, 140, 1868

Zavala J. A. et al., 2018, Nature Astronomy, 2, 56